Chapter 3

Copper(II) complexes incorporating NNN-tridentate hydrazone as proligand

Part (A): Synthesis and structural characterization of Copper(II) complexes with flexible hydrazone: Structural diversity, Hirshfeld analysis, density functional calculations and biological study

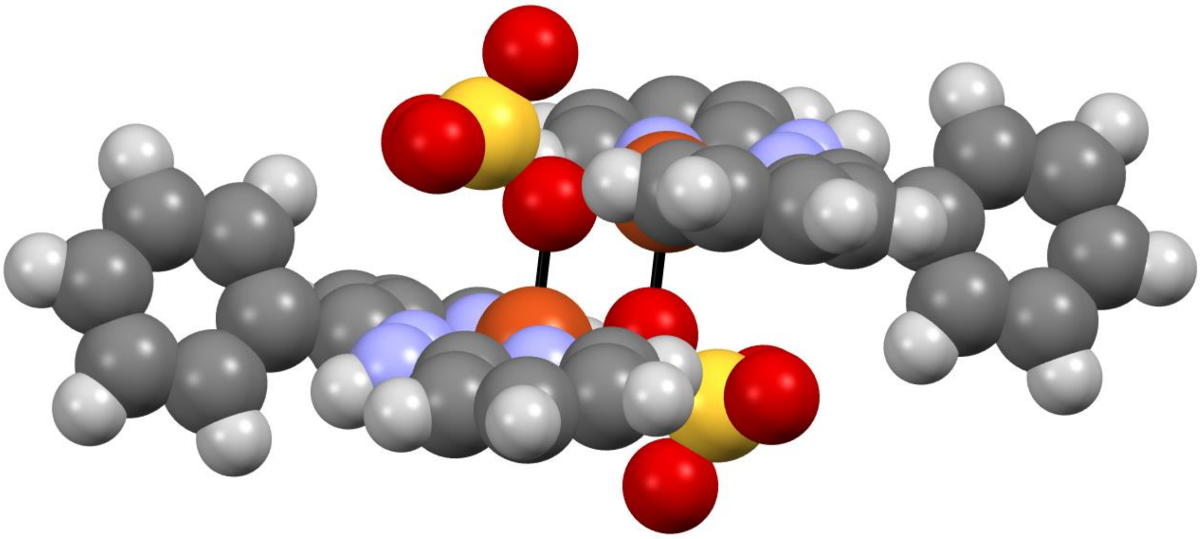

1 Introduction

The design and synthesis of binuclear complexes secured considerable attention owing to their interesting physicochemical properties [1-4]. Binuclear complexes of ions rendered the basis of the field of molecular magnetism and offered a new idea in chemistry and physics [5-9]. The two metal centres should be able to interact magnetically, which has led to the synthesis of binuclear complexes which is an area of ongoing research interest of inorganic chemists [10]. Sulphate bridged binuclear complexes are of much importance owing to their wide applications in synthetic, biological and supramolecular chemistry [11-17]. Sulphate anions are interesting because they can bind the metal centres in a bidentate, tridentate, or bridging mode [18-22].

Hydrazones are considered privileged ligands and are used for the synthesis of various metal complexes. The hydrazone copper complexes are attractive models for the demonstration of the active site of biological copper enzymes [23-33]. The enzymatic properties of such enzymes are associated with the coordination sites of the metal active centres [34]. Copper(II) complexes with hydrazones show the features of superoxide dismutase (SOD) metalloenzymes and act as a bio-inspired catalyst for the dismutation of superoxide anion ($O_2^{\cdot -}$). SOD functions as an important antioxidant defense against various diseases like cancer, diabetes, cardiovascular problems, Ischemia-reperfusion injury and aging [35]. The above objective has been performed with the synthesis, characterization and bioactivity measurements of two new copper(II) complexes viz., $[Cu(Cl)_2(L)]$ **1** and $[Cu_2(\mu\text{-}SO_4)_2(L)_2]$ **2**. Quantum chemical calculations were also carried to provide the nature of orbitals along with structural parameters.

2. Experimental

2.1 Materials and instrumentation

All solvents were dried and distilled before their use following standard procedures [36]. Reagent grade chemicals were used throughout and HPLC grade solvents were employed for spectroscopic studies. The metal salts were purchased from Sigma-Aldrich Chemical Co. Pvt. Ltd. and used as received.

2.2 Synthesis of Ligand HL

Schiff base ligand HL = (Z)-2-(phenyl(2-(pyridin-2-yl)hydrazono)methyl)pyridine was synthesized by taking 2-hydrazinopyridine (1.091g, 10 mmol) in absolute ethanol (50 mL) and 2-benzoyl pyridine (0.78g, 10 mmol) was added with few drops of glacial acetic acid as a catalyst. The synthesis of a ligand is shown in Scheme 1. The resultant mixture was stirred at room temperature for 30 min and then refluxed at 75°C for 3 hrs. The yellowish solution was filtered and the filtrate was kept for slow evaporation at room temperature to yield a light-yellow polycrystalline sample. The Schiff base was washed with ethanol and dried over fused $CaCl_2$.

Yield: 75%. Anal. Calc. for $C_{17}H_{14}N_4$ (274.33 g mol^{-1}): C, 74.52; H, 5.54; N, 20.04%. Found: C, 74.55; H, 5.51; N, 20.06%. FTIR (KBr, cm^{-1}): 1592 ν(C=N). ^1H NMR (DMSO-d_6 400 MHz) δ: 12.9 (s, 1H, -NH-), 8.8 (d, 2H, CH=N) 8.0-7.2 (t, 3H, CH benzylidenimin), 8.8–7.8 (m, 8H, CH 2-pyridiene) ppm. ^{13}C NMR (DMSO-d_6 400 MHz) δ: 156 (CH=N-), 152 (Ar-CH=N), 152 (C-NH-), 149-105 (Ar-C) ppm.

2.3. Synthesis of Complex$[Cu(Cl)_2(L)]$ 1

The Schiff base ligand (0.274g, 1.0 mmol) was dissolved in methanol (20 mL). A solution of $CuCl_2.2H_2O$ (0.134 g, 1.0 mmol) in methanol (20 mL) was added dropwise to the above solution with stirring for 5 hrs to give a green colour solution. The resulting solution was filtered. The filtrate was left for slow evaporation at room temperature. Plate-like crystals were formed from the solution two weeks later. These crystals were washed with hot distilled water and then ethanol to remove impurities. The crystals were dried under a vacuum.

Yield: 80%. Anal. Calc. for $C_{17}H_{15}Cl_2CuN_4$ (408.77 g mol^{-1}): C, 49.80; H, 3.65; N, 13.61%. Found: C, 49.83; H, 3.69; N, 13.60%. FTIR (KBr, cm^{-1}): 1564 ν(C=N), 417 (s) ν(Cu–N).

2.4 Synthesis of Complex $[Cu_2(\mu\text{-}SO_4)_2(L)_2]$ 2

The Schiff base ligand (0.274 g, 1.0 mmol) was dissolved in methanol (20 mL). A solution of $CuSO_4.5H_2O$ (0.159 g, 1.0 mmol) in methanol (20 mL) was added dropwise to the above solution with stirring for 5 hrs to give a green clear solution. The resulting solution was filtered. The filtrate was left for slow evaporation at room temperature. Plate-like crystals were formed from the solution two weeks later. These crystals were washed with hot distilled water and then ethanol to remove impurities. The crystals were dried under a vacuum.

Yield: 80%. Anal. Calc. for $C_{68}H_{80}Cu_4N_{16}O_{28}S_4$ (1951.88 g mol^{-1}): C, 46.82; H, 3.75; N, 12.35%. Found: C, 46.84; H, 3.72; N, 12.32%. FTIR (KBr, cm^{-1}): 1568 ν(C=N), 462(s) ν(Cu-O), 417(s) ν(Cu–N).

2.5 Methods and physical measurements

Elemental analyses were carried out using an Elementar Vario EL III Carlo Erba 1108 Analyzer. NMR spectrum of the ligand was recorded in DMSO-d_6 on a Bruker Advance 400 (FT-NMR) multinuclear spectrometer. Chemical shifts were reported in parts per million (ppm) using tetramethylsilane (TMS) as an internal standard. The accelerating voltage was 10 kV and the spectra were recorded at room temperature. UV-vis spectra were recorded at room temperature using a Shimadzu UV-vis Spectrophotometer UV-1601 in quartz cells. Infrared (IR) spectra (4000-400cm^{-1}) were collected using the KBr pellet technique on a Perkin-Elmer spectrophotometer. The low and room temperature electron paramagnetic resonance (Epr) spectra were recorded using a Varian E-line Century Series Spectrometer equipped with a dual cavity and operating at the X-band with 100 kHz modulation frequency. Varian quartz tubes were used for measuring Epr spectra of polycrystalline samples and frozen solutions. The Epr spectra were calibrated with tetracyanoethylene (TCNE) as a marker (g = 2.00277). The Epr parameters for copper(II) complexes were determined accurately from a computer simulation program19. Mass spectra of the ligand were recorded on Trace GC ultra DSQ II Cyclic voltammetry was performed using a BAS-100 Epsilon Electrochemical Analyzer on complexes in DMSO solutions using Ag/AgCl and glassy carbon as reference electrodes. All measurements were carried out at room temperature under a nitrogen atmosphere. The solutions were 10^{-3} mol dm^{-3} in the complex and 0.1 mol dm^{-3} in tetrabutylammonium perchlorate (TBAP) as a supporting electrolyte. Ferrocene (Fe) was added to the solution as an internal standard. Magnetic measurements at variable temperatures were performed on crushed single crystals of complexes using a Quantum Design MPMSXL SQUID (Superconducting Quantum Interference Device) magnetometer. The measurements were performed over a temperature range of 2–300 K under a magnetic field of 0.5 T. The data were corrected for the intrinsic diamagnetic contributions based on Pascal’s constants, the Temperature-Independent Paramagnetism (TIP) and the sample holder contribution. X-ray crystallographic data of complexes were collected on a Bruker APEX-II diffractometer using graphite monochromated MoKα radiation (λ = 0.71073 Å). The crystal orientation, cell refinement and intensity measurements were made using a CAD-4PC performing C-scan measurements. The structures were solved by direct methods using SHELXS-97 and refined by full-matrix least-squares using SHELXL-97 [37-40]. Crystallographic data of complexes collected on a Rigaku-Oxford Diffraction Gemini Eos diffractometer using graphite monochromated CuKα radiation (λ = 1.54184 Å) for L and graphite monochromated MoKα radiation for **1** and **2**, respectively. For both systems, all non-hydrogen atoms were refined anisotropically and all hydrogen atoms were geometrically fixed in the calculated positions. Crystals suitable for single-crystal X-ray analysis of all complexes were grown by slow evaporation of the reaction mixtures at room temperature. Single crystals suitable for dimensions for single-crystal X-ray analysis were mounted on glass fibers with the Bruker instrument and polymer loops with the Gemini instrument and used for data collection. A simultaneous TGA was performed using TG-DTA 6300 INCARP EXSTAR 6000 at a heating rate of 10 °C/min in the temperature range of 25-600 °C with a nitrogen atmosphere maintained throughout the measurement.

2.6 Computational study

Theoretical calculations by density functional theory (DFT) were performed regarding molecular structure optimization and HOMO-LUMO energies etc. of complexes **1** and **2**. Full geometry optimizations were carried out using the density functional theory (DFT) method at the B3LYP level for the complex [41]. All DFT calculations were carried out starting from the experimental single-crystal X-ray data as input geometries. All elements except Cu were assigned the LANL2DZ basis set [42]. LANL2DZ with effective core potential for Cu atom was used [43]. In the computational model, the cationic complex was taken into account. All calculations were carried out with the GAUSSIAN09 program [44], with the aid of the Gauss View visualization program. Vertical electronic excitations based on B3LYP optimized geometries were evaluated using the time-dependent density functional theory (TDDFT) formalism [45] in DMSO, using a conductor-like polarizable continuum model (CPCM) [46].

2.7 Antioxidant SOD activity

The antioxidant SOD activities of complexes **1** and **2** were assessed using alkaline DMSO as a source of superoxide radical ($O_2^{\bullet-}$) and nitro blue tetrazolium chloride (NBT) as scavengers [47-49]. The quantitative reduction of NBT to formazan $O_2^{\cdot -}$ was followed spectrophotometrically at 450 nm. The SOD activity was obtained by plotting the percentages of inhibition NBT reduction (%) *vs* the concentrations of complexes. The unit of SOD activity is the concentration of the enzyme or complex that induces 50% inhibition (IC_{50}) in the reduction of NBT. Two assays were carried out for each concentration of the metal complex.

2.8 Anti-cancer Activity

Antiproliferative properties of the present complexes studied *in vitro* on various carcinoma cell lines.

2.8.1 Cell culture condition

For cytotoxicity determination, we have used four different human cancer cell lines viz., IMR 32 (neuroblastoma), MCF 7 (breast cancer), HepG2 (hepatocellular carcinoma) and A549 (lung cells) were procured from the National center for cell science (NCCS), Pune. Cells were cultured in Dulbecco's Modified Eagle Medium (DMEM) supplemented with10% FBS and 1% antibiotics. All the cell lines were maintained at 37°C temperature with 100% relative humidity and 5% CO_2.

2.8.2 Cytotoxicity Assay

Cell viability was measured by using MTT assay (MTT = 3-(4,5-dimethyl-2-thiazolyl)-2,5-diphenyl-2H-tetrazolium bromide). Cells were seeded in 96 well plates at a density of 8000 cells/well and incubated overnight for cell adhesion. Cells were treated with a synthesized compound for 24 hrs and incubated at 37 °C temperature in a CO_2 incubator. Cisplatin was used as a reference drug. After incubation time, cells were washed by PBS and exposed to MTT (5 mg/mL) for 4 hrs in dark at 37 °C. The medium with MTT was removed and formed formazan crystal was dissolved in 200 ml of DMSO. At the end of the reaction, optical density was measured at 540nm using an ELISA plate reader (ELX800 Universal Microplate Reader, USA). % inhibition concentration was calculated using a formula of % inhibition concentration = 100 – (OD of treated/OD of Control) × 100.

3 Results and discussion

The copper(II) complexes having the general composition[$Cu(Cl)_2(L)$] **1** and [$Cu_2(\mu\text{-}SO_4)_2(L)_2$] **2** have been synthesized by a general procedure. These complexes have been characterized by FT-IR, UV–Vis, CV and X-ray analysis. The SOD and anti-cancer activity of complex have been also evaluated. The complexes are insoluble in water and non-polar solvents, but soluble in DMF, DMSO, acetonitrile and chlorinated solvents.

3.1 Synthesis and structural characterization

The reaction of Schiff base ligand HL = (Z)-2-(phenyl(2-(pyridin-2-yl)hydrazono)methyl)pyridine condensation of 2-hydrazino pyridine and 2-benzoyl pyridine with either $CuCl_2.2H_2O$ and $Cu(SO_4).5H_2O$ in a 1:1 molar ratio yields [$Cu(Cl)_2(L)$] **1** and [$Cu_2(\mu\text{-}SO_4)_2(L)_2$] **2**, in which the NH group of HL remains deprotonated (Table 1). The synthetic routes used for the synthesis of **1** and **2** are depicted in Scheme 2. These complexes were synthesized in good yield. Both complexes **1** and **2** are air-stable. All general characterizations were carried out with crystalline samples. Microanalyses showed that the components of both complexes are well consistent with the results of molecular structural analysis. Single crystal X-ray analysis showed that complex **1** is mononuclear whereas **2** is the binuclear complex.

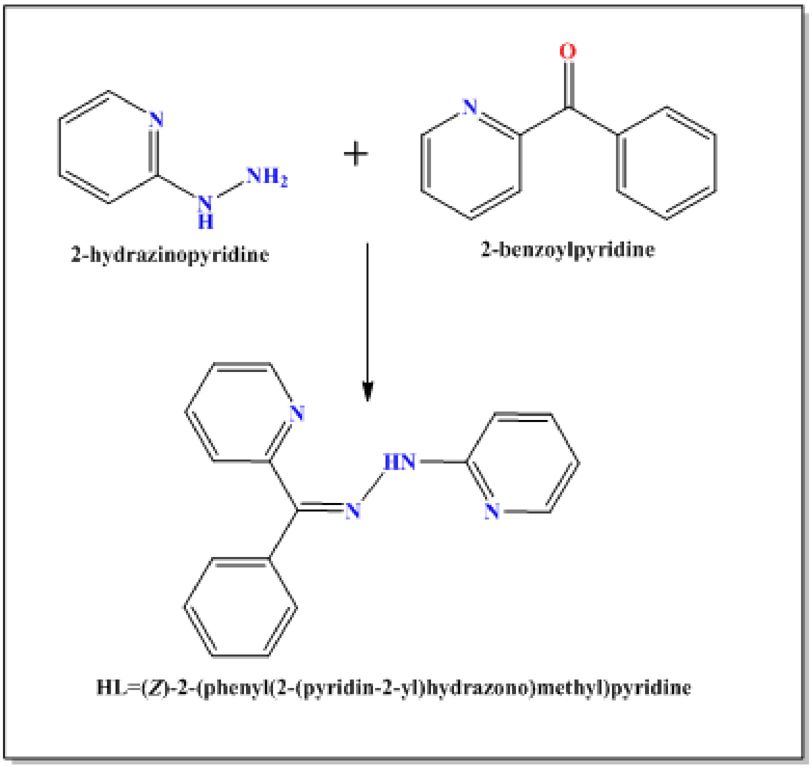

Scheme 1 Synthetic route of Ligand (**HL**).

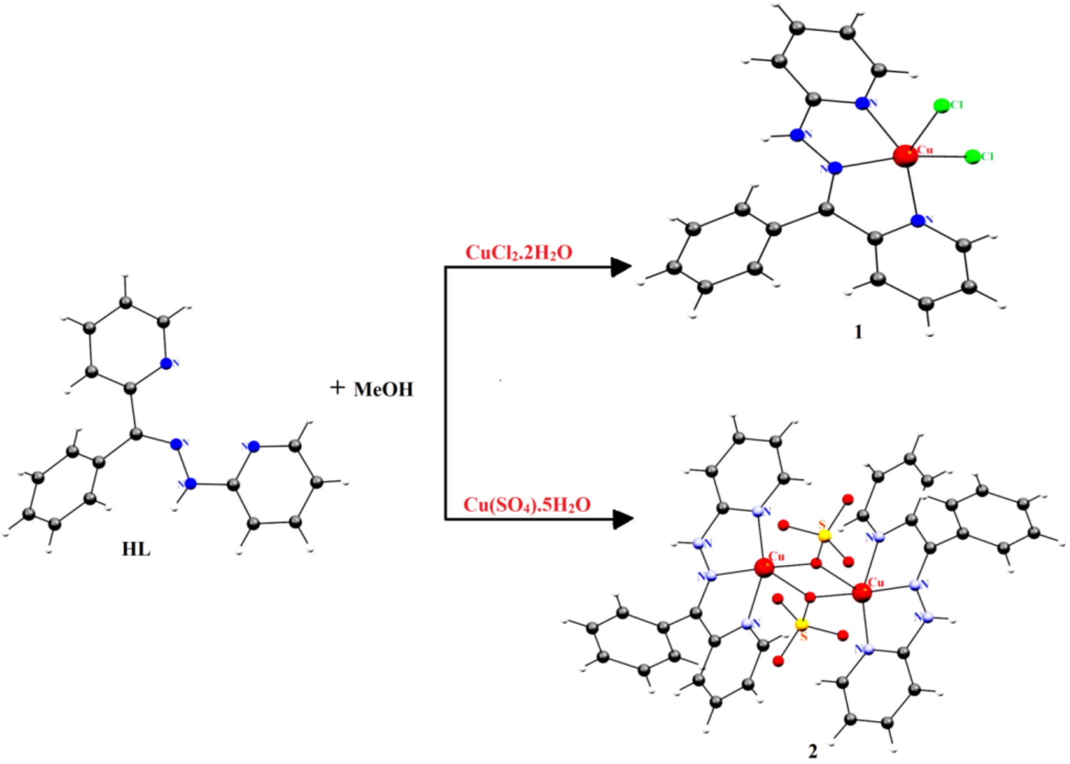

Scheme 2 Synthetic route of metal complexes **1** and **2.**

Table 1 Physical and elemental analysis of ligand and complexes.

Compound	Yield (%)	M.P. (°C)	MW g/mol	Colour	Λ^b	Elemental Analysis (%)		
						C	H	N
HL	75	140	274.32	Yellow	5.34	74.45(74.43)	5.14 (5.14)	20.42(20.42)
1	84	>250	408.76	Green	14.26	49.95(49.90)	3.45 (3.46)	13.70 (13.71)
2	82	>250	866.01	Green	22.04	47.06(47.08)	3.25 (3.27)	12.91 (12.92)

[a] **Molar conductance (Ω^{-1} cm^2 mol^{-1}) of 10^{-3} M solutions in DMSO.**

[b] **Calculated values are given in parentheses**

3.2 NMR spectra of ligand

The ^1H and ^{13}C NMR spectra of ligand (HL) were performed in DMSO-d_6 solvent to get information about the crystal structure. In proton NMR of ligand, we observed that (-NH-) proton peak is obtained at 12.9 ppm. Similarly, the aromatic ring proton (CH=N-) peak is observed at 8.8 ppm. Aromatic (CH=CH) proton peak is observed at ~ 8 ppm. All other aromatic peak is observed in the range of 7.9 to 6.8 ppm. In the ^{13}C-NMR spectrum of ligand azomethine (-CH=N), carbon peak at 156 ppm and (-C-NH-) carbon peak is obtained at 152 ppm. Similarly, all other carbon peaks aromatic and aliphatic are observed in the range 149 to 105 ppm. The ^1H and ^{13}C NMR spectra of ligand (HL) are shown in Fig. 1 and 2.

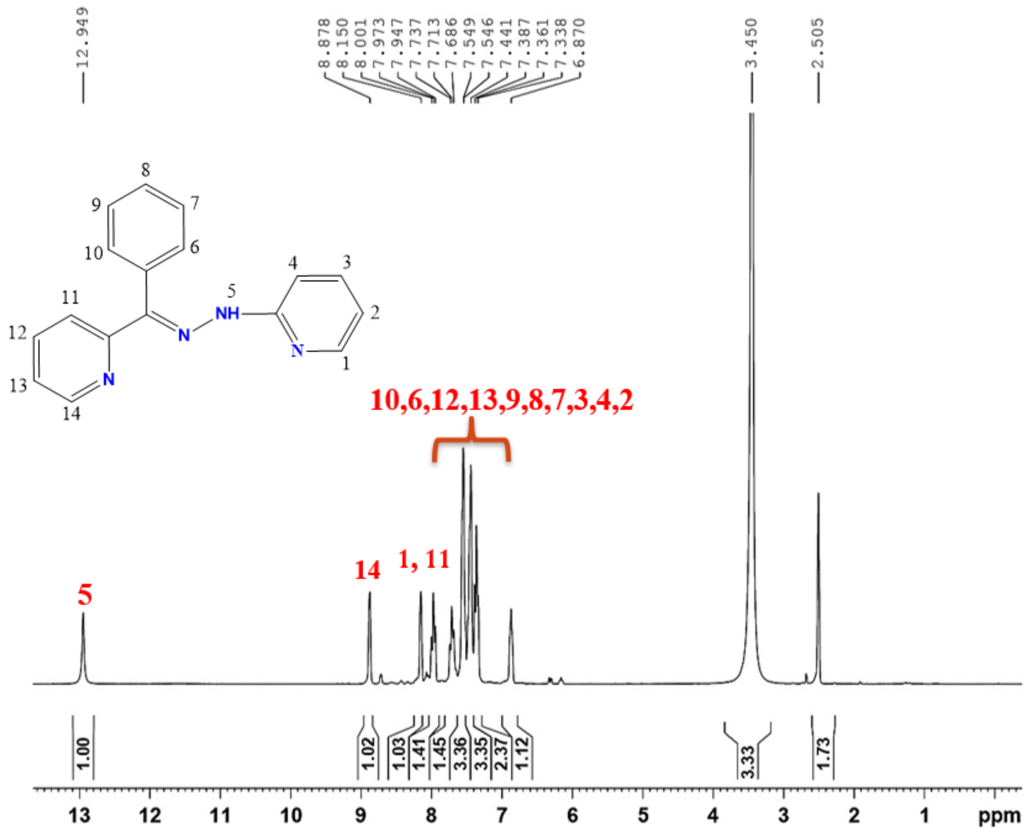

Fig. 1. ^{1}H NMR spectrum of Ligand **HL.**

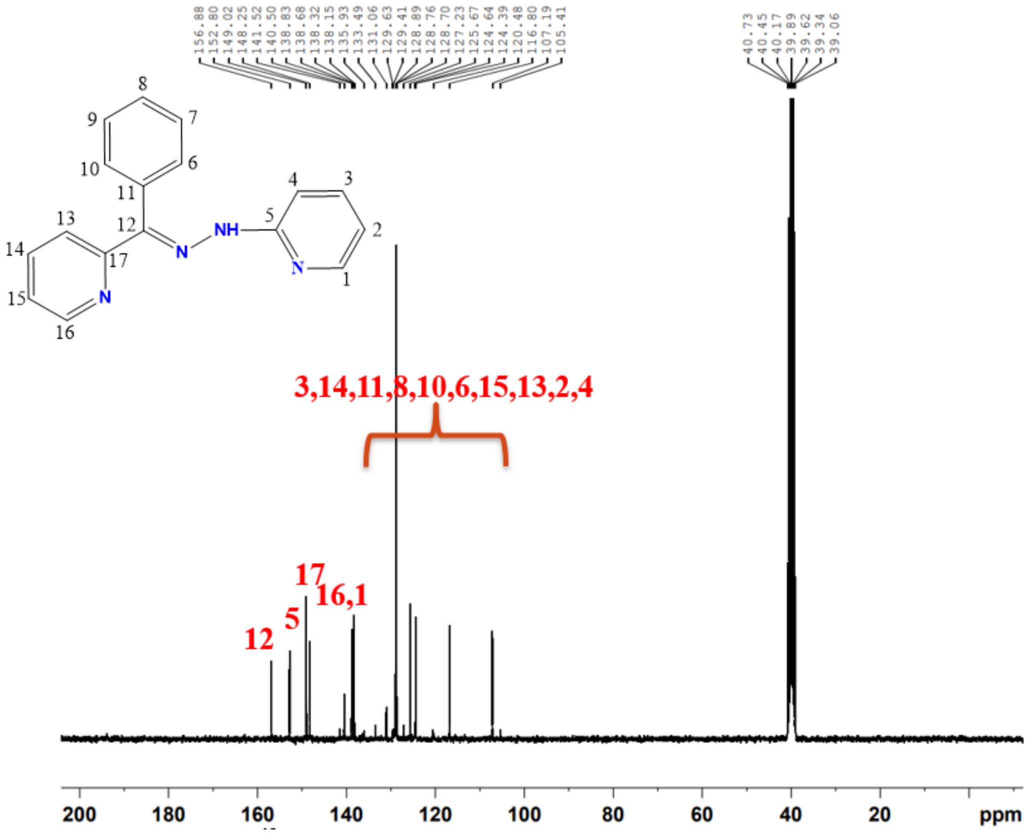

Fig. 2. ^{13}C NMR spectrum of Ligand **HL.**

3.3 FTIR analysis

In the FTIR spectrum of complex **1**, peaks at 3433 and 1459 cm^{-1} are characteristic peaks that are assigned for N-H stretching and bending modes respectively. Similarly, for complex **2**, peaks at 3406 and 1464 cm^{-1} are observed. The sharp $> \mathrm{C} = \mathrm{N}$, stretching vibration bands corresponding to the imine group of Schiff base framework appear at 1568 cm^{-1} and Skelton vibrations of phenyl groups at 1480 and 1542 cm^{-1}. The redshifts in the vibrational absorption bands of $> C = N$ the group composed of 1592 cm^{-1} of free Schiff base agree with the coordination of Schiff base to the copper(II) center [50]. The observed vibrational bands at 427 and 462 cm^{-1} are due to ν(M-N) and ν(M-O) stretching frequencies in complex **2**. Other bands associated with the Schiff base showed minor shifts, suggesting that the electron density of the bonds has been altered on coordination [51]. FTIR spectra of ligand and complexes are shown in Fig. 3-5.

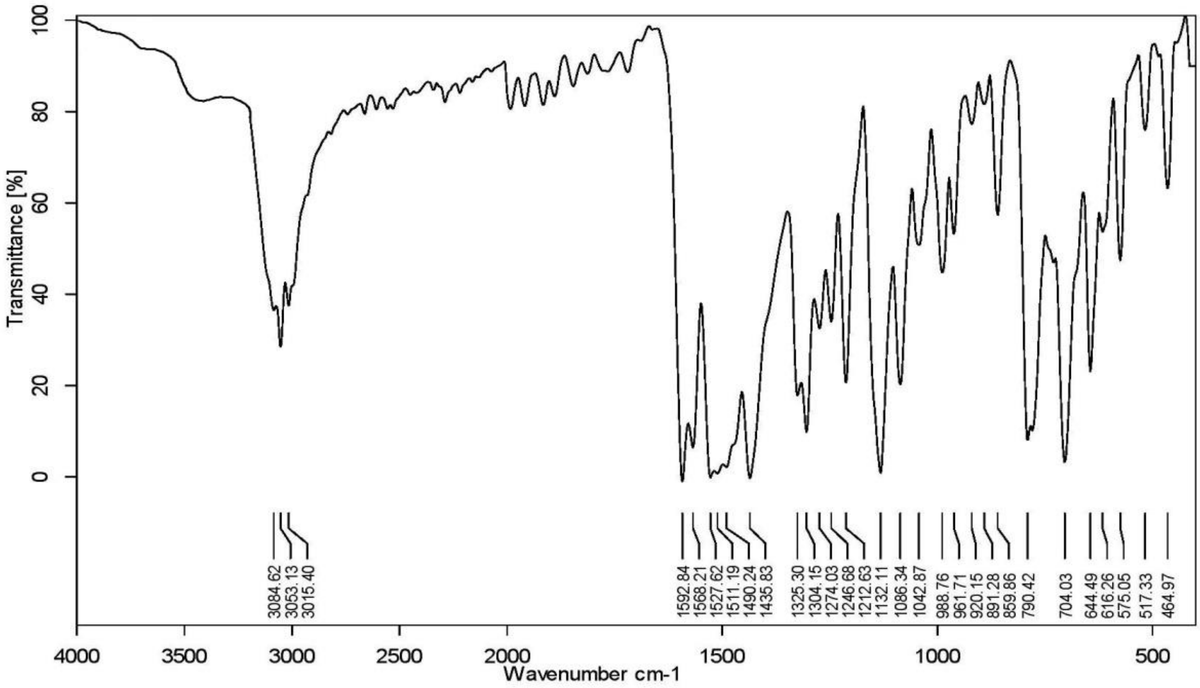

Fig. 3. FTIR spectrum of Ligand **HL**.

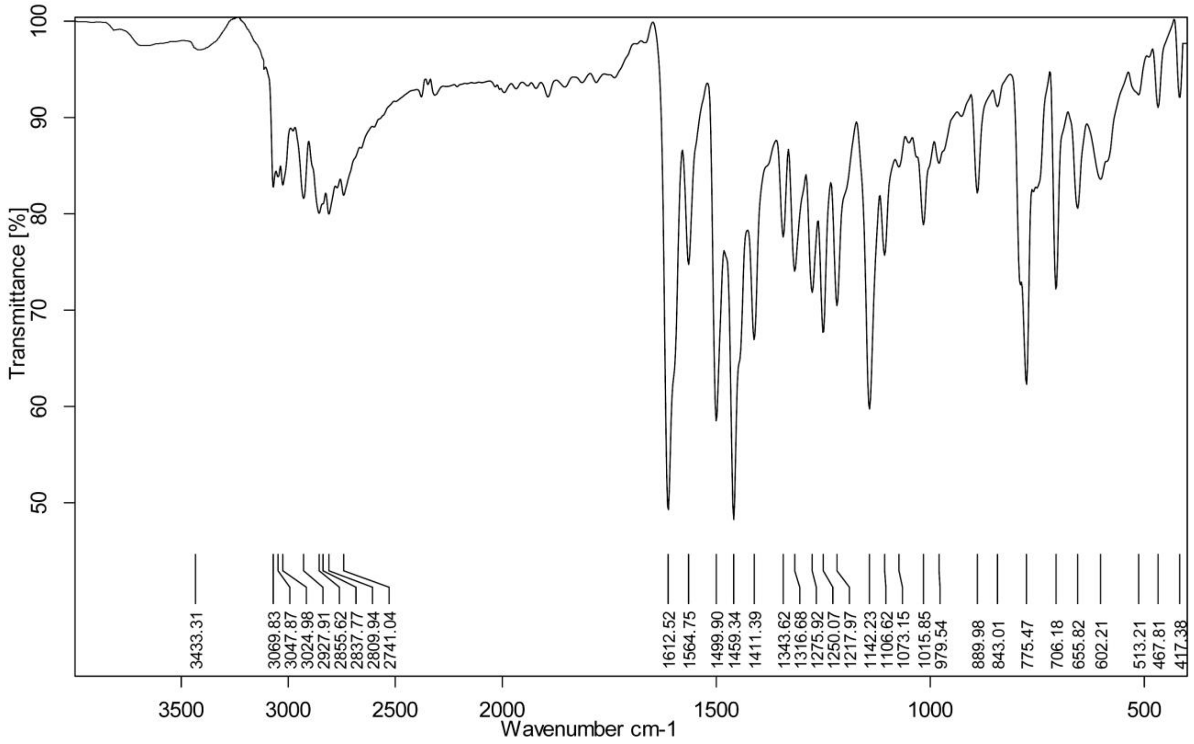

Fig. 4. FTIR spectrum of complex **1.**

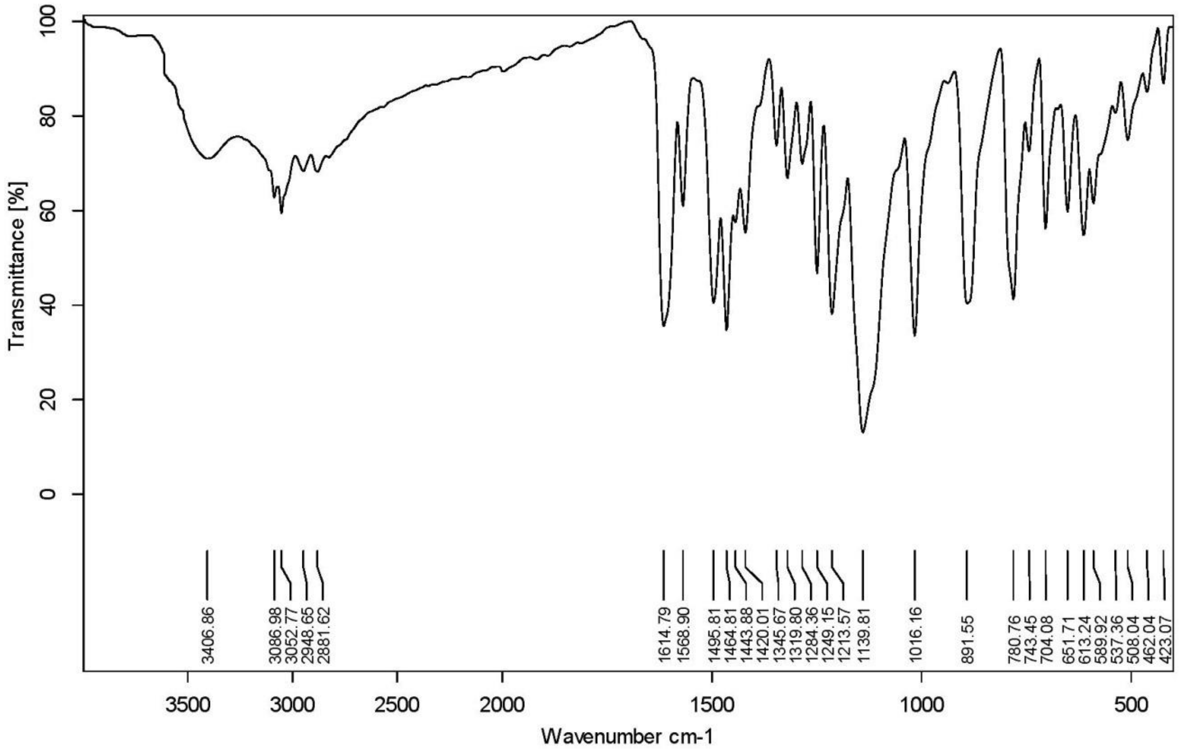

Fig. 5. FTIR spectrum of complex **2.**

3.4 Molecular structure of HL and complexes

An ORTEP diagram with atom-labeling of HL is shown in Fig. 6. The crystal refinement data of HL are collected in Table 2. Bond lengths and angles are shown in Table 3. X-ray analysis reveals that imino nitrogen is protonated Fig. 6. Both pyridine rings remain in the plane while phenyl rings out off plane. The bond length in between C1 and N3 azomethine nitrogen (>C=N) is smaller compared to C7 and N2 protonated imino nitrogen (Table 3). The smaller bond length is due to the presence of a double bond in between C1 and N3 (azomethine nitrogen). The ligand molecules possess three H-acceptors (N1, N3 and N4) which are sp^2 hybridized nitrogen atoms. These nitrogen atoms exert one intramolecular (N2-H2···N4 with d(H-A) 1.908(17)) and two intermolecular (C11-H11...N3 and C15-H15...N1 with d(H-A) 2.69 and 2.66) H-bonding as shown in Fig 7. Due to intramolecular H-bonding S(5) self-moiety (five-membered pseudo-ring) is formed. The hydrogen bonding parameters are collected in Table 4. The intramolecular H-bonding has a considerable short distance (Table 5) using these H-bondings each molecule is bonded to two neighboring molecules thus creating a 2D non-covalent network of the ligand molecule which runs parallel to the ab-plane (Fig. 7). Additionally, the structure of the molecule also exerts three C-H···π interactions with π-electrons of the phenyl ring of the same molecule and pyridyl ring of terminal pyridyl ring of the neighbouring molecule of ligand one more C-H···π interaction is exerted by C-H of this terminal pyridine ring and π-electrons of the phenyl ring of benzoyl moiety of neighbouring ligand molecule(Fig 8). The crystal packing of ligand represents a 2D supramolecular structure from classical C/N-H···N hydrogen bonds and a 3D network when additional C-H···N and C-H···π interactions are taken into account (Fig 9). The classical hydrogen bonds are the main supramolecular interactions.

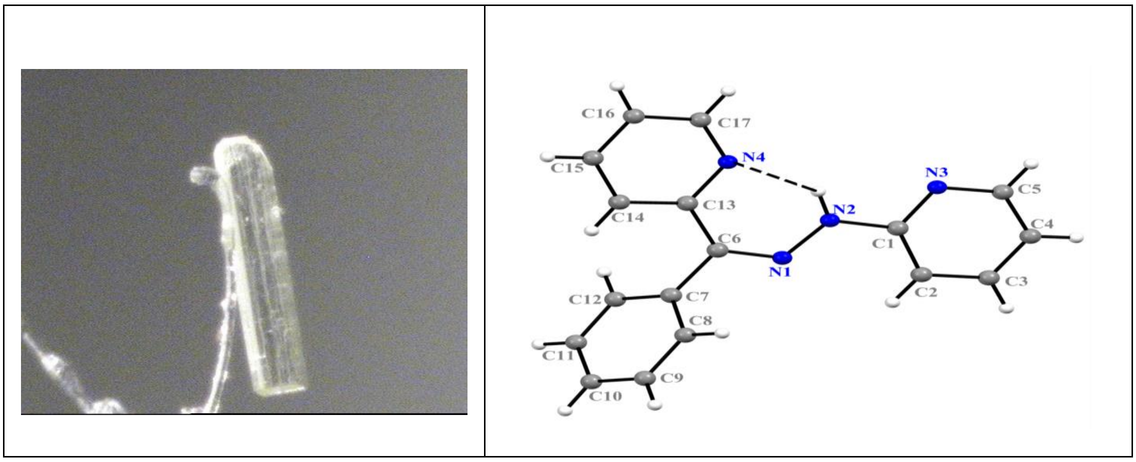

Fig. 6. The ORTEP diagram of **HL** with crystal image.

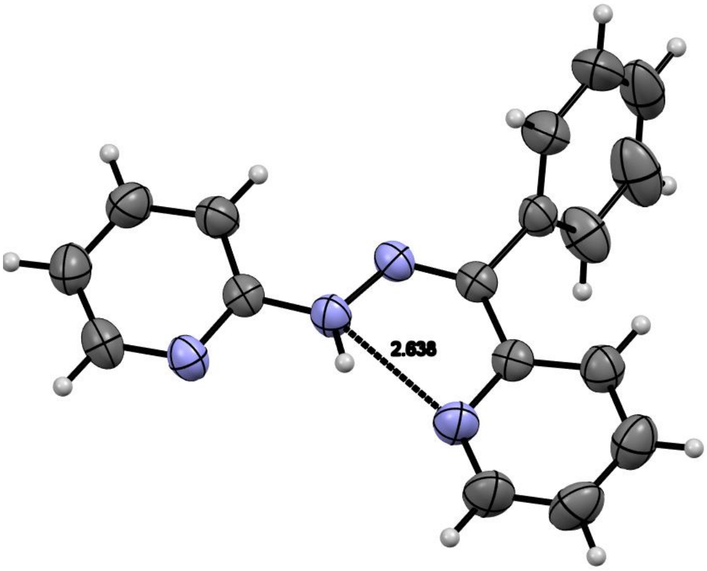

Fig. 7. Hydrogen bonding interactions of **HL.**

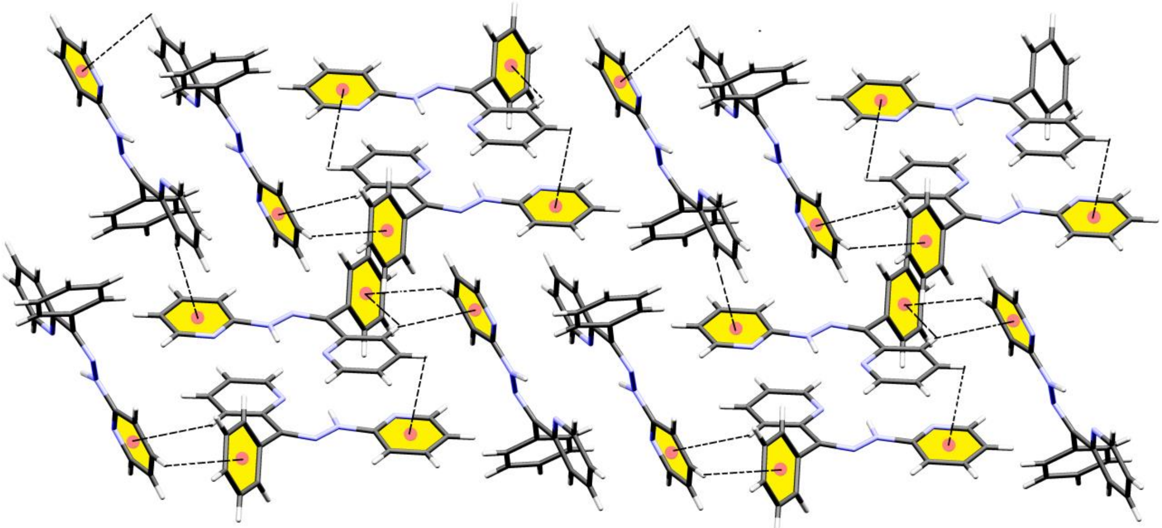

Fig. 8. 2D array of HL containing C-H···π interactions of **HL.**

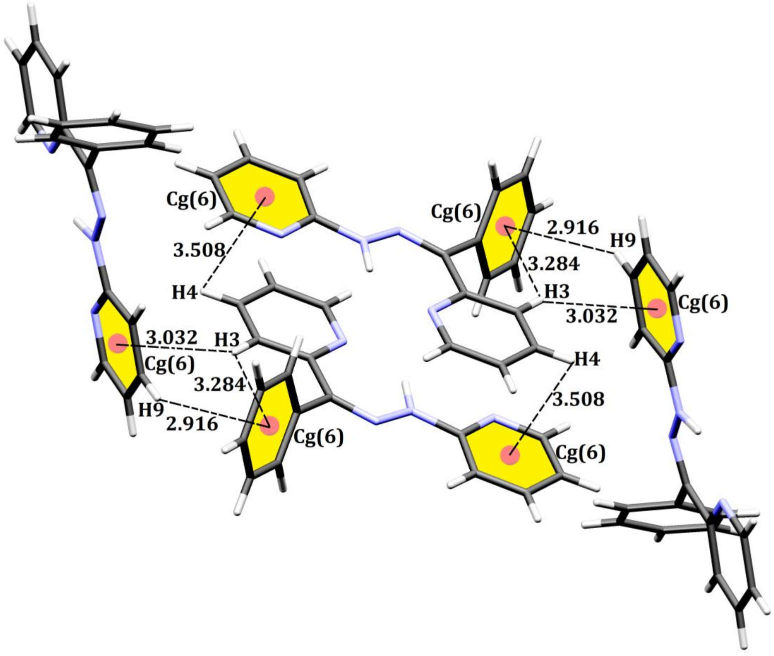

Fig. 9. The C-H···π interactions in **HL**. Cg(6) is the centroid of phenyl ring containing atoms C(7) to C(11) and C(12) to C(17).

Table 2 Crystal data and structure refinement for **HL**.

	HL
Empirical formula	$C_{17}H_{14}N_4$
Formula weight	274.32
Temperature/K	293(2)
Wavelength	0.71073
Crystal system	Monoclinic
Space group	*P 21/n*
***a*/Å**	9.045(2)
***b*/Å**	10.3012(16)
***c*/Å**	15.581(4)
***α*/°**	90
***β*/°**	93.977(11)
***γ*/°**	90
Volume/Å^3	1448.3(6)
Z	4
ρ_{calc}g/cm^3	1.258
μ/mm^{-1}	0.078
F(000)	576
Crystal size/mm^3	0.120 x 0.100 x 0.100
2Θ range for data collection/°	2.621 to 25.026

Index ranges	-10<=h<=10, -11<=k<=12, -18<=l<=18
Reflections collected	10693
Independent reflections	2541 [R(int) = 0.0341]
Completeness to theta = 25.242°	96.5 %
Refinement method	Full-matrix least-squares on F^2
Data/restraints/parameters	2541 / 0 / 190
Goodness-of-fit on F^2	1.044
Final R indexes [I>=2σ (I)]	R1 = 0.0484, wR2 = 0.1145
R indexes [all data]	R1 = 0.0667, wR2 = 0.1246
Extinction coefficient	n/a
Largest diff. peak/hole / e Å^{-3}	0.173 and -0.160

Table 3 Bond Lengths and Bond Angles of **HL**.

HL			
Bond lengths			
N(1)-C(6)	1.301(2)	N(4)-C(17)	1.335(2)
N(1)-N(2)	1.3464(18)	N(4)-C(13)	1.350(2)
C(1)-N(3)	1.330(2)	N(3)-C(5)	1.338(2)
C(1)-N(2)	1.385(2)	C(1)-C(2)	1.389(2)
Bond angles			
C(6)-N(1)-N(2)	119.76(14)	N(1)-C(6)-C(13)	127.87(15)
N(3)-C(1)-N(2)	113.58(14)	N(1)-C(6)-C(7)	112.72(14)
N(3)-C(1)-C(2)	123.71(15)	N(4)-C(13)-C(14)	121.09(16)
N(2)-C(1)-C(2)	122.70(15)	N(4)-C(13)-C(6)	118.04(14)
N(1)-N(2)-C(1)	119.63(13)	C(14)-C(13)-C(6)	120.87(15)
C(17)-N(4)-C(13)	117.95(16)	N(4)-C(17)-C(16)	123.89(19)

Table 4 Hydrogen bonds (**Å**) in the crystal structure of **HL**.

D-H···A	d(D-H)	d(H-A)	d(D-A)	D-H-A/°
N(2)-H(2)...N(4)	0.86	1.97	2.638(2)	134.1

Table 5 Geometric features (distances in Å and angles in degrees) of the C-H/π interactions obtained for **HL**.

	$C-H\cdots Cg$ (Ring)	$H\cdots Cg$ (Å)	$\angle C-H\cdots Cg$ (°)	$C\cdots Cg$ (Å)
HL	$C(4)-H(4)\cdots Cg\ (6)$	3.508	80.42	3.479
	$C(3)-H(3)\cdots Cg\ (6)$	3.032	137.53	3.787
	$C(9)-H(9)\cdots Cg\ (6)$	2.916	127.25	3.572
	$C(3)-H(3)\cdots Cg\ (6)$	3.284	125.99	3.918

The Molecular structures of complex **1** are shown in Fig. 10-13 respectively. Complex **1** is mononuclear, whereas **2** is the binuclear complex. Crystal data and structure refinement details are shown in Table 6. Selected bond distances and angles are presented in Table 7. In both complexes, Schiff base ligand acts tridentate *via* NNN donor atom set and is mono diprotonated (L^{-}).

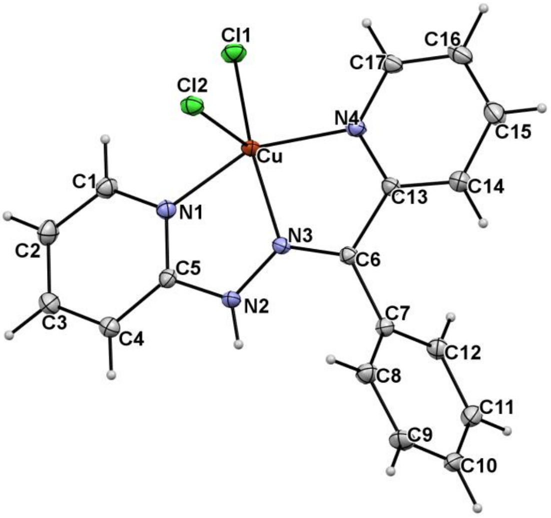

Fig. 10. Molecular structure of complex **1**.

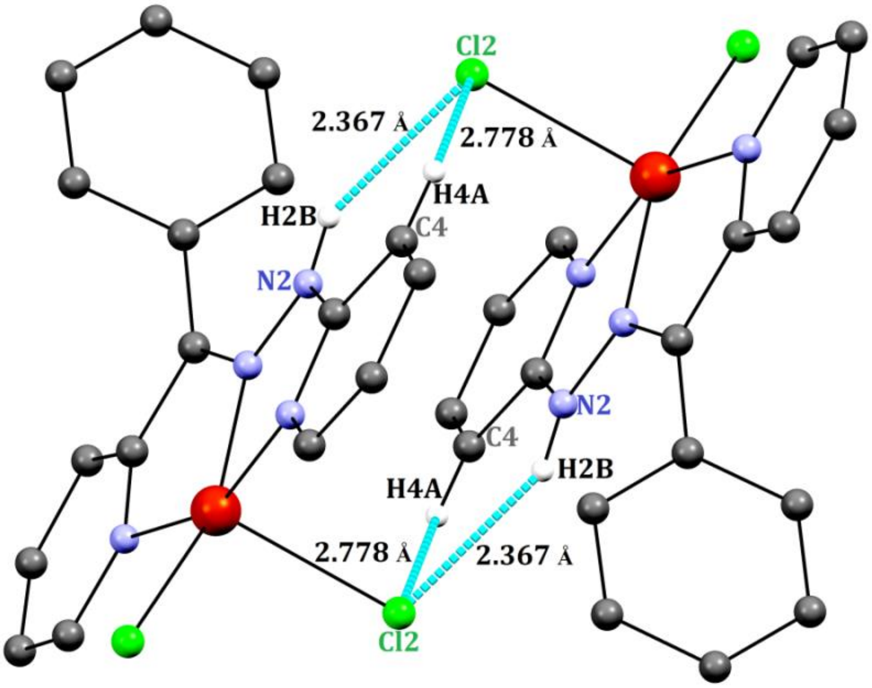

Fig. 11. The co-former Him interaction with hydrogen bonded motif in complex **1**.

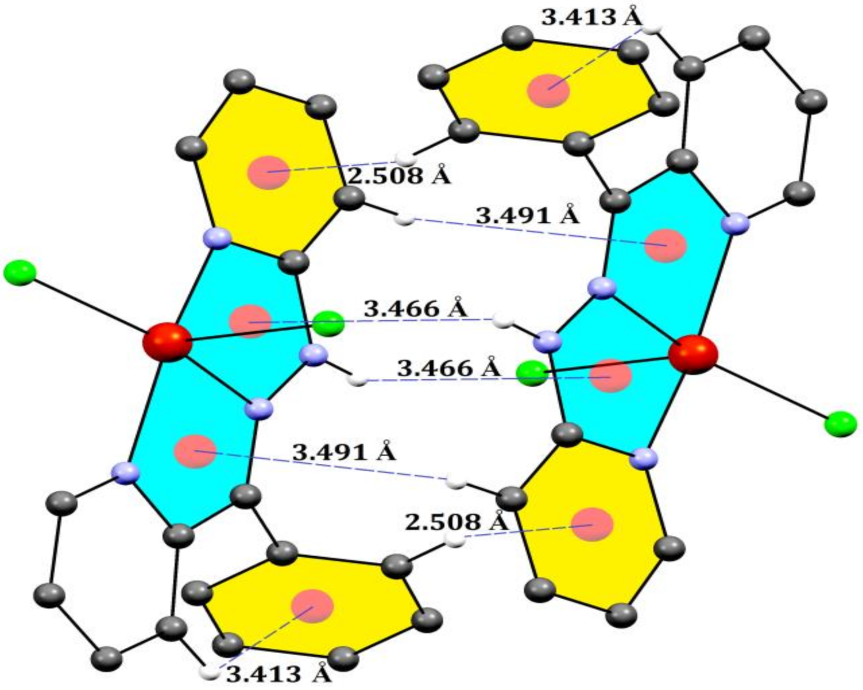

Fig. 12. $C - H \cdots \pi$ (metal chelate) interactions of complex **1**.

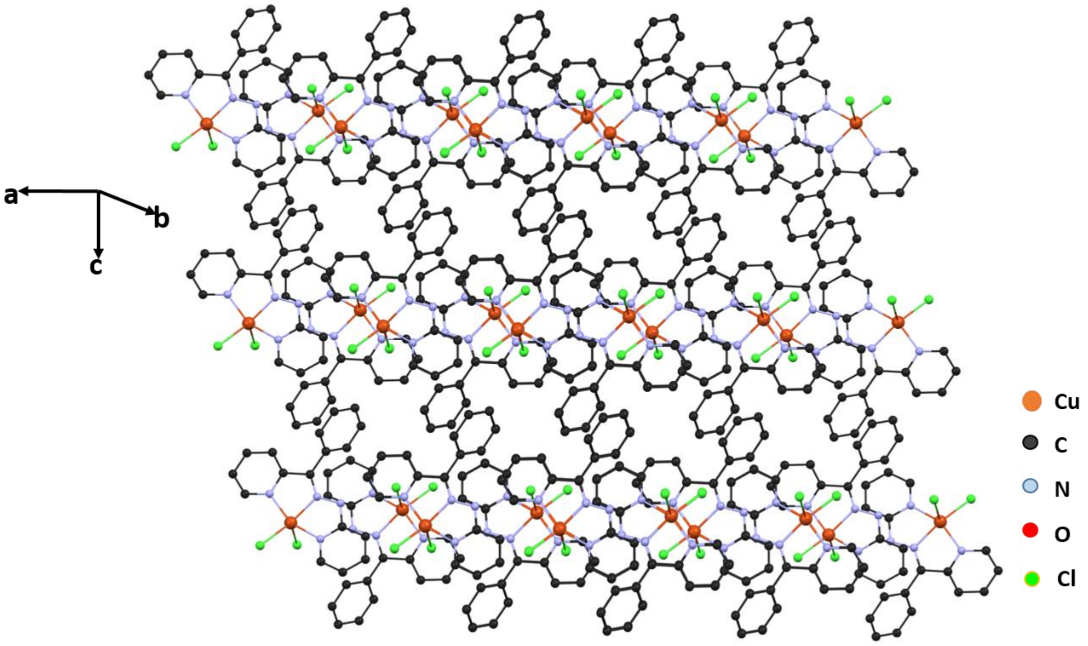

Fig. 13. Stereoscopic view of the cell of complex **1** down the b-axis (the a-axis is vertical).

The molecular structure of complex **1** consists of a discrete mononuclear $[CuL(Cl_2)]$ unit. A perspective view of the structures together with the atom labeling scheme of complex **1** is shown in Fig. 10 the copper(II) ion is five coordinated with a geometry that is intermediate between a trigonal bipyramid (c_3v) and a square-based pyramid (c_4^1v). distortion in geometry is described by addition and his co-worker [52]. According to the procedure indicated addition parameter (τ_5), the copper(II) atom has a τ value of 0.088 ($\tau_5 = \frac{(\beta-\alpha)}{60}$, β and α are the largest angles in the coordination sphere), thus coordination environment can be better described as a distorted square pyramidal structure in which the fourfold polyhedral is comprised of N1, N2, N3 and Cl1 with axial atom Cl_2. The Cu-Cl_2 bond length is longer than equatorial bonds, which results from the Jahn-Teller effect. The slight distortion in the basal plane of the coordination polyhedral may be due to the strain imposed by the Schiff base to the copper(II) center during coordination. The axially coordinated Cl2 atom has longer bond distance [2.5116(6) Å] than equatorially coordinated Cl1 [2.2429(5) Å] atom. The copper(II) ion is shifted by 0.249 Å towards the axially bound Cl2 atom from the basal plane. In addition to H-bonding, various $C - H \cdots \pi$(aryl or metal chelates) are detected having ring centroid ($H \cdots C_g$) distances in the range 2.508-3.491 Å (Fig. 12). $CH \cdots \pi$ interactions are responsible for extra stabilization in its solid-state. The axially coordinated Cl2 atom is involved in a hydrogen bond interaction with H-atoms of an adjacent molecule. The involved Cl2 atom showed bifurcated interactions thus forming two $R_2^1(6)$ membered heterosynthons (Fig. 11). The hydrogen bond parameters are presented in Table 8. The two $R_2^1(6)$ motifs areresponsible for the formations of the homodimer. The intermolecular CH···π (aryl and metalchelate) interactions are also responsible for the formation of homodimer (two co-crystals). Stereoscopic view of the cell of complex **1** down the b-axis (the a-axis is vertical) Fig. 13.

Single crystal X-ray structures were determined for all co-crystals for a better understanding of molecular packing and non-covalent interactions among the molecules, in particular, supramolecular architectures. The molecular structure of **2** reveals co-crystals of monomer and in 1:1 ratio binuclear copper(II) complexes Fig. 14. The binuclear co-crystal of complex **2** has a non-centrosymmetric structure with a binuclear $Cu_2(Cu\text{-}O\text{-}R)_2$ rectangular core. One oxygen atoms of sulfate anion act as a bridge between two copper(II) metal centers. The coordination geometry around each copper(II) center is distorted pyramidal. The relative amounts of the distorted square pyramidal are given by an Addition's factor (τ_5) [53]. The τ_5 values for two copper(II) centers are estimated as $(\tau_5)_1 = 0.3$ and $(\tau_5)_2 = 0.2$. Thus, the coordination environment of each copper(II) is a slightly distorted square pyramidal structure in which four equatorial sites comprised of O(1A), N(3A), N(1A) and N(A) with the axial position occupied by one of the oxygen atoms of sulphate anion coordinated to the second copper(II) center, acting as bridging ligand. In the binuclear motif, Cu···Cu distance is 3.266 Å. The two copper atoms are separated by 1.930 Å through bridging atoms of oxygen atoms of sulphate anions and a Cu-(M-O)-Cu angles of 101.41 and 89.10, respectively. The values of these angles exhibit an anti-ferromagnetic coupling. The copper(II)-copper(II) distance is within the usual range for this type of complex [54, 55]. The monomer unit of this binuclear complex is shown in Fig. 14-17. The coordination environment of the copper(II) center is distorted square pyramidal with a τ_5 factor of $\frac{\beta-\alpha}{60^\circ}$, suggesting that the coordination geometry is slightly distorted square pyramidal. This considerably less distortion is consistent with crystallographically imposed symmetry (plane comprised by N1B, N3B, N3B and O1B) since the equatorial plane of the complex is formed by these donor atoms and a long axial Cu(2)-O1W bond. The guest mononuclear motif has Penta coordinated around the copper(II) center. The selected bond lengths and bond angles are presented in Table 7. The basal plane at the copper center comprises two pyridine nitrogen and one azonitrogen of L^-. One perchlorate anion takes the fourth position of the basal plane. In the axial position of the metal coordination sites, one oxygen atom of water molecule remains. Thus, the geometry of copper ion in this motif can be described by the square pyramidal structure in which the c_4 axis is composed of N1B, N3B, N4B and O1B atoms. The relative amounts of square pyramidal components are indicated by τ_5 [56]. The value of τ_5 is 0.262. The value of τ_5 describes as distorted square pyramidal geometry. The Cu2-O1W is the longest distance than other distances from Cu- center to other atoms, a fact which is consistent with O1W being the apex of the pseudo square pyramid for Jahn-Teller distortion.

The arrangement of two species present in the lattice structure allows a certain degree of hydrogen bonding interactions throughout the crystal (Fig. 15). The binuclear unit and two mononuclear units present a double interaction (intermolecular H-bonding). The H-atom of an axially coordinated water molecule from H1W2···O1A (dHA = 1.933 Å). Similarly, phenyl ring of Schiff base forms H-bonding with the oxygen atom of coordinated water molecules of the monomer of the type $\mathrm{C11A-H11A\cdots O1W}$ (dHO = 2.662 Å). There are also several intermolecular hydrogen bonding interactions involving O/H atoms of water molecules with O of sulphate or Schiff base atoms. All kinds of interaction parameters are presented in Table 8. In complex **2**, the interesting features of the structure are the formation of supramolecular assembly through H-bonding interactions of coordinated/uncoordinated sulphate and water molecules. The hydrogen atoms, H and..H attached to C, (C_g1) are involved in intermolecular $\mathrm{C-H\cdots\pi}$(aryl) interactions and the H-atoms of H……(C_g1) and H….(C_g2), attached to C and C are involved in intermolecular $\mathrm{S-H\cdots\pi}$ interaction of the binuclear complex with ring centroid (H…C_g). $\mathrm{CH\cdots\pi}$ interactions along with other H-bonding interactions contribute extra stabilization in their solid-state. A stereoscopic projection of the molecular arrangement within the unit cell along the b-axis is shown in Fig. 17. The two monomers and one dimer unit constitute a 1D pattern.

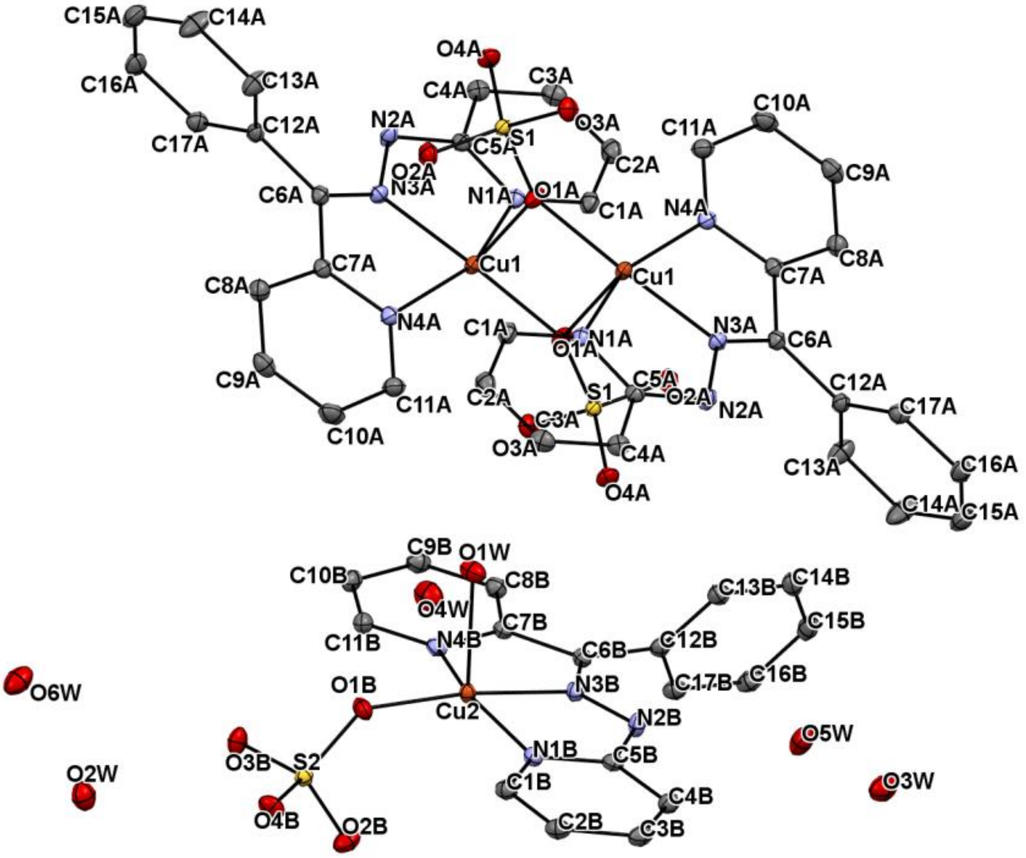

Fig. 14. Molecular structure of complex **2.**

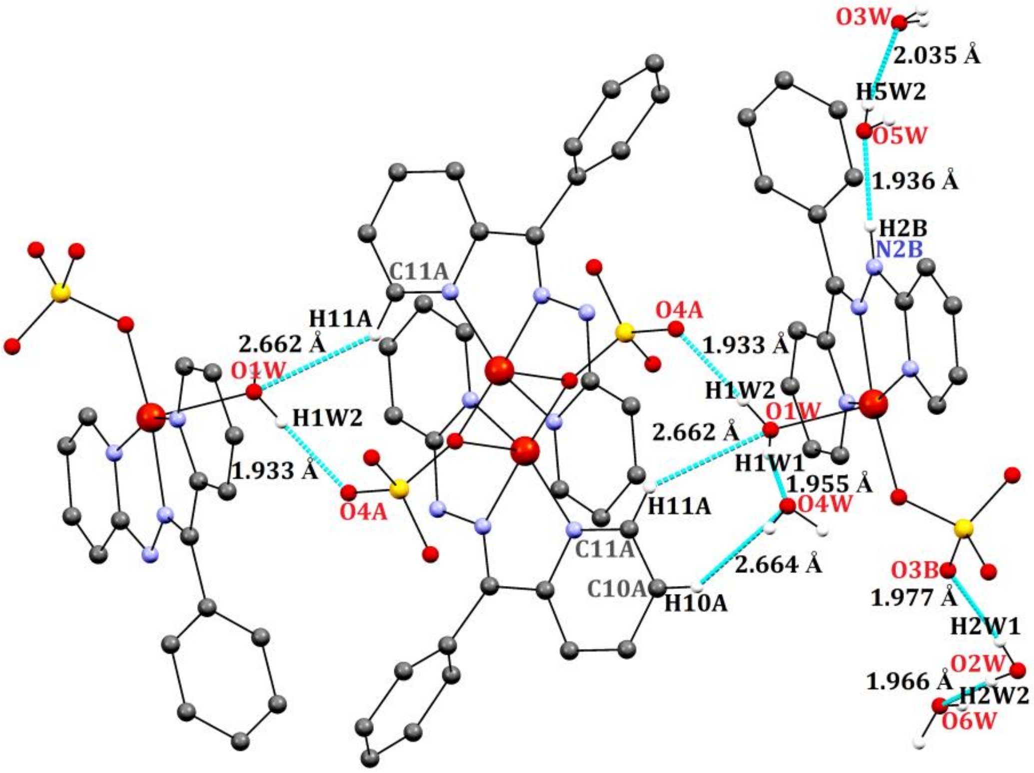

Fig. 15. The interaction with hydrogen bonded motif in stoichiometry co-crystals of complex **2.**

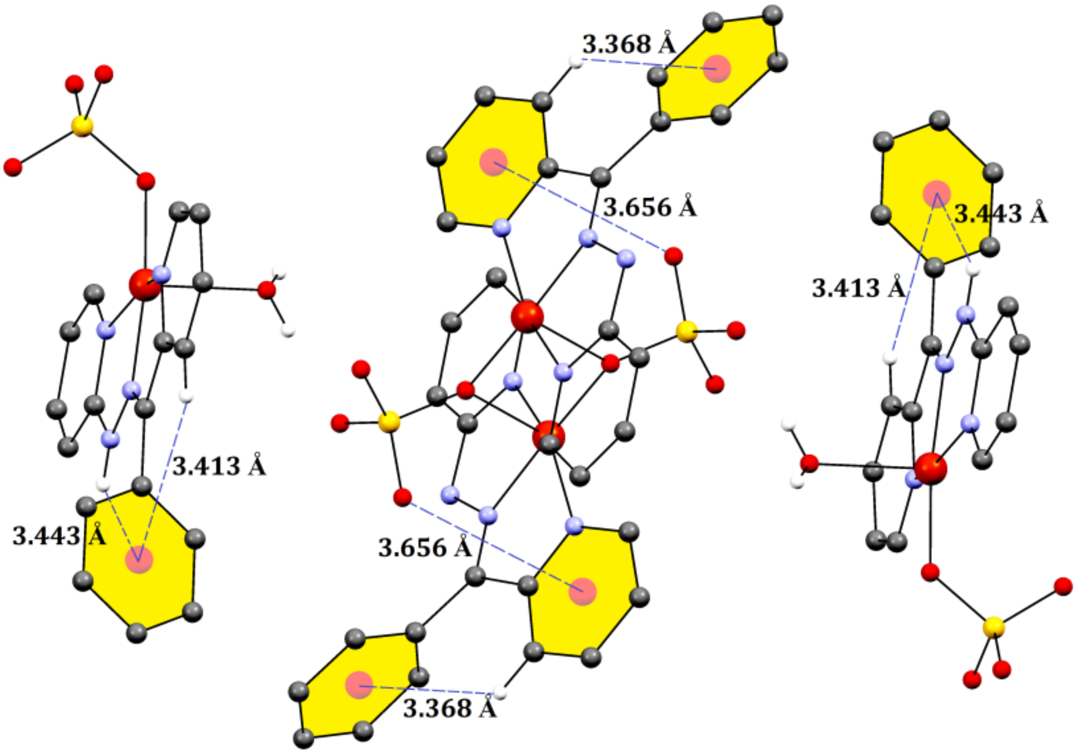

Fig. 16. Intermolecular $\mathrm{C-H\cdots\pi}$ (metal chelate) interactions of complex **2**.

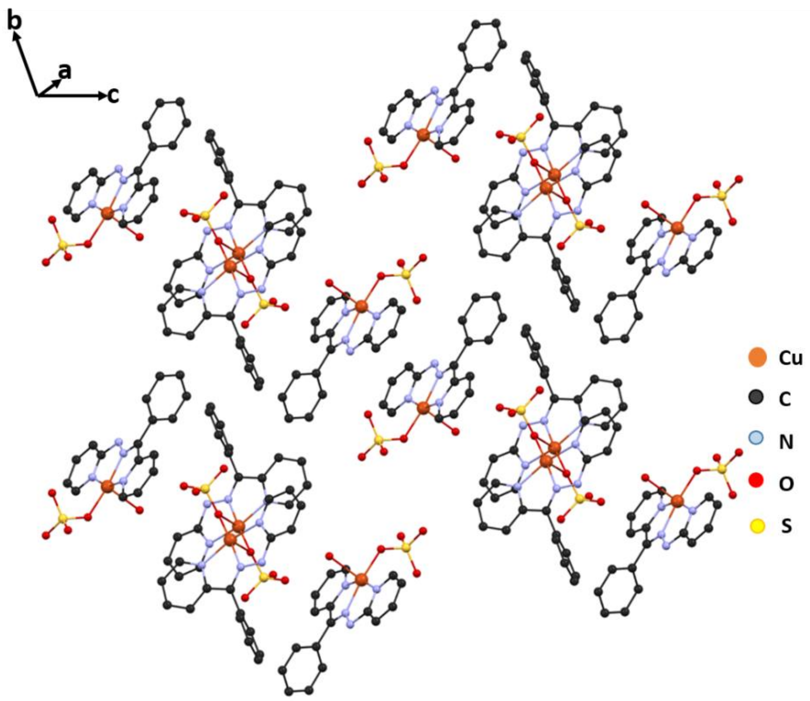

Fig. 17. Stereoscopic view of the cell of complex **2** down the b-axis (the a-axis is vertical).

Table 6 Crystal data and structure refinement for complexes **1** and **2**.

	1	2
Empirical formula	$C_{17}H_{14}Cl_2CuN_4$	$C_{68}H_{80}Cu_4N_{16}O_{28}S_4$
Formula weight	408.76	1951.88
Temperature (K)	100(2)	100(2)
Wavelength (Å)	0.71073	0.71073
Crystal system	Triclinic	Triclinic
Space group	*P -1*	*P -1*
a (Å)	8.4475(3)	8.2118(2)
b(Å)	9.6940(3) Å	14.8543(3)
c(Å)	11.4276(3) Å	17.2565(4)
α (°)	93.352(2)	74.1250(10)
β (°)	110.877(2)	80.5990(10)
γ (°)	105.187(2)	74.2080(10)
Volume ($Å^3$)	831.78(5)	1939.25(8)
Z	2	1
Density (calculated) (Mg/m^3)	1.632	1.671
Absorption coefficient (mm^{-1})	1.640	1.284
F(000)	414	1004
Crystal size (mm^3)	0.23 x 0.16 x 0.12	
Theta range for data collection (°)	2.652 to 33.256	2.547 to 28.328°.

Index ranges	-13<=h<=13, -14<=k<=14,-17<=l<=17	-10<=h<=10, -19<=k<=19,-23<=l<=23
Reflections collected	23733	28965
Independent reflections	6350 [R(int) = 0.0594]	9599 [R(int) = 0.0212]
Completeness to theta = 25.242°	99.9 %	99.8 %
Refinement method	Full-matrix least-squares on F^2	Full-matrix least-squares on F^2
Data / restraints / parameters	6350 / 0 / 217	9599 / 0 / 597
Goodness-of-fit on F^2	1.058	1.062
Final R indices [I>2sigma(I)]	R1 = 0.0426,wR2 = 0.0918	R1 = 0.0252, wR2 = 0.0614
R indices (all data)	R1 = 0.0665, wR2 = 0.1008	R1 = 0.0307, wR2 = 0.0649
Largest diff. peak and hole (e.Å^{-3})	1.124 and -1.049	0.428 and -0.490

Table 7 Bond lengths [Å] and angles [°] for complexes **1** and **2**.

1					
Bond lengths					
XRD data		**DFT**	**XRD data**		**DFT**
Cu-N(3)	1.9856(16)	1.9856	Cu-Cl(1)	2.2429(5)	2.2429
Cu-N(1)	2.0065(17)	2.0065	Cu-Cl(2)	2.5116(6)	2.5116
Cu-N(4)	2.0177(18)	2.0177			
Bond angles					
N(3)-Cu-N(1)	79.14(7)	79.14	N(4)-Cu-Cl(1)	98.35(5)	98.35
N(3)-Cu-N(4)	79.33(7)	79.36	N(3)-Cu-Cl(2)	96.27(5)	96.27
N(1)-Cu-N(4)	155.75(7)	156.13	N(1)-Cu-Cl(2)	95.15(5)	95.18
N(3)-Cu-Cl(1)	161.04(5)	161.38	N(4)-Cu-Cl(2)	98.15(5)	98.23
N(1)-Cu-Cl(1)	98.39(5)	98.39	Cl(1)-Cu-Cl(2)	102.68(19)	103.69
2					
Bond lengths					
Cu(1)-O(1A)	1.9303(11)	1.9303	Cu(2)-O(1B)	1.9214(11)	1.9214
Cu(1)-N(3A)	1.9557(13)	1.9557	Cu(2)-N(3B)	1.9593(13)	1.9601
Cu(1)-N(1A)	2.0087(13)	2.0086	Cu(2)-N(1B)	2.0032(13)	2.0032
Cu(1)-N(4A)	2.0136(13)	2.0136	Cu(2)-N(4B)	2.0163(13)	2.0163
Cu(1)-O(1A)	2.2806(11)	2.2806	Cu(2)-O(1W)	2.1841(12)	2.1841
Sulfur ion					
S(1)-O(2A)	1.4538(11)	1.4538	O(1B)-S(2)	1.5029(11)	1.5031
S(1)-O(4A)	1.4653(11)	1.4652	O(2B)-S(2)	1.4685(12)	1.4685
S(1)-O(3A)	1.4684(11)	1.4684	O(3B)-S(2)	1.4714(12)	1.4714

S(1)-O(1A)	1.5400(11)	1.5399	O(4B)-S(2)	1.4697(12)	1.4697
Bond angles					
O(1A)-Cu(1)-N(3A)	176.68(5)	176.68	O(1B)-Cu(2)-N(3B)	173.08(5)	173.08
O(1A)-Cu(1)-N(1A)	103.74(5)	103.89	O(1B)-Cu(2)-N(1B)	97.29(5)	97.29
N(3A)-Cu(1)-N(1A)	79.57(5)	79.57	N(3B)-Cu(2)-N(1B)	79.53(5)	79.53
O(1A)-Cu(1)-N(4A)	97.11(5)	97.11	O(1B)-Cu(2)-N(4B)	101.95(5)	102.31
N(3A)-Cu(1)-N(4A)	79.58(5)	79.58	N(3B)-Cu(2)-N(4B)	80.02(5)	80.02
N(1A)-Cu(1)-N(4A)	157.67(5)	158.37	N(1B)-Cu(2)-N(4B)	157.36(5)	158.11
O(1A)-Cu(1)-O(1A)#1	78.59(5)	78.59	O(1B)-Cu(2)-O(1W)	89.11(5)	89.24
N(3A)-Cu(1)-O(1A)#1	101.25(5)	101.25	N(3B)-Cu(2)-O(1W)	97.50(5)	97.50
N(1A)-Cu(1)-O(1A)#1	99.58(5)	99.58	N(1B)-Cu(2)-O(1W)	100.44(5)	100.44
N(4A)-Cu(1)-O(1A)#1	92.24(5)	92.24	N(4B)-Cu(2)-O(1W)	91.74(5)	91.74
Sulfur ion					
O(2A)-S(1)-O(4A)	111.95(7)	111.95	O(2B)-S(2)-O(4B)	111.63(7)	111.63
O(2A)-S(1)-O(3A)	112.77(7)	112.77	O(2B)-S(2)-O(3B)	110.98(7)	110.98
O(4A)-S(1)-O(3A)	111.41(7)	111.41	O(4B)-S(2)-O(3B)	109.98(7)	109.98
O(2A)-S(1)-O(1A)	107.66(7)	106.84	O(2B)-S(2)-O(1B)	109.38(7)	109.59
O(4A)-S(1)-O(1A)	106.30(7)	106.30	O(4B)-S(2)-O(1B)	107.22(7)	107.22
O(3A)-S(1)-O(1A)	106.30(6)	106.30	O(3B)-S(2)-O(1B)	107.48(7)	107.48

Symmetry transformations used to generate equivalent atoms: #1 -x+1,-y+1,-z+1

Table 8 Hydrogen bonds [Å and °] for complexes **1** and **2**.

D-H...A	d(D-H)	d(H...A)	d(D...A)	<(DHA)	Symmetry transformations
1					
N(2)-H(2B)...Cl(2)#1	0.88	2.37	3.1579(16)	149.6	#1 -x+1,-y+1,-z+1
C(1)-H(1A)...Cl(1)	0.95	2.84	3.392(2)	117.8	
C(4)-H(4A)...Cl(2)#1	0.95	2.78	3.531(2)	136.8	
C(16)-H(16A)...Cl(1)#2	0.95	2.73	3.669(2)	168.6	#2 -x,-y+2,-z+1
C(17)-H(17A)...Cl(1)	0.95	2.90	3.428(2)	116.4	
2					
N(2A)-H(2A)...O(3A)#1	0.83(2)	1.97(2)	2.7291(17)	153(2)	#1 -x+1,-y+1,-z+1
C(1A)-H(1AA)...O(2A)	0.95	2.48	3.360(2)	153.6	
C(4A)-H(4AA)...O(3A)#2	0.95	2.57	3.1928(19)	123.7	#2 -x,-y+1,-z+1
O(1W)-H(1W1)...O(4W)	0.82(2)	1.96(2)	2.7573(19)	167(2)	
O(1W)-H(1W2)...O(4A)	0.81(3)	1.93(3)	2.7382(17)	177(3)	
N(2B)-H(2B)...O(5W)	0.82(2)	1.94(2)	2.7460(19)	168(2)	
C(2B)-H(2BA)...O(3B)#3	0.95	2.59	3.253(2)	127.0	#3 x+1,y,z
C(10B)-H(10B)...O(4W)#4	0.95	2.56	3.406(2)	148.9	#4 x-1,y,z
C(11B)-H(11B)...O(3B)	0.95	2.56	3.403(2)	147.8	
O(2W)-H(2W1)...O(3B)	0.78(3)	1.98(3)	2.7596(18)	175(2)	
O(2W)-H(2W2)...O(6W)	0.81(3)	1.97(3)	2.767(2)	171(3)	
O(3W)-H(3W1)...O(4B)#5	0.80(3)	1.99(3)	2.7832(18)	172(3)	#5 -x+1,-y+2,-z
O(3W)-H(3W2)...O(2W)#6	0.80(3)	2.03(3)	2.8173(19)	168(3)	#6 -x,-y+2,-z
O(4W)-H(4W1)...O(6W)#3	0.84(3)	2.05(3)	2.874(2)	166(3)	
O(4W)-H(4W2)...O(2W)#7	0.82(3)	2.09(3)	2.8720(19)	159(3)	#7 -x+1,-y+1,-z
O(5W)-H(5W1)...O(2B)#5	0.77(3)	2.05(3)	2.8268(18)	177(3)	
O(5W)-H(5W2)...O(3W)	0.77(3)	2.03(3)	2.774(2)	161(3)	
O(6W)-H(6W1)...O(4B)#4	0.79(3)	2.01(3)	2.7824(19)	164(3)	
O(6W)-H(6W2)...O(3B)#8	0.84(3)	1.98(3)	2.8051(18)	169(3)	#8 -x,-y+1,-z

3.5 Electronic spectra

The electronic spectra were recorded using DMSO (3.0 × 10^{-3} M) solutions of **1** and **2**. The UV-visible absorption spectroscopy is also a useful technique that has been frequently imploded to the structural information. A strong absorption band in the electronic spectra of the complexes **1** and **2** at 278 nm was attributed to the π-π^* transition of aromatic rings and azomethine groups. The absorption band at 385 nm is due to ligand to metal charge transfer (LMCT) from the $> C = N$ group to copper(II) [57]. Furthermore, the complexes exhibit a copper-based *d-d* band at ~580 nm and transition occur from $^2E_g \rightarrow 2T2g$ [58]. The spectral properties of both complexes are almost similar (Fig. 18).

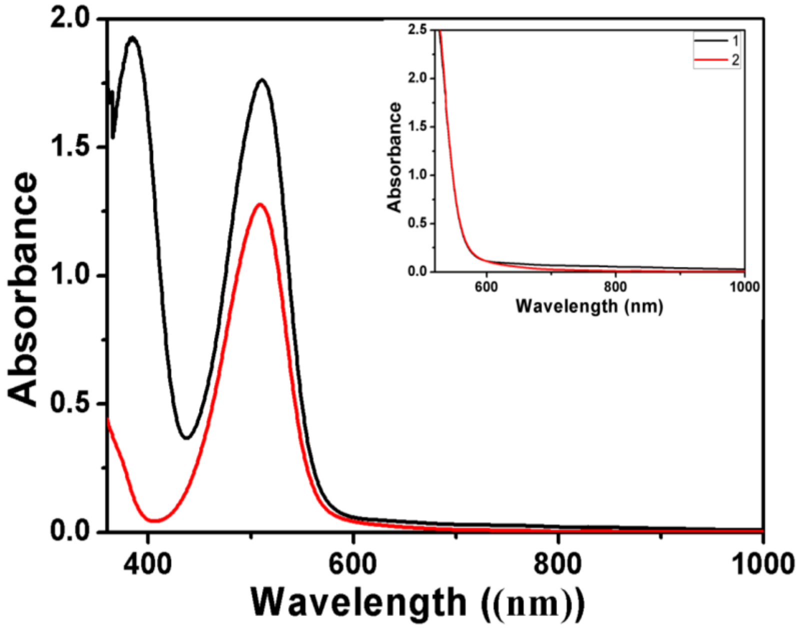

Fig. 18. UV-visible spectra of copper(II) complexes **1** and **2** in DMSO solution 3.0 x 10^{-3} M. Inset 3.0 × 10^{-3} M in DMSO solution expanded region of visible region is given.

3.6 Electrochemical studies

The electrochemical behaviours of both complexes were studied using cyclic voltammetry (CV) and differential pulse voltammetry (DPV) techniques. The CV and DPV diagrams are shown in Fig. 19. Both complexes display two reduction peaks at +0.21 V ($Cu^{2+} \rightarrow Cu^{+1}$) and -0.34 V ($Cu^{+} \rightarrow Cu^{0}$) and one oxidation peak at -0.28 V ($Cu^{0} \rightarrow Cu^{2+}$) of **1** and reduction peaks at -0.20 and -0.27 along with oxidation peak at -0.15 V ($Cu^{0} \rightarrow Cu^{2+}$) for **2,** respectively**.** This may be due to the chemical oxidation of copper during the complexation processes i.e., during complexation processes the Cu^{+1} species is transformed to Cu^{2+} and ligand is reduced at a more negative potential (Fig. 19 a) on increasing the scan rate peak currents increases linearly, supporting the diffusion effect on the electrochemical (E_C) mechanism [59]. In both complexes show two reduction processes ($Cu^{II}Cu^{II} + e^{-} \rightarrow Cu^{II}Cu^{I}$ and $Cu^{II}Cu^{I} + e^{-} \rightarrow Cu^{I}Cu^{I}$) vs AgCl references, both involving an identical number of electrons as revealed from differential pulse voltammetry (DPV) experiments. The value of the second reduction potential of **2** is less negative than that of **1**, but the first reduction potential values are nearly identical. Such a less negative reduction potential of complex **1** may be attributed due to the high molecular weight of **2**. The DPV technique is a very good electrochemical technique for resolving reduction peak potentials with a small difference in peak potentials (180 mV) [60]. This technique further supports the existence of two reduction processes (Fig. 19b) and also in agreement with the foregoing results [61].

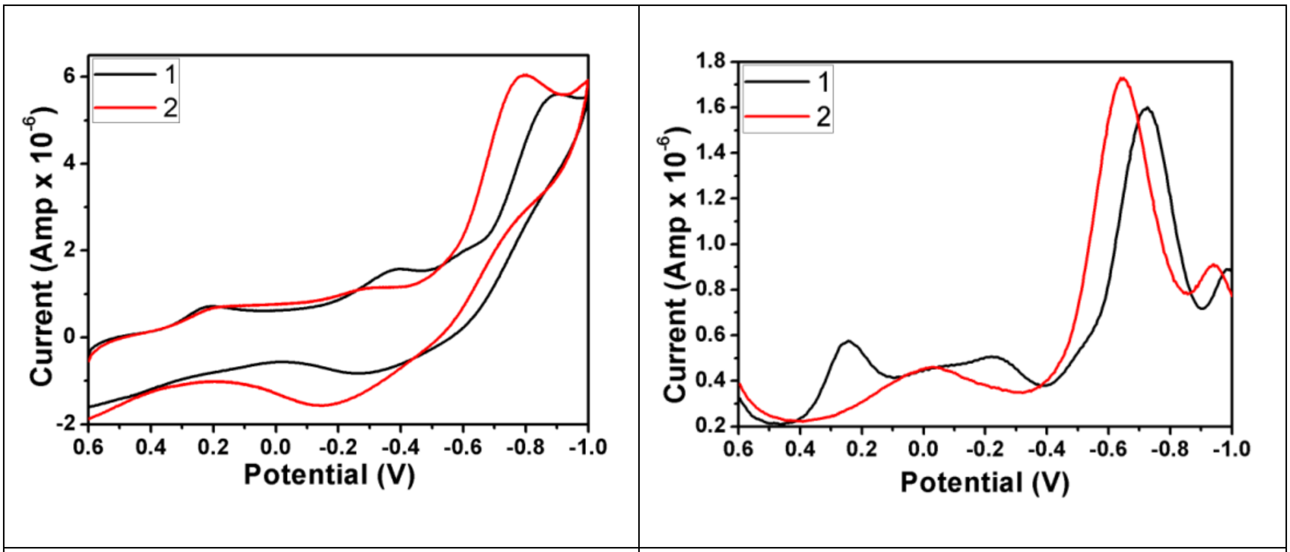

(a) **(b)**

Fig. 19. (a) Cyclic voltammograms of complexes **1** and **2** in DMSO at an Ag/AgCl electrode with a scan rate of 300 mV s^{-1} and temperature 20°C. (b) Differential pulse voltammogram of complexes **1** and **2** at room temperature using a scan rate of 20 mV s^{-1}in DMSO. The pulse amplitude is 50 mV.

3.7 EPR measurements

The Epr spectra of complexes **1** and **2** were measured in a Varian E-line Spectrometer working in the X-band at RT of polycrystalline and LNT of frozen solutions. The Epr spectra of these complexes were recorded in polycrystalline samples at RT and in DMSO solution $(3 \times 10^{-3}\ \mathrm{M})$ at LNT (Fig. 20). The derived parameters are presented in Table. The Epr spectra of complexes in polycrystalline are typical of triplet state (S=1). The polycrystalline room temperature spectra of both complexes without hyperfine structure are found for both complexes. The signal (half field) for $\Delta Ms = \pm 2$ is weak in both complexes. The occurrence of such dimeric triplet state in **1** is due to dipole-dipole interactions. Such interactions are responsible for the formation of dimer which has already been explained in single-crystal X-ray discussion. In complex **1** dipole-dipole interactions survive in DMSO solution at LNT (Fig.5), whereas complex **2** decomposed in DMSO and has to yield spectral features of the mononuclear complex. In binuclear complexes **2** $(\Delta M_s = \pm 2)$ signals were found although in sulphato bridged complex it is weak. Polycrystalline spectra are similar in appearance with $g_{\parallel}$ and $g_{\perp}$signals. The values of polycrystalline state for complex **1** $g_{\parallel} = 2.216$, $g_{\perp} = 2.067$, G

= 2.56 and $g_{\|} = 2.190$, $g_{\perp} = 2.072$, G = 2.93 for complex **2**. The exchange interaction parameter G, of complexes, suggests that there is an interaction (G<4) between two copper centers. The $\Delta M_s = \pm 2$ is strong in complex **2.** These observations are in agreement with the antiferromagnetic interaction between copper ions in both complexes [62]. The frozen DMSO solution yielded the parameters for complex **1** $g_{\|} = 2.219$, $g_{\perp} = 2.063$ and $A_{\|} = 167$ G. The nearly axial character of g-tensor with $g_{\|} > g_{\perp} > 2.023$ indicates that the ground state arises from a $d_{x^2-y^2}$ orbital, which is in-agreement with τ_5 = 0.262 of the square pyramidal coordination sphere [63]. Such broadband features are consistent with the magneto-chemical properties that indicated a spin-spin interaction [64]. Frozen solution Epr spectrum of complex **2** shows four lines, typical of copper(II) ions (I = 3/2), as a result of the hyperfine interaction between the unpaired electrons and copper(II) center the values of $g_{\|}$ = 2.284, $g_{\perp}$= 2.057 and $A_{\|}$ = 167 G. As $g_{\|} > g_{\perp}$, a square pyramidal geometry can be proposed for copper(II) centers. Such observations are suggestive of dissociation of this complex into two mononuclear copper(II) species.

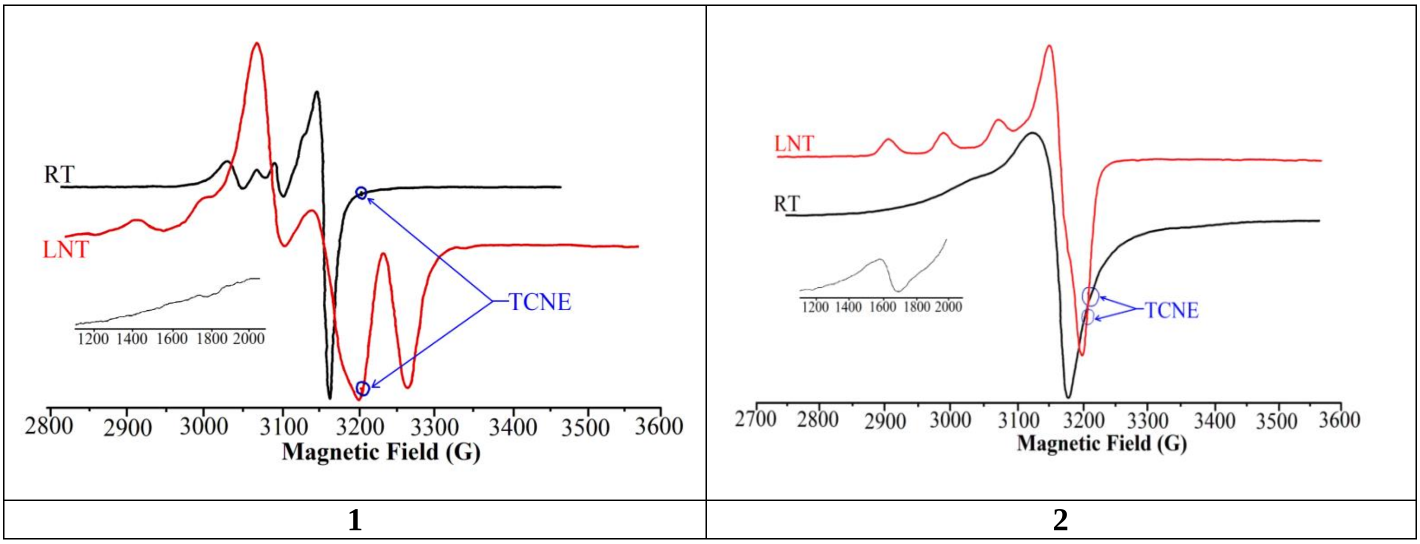

1 **2**

Fig. 20. X-band EPR spectra of complex 1 and 2 in the polycrystalline state (RT) and DMSO solution at LNT. Inset: EPR spectra showing half-field signals.

3.8 Thermal gravimetric analysis

The thermal behaviours of complexes was studied by thermal gravimetric analysis. The curves of thermo-gravimetric analysis (TG) are displayed in Fig. 21. Thermal decomposition of the copper complexes occurs at the temperature range of 100-530°C showing high thermal stability of the complexes. The thermal decomposition process of the copper complex occurs in two steps and three steps in complex **1** and **2** respectively are shown in Scheme 3. In the TG graph of the complex **1**, the weight loss at 250-360 °C is associated with the separation of the ligand molecule, while the next step with the weight loss at 400-500 °C is attributed to the loss of Cl_2 moieties and in final step leaving behind CuO as the final product. In the TG graph of complex **2** thermal dehydration of complex occurs at a range of 100-200°C due to loss of water molecules. In the next step to loss of ligand took at 280-370 °C while in the final step a weight loss occurs at 400-500°C due to the removal of SO_4 molecule. The copper oxide CuO, which is stable up to 514 °C was obtained as a final product [65-67].

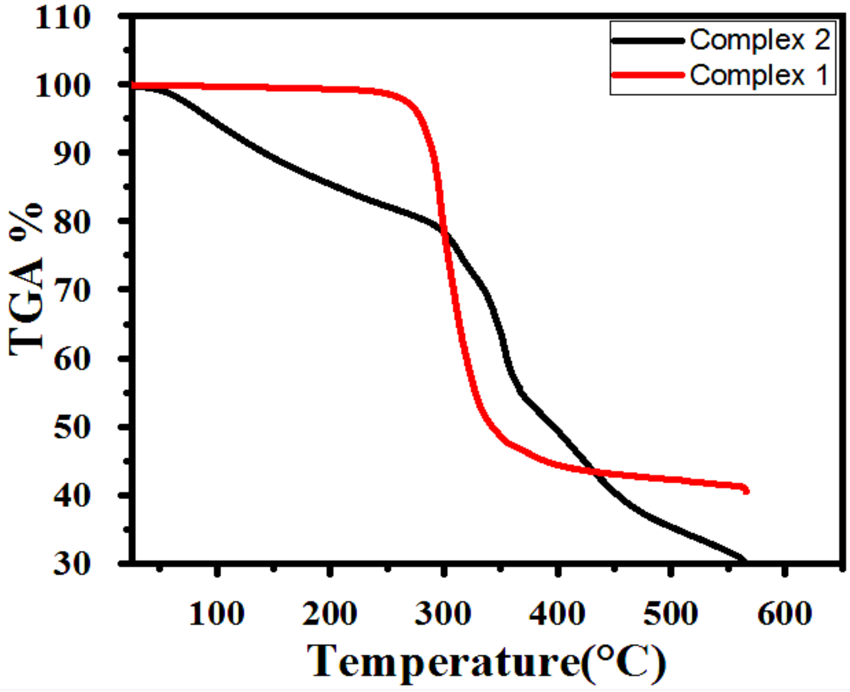

Fig. 21. TGA curves of complexes **1** and **2.**

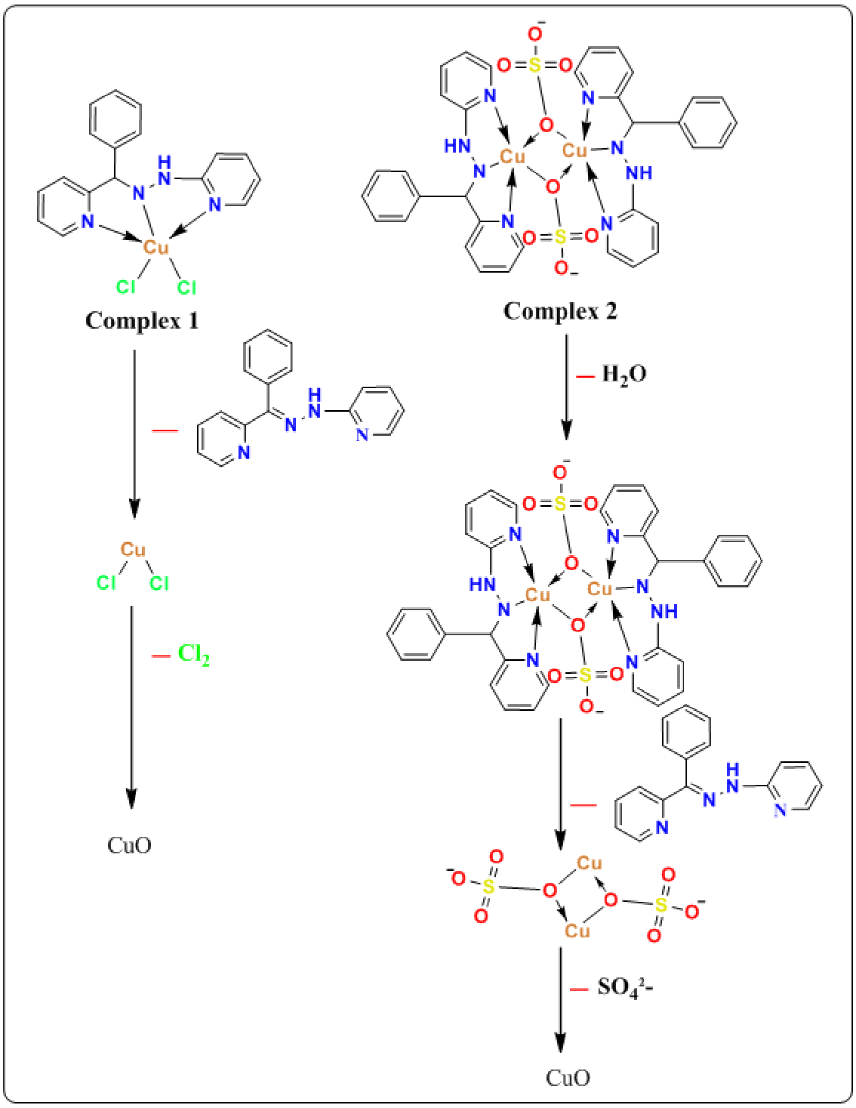

Scheme 3 TG Decomposition pattern of complexes.

3.9. Cryomagnetic susceptibility studies

The thermal variation $\chi_M T$ (χ_M = molar magnetic susceptibility) for **1** and **2** in the temperature range 300-2 K is shown in Fig. 7. The value of the $\chi_M T$ product obtainedat room temperature for complex **1** is 0.43 cm^3 Kmol^{-1}, which is slightly larger than the value expected for an isolated S = ½ copper(II) ion (0.375 cm^3 K mol^{-1}). On cooling, the $\chi_M T$ product remains roughly constant until approximately 45 K when a slight decrease in thisvalue is observed. Further cooling of the sample leads to a sharper decrease in $\chi_M T$ which is ascribed to antiferromagnetic interactions (Fig. 22).

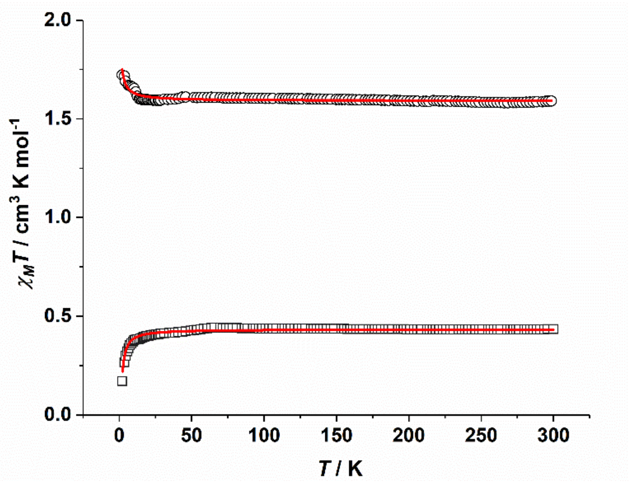

Fig. 22. Temperature dependence of the *product* $\chi_M T$ of complexes **1** (squares) and **2** (circles) measured under a magnetic field of 0.5 T. The solid lines represent the fit of the data as described in the text.

Taking into account the crystal structure of **1**, which is formed by mononuclear copper(II) species, it is reasonable to consider that the interactions occur through space and hydrogen bonds between S = ½ ions situated at the shortest intermolecular distances. It must be pointed out that although hydrogen bonds are medium-range interactions, they can strongly influence the magnetic properties of the compounds in some cases [68]. A view of the packing of the structure of **1** along the *a*-axis shows alternating intermolecular Cu···Cu distances of 4.031 and 6.595 Å that form an imaginary zigzag chain with a Cu···Cu···Cu angle of 130.07°. Moreover, the structure displays hydrogen bonding between the mononuclear species whose copper ions are placed at 6.595 Å (Fig. 23).

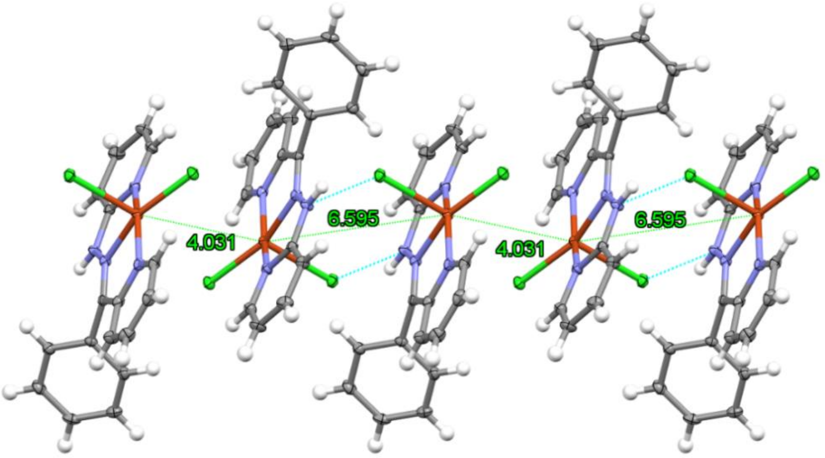

Fig. 23. View of complex **1** along *a* crystallographic axis showing the shortest intermolecular Cu···Cu distances (Å) and the hydrogen bonds between mononuclear species.

In a first approach, the $\chi_M T$data of **1** was fitted with an alternating Heisenberg linear chain model whose spin Hamiltonian is the following:

$$H \;=\; -J \sum_{i=1}^{\frac{n}{2}} [S_{2i} \cdot S_{2i-1} + \alpha S_{2i} \cdot S_{2i+1}],$$

where J is the exchange coupling constant and α takes into account the distortion in the chain with values ranging from $\alpha = 0$ (isolated dimers) to $\alpha = 1$ (uniform chain of S = spins). The analytical expression employed in the fit is:

$$\chi_M = \frac{Ng^2\beta^2}{kT}\frac{A + Bx + Cx^2}{1 + Dx + Ex^2 + Fx^3}$$

where N, g, $\beta$and k have their usual meanings, $x = |J| / kT$ and A-F are functions of α [69]. The best parameters obtained were g= 2.15, α= 0.68, and $J = -1.8$ cm^{-1} with σ^2= 5.77×10^{-4} (Fig. 23). Therefore, antiferromagnetic coupling constants of −1.8 and −1.2 cm^{-1} along a1D arrangement of S = ½ spins have been deduced from this fit. Although the value of α suggests that there are no magnetically isolated dimers in the structure, the experimental data of **1** were fitted in a second approach with the Bleany-Bowers equation for comparison:

$$\chi_M = \frac{2Ng^2\beta^2}{3KT}\frac{3}{3 + \exp\left(-\frac{J}{KT}\right)}$$

(derived from the $H = -J\, S_1 \cdot S_2$ Hamiltonian)

The best fit of the data with this model led to g and J values of 2.16 and -3.2cm^{-1}, respectively (Fig. 24). This model considers only one magnetic exchange pathway in the structure and a larger value of J in absolute value was obtained. The $\chi_M T$ product of **2** at room temperature is 1.66 cm^3 K mol^{-1}. This value is closed to the one expected (1.50 cm^3 K mol^{-1}) for the four S = ½ copper(II) ions that comprise the structure of this compound. A Curie-like behaviours is observed in the 300-15 K range and an increase of the $\chi_M T$ value on lowering the temperature, ascribed to ferromagnetic interactions, is observed bellow 15 K (Fig. 24). The $\chi_M T$ *vs* T data were fitted using a model that takes into account the magnetic contribution of a copper(II) dimer through the Bleany Bowers equation (see above) and the contribution of two copper(II) monomers. Therefore, it has been considered that an intra dimer ferromagnetic coupling is responsible for the magnetic behaviour observed in **2**. The g value of the monomeric copper(II) ions was fixed to the value of 2 to obtain realistic values. The best data obtained from this fit were g = 2.12 and J = 1.4 cm^{-1} with σ^2 = 1.08×10^{-4}.

A slightly distorted square-pyramidal coordination is observed in the two copper(II) ions that form the dimer of **2**. The copper(II) ions are double bridged by one oxygen atom of each of the two sulphate anions in the structure of the dimer. The dimer displays a Cu···Cu distance of 3.266 Å, Cu-O distances of 2.281 and 1.930Å and Cu-O-Cu angle of 101.41° (see the structural characterization part for more information). These parameters are relevant because it is well known that antiferromagnetic or ferromagnetic interactions of very different magnitude can be observed in similar dimeric copper(II) complexes depending on the geometry, the τ parameter,the Cu-O-Cu angle, and the Cu-O and Cu···Cu distances [70]. However, it is frequent to observe opposed effects of these parameters and, indeed, it has been observed that it is particularly difficult to predict the sign and the value of the coupling constant in similar systems in which the copper(II) ions are double bridged similarly to that found in **2** [71]. Nevertheless, it must be pointed out that both complexes display antiferromagnetic interactions. To the best of our knowledge, this is the first example of a dimeric copper(II) complex in which two oxygen atoms of two sulphate anions mediate a ferromagnetic coupling.

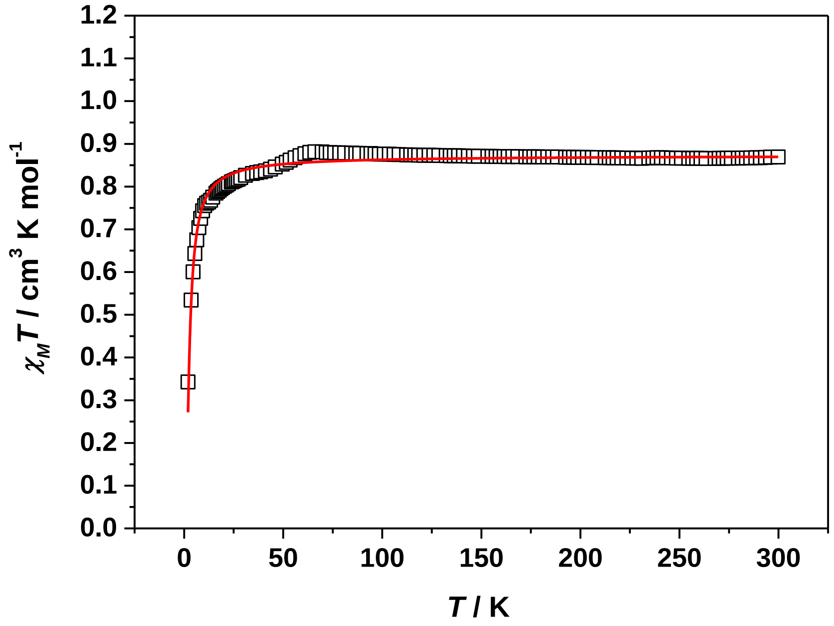

Fig. 24. $\chi_M T$ *vs* T data (with χ_M being the molar magnetic susceptibility per two Cu^{2+} ions) of complex 2 measured under a magnetic field of 0.5 T. The red line is obtained by fitting the experimental data to the Bleany-Bowers equation as explained in the main text.

3.10 ESI-Mass analysis

The Mass analysis of complexes was performed using ESI-Mass method in positive mode to get information about the molecular mass of the complexes. The molecular ion peaks in both complexes was obtained in $[M + 1]^+$mode. The mass spectra of complexes are given in Fig. 25 and 26.

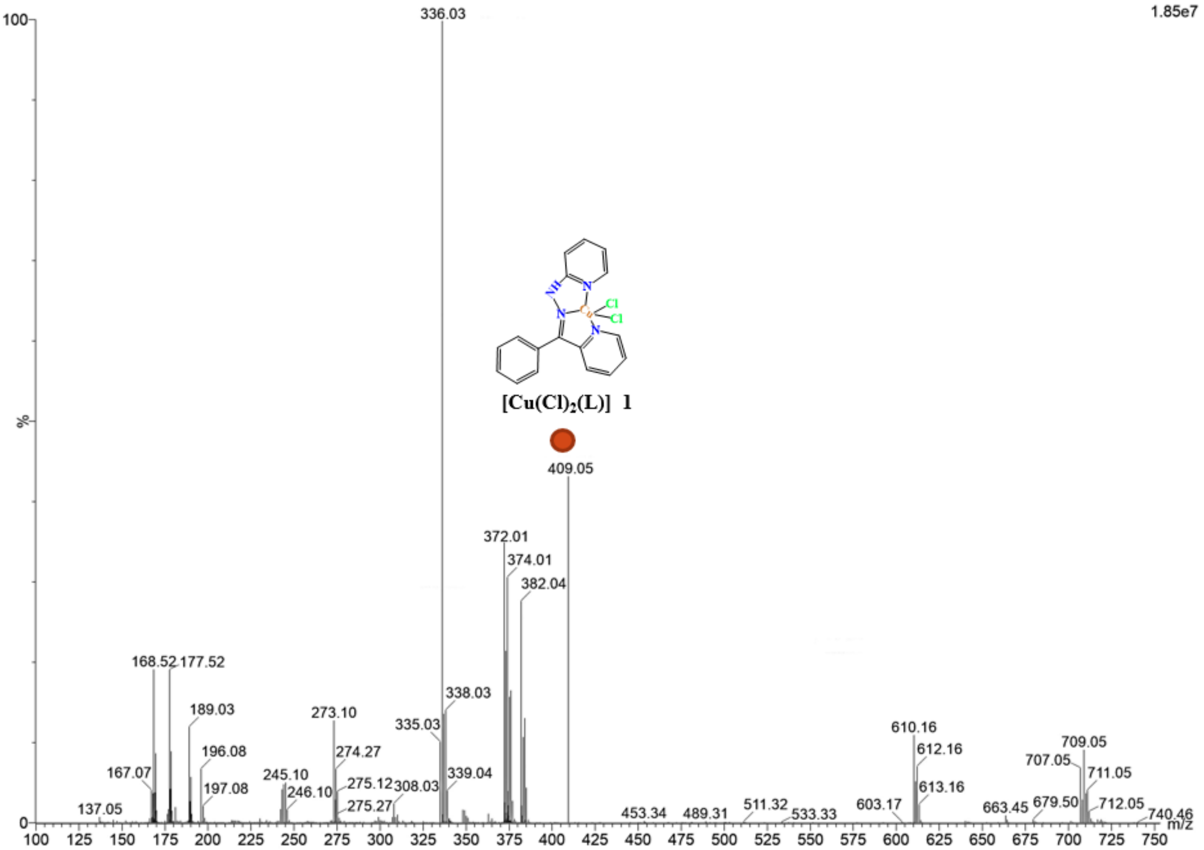

Fig. 25. Mass spectrum of complex **1**.

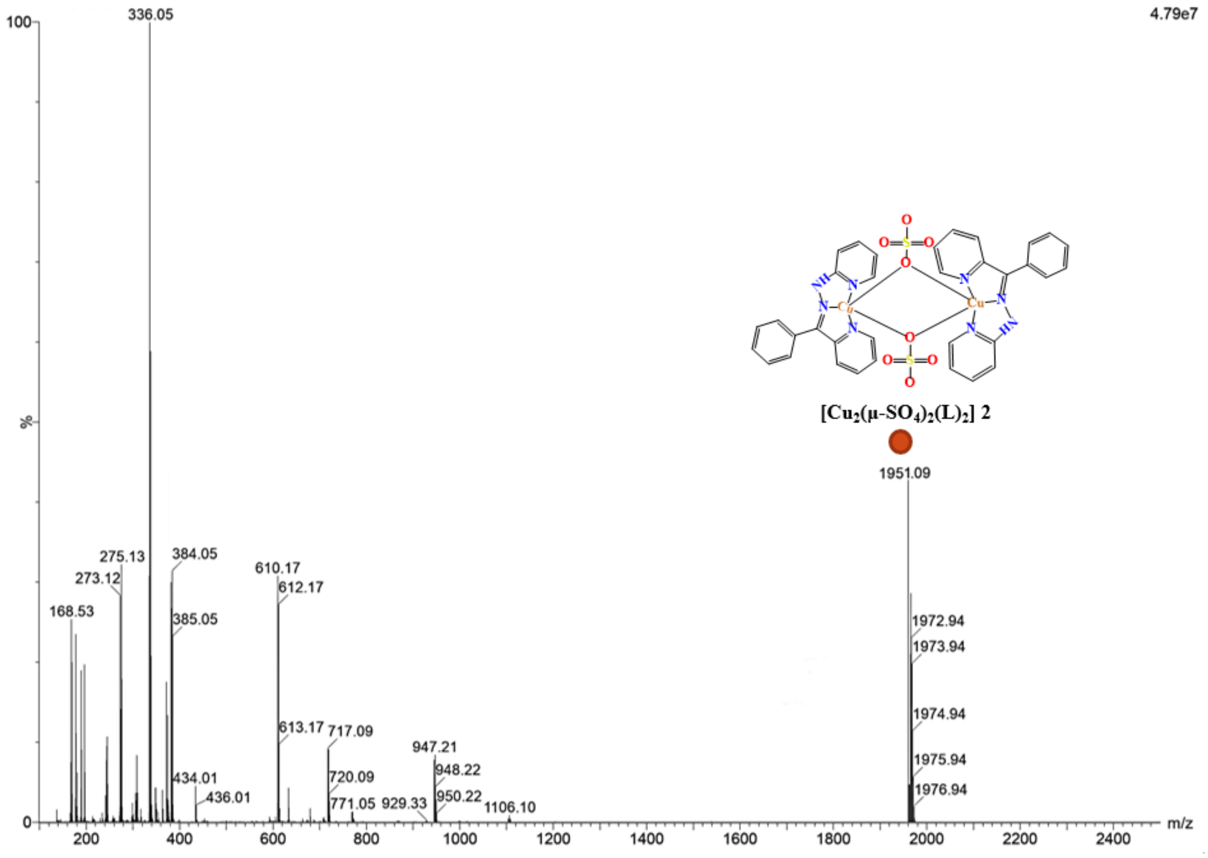

Fig. 26. Mass spectrum of complex **2**.

3.11 DFT calculations

3.11.1 Computational calculations of complexes

To help the physicochemical data (Epr and CV) DFT calculations were executed on complexes **1** and **2**. Geometry optimization was performed using density functional theory (DFT) at the B3LYP basic set [72, 73]. The optimized structure of complexes is shown in Fig. 27 and 28. The analysis of the frontier molecular orbital of the optimized structures shows that, in the gas phase, the highest occupied molecular orbitals (HOMOs) and lowest occupied orbitals (LUMOs) of both complexes are similar in energy. The graphical representations (counter plots) of frontier molecular orbitals (FMO) are depicted in Fig. 29. It is observed that the HOMOs of both complexes were mainly ligand centered, with the major contributions due to the *p* orbitals of donor atoms. From these observations it is easy to find out why the electrochemical potential is equal in magnitude because the oxidation takes place on the coordinating tridentate ligand, the potentials are likely to be slightly influenced by the nature of bridging ligand. The HOMO-LUMO energies are descriptors that play an important role in deciding the wide range of chemical interactions [74]. The FMOs give an insight into the reactivity of complexes and active sites can be understood by the distribution of frontier orbitals. Theoretical transition levels energy gap (ΔE) between HOMO and LUMO are shown in Table 9. On perusal of the HOMO-LUMO energy gap, it is observed that the gap (ΔE) is higher in both complexes. This higher ΔE implies that energy is higher and high chemical reactivity.

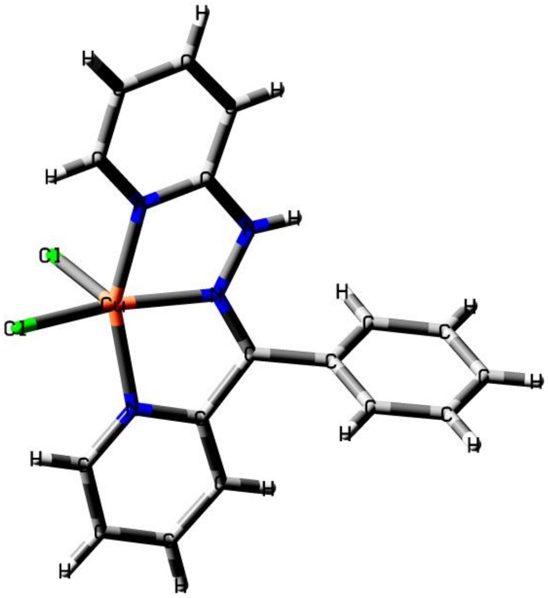

Fig. 27. Optimized structure of complex **1**.

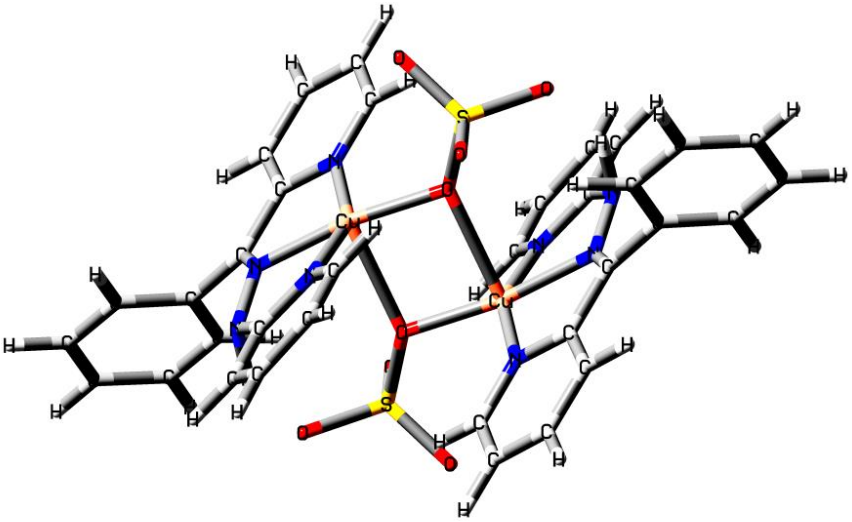

Fig. 28. Optimized structure of complex **2**.

Table 9 Molecular orbital energies and energy gap (ΔE).

Level	Molecular Orbital Energy(eV)		ΔE	
	1	**2**	**1**	**2**
HOMO	-3.896	-5.392		
LUMO	-1.008	-4.638	2.888	0.754
HOMO-1	-4.519	-6.335		
LUMO+1	+0.773	-2.808	3.746	3.527
LUMO	-5.025	-6.401		
LUMO+2	-0.728	-2.784	4.297	3.617

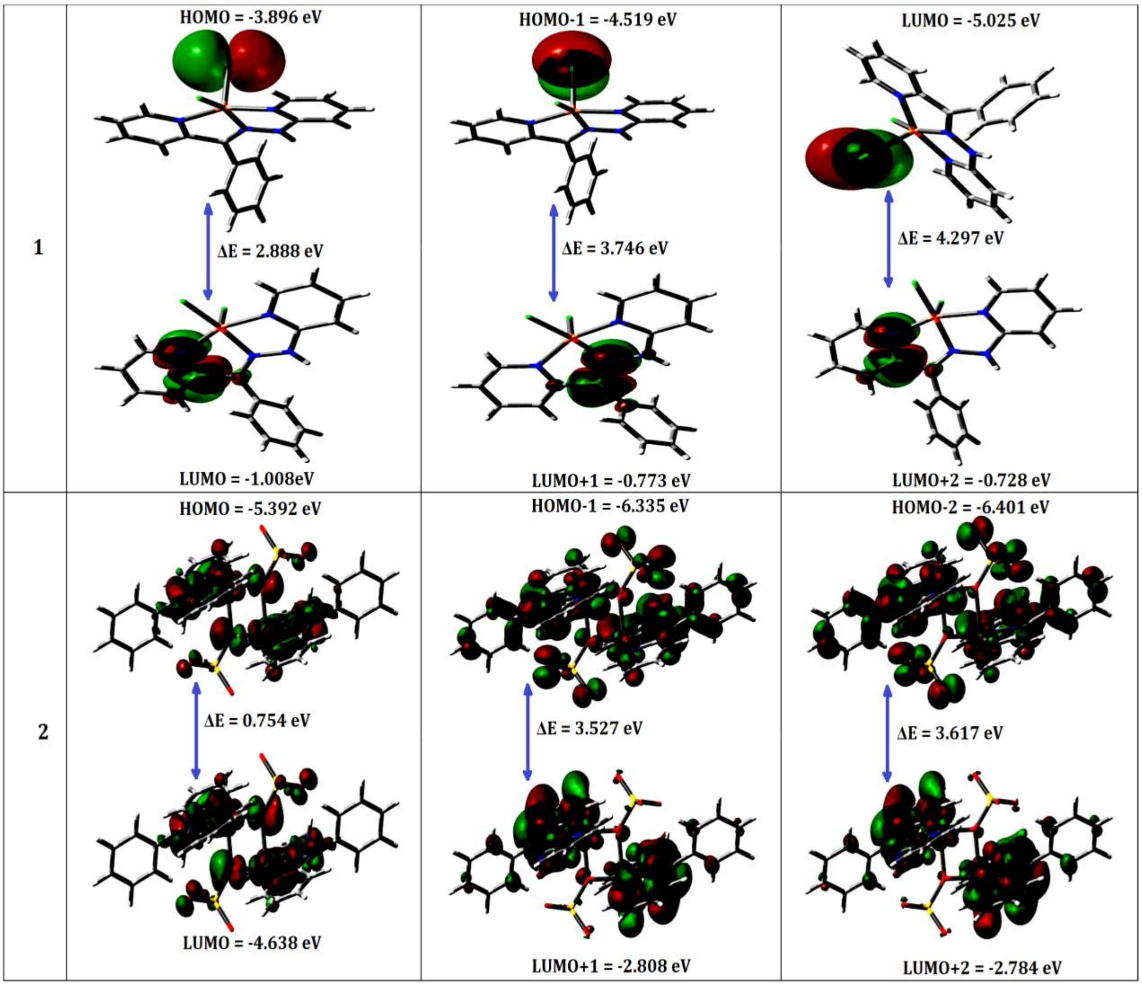

Fig. 29. HOMO-LUMO structures with energy level diagrams of complex **1** and **2**.

3.11.2 Spin density of complexes

The calculated spin densities were performed using the B3LYP/LANL2DZ as basis sets for both complexes. Fig.30. illustrates the spin densities for the ground state. The spin density distributions are mainly delocalized into the copper atom and those atoms which are directly coordinated to the copper atom [75]. The spin density plots of complexes are shown in Fig. 30. The positive signed densities are spread over the metal center and the negative signed spin densities are distributed over the coordinated donor atoms. Such spin density distributions were also in agreement with HOMO-LUMO shapes observed in both complexes. It is also shown from DFT calculations that the DFT data agrees with Epr spectral data from which a mainly ligand centered character of the unpaired electron in $d_{x^2-y^2}$ along with axial features of Epr signals was concluded [76].

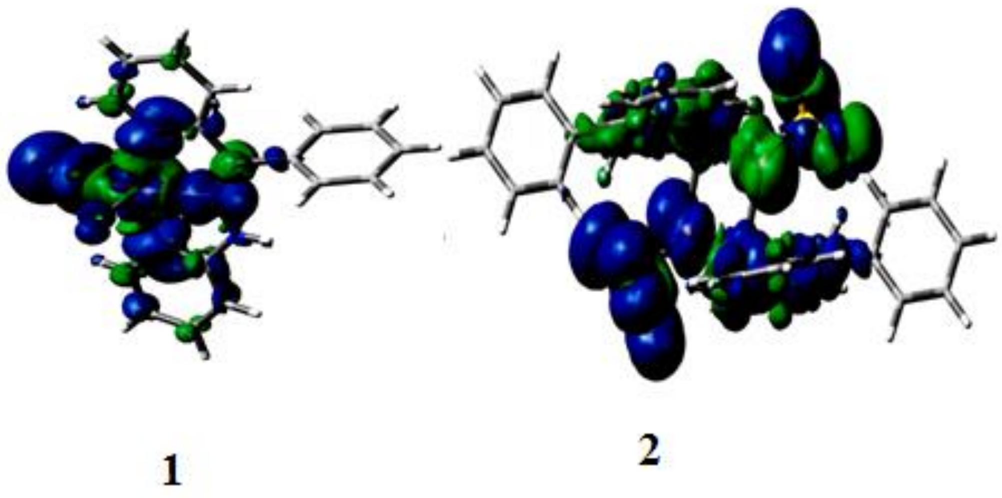

Fig. 30. Spin density plots of complex **1** and **2**.

3.11.3 Natural bond order (NBO) analysis

The NBO analysis of the synthesized complexes **1** and **2** has been carried out using the B3LYP/LAN2DZ basis set. The computed bond lengths and bond angles are explicitly similar to the experimentally observed values (Table 7). NBO analysis provides details about the natural charges between occupied Lewis-type orbitals and unoccupied non-Lewis NBOs (Rydberg), which correlates with stabilizing donor-acceptor interactions [77, 78]. As per NBO analysis, all the interaction in Cu(II) ions and donor atoms are considered as coordination bonds (N→Cu, Cl→Cu and O→Cu). Such type of interaction attributes to a donation of the electron density from the lone pair orbital on the donor atoms (N/Cl/O), LP(Cl) or LP(O) to the anti-bonding orbital on the Cu(II) LP*(Cu). The involved selected orbitals in interaction are shown in Fig. 31.

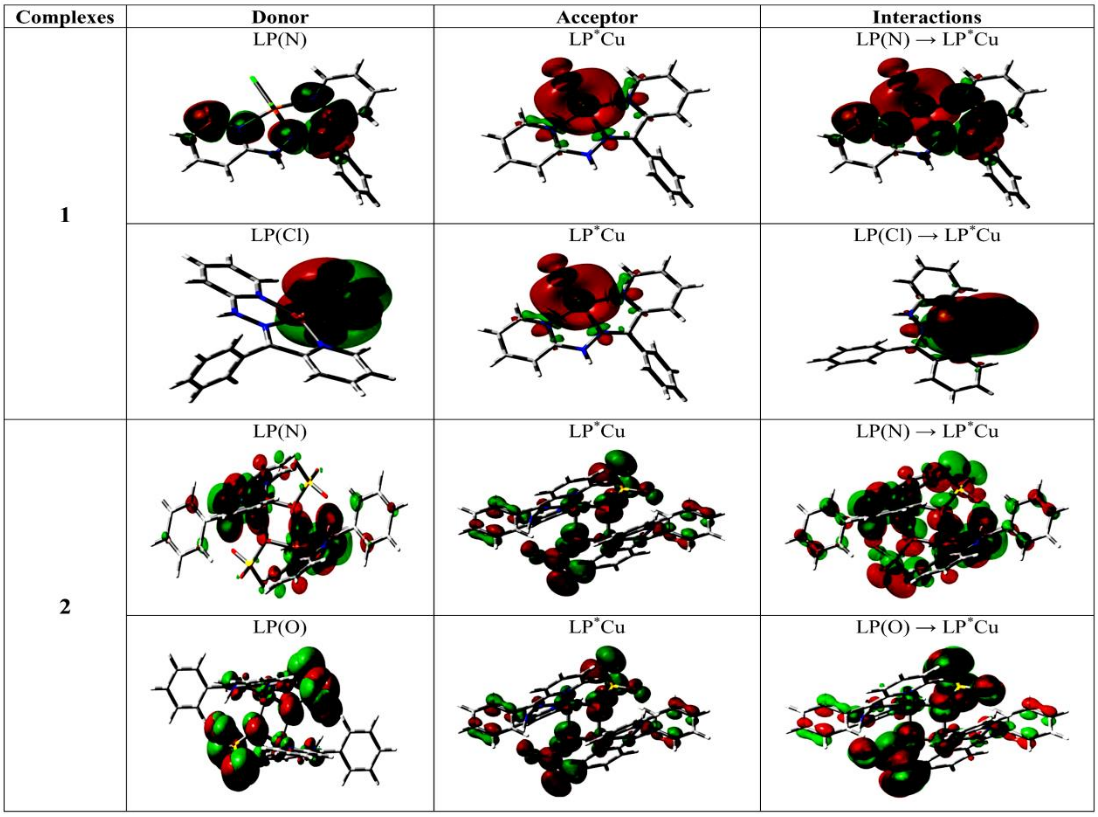

Fig. 31. The donor and acceptor orbitals involved in the LP(N)/ LP*(Cu) and LP(O)/ LP*(Cu) interactions.

The natural electronic configuration of Cu atoms are [Ar] $3d^{9.36}$ $4s^{0.35}$ $4p^{0.64}$, $5p^{0.02}$ in **1** and [Ar] $3d^{9.46}$ $4s^{0.26}$ $4p^{0.37}$, $5p^{0.01}$. Similarly, natural atomic configurations in copper ions are Cu^{2+} = +0.638, Cl_1 = -0.479, Cl_2 = -0.622, N_2 = -0.350, N_3 = -0.287 and N_4 = -0.507 in 1 and Cu^{2+} =+0.905, O_{1A} = -1.015, O_{1B} = -1.011, N_1 = -0.557, N_2 = -0.306 and N_3 = -0.312 in **2**. For **1**, 17.996 electrons are distributed as core electrons, 10.341 electrons as valence on 4s, 3d and 4p orbitals and 0.025 electrons as Rydberg electrons on the 5p orbital giving a total electron count of 28.362. This is compatible with the calculated natural charge of the Cu atom (+0.6382) which is correlated to the difference between 28.362 and the total number of electrons in an isolated copper atom (29 e). Likewise, core, valence, Rydberg electrons and the natural charge on the copper atom in **2** are 17.994, 10.089, 0.012 and +0.905 respectively. Before complexation, the charge on a copper ion is +2, despite the fact, the charges on copper(II) ion in complexes **1** and **2** are +0.638 and +0.905 respectively.

Second-order perturbation stabilization energies analogous to the intermolecular charge transfer interaction (donor-acceptor) of complexes were obtained using the

B3LYP/LAN2DZ basis set. The computed intermolecular charge transfer energies (E) for complexes 0.25 kcal/mol for **1** and 0.50 kcal for **2** are due to the electron delocalization around the coordinated ligands. The fact the complexes **1** and **2** may give rise to quite different intermolecular charge transfer energy. Complex **2** had a stronger (two times of 1) intermolecular charge transfer due to the presence of two bridged copper atoms. This is also confirmed with results obtained for frontier molecular orbitals (HOMO and LUMO) energy gaps (ΔE).

The HOMO-LUMO energy gap allows information about the reactivity and nature (soft or hard) of the molecule. Energies of six frontier molecular orbitals (FMOs) for complexes **1** and **2** were noticed negative values demonstrating that the present complexes are stable [79]. The energy gap (ΔE) in between E_{LUMO} and E_{HOMO} in **1**>**2**. The ΔE is also used to predict the global reactivity descriptors, which additionally describes the internal charge transfer, susceptivity and stability of molecules [80-83]. The global reactivity descriptors such as electronegativity (χ), global hardness (η), global electrophilicity (ω), electron donor capability (ω^-), electron acceptor capability (ω^+) and global softness (σ) are calculated using the formulas based on Koopman's theorem.

$$\text{Electronegativity } (\chi) = \tfrac{1}{2}\,(E_{Homo} + E_{Lumo})$$

$$\text{Global hardness } (\eta) = \tfrac{1}{2}\,(E_{Homo} - E_{Lumo})$$

$$\text{Global softness } (\sigma) = 1/\eta$$

$$\text{Electrophilicity } (\omega) = \chi 2 / 2\eta$$

$$\text{Electron donating capability } (\omega^-) = (3E_{HOMO} + E_{LUMO})^2 / 16(E_{HOMO} - E_{LUMO})$$

$$\text{Electron accepting capability } (\omega^+) = (E_{HOMO} + 3E_{LUMO})^2 / 16(E_{HOMO} - E_{LUMO})$$

The values of global reactivity parameters are presented in Table S6. On the perusal of reactivity parameters shown in Table 11, it was observed that all parameters of **2** are greater than that of **1** except global hardness. This fact can be explained as complex **1** with greater resistance to change with the number of electrons. In complex **2** ligands could be more coordinated with the metal surface than in **1** [84]. Dipole moment(μ) of these complexes is also estimated in different *x*, *y* and *z* coordinates. Table 12 is equipped with dipole moment value and its component along *x*, *y* and *z* directions. The result reveals that the higher value of μ is found to be in **1**, while at least in **2**. In the literature, the urea molecule is widely found as a reference for the comparison of dipole moment. The dipole moment of **1** greater than the urea molecule, while of **2** is least due to its symmetric structure [85].

Table 11 Global reactivity parameters of complexes in eV calculated by DFT B3LYP / LANL2DZ basic Set.

Complexes	χ	η	Ω	ω^-	ω^+	Σ
1	2.452	1.444	4.163	2.054	0.610	0.346
2	5.014	0.377	33.342	2.698	2.321	1.326

Table 12 The dipole moment of complexes.

Complexes	μ_x	μ_y	μ_z	μ(D)
1	11.5013	-7.8687	-4.1478	14.5401
2	0.0001	0.0003	-0.0007	0.0008

3.12 Hirshfeld Surface Analysis of HL and complexes

Molecular Hirshfeld surfaces [86] in the crystal structure were constructed on the basis of the electron distribution calculated as the sum of spherical atom electron densities [87, 88]. For a given crystal structure and a set of spherical atomic densities, the Hirshfeld surface is unique [89]. The normalized contact distance (d_{norm}) based on both d_e and d_i (where d_e is distance from a point on the surface to the nearest nucleus outside the surface and d_i is distance from a point on the surface to the nearest nucleus inside the surface) and the vdW radii of the atom, as given by eq 1 enables identification of the regions of particular importance to intermolecular interactions [86]. The combination of d_e and d_i in the form of two-dimensional (2D) fingerprint plot [90, 91] provides a summary of intermolecular contacts in the crystal [86]. The Hirshfeld surfaces mapped with d_{norm} and 2D fingerprint plots were generated using the Crystal-Explorer 2.1 [92]. Graphical plots of the molecular Hirshfeld surfaces mapped with d_{norm} used a red-white-blue colour scheme, where red highlight shorter contacts, white represents the contact around vdW separation, and blue is for longer contact. Additionally, two further coloured plots representing shape index and curvedness based on local curvatures are also presented in this paper [93].

$$d_{\text{norm}} = \frac{d_i - r_i^{\text{vdW}}}{r_i^{\text{vdW}}} + \frac{d_e - r_e^{\text{vdW}}}{r_e^{\text{vdW}}} \qquad (1)$$

The Hirshfeld surfaces for the ligand is resented in Figure 32(a). For this ligand the d_{norm} surface is mapped between the range of -0.5 to 1.2 Å, shape index is constructed between -0.9

to 0.9 Å and the curvedness is mapped in the range -4.0 to 0.4 Å. All of these surfaces are presented in transparent fashion to offer better visualization of all the aromatic rings present in the ligand. The N···H as well as C-H···π interactions as discussed in the molecular structure description (*vide supra*) are visualised as different type of spots in the d_{norm} surface. The large circular deep red depressions in d_{norm} surface is indicating hydrogen N···H interactions while C−H···π interactions are evidenced as faint red shaded area.

Another very pertinent result of the Hirshfeld surface analyses is the fingerprint plots (Fig. 32(b)). In fingerprint plots the complementary regions are presented in the mode where one molecule act as donor ($d_e > d_i$) and another behave as acceptor ($d_e < d_i$). Apart from this, the total fingerprint plots have been decomposed to focus on the particular atom pair close contacts. This enabled separation of contributions from different interaction types, which usually overlap in the full fingerprint. The fingerprint plot of the ligand possess equal sized spikes and represents varied interactions of the ligand (vide infra).

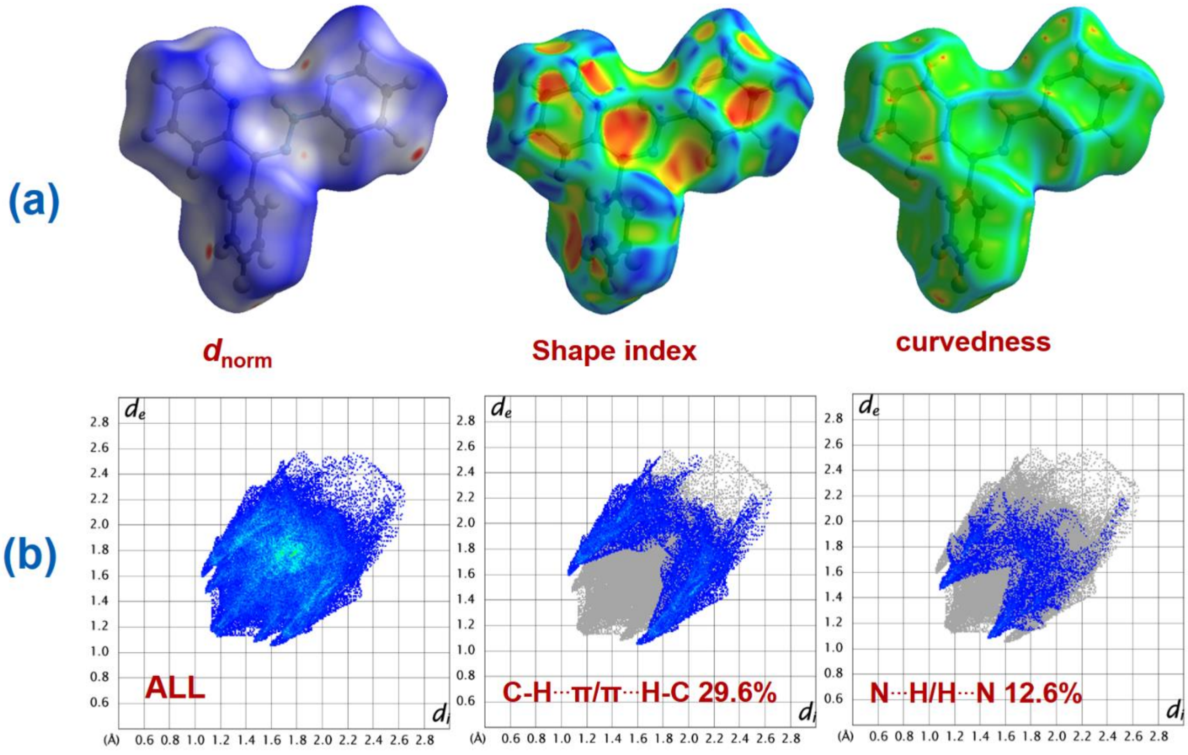

Fig. 32(a). Hirshfeld surfaces mapped with d_{norm}, shape index and curvedness for the ligand; (b). Fingerprint plots for the ligand showing percentages of contact contributed to the total Hirshfeld surface area of the ligand molecule.

The most important interaction in the ligand is the N···H interaction which appear as discrete spikes 1.1 Å < (d_e + d_i) < 2.2 Å in the total fingerprint plot of the ligand. The

Hirshfeld surface calculation revealed that this interaction is contributing 12.6% of the total Hirshfeld surface area. In addition, another important weak interaction in the molecule is C-H···π interactions which too is appearing as the distinct pair of spikes in the total fingerprint plot between the range 1.05 Å < (d_e + d_i) < 2.55 Å. This interaction is exhibiting 29.6% contribution in the total Hirshfeld surface.

The Hirshfeld surfaces for both the copper complexes **1** and **2** have been shown in Fig. 33. For better visualization of aromatic as well as the chelate rings in both the complexes the surfaces are plotted in transparent manner. The d_{norm} surface for both the complexes are mapped between -0.3 to 1.4 Å range, shape index plots are constructed between -0.9 to 0.9 Å while curvedness plots are mapped in the range -4.0 to 0.4 Å. In **1**, the Cl···H and in **2** the O···H interactions which have been discussed in the supramolecular architecture section for both the complexes (vide supra) can be seen as the large circular deep red depressions. The relatively weaker H···π interactions are also present in the as faint red shaded area in the corresponding d_{norm} surfaces.

Another very relevant result of the Hirshfeld surface analyses are the fingerprint plots Fig. 34. In these two-dimensional plots, the complementary regions can be shown in the manner where one molecule act like donor (d_e > d_i) and another as acceptor (d_e < d_i). Additionally, the total fingerprint plots (represented as ALL in the Fig. 34) can be split-apart in several fragments tolay emphasis on the particular atom pair close contacts. This enables estimation of contributions coming from various interactions existing in the molecule. The fingerprint plots of both the complexes display equal sized spikes as the light blue region which represents various interactions existing in the complex (vide infra). In **1**, the most important interaction in the ligand is the H···Cl/Cl···H interaction which appear as discrete spikes 1.45 Å < (d_e + d_i) < 2.43 Å in the total fingerprint plot of this complex. The Hirshfeld surface calculation revealed that this interaction is having contribution of 20.9% in its total Hirshfeld surface. In **2**, the most important is the O···H/H···O interaction which too is appearing as sharp spikes in the region 0.9 Å < (d_e + d_i) < 2.7 Å and is contributing 24.5% of the total Hirshfeld surface area. Apart from this both the complexes exhibit H···π interactions which in the case of **1** is of C-H···π type while in **2** they are of C-H···π as well as S-H···π types. In **1** this interaction appears in 1.0Å < (d_e + d_i) < 2.8 Å while in **2** it can be seen in the area 1.0 Å < (d_e + d_i) < 2.5 Å. These interactions are contributing 24.8% and 21.2% in the total Hirshfeld surface area of **1** and **2**, respectively.

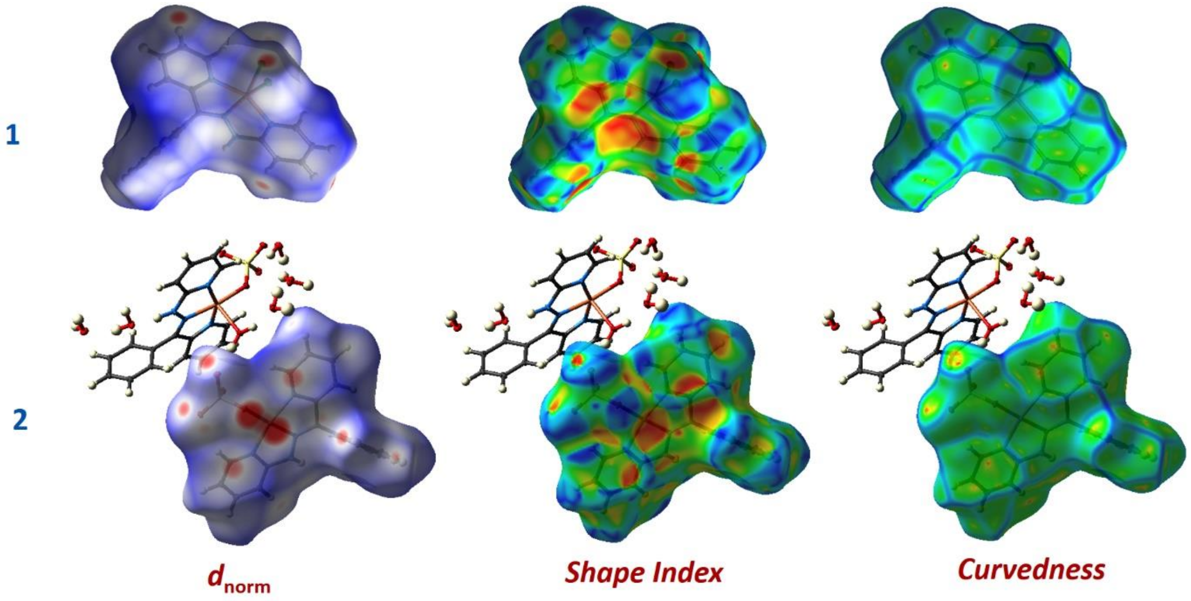

Fig. 33. Hirshfeld surfaces mapped with d_{norm}, shape index and curvedness for the complexes **1** and **2**.

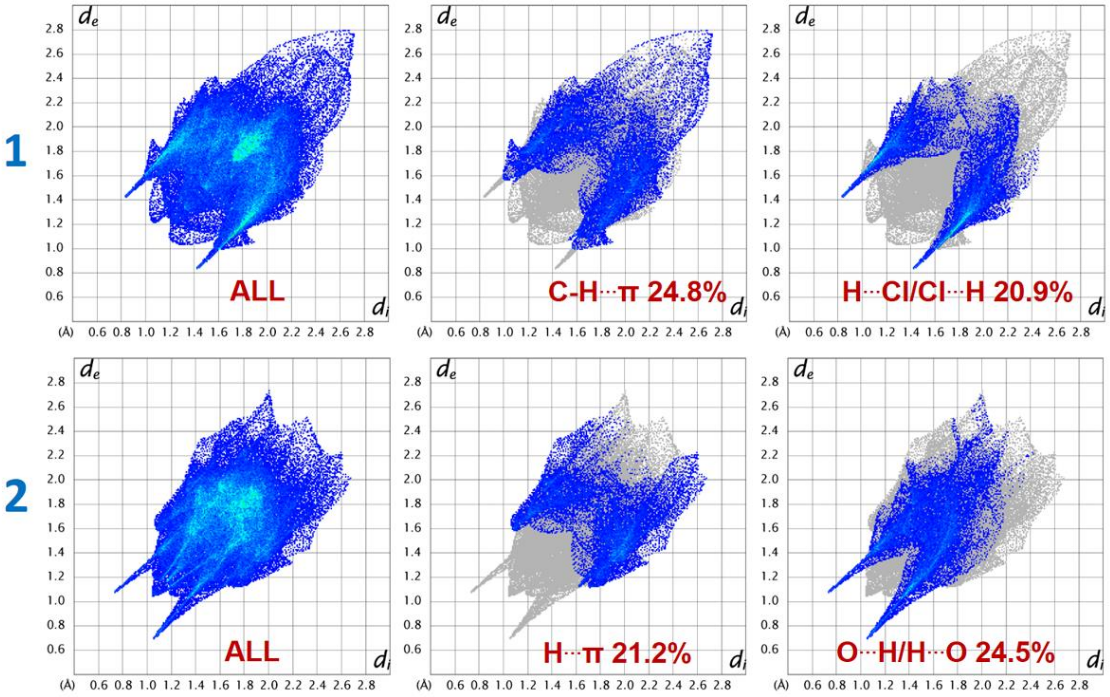

Fig. 34. Fingerprint plots for the ligand showing percentages of contact contributed to the total Hirshfeld surface area in complexes **1** and **2**.

3.13. Reactivity with superoxide

Superoxide anion ($O_2^{\cdot-}$) is often employed to get information on M - $O_2^{\cdot-}$ interactions. The *in vitro* antioxidant superoxide reactivity of complexes has been evaluated using the alkaline DMSO-nitro blue tetrazolium (NBT) method [94-96]. The plot of percent inhibition

(% Inhibition) is presented in Fig. 35. The concentrations of the reduction (IC_{50}) were determined for both complexes. Superoxide dismutase activity and catalytic constant (K_{cat}) also evaluated. These SOD data are compared with similar known SOD mimics as presented in Table 13 [94, 97-100]. The results reveal that both complexes are more efficient than Vitamin C(Vc), which is the standard for antioxidant superoxide dismutase [60, 61]. The SOD activity of complex **1** is higher than **2**. The SOD activities of present complexes are comparable to those of reported SOD mimics but lower than the best-reported value. The difference in SOD data between **1** and **2** may be ascribed due to the structural variation.

The catalytic SOD cycle based on the molecular structures can be depicted in Scheme 4. The catalytic reaction starts when $O_2^{\cdot -}$ is electrostatically guided into the active site channel [101, 102]. It associated and binds directly to the copper(II) center and gives its electron via an inner-sphere mechanism. Oxygen molecule no longer charged and diffuses out of the active site channel. In the second half of the catalytic cycle, $O_2^{\cdot -}$ is electrostatically drawn into the active site channel. As the electron is accepted by the reduced copper center Cu(I) via an outer sphere electron-transfer mechanism, $O_2^{\cdot -}$ accepts a proton (H^+) simultaneously from the water molecule. The copper(II) ion can now move to reform the molecular structure and hydrogen peroxide (H_2O_2) diffuses out of the active site channel [103]. This catalytic cycle permits to propose a structure-based cyclic mechanism for Cu-Zn SOD catalytic action.

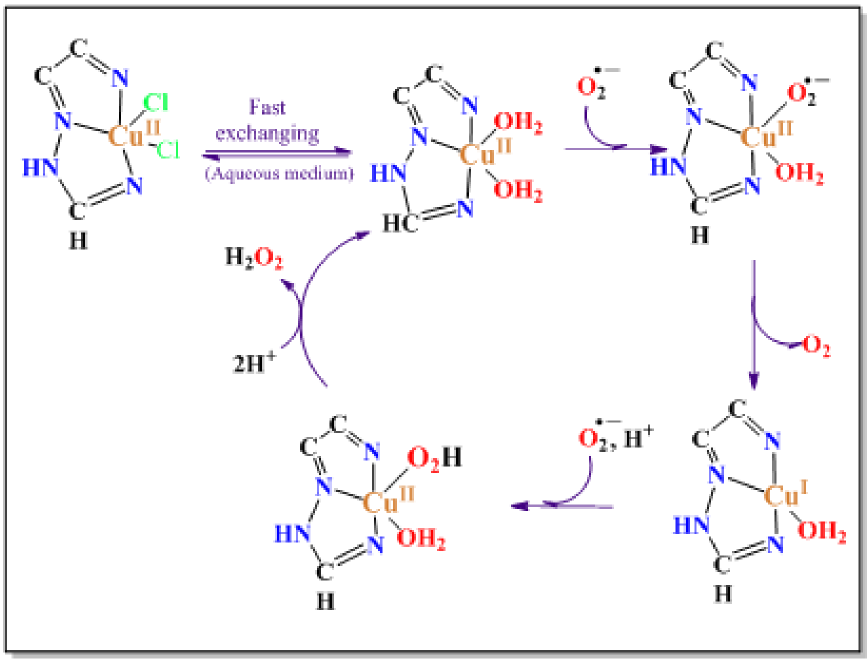

Scheme 4 The suggested mechanism of $O_2^{\cdot -}$dismutation reaction catalyzed by a complex.

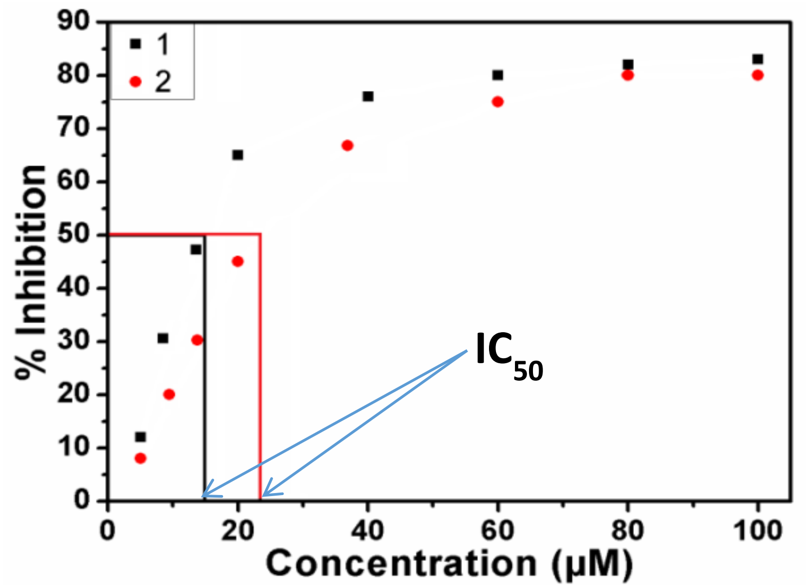

Fig. 35. A plot of % inhibition of NBT reduction vs concentration of complexes **1** and **2**.

Table 13 SOD activities (IC$_{50}$ values kinetic catalytic constant and SOD activity) of Cu(II) complexes.

S. No.	Complex	IC$_{50}$ (μM)	SOD activity (μM^{-1})	k$_{cat}$ (M^{-1}S^{-1})	Reference
1.	Vc	852	1.17	0.39	60, 61
2.	[Cu(acetyl salicylate)$_2$]	23	43.48	14.36	97,98
3.	$[Cu(L^1)(H_2O)] NO_3$	6	166.67	55.44	99,100
4.	$[Cu(L)(NO_3)]$	16	62.50	20.79	99,100
5.	Native Cu-Zn SOD	-	0.04	25000	94
6.	$[Cu(im)Cu(pip)_2]_3^+$	0.50	2000	665.28	94
7.	$[Cu(L)Cl_2]$	15	66.67	22.18	Present work
8.	$[Cu_2(\mu\text{- }SO_4)(L)_2]$	22	45.45	15.12	Present work

L^1 = 4-chloro-2-{(E)-[2-(pyridin-2-yl)hydrazinylidene]methyl}phenol.

3.14. Cytotoxicity Assay

The anticancer activity of complexes **1**, **2** and ligand (**HL**) was assessed against four types of cancer cell lines IMR 32 (neuroblastoma), MCF 7 (breast cancer), HepG2 (hepatocellular carcinoma) and A549 (lung cells) have been examined in comparison with the positive standard cisplatin under identical conditions by using MTT assay. The ability of the drugs to inhibit cell proliferation is an important character to prove its efficacy as a therapeutic drug. However, the major challenging aspect of synthesizing new chemotherapeutic agents is selectivity toward cancerous cells compared with the normal cells [104-106]. It is found that the compounds exhibit significant cytotoxic activities after 24 hrs of exposure. The IC_{50} value (concentration required for 50% inhibition of cell growth) was calculated and the IC_{50} value of different synthesized compounds is shown in Table 14. Cell growth was observed inhibited on increasing concentration, indicating that **1**, **2**, **HL** and cisplatin had the potential to arrest cell survival. On comparison of different compound IC_{50} values with cisplatin, both complexes **1**, **2** and **HL** showed promising cytotoxicity on the selected cancerous cell of the study (A549, IMR322, HepG2 and A549). Among all compounds, cell proliferation was depleted highest on HL exposure. The IC_{50} value of lung carcinoma cells on HL treatment was observed lowest whereas compounds **1** and **2** were more effective for hepatocellular carcinoma. Copper compounds are potentially cytotoxic because they exhibit a transition between Cu(II) and Cu(I) that can result in the generation of superoxide and hydroxyl radicals and induces cell death [107]. From the preceding discussion, it is evident that both complexes and ligand showed better efficiency in terms of *in vitro* anticancer activity. In comparison to all cell lines, compounds were observed more potent against HepG2 and A549 cell lines [108, 109].

Table 14 The *in vitro* cytotoxic activity (expressed as IC_{50}) of copper complexes against the different cell lines.

Compound	**IC_{50} Value(μM)**			
	MCF 7	**IMR 32**	**HepG2**	**A549**
1	105.6236	112.6543	101.209	119.194
2	184.2575	207.68	168.6424	174.107
Ligand	84.27725	87.56933	79.88781	75.169
Cisplatin	34.59	38.99	31.04	25.33

4. Conclusions

Two new mono and binuclear copper(II) complexes were synthesized by a biomimetic strategy and their structures were solved by single-crystal X-ray and various spectral techniques. All the copper centers in both complexes have pentacoordinate geometries. This kind of geometry has been observed also some known di- or polynuclear copper(II) complexes [110, 111]. Low-temperature susceptibility measurements revealed that the copper(II) centers in both complexes **1** and **2** are weakly anti-ferromagnetically coupled. Complex **2** is a unique example showing Ferro- and antiferromagnetic couplings. The ferromagnetic coupling in the two symmetric sulphate bridges fully agrees with the previous magneto-structural correlations [112]. Antioxidant SOD activities were also examined. Both complexes are potent SOD mimics. The structures-activity relationship for complexes was studied to support the experimental findings to assess some important parameters, *viz.*, bond length, bond angle, HOMO-LUMO energy gap (ΔE), global reactivity descriptors, dipole moment, second-order perturbation energies and spin density. The antioxidant SOD and antiproliferative properties *in vitro* suggest the encouraging applications of **1** and **2** in biology and pharmaceuticals sciences.

References

1 A.L. Gavrilova, B. Bosnich, Chem. Rev. 104 (2004) 349-384.
2 P. Guerriero, S. Tamburini, P.A. Vigato, Coord. Chem. Rev. 139 (1995) 17.
3 D. Kong, J. Reibenspies, J. Mao, A. Clearfield, A.E. Martell, Inorg. Chim. Acta 342 (2003) 158-170.
4 U. Casellato, S. Tamburini, P. Tomasin, P.A. Vigato, Inorg. Chim. Acta 357 (2004) 4191-4202.
5 B. Bleaney, K.D. Bowers, Proc. R. Soc. A 214 (1952) 451-465.
6 O. Kahn, Angew. Chem., Int. Ed. Engl. 24 (1985) 834-850.
7 A. Bencini, D. Gatteschi, Electron Paramagnetic Resonance of Exchange Coupled Systems, Springer-Verlag, Berlin, (1990).
8 O. Kahn, Molecular Magnetism, Wiley VCH, New York, (1993).
9 O. Kahn, Acc. Chem. Res. 33 (2000) 647-657.
10 P.A. Vigato, V. Peruzzo, S. Tamburini, Coord. Chem. Rev. 256 (2012) 953-1114.
11 T.D. Hamilton, G.S. Papaefstathiou, L.R. MacGillivray, Cryst. Eng. Comm. 4 (2002) 223-226.
12 X.M. Ouyang, Z.W. Li, T. Okamura, Y.Z. Li, W.Y. Sun, W.X. Tang, N. Ueyama, J. Solid State Chem. 177 (2004) 350-360.
13 L.K. Thompson, Z. Xu, A.E. Goeta, J.A.K. Howard, H.J. Clase, D.O. Miller, Inorg. Chem. 37 (1998) 3217-3229.
14 H. Araki, K. Tsuge, Y. Sasaki, S. Ishizaka, N. Kitamura, Inorg. Chem. 44 (2005) 9667-9675.
15 S.G. Telfer, T. Sato, T. Harada, R. Kuroda, J. Lefebvre, D.B. Leznoff, Inorg. Chem. 43 (2004) 6168-6176.

16 Y.-K. He, Z.-B. Han, Acta Crystallogr. Sect. E 62 (2006) m2676-m2677.

17 K.K. Sarker, D. Sardar, K. Suwa, J. Otsuki, C. Sinha, Inorg. Chem. 46 (2007) 8291-8301.

18 Y. Okubo, A. Okamura, K. Imanishi, J. Tachibana, K. Umakoshi, Y. Sasaki, T. Okamura, Bull. Chem. Soc. Jpn. 72 (1999) 2241-2247.

19 B. Greener, S.P. Foxon, P.H. Walton, New J. Chem. 24 (2000) 269-273.

20 N. Lah, I.K. Cigic, I. Leban, Inorg. Chem. Commun. 6 (2003) 1441-1444.

21 S.G. Telfer, T. Sato, T. Harada, R. Kuroda, J. Lefebvre, D.L. Leznoff, Inorg. Chem. 43 (2004) 6168-6176.

22 A.H.I. Venkato Jr., A.J. Bortuluzzi, V. Drago, M.A. Novak, A. Neves, J. Braz. Chem. Soc. 17 (2006) 1584-1593.

23 R. Glier, M. Jorand, C. Waegell, B. Waegell, J. Chem. Soc., Chem. Commun. (1990) 1752.

24 K.D. Karlin, Z. Tyeklar, Bioinorganic Chemistry of Copper, Chapman and Hall, New York, (1993).

25 B. Reinhammer, Copper Proteins and Copper Enzymes, CRC Press, Boca Raton, FL, (1984).

26 K.A. Magnus, H. Ton-That, J.E. Carpenter, Chem. Rev. 94 (1994) 727.

27 E.I. Solomon, U.M. Sundaram, T.E. Mackonkin, Chem. Rev. 96 (1996) 2563-2606.

28 N. Kitajima, Y. Moro-oka, Chem. Rev. 94 (1994) 737-757.

29 S. Ryan, H. Adams, D.E. Fenton, M. Becker, S. Schindler, Inorg. Chem. 37 (1998) 2134-2140.

30 P.L. Holland, W.B. Tolman, Coord. Chem. Rev. 55 (1999) 190-192.

31 H. Decker, R. Dillinger, F. Tuczek, Angew. Chem. Int. Ed. 39 (2000) 1591-1595.

32 N.C. Gerdemann, C. Eicken, B. Krebs, Acc. Chem. Res. 35 (2002) 183-191.

33 G. Dutta, R.K. Debnath, A. Kalita, P. Kumar, M. Sarma, R.B. Shankar, B. Mondal, Polyhedron 30 (2011) 293-298.

34 S.J. Lippard, Bioinorganic chemistry: a maturing frontier, Science 261 (1993) 699-700.

35 Y.P. Singh, R.N. Patel, Y. Singh, D.C. Lazarteb, R.J. Butcher, Dalton Trans. 46 (2017) 2803-2820.

36 D.D. Perrin, W.L.F. Armango, D.R. Perrin, Purification of Laboratory Chemicals, Pergamon, Oxford, U.K., 1986.

37 G.M. Sheldrick, SHELXS-97, Program for the Solution of Crystal Structures, University of Göttingen, Göttingen, Germany, 1997.

38 G.M. Sheldrick, Acta Crystallogr. A46 (1990) 467-473.

39 G.M. Sheldrick, SHELXL-97, Program for the Refinement of Crystal Structures, University of Göttingen, Göttingen, Germany, 1997.

40 G.M. Sheldrick, Acta. Crystallogr. A64 (2008) 112-122.

41 G.A. Petersson, M.A. Al-Laham, J. Chem. Phys. 94 (1991) 6081-6090.

42 P.J. Hay, W.R. Wadt, J. Chem. Phys. 82 (1985) 270-283.

43 M.J. Frisch, G.W. Trucks, H.B. Schlegel, G.E. Scuseria, M.A. Robb, J.R. Cheeseman, G. Scalmani, V. Barone, B. Mennucci, G.A. Petersson, H. Nakatsuji, M. Caricato, X.

Li, H.P. Hratchian, A.F. Izmaylov, J. Bloino, G. Zheng, J.L. Sonnenberg, M. Hada, M. Ehara, K. Toyota, R. Fukuda, J. Hasegawa, M. Ishida, T. Nakajima, Y. Honda, O. Kitao, H. Nakai, T. Vreven, J.A. Montgomery Jr., J.E. Peralta, F. Ogliaro, M. Bearpark, J.J. Heyd, E. Brothers, K.N. Kudin, V.N. Staroverov, R. Kobayashi, J. Normand, K. Raghavachari, A. Rendell, J.C. Burant, S.S. Iyengar, J. Tomasi, M. Cossi, N. Rega, J.M. Millam, M. Klene, J.E. Knox, J.B. Cross, V. Bakken, C. Adamo, J. Jaramillo, R. Gomperts, R.E. Stratmann, O. Yazyev, A.J. Austin, R. Cammi, C. Pomelli, J.W. Ochterski, R.L. Martin, K. Morokuma, V.G. Zakrzewski, G.A. Voth, P. Salvador, J.J. Dannenberg, S. Dapprich, A.D. Daniels, O. Farkas, J.B. Foresman, J.V. Ortiz, J. Cioslowski, D.J. Fox, Gaussian 09, Revision D.01, Gaussian Inc., Wallingford CT, (2009).

44 R. Bauernschmitt, R. Ahlrichs, Chem. Phys. Lett. 256 (1996) 454-464.

45 M. Cossi, N. Rega, G. Scalmani, V. Barone, J. Comput. Chem. 224 (2003) 669-681.

46 T. Mosmann, J. Immunol. 65 (1993) 55-63.

47 R.N. Patel, D.K. Patel, K.K. Shukla, Y. Singh, J. Coord. Chem. 66 (2013) 4131-4143.

48 R. G. Bhirud, T. S. Shrivastava, Inorg. Chim. Acta 173 (1990) 121–125.

49 R. Konecny, J. Li, C.L. Fisher, V. Dillet, D. Bashford, L. Noodleman, Inorg. Chem. 38 (1999) 940-950.

50 M. Sutradhar, M.V. Kirillova, M.F.C.G. Silva, C.M. Liu, A.J.L. Pombeiro, Dalton Trans. 42 (2013) 16578-16587.

51 L. Valencia, R. Bastida, M.C.F. -Fernández, A. Macías, M. Vicente, Inorg. Chim. Acta. 358 (2005) 2618-2628.

52 A.W. Addison, T.N. Rao, J. Reedijk, J.V. Rijn, G.C. Verschoor, J. Chem. Soc. Dalton Trans. 7 (1984) 1349-1356.

53 N. Goel, U.P. Singh, J. Phys. Chem. A 117 (2013) 10428-11043.

54 N. Goel, N. Kumar, J. Mol. Struct. 1071 (2014) 60-70.

55 G.A. Jeffrey, W. Saenger, In: Hydrogen Bonding in Biological Structures, Springer-Verlag, Berlin, 1996, pp. 3-14.

56 O.P. Anderson, A.B. Packard, Inorg. Chem. 19 (1980) 2941-2945.

57 L.K. Thompson, S.K. Mandal, S.S. Tandon, J.N. Bridson, M.K. Park, Inorg. Chem. 35 (1996) 3117-3125.

58 J.K. McCusker, J.B. Vincent, E.A. Schmitt, M.L. Mino, K. Shin, D.A.K. Coggin, P.M. Hagen, J.C. Huffman, G. Christou, D.N. Hendrickson, J. Am. Chem. Soc. 113 (1991) 3012-3021.

59 M. Iqbal, I. Ahmad, S. Ali, N. Muhammad, S. Ahmed, Polyhedron 50 (2013) 524-531.

60 Y. Singh, R.N. Patel, S.K. Patel, A.K. Patel, N. Patel, R. Singh, R.J. Butcher, J.P. Jasinski, A. Gutierrez, Polyhedron 171 (2019) 155-171.

61 R.N. Patel, Y. Singh, Y.P. Singh, A.K. Patel, N. Patel, R. Singh, R.J. Butcher, J.P. Jasinski, E. Colacio, M.A. Palacios, New J. Chem. 42 (2018) 3112-3136.

62 W.A. Alves, S.A. Almeida-Folho, R.H.A Santos, A.M.D.C. Ferreira, Inorg. Chem. Commun. 6 (2003) 294-299.

63 E. Garribba, G. Micera, J. Chem. Educ. 83 (2006) 1229-1232.

64 H. Guinaudeau, V. Elango, M. Shamma and V. Fajardo, J. Chem. Soc., Chem. Commun. (1982) 1122-1125.

65 H. Lavrenyuk, O. Mykhalichko, B. Zarychta, V. Olijnyk, B. Mykhalichko, J. Cord. Chem. 69 (2016) 2666-2676.

66 A. Bartyzel, J. Therm. Anal. Calorim. 131 (2018) 1221-1236.

67 S. Chandraleka, G. Chandramohan, Afr. J. Pure Appl. Chem. 8 (2014) 162-175.

68 (a) J.A. Bertrand, T.D. Black, P.G. Eller, F.T. Helm, R. Mahmood, Inorg. Chem. 15 (1976) 2965-2970; (b) H. Muhonen, Inorg. Chem. 25 (1986) 4692-4698; (c) N. Arulsamy, J. Glerup, D.J. Hodgson, Inorg. Chem. 33 (1994) 2066-2068; (d) W. Plass, A. Pohlmann, J. Rautengarten, Angew. Chem. 113 (2001) 4333-4333; (e) J. Tang, J.S. Costa, A. Golobi, B. Kozlev, A. Robertazzi, A.V. Vargiu, P. Gamez, J. Reedijk, Inorg. Chem. 48 (2009) 5473-5479; (f) A. Okazawa, T. Ishida, Chem. Phys. Lett. 480 (2009) 198-202; (g) M.S. Raya, A. Ghosh, R. Bhattacharya, G. Mukhopadhyay, M.G.B. Drew, J. Ribas, Dalton Trans. 252 (2004) 252-259; (h) C. Desplanches, E. Ruiz, S. Alvarez, Chem. Commun. (2002) 2614-2615; (i) C. Desplanches, E. Ruiz, A.R. -Fortea, S. Álvarez, J. Am. Chem. Soc. 124 (2002) 5197-5205; (j) F.A. Cotton, S. Herrero, R.J. -Aparicio, C.A. Murillo, F.A. Urbanos, D. Villagrán, X. Wang, J. Am. Chem. Soc. 129 (2007) 12666-12667; (k) M. Cortijo, R.G. -Prieto, S. Herrero, R.J. -Aparicio, P.S. -Rivera, Eur. J. Inorg. Chem. 32 (2013) 5523-5527; (l) M. Granelli, A.M. Downward, R. Huber, L. Guénée, C. Besnard, K.W. Krämer, S. Decurtins, S.-X. Liu, L.K. Thompson, A.F. Williams, Eur. J. Chem. 23 (2017) 7104-7112.

69 O. Khan, Molecular Magnetism, VCH Publishers: New York, 1993.

70 (a) S. Basak, S. Sen, P. Roy, C.G. -García, D.L. Hudges, R.J. Butcher, E. Garriba, S. Mitra, Aust. J. Chem. 63 (2010) 479-489; (b) E. Ruiz, J. Cano, S. Álvarez, P. Alemany, J. Am. Chem. Soc. 120 (1998) 11122-11129; (c) V.H. Crawford, H.W. Richardson, J.R. Wasson, D.J. Hodgson, W.E. Hatfield, Inorg. Chem., 15 (1976) 2107-2110.

71 K. Dankhoffa, B. Weber, Cryst. Eng. Comm. 20 (2018) 818-828.

72 A.D. Backe, J. Chem. Phys. 98 (1992) 5648-5692.

73 C. Lee, W. Yang, R.G. Parr, Motor. Phys. Rev. B Condens. Matter 37 (1988) 785-789.

74 Z. Zhou, R.G. Parr, J. Am. Chem. Soc. 112 (1990) 5720-5724.

75 J. Adhikary, P. Chakraborty, S. Das, T. Chattopadhyay, A. Bauza, S.K. Chattopadhyay, B. Ghosh, F.A. Mautner, A. Frontera, D. Das,Inorg. Chem. 52 (2013) 13442-13452.

76 A. Klien, D.A. Vicic, C. Biewer, I. Kieltch, K. Stirnat, C. Hamacher, Organometallics 31 (2012) 5334-5341.

77 A.E. Reed, L.A. Curtiss, F. Weinhold, Chem. Rev. 88 (1988) 899-926.

78 S. Nawaz, A. Ghaffar, W. Zierkiewicz, M.M.-ul-Mehboob, Khurram, M.N. Tahir, A.A. Isab, S. Ahmad, J. Mol. Struct. 1137 (2017) 784-791.

79 R. Jawari, M. Hussian, M. Khalid, M.U. Khan, M.N. Tahir, M.M. Naseer, A.A.C. Braga, Z. Shafiq, Inorg. Chim. Acta. 486 (2019) 162-171.

80 R.G. Parr, L. Szentpály, S. Liu, J. Am. Chem. Soc.121 (1999) 1922-1924.

81 R.G. Parr, R.A. Donnelly, M. Levy, W.E. Palke, J. Chem. Phys. 68 (1978) 3801-3807.

82 P.K. Chattaraj, U. Sarkar, D.R. Roy, Chem. Rev.106 (2006) 2065-2091.

83 A. Lesar, I. Milosev, Phys. Lett. 483 (2009) 198-203.

84 A. Kokalj, Chem. Phys. 393 (2012) 1-12.

85 P.N. Prasad, D.J. Williams, Introduction to non-linear effect in molecules and polymer, John Wiley & Sons, New York, 1991.

86 M.A. Spackman, J.J. McKinnon, Cryst. Eng. Comm. 4 (2002) 378-392.

87 M.A. Spackman, P.G. Byrom, Chem. Phy. Lett. 267 (1997) 215-220.

88 J.J. McKinnon, A.S. Mitchell, M.A. Spackman, M. A. J. Eur. Chem. 4 (1998) 2136-2141.

89 J.J. McKinnon, M.A. Spackman, A.S. Mitchell, Acta Crystallogr. Sec. B 60 (2004) 627-668.

90 A.L Rohl, M. Moret, W. Kaminsky, K. Claborn, J.J. McKinnon, B. Kahr, Cryst. Growth Des. 8 (2008) 4517-4525.

91 A. Parkin, G. Barr, W. Dong, C.J. Gilmore, D. Jayatilaka, J.J. McKinnon, M.A. Spackman, C.C. Wilson, Cryst. Eng. Comm. 9 (2007) 648-652.

92 S.K.Wolff, D.J. Greenwood, J.J. McKinnon, D. Jayatilaka, M.A. Spackman, Crystal Explorer 2.0; University of Western Australia: Perth, Australia, 2007.

93 J.J. Koenderink, A.J. van Doorn, A. J. Image Vision Comput.10 (1992) 557 564.

94 U. Weser, L.M. Schubotz, E. Lengfelder, J. Mol. Catal. 13 (1981) 249-261.

95 Y.P. Singh, R.N. Patel, Y. Singh, D.C. –Lazarteb, R.J. Butcher, Dalton Trans. 46 (2017) 2803-2820.

96 R. Konecny, J. Li, C.L. Fisher, V. Dillet, D. Bashford, L. Noodleman, Inorg. Chem. 38 (1999) 940-950.

97 B.J. Hathaway, Structure and Bonding, Berlin, 57 (1984) 55-118.

98 E. Garriba, J. Micera, J. Chem. Educ. 83 (2006) 1229-1232.

99 A.K. Patel, R.N. Jadeja, H. Roy, R.N. Patel, S.K. Patel, R.J. Butcher, J. Mol. Strut. 1185 (2019) 341-350.

100 Y. Singh, R.N. Patel, Y.P. Singh, A.K. Patel, N. Patel, R. Singh, R.J. Butcher, J.P. Jasinski, E. Colacio, M.A. Palacios, Dalton Trans. 46 (2017) 11860-11874.

101 R.G. Bhirud, T.S. Srivastava, Inorg. Chim. Acta. 173 (1990) 121-125.

102 E.D. Getzoff, J.A. Tainer, M.M. Stempien, G.I. Bell, R.A. Hallewell, Proteins. 5 (1989) 322-336.

103 E.D. Getzoff, D.E. Cabelli, C.L. Fisher, H.E. Parge, M.S. Viezzoli, L. Banci, R.A. Hallewell, Nature. 358 (1992) 347-351.

104 J. Qi, Y. Gou, Y. Zhang, K.Yang, S. Chen, L. Liu, X. Wu, T. Wang, W. Zhang, F. Yang, J. Med. Chem. 59 (2016) 7497-7511.

105 M.C. Alley, D.A. Scudiero, A. Monks, M.L. Hursey, M.J. Czerwinski, D.L. Fine, B.J. Abbott, J.G. Mayo, R.H. Shoemaker, M.R. Boyd, Cancer Res. 48 (1988) 589-601.

106 S.S. Bhat, A.A. Kumbhar, H. Heptullah, A.A. Khan, V.V. Gobre, S.P. Gejji, V.G. Puranik, Inorg. Chem. 50 (2011) 545-558.

107 B. Paul, T. Chounwou, C. Newsome, J. Williams, K. Glass. Met. Ions Biol. Med. 10 (2008) 285-290.

108 F.R.G. Bergamini, J.H.B. Nunes, M.A. de Carvalho, M.A. Ribeiro, P.P. Pavia, T.P. Banzato, A.L.T.G. Ruiz, J.E. Carvalho, W.R. Lustri, D.O.T.A. Martins, A.M.C. Ferreria, P.P. Corbi, Inorg. Chim. Acta. 484 (2019) 491-502.

109 J. Wang, Y. Gou, Z. Zhang, P. Yu, J. Qi, Q. Qin, H. Sun, X. Wu, H. Liang, F. Yang, Mol. Pharmaceutics 15 (2018) 2180–2193.

110 G.A. van Albada, J.G. Haasnoot, J. Reedijk, M.B. Cingi, A.M. Manotti-Lanfredi, F. Ugozzoli, Polyhedron 14 (1995) 2467-2473.

111 J.E. Bol, W.L. Driessen, J. Reedijk, J. Chem. Soc., Chem. Commun. (1995) 1365-1366.

112 S. Naiya, C. Biswas, M.G.B. Drew, C.J. Gomez-Garcia, J.M. Clemente-Juan, A. Ghosh, Inorg. Chem. 49 (2010) 6616-6627.

Published Paper from this Chapter

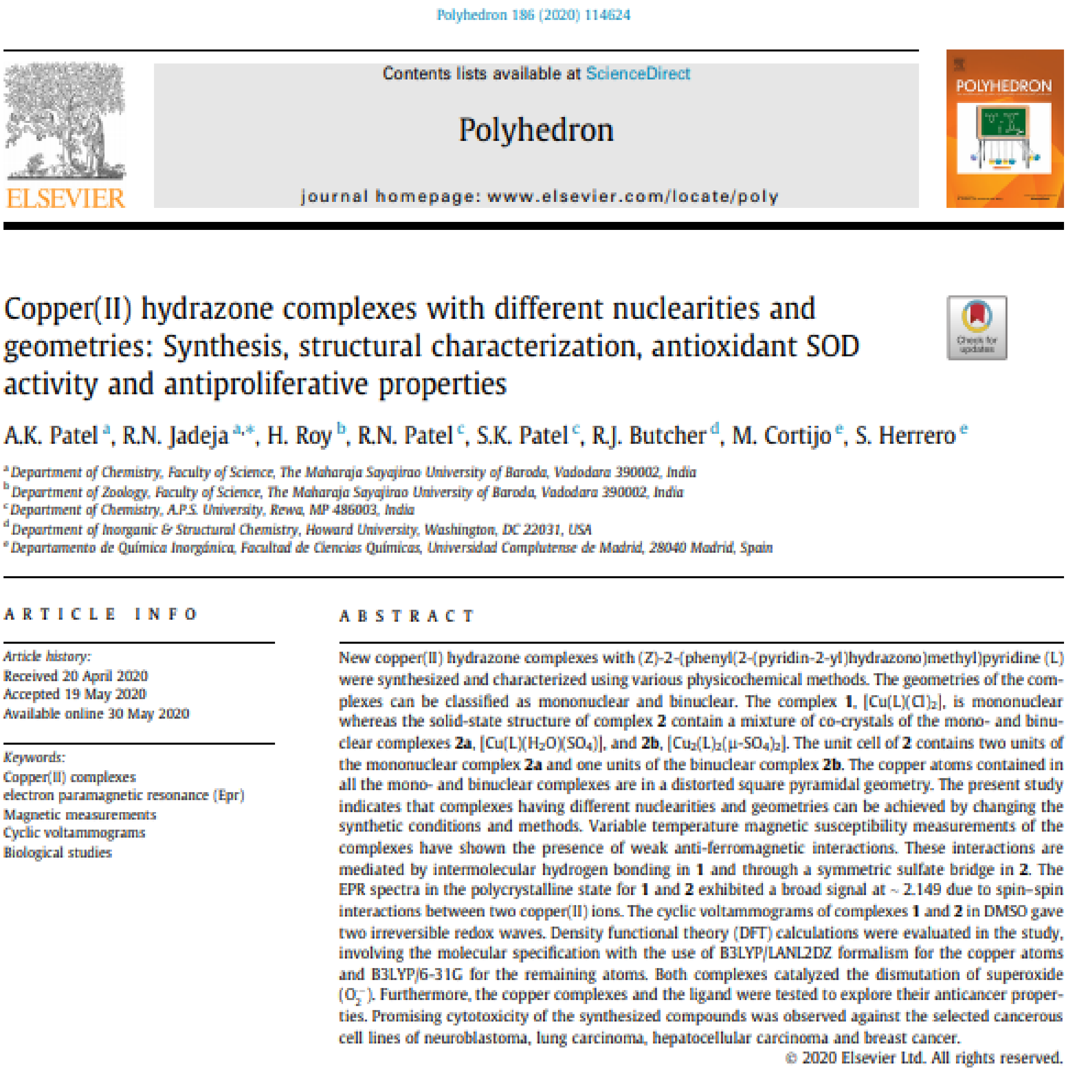

Polyhedron 186 (2020) 114624

Contents lists available at ScienceDirect

Polyhedron

journal homepage: www.elsevier.com/locate/poly

Copper(II) hydrazone complexes with different nuclearities and geometries: Synthesis, structural characterization, antioxidant SOD activity and antiproliferative properties

A.K. Patel [a], R.N. Jadeja [a,*], H. Roy [b], R.N. Patel [c], S.K. Patel [c], R.J. Butcher [d], M. Cortijo [e], S. Herrero [e]

[a] *Department of Chemistry, Faculty of Science, The Maharaja Sayajirao University of Baroda, Vadodara 390002, India*
[b] *Department of Zoology, Faculty of Science, The Maharaja Sayajirao University of Baroda, Vadodara 390002, India*
[c] *Department of Chemistry, A.P.S. University, Rewa, MP 486003, India*
[d] *Department of Inorganic & Structural Chemistry, Howard University, Washington, DC 22031, USA*
[e] *Departamento de Química Inorgánica, Facultad de Ciencias Químicas, Universidad Complutense de Madrid, 28040 Madrid, Spain*

ARTICLE INFO

Article history:
Received 20 April 2020
Accepted 19 May 2020
Available online 30 May 2020

Keywords:
Copper(II) complexes
electron paramagnetic resonance (Epr)
Magnetic measurements
Cyclic voltammograms
Biological studies

ABSTRACT

New copper(II) hydrazone complexes with (Z)-2-(phenyl(2-(pyridin-2-yl)hydrazono)methyl)pyridine (L) were synthesized and characterized using various physicochemical methods. The geometries of the complexes can be classified as mononuclear and binuclear. The complex **1**, $[Cu(L)(Cl)_2]$, is mononuclear whereas the solid-state structure of complex **2** contain a mixture of co-crystals of the mono- and binuclear complexes **2a**, $[Cu(L)(H_2O)(SO_4)]$, and **2b**, $[Cu_2(L)_2(\mu\text{-}SO_4)_2]$. The unit cell of **2** contains two units of the mononuclear complex **2a** and one units of the binuclear complex **2b**. The copper atoms contained in all the mono- and binuclear complexes are in a distorted square pyramidal geometry. The present study indicates that complexes having different nuclearities and geometries can be achieved by changing the synthetic conditions and methods. Variable temperature magnetic susceptibility measurements of the complexes have shown the presence of weak anti-ferromagnetic interactions. These interactions are mediated by intermolecular hydrogen bonding in **1** and through a symmetric sulfate bridge in **2**. The EPR spectra in the polycrystalline state for **1** and **2** exhibited a broad signal at ~ 2.149 due to spin–spin interactions between two copper(II) ions. The cyclic voltammograms of complexes **1** and **2** in DMSO gave two irreversible redox waves. Density functional theory (DFT) calculations were evaluated in the study, involving the molecular specification with the use of B3LYP/LANL2DZ formalism for the copper atoms and B3LYP/6-31G for the remaining atoms. Both complexes catalyzed the dismutation of superoxide (O_2^-). Furthermore, the copper complexes and the ligand were tested to explore their anticancer properties. Promising cytotoxicity of the synthesized compounds was observed against the selected cancerous cell lines of neuroblastoma, lung carcinoma, hepatocellular carcinoma and breast cancer.

Chapter 3

Copper(II) complexes incorporating NNN-tridentate hydrazone as proligand

Part (B): Penta-coordinated copper(II) complexes with hydrazido based ligand and imidazole as auxiliary ligand: Synthesis, spectral characterization and SOD mimetic activities

1 Introduction

The biological activity of metalloproteins is generally associated with a distinct coordination environment of the metal active sites [1, 2]. For example, Cu(II)-Zn(II) superoxide dismutase (Cu(II)-Zn(II) SOD), a ubiquitous metalloenzyme present in living system, is believed to protect cells against the oxidative damage by catalyzing the dismutation of the superoxide ($O_2^{\cdot -}$) to oxygen molecule(O_2) and hydrogen peroxide(H_2O) [3, 4]. Therefore, main function of SOD is to prevent oxidative damage of cells by the anticancer and anti-aging mechanism [5-7]. Many small molecular weight copper(II) complexes provide models for metalloproteins activities and awareness towards the design of new catalysts [8-18].

Copper complexes with hydrazone Schiff base ligand are of current interest as structural models of magnetic and structural biological systems. Hydrazone Schiff bases are organic compounds with appropriate structural features and can react with metal ions to form metal chelates either as a neutral ligand (L) or in monoanionic form HL. The metal sites of theses metal chelates can yield unique characteristic features about it. The coordination opportunities of hydrazones Schiff bases are established by using carbonyl compounds (aldehydes or ketones), which includes additional donor atoms [19-24]. These Schiff bases also have continued attention owing to their structural diversity and co-ordination features. One such interesting hydrazone ligand is (Z)-2-(phenyl(2-(pyridin-2-yl)hydrazono)methyl)pyridine (L) . This ligand L has three potential donors, a N atom from azo and two pyridine N atoms. This ligand with copper(II) chloride forms five coordinated complex [25]. Using this ligand (L) and imidazoles as auxiliary ligands six new mixed ligand complexes have been synthesized.

Imidazole is a planar five membered heterocyclic compound and two nitrogen atoms present in 1st and 3rd positions of its heterocyclic ring. It is a constituent of several natural products including purine, histamine and nucleic acid. This aromatic compound is ionisable and improves pharmacokinetic properties of model molecules and thus used as a medicant to optimize solubility and bioavailability parameters of poorly model molecules. The adding of imidazole is an important synthetic strategy in drug discovery. The high therapeutic features of the imidazole related drugs have promoted the medicinal chemists to synthesize a large number of chemotherapeutics compounds. The molecular formulations of these complexes are as $[Cu(L)(ImH)_2](ClO_4)_2$ **(1)**, $[Cu(L)(2\text{-}MeImH)_2](ClO_4)_2$ **(2)**, $[Cu(L)(2\text{-}EthImH)_2](ClO_4)_2$

(3), $[Cu(L)(BenzImH)_2](ClO_4)_2$ **(4)** and $[Cu(L)(2\text{-}MeBenzImH)_2](ClO_4)_2$ **(5)** (Where ImH = Imidazole, 2-MeImH = 2-Methylimidazole, 2-EthImH = 2-Ethylimidazole, BenzImH = Benzimidazole, 2-MeBenzImH = 2-Methylbenzimidazole**)**. The spectral and electrochemical behaviour of these complexes were also studied. The magnetic properties of these complexes are similar from those of previously reported mononuclear copper(II) complexes with Schiff bases and co-ligands. Additionally, in this chapter SOD mimetic activities have been examined and compared with known SOD mimics.

2 Experimental

2.1 Methods and physical measurements

Elemental analyses were carried out using an Elementar Vario EL III Carlo Erba 1108 Analyzer. ^{1}H NMR spectrum of the ligand was recorded in DMSO-d_6 on a Bruker Advance 400 (FT-NMR) multinuclear spectrometer. Chemical shifts were reported in parts per million (ppm) using tetramethyl silane (TMS) as an internal standard. The accelerating voltage was 10 kV and the spectra were recorded at room temperature. UV-Vis spectra were recorded at room temperature using a Shimadzu UV-Vis Spectrophotometer UV-1601 in quartz cells. Infrared (IR) spectra (4000-400cm^{-1}) were collected using the KBr pellet technique on a Perkin-Elmer spectrophotometer. The low and room temperature electron paramagnetic resonance (Epr) spectra were recorded using a Varian E-line Century Series Spectrometer equipped with a dual cavity and operating at the X-band with 100 kHz modulation frequency. Varian quartz tubes were used for measuring Epr spectra of polycrystalline samples and frozen solutions. The Epr spectra were calibrated with tetracyanoethylene (TCNE) as a marker (g = 2.00277). The Epr parameters for copper(II) complexes were determined accurately from a computer simulation program 19. Mass spectra of the ligand were recorded on Trace GC ultra DSQ II Cyclic voltammetry was performed using a BAS-100 Epsilon Electrochemical Analyzer on complexes in DMSO solutions using Ag/AgCl and glassy carbon as reference electrodes. All measurements were carried out at room temperature under a nitrogen atmosphere. The solutions were 10^{-3} mol dm^{-3} in the complex and 0.1 mol dm^{-3} in tetrabutylammonium perchlorate (TBAP) as a supporting electrolyte. Ferrocene (Fe) was added to the solution as an internal standard. Molar conductivities of the freshly prepared 1.0×10^{-3} M DMSO solutions were measured on a Systronics Conductivity 308 TDS meter.

2.2 Computational study

Theoretical calculations by density functional theory (DFT) were performed regarding molecular structure optimization and HOMO-LUMO energies etc. of complexes. Full geometry optimizations were carried out using the density functional theory (DFT) method at the B3LYP level for the complex [26]. All DFT calculations were carried out starting from the experimental single-crystal X-ray data as input geometries. All elements except Cu were assigned the LANL2DZ basis set [27]. LANL2DZ with effective core potential for Cu atom was used [28]. In the computational model, the cationic complex was taken into account. All calculations were carried out with the GAUSSIAN09 program, [29] with the aid of the Gauss View visualization program.

2.3. Antioxidant SOD activity

The antioxidant SOD activities of the complexes were carried out using alkaline DMSO as a source of superoxide radical ($O_2^{\cdot-}$) and nitro blue tetrazolium chloride (NBT) as scavenger [30-32]. The quantitative reduction of NBT to Formosan by $O_2^{\cdot-}$ was followed spectrophotometrically at 450 nm. The SOD activity was obtained by plotting the percentages of inhibition NBT reduction (%) *vs* the concentrations of complexes. The unit of SOD activity is the concentration of the enzyme or complex that induces 50% inhibition (IC_{50}) in the reduction of NBT. Two assays were carried out for each concentration of the metal complex.

Caution! Even though the copper(II) perchlorate complexes isolated in this study were not found to be shock sensitive, care is advised during the synthesis.

2.4 Synthesis of Ligand

The hydrazone ligand was synthesized by monocondensing 10 mL ethanolic solution of each 2-hydrazinopyridine (1.091g, 10 mmol) in absolute ethanol (50 mL) and 2-benzoylpyridine (0.780 g, 10 mmol) by adding with few drops of glacial acetic acid as a catalyst [25]. The resulting reaction mixture was refluxed for 1 hrs and solution was cooled to room temperature. The cooled solution was filtered and filtrate was left for slow evaporation at room temperature. The obtained Schiff base was washed with cold ethanol and stored in $CaCl_2$ desiccator.

Yield: 1.10g (75%). Anal. Calc. for $C_{17}H_{14}N_4$ (274.33 g mol^{-1}): C, 74.52; H, 5.54; N, 20.04%. Found: C, 74.50; H, 5.56; N, 20.03%. FTIR (KBr, cm^{-1}): 1592 ν(C=N). ^{1}H NMR (DMSO-d_6 400 MHz) δ: 12.9 (s, 1H, -NH-), 8.8 (d, 2H, CH=N) 8.0-7.2 (t, 3H, CH benzylidenimin), 8.8–7.8 (m, 8H, CH 2-pyridiene) ppm. ^{13}C NMR (DMSO-d_6 400 MHz) δ: 156 (CH=N-), 152 (Ar-CH=N), 152 (C-NH-), 149-105 (Ar-C) ppm.

2.5 Synthesis of complex $[Cu(L)(ImH)_2](ClO_4)_2$ 1

To a methanolic solution (10 mL) of $Cu(ClO_4)_2.6H_2O$ (0.370 g, 1 mmol) HL (0.274 g, 1 mmol) was added while stirring. A methanolic solution (10 mL) of imidazole (0.136 g, 2 mmol) was added to the above solution drop-wise and resulting reaction mixture gradually changed to green colour. After 1 hrs of stirring the microcrystalline solid was filtered and washed with ethanol. This microcrystalline powder was isolated and dried in $CaCl_2$ desiccator.

Yield: 81%. Anal. Calc. for $C_{23}H_{22}Cl_2CuN_8O_8$ (672.92 g mol^{-1}): C, 41.05; H, 3.30; N, 16.66%. Found: C, 41.07; H, 3.32; N, 16.64%. FTIR bands (KBr, cm^{-1}): 1537 ν(C=N),1086 ν(N–N). ESI-Mass (m/z): 672.02.

2.6 Synthesis of complex $[Cu(L)(2\text{-}MeImH)_2](ClO_4)_2$ 2

Methanolic solution (10 mL) of $Cu(ClO_4)_2.6H_2O$ (0.370 g, 1 mmol) was added to a stirred solution of HL (0.274 g,1 mmol). To this reaction mixture 10 mL of methanolic solution of 2-methyl imidazole (0.164 g, 2 mmol) was added drop-wise and resulting reaction mixture gradually changed to green colour. This reaction mixture was stirred for 1 hrs and then filtered. The slow evaporation of the filtrated afforded green microcrystalline powder. This microcrystalline powder was isolated and kept in $CaCl_2$ desiccator.

Yield: 82%. Anal. Calc. for $C_{25}H_{26}Cl_2CuN_8O_8$ (700.98 g mol^{-1}): C, 42.84; H, 3.74; N, 15.99%. Found: C, 42.82; H, 3.71; N, 15.96%. FTIR bands (KBr, cm^{-1}): 1569 ν(C=N), 1020 ν(N–N). ESI-Mass (m/z): 702.06.

2.7 Synthesis of complex $[Cu(L)(2\text{-}EthImH)_2](ClO_4)_2$ 3

A methanolic solution (10 mL) of $Cu(ClO_4)_2.6H_2O$ (0.370 g, 1 mmol) was added slowly to a methanolic solution (10 mL) of HL (0.274 g, 1 mmol) while stirring. To this reaction mixture 10 mL of methanolic solution of 2-ethylimidazole (0.192 g, 2 mmol) was added drop-wise and resulting reaction mixture slowly changed to green colour. This reaction mixture stirred for 2 hrs and then filtered. The slow evaporation of the filtered afforded green microcrystalline powder. This microcrystalline powder was isolated and kept in $CaCl_2$ desiccator.

Yield: 82%. Anal. Calc. for $C_{27}H_{30}Cl_2CuN_8O_8$ (729.03 g mol^{-1}): C, 44.48; H, 4.17; N, 15.39%. Found: C, 44.46; H, 4.18; N, 15.40%. FTIR bands (KBr, cm^{-1}): 1572 ν(C=N), 1093 ν(N–N). ESI-Mass (m/z): 729.32.

2.8 Synthesis of complex $[Cu(L)(BenzImH)_2](ClO_4)_2$ 4

To a methanolic solution (10 ml) of $Cu(ClO_4)_2.6H_2O$ (0.370 g, 1 mmol) was added 10 mL methanolic solution of HL (0.274 g, 1 mmol) while stirring. To this reaction mixture 10 ml of methanolic solution of benzimidazole (0.236 g, 2 mmol) was added drop-wise and resulting reaction mixture gradually changed to green colour. This reaction mixture was stirred for 2 hrs and then filtered. The slow evaporation of the filtrate afforded green microcrystalline powder. This microcrystalline powder was isolated from the filtrate and kept in $CaCl_2$ desiccator.

Yield: 80%. Anal. Calc. for $C_{31}H_{26}Cl_2CuN_8O_8$ (773.04g mol^{-1}): C, 48.17; H, 3.39; N, 14.51%. Found: C, 48.18; H, 3.37; N, 14.53%. FTIR bands (KBr, cm^{-1}): 1563 ν(C=N), 1018 ν(N–N). ESI-Mass (m/z): 773.04.

2.9 Synthesis of complex $[Cu(L)(2\text{-}MeBenzImH)_2](ClO_4)_2$ 5

A methanolic solution (10 mL) of $Cu(ClO_4)_2.6H_2O$ (0.370 g, 1 mmol) was added while stirring to a 10 mL methanolic solution of HL (0.274 g, 1 mmol). To this reaction mixture 10 mL of methanolic solution of 2-methylbenzimidazole (0.264 g, 2 mmol) was added drop-wise and resulting reaction mixture was stirred for 2 hrs. It is gradually changed to green colour. The obtained green solution was kept at room temperature for slow evaporation after 2-3 days a green solid slowly separated out. This green microcrystalline powder was isolated and kept in $CaCl_2$ desiccator.

Yield: 75%. Anal. Calc. for $C_{33}H_{30}Cl_2CuN_8O_8$ (801.10 g mol^{-1}): C, 49.50; H, 3.77; N, 13.96%. Found: C, 49.53; H, 3.75; N, 13.94%. FTIR bands (KBr, cm^{-1}): 1563 ν(C=N), 1018 ν(N–N). ESI-Mass (m/z): 802.04.

3 Results and discussion

The hydrazone ligand (HL) was synthesized as per reported method [25]. The reaction of $Cu(ClO_4)_2.6H_2O$ with hydrazone and co-ligands led to the formation of mononuclear **1-5** complexes. The reaction conditions for synthesis of hydrazone and complexes are shown in Scheme 1 and 2. These complexes were isolated in good yield and characterized using UV-vis, FTIR and epr spectral physico-cemical techniques. The all complexes are insoluble in water and non-polar organic solvents but are highly soluble in DMSO and CH_3CN. These complexes are stable in air.

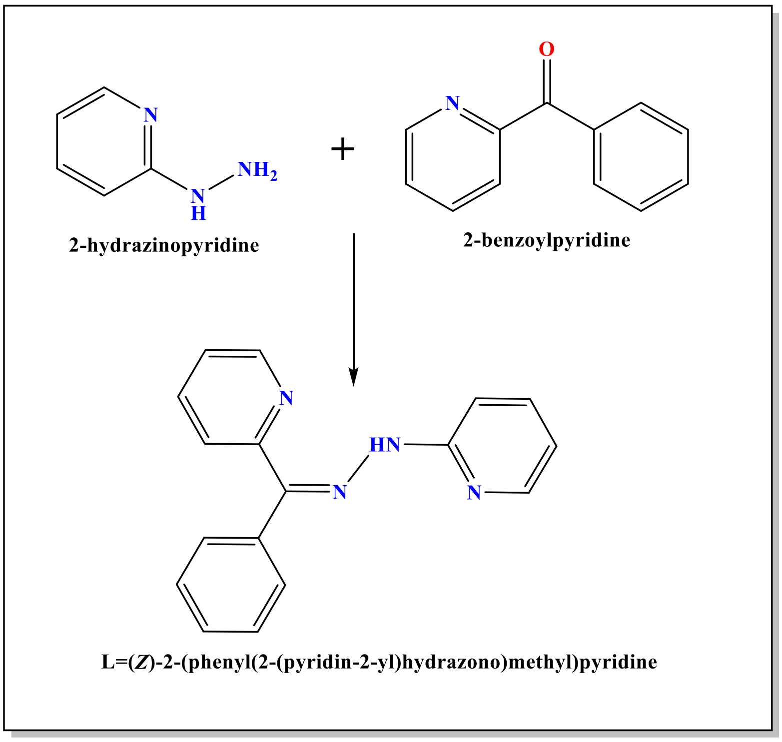

Scheme 1 Synthetic route of ligand (L).

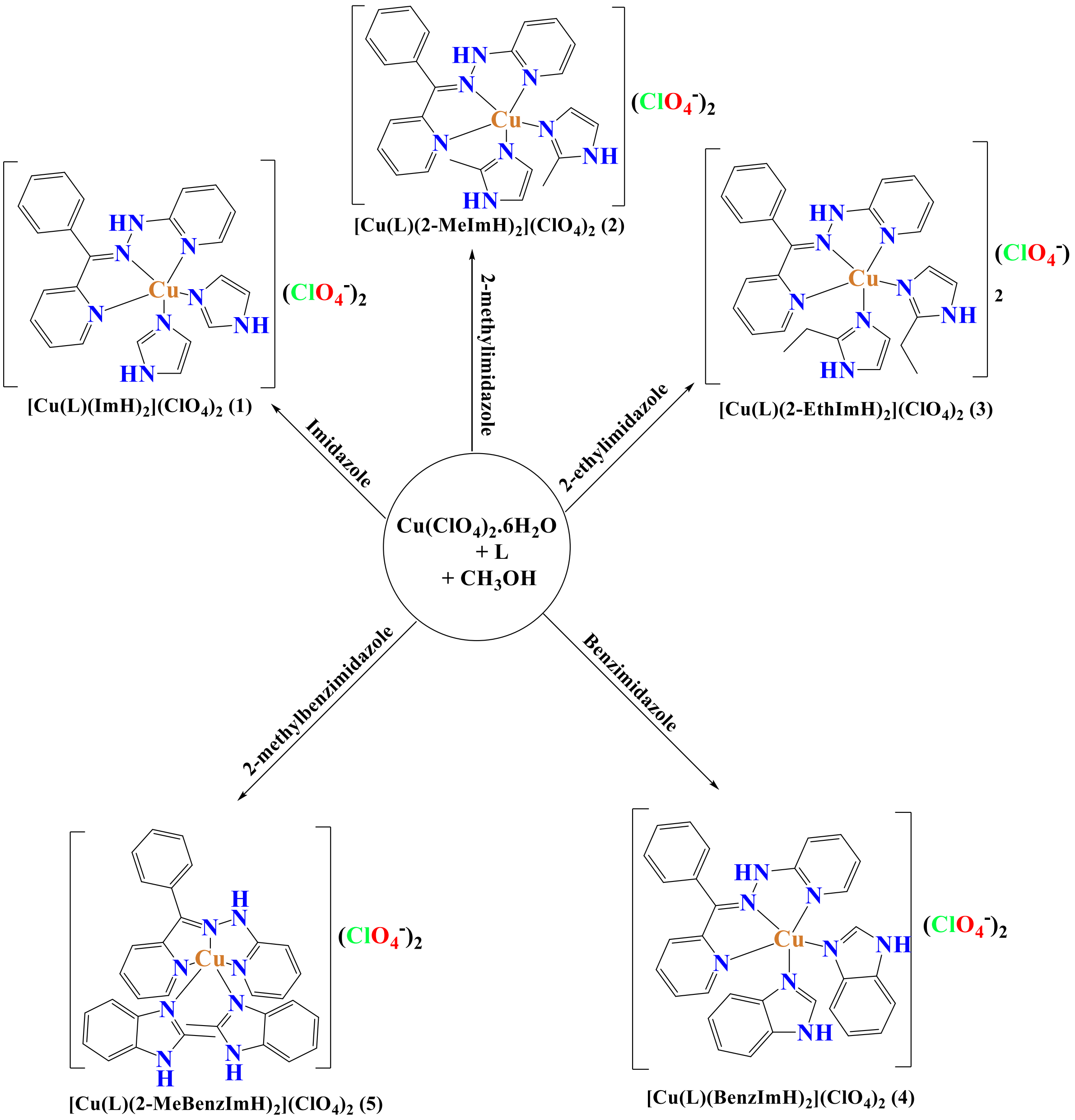

Scheme 2 General synthetic route of complexes **1-5**.

3.1 NMR spectra of ligand

The NMR analysis of ligand were performed in DMSO-d_6 solvent to get information about the crystal structure. In proton NMR of ligand we observed that NH proton peak is obtained at 12.9 ppm. Similarly, aromatic ring proton (CH=N) peak is observed at 8.8 ppm. Aromatic (CH=CH) proton peak is observed at ~ 8 ppm. All other aromatic peak is observed in the range of 7.9 to 6.8 ppm. In ^{13}C-NMR spectrum of ligand azomethine carbon peak at 156.8 ppm. Similarly, all other carbon peaks aromatic and aliphatic is observed in the range 152. to 105.4 ppm. The proton ^{1}H and ^{13}C NMR spectra are shown in Fig. 1 and 2.

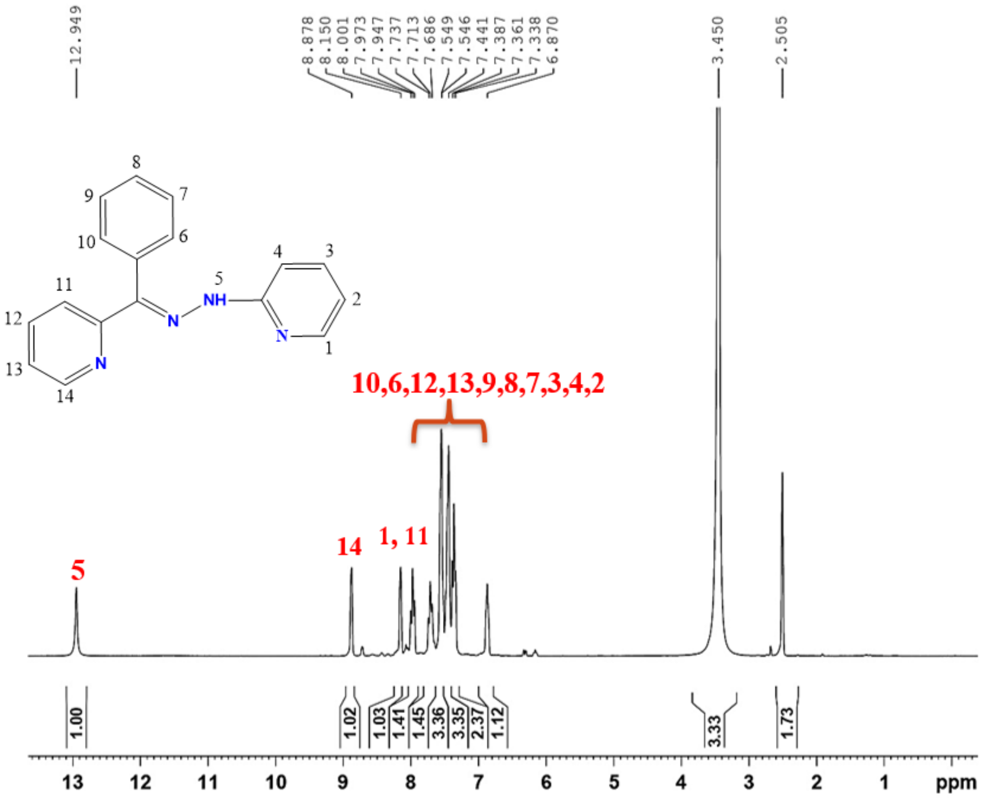

Fig. 1. ^{1}H NMR of Ligand (**HL**) in DMSO-d$_6$ solvent.

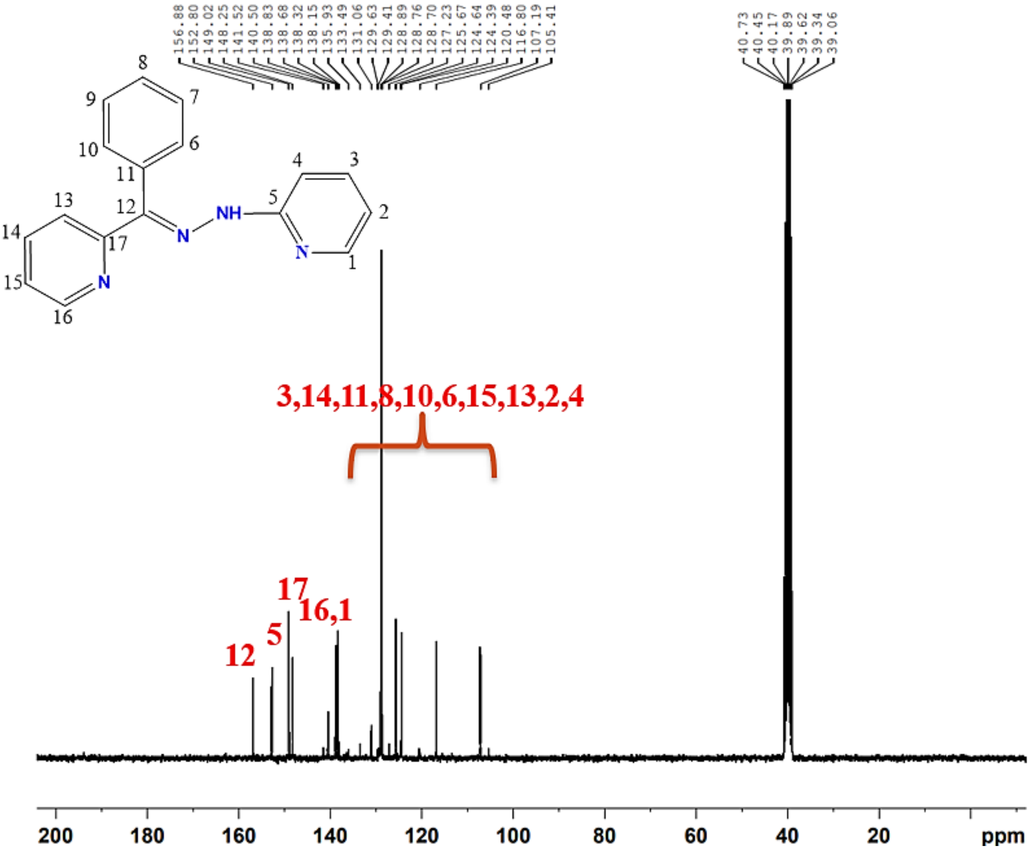

Fig. 2. ^{13}C NMR of Ligand (**HL**) in DMSO-d$_6$ solvent.

3.2 FTIR spectral studies

The FTIR spectra of hydrazone ligand (HL) as well as complexes **1-5** have been recorded to get a preliminary idea about the binding mode of the ligands. The FTIR spectra of all five complexes showed an absorption band in the range of 1537-1572 cm^{-1}, which was assigned to ν(>C=N) stretching of hydrazone moiety present in the complexes, although the band at 1445-1463 cm^{-1} was attributed to benzene ring vibration. The shift towards higher wave number (red shift) of the >C=N group, 1537-1572 cm^{-1} compared to the hydrazone ligand are in accord with the coordination of the hydrazone to the metal centre [33]. The absorption bands for perchlorate anion come out at 1100-1105 cm^{-1} [34-37]. The absorption band corresponding to ν(N-N) of L is observed at 988 cm^{-1}. The increase of this frequency in IR spectra of complex is owing to increase in the bond strength and again confirms the coordination of azomethine nitrogen [38]. The bands corresponding to ν(M-N) and ν(M-O) are shown at 411-423 and 418-486cm^{-1} respectively. Similarly, an absorption peak at 3417-3421 cm^{-1} is characteristic for ν(N-H) stretching mode. The other absorption bands associated with hydrazone ligand revealed minor shifts, indicating that the electron density of the bonds have been changed on coordination [39]. The FTIR spectra of ligand and complexes is shown in Fig. 3-8.

Table 1. FTIR spectral band assignments of L and complexes.

Compounds	ν(NH)	ν(>C=N)	ν(N-N)	ν(Cu-O)	ν(Cu-N)
L	3084	1592	988	-	-
1	3420	1537	1086	486	423
2	3396	1569	1020	461	421
3	3417	1572	1093	461	419
4	3421	1563	1018	418	411
5	3421	1563	1018	419	411

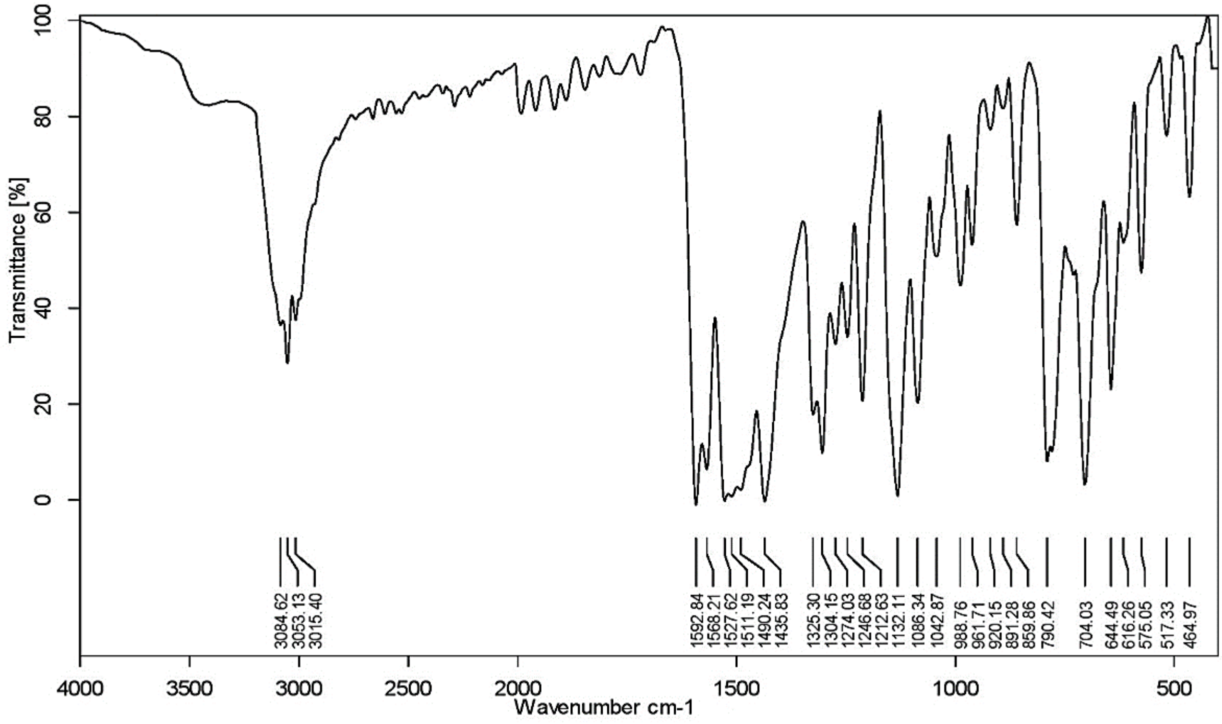

Fig. 3. FTIR spectrum of ligand HL.

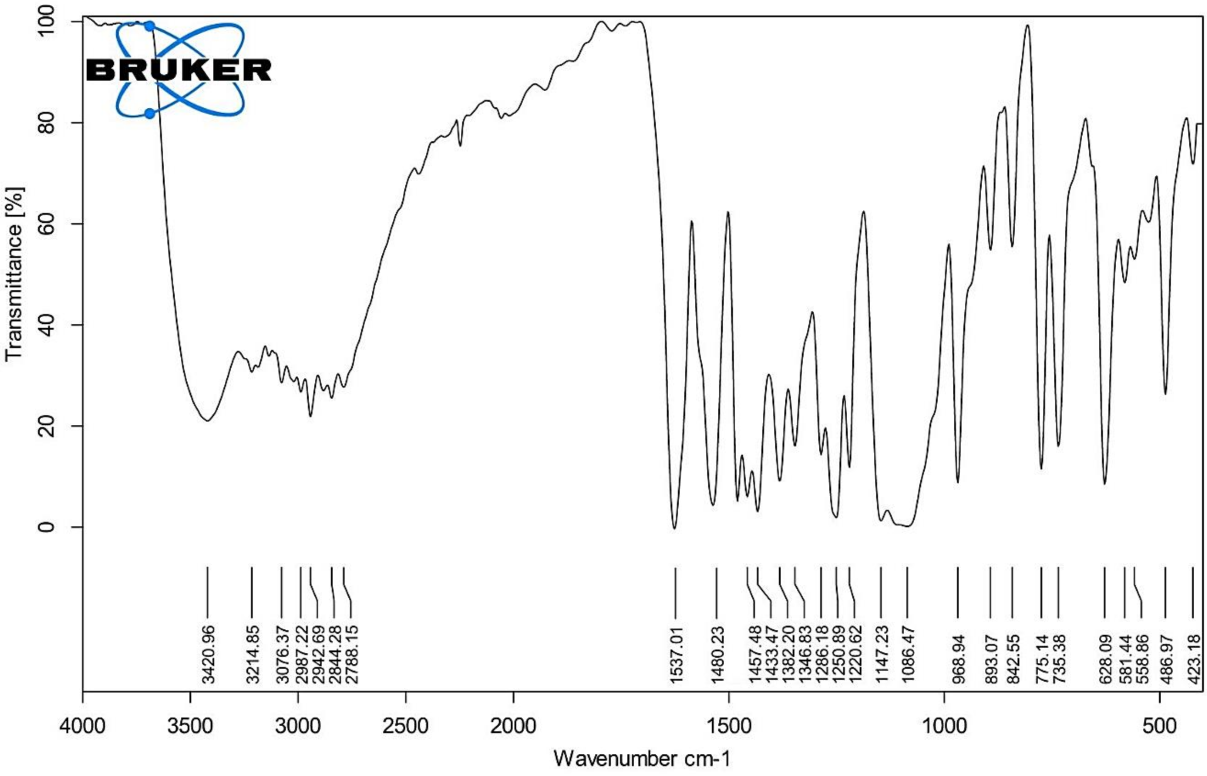

Fig. 4. FTIR spectrum of complex **1**.

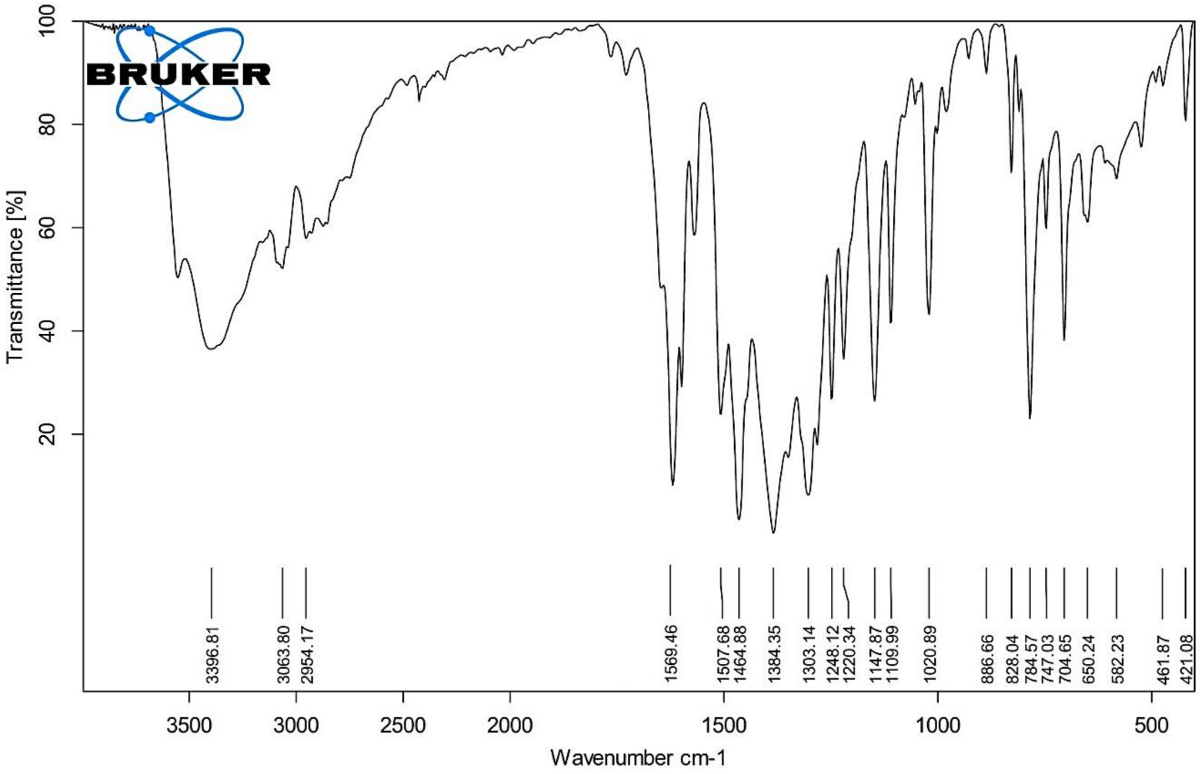

Fig. 5. FTIR spectrum of complex **2**.

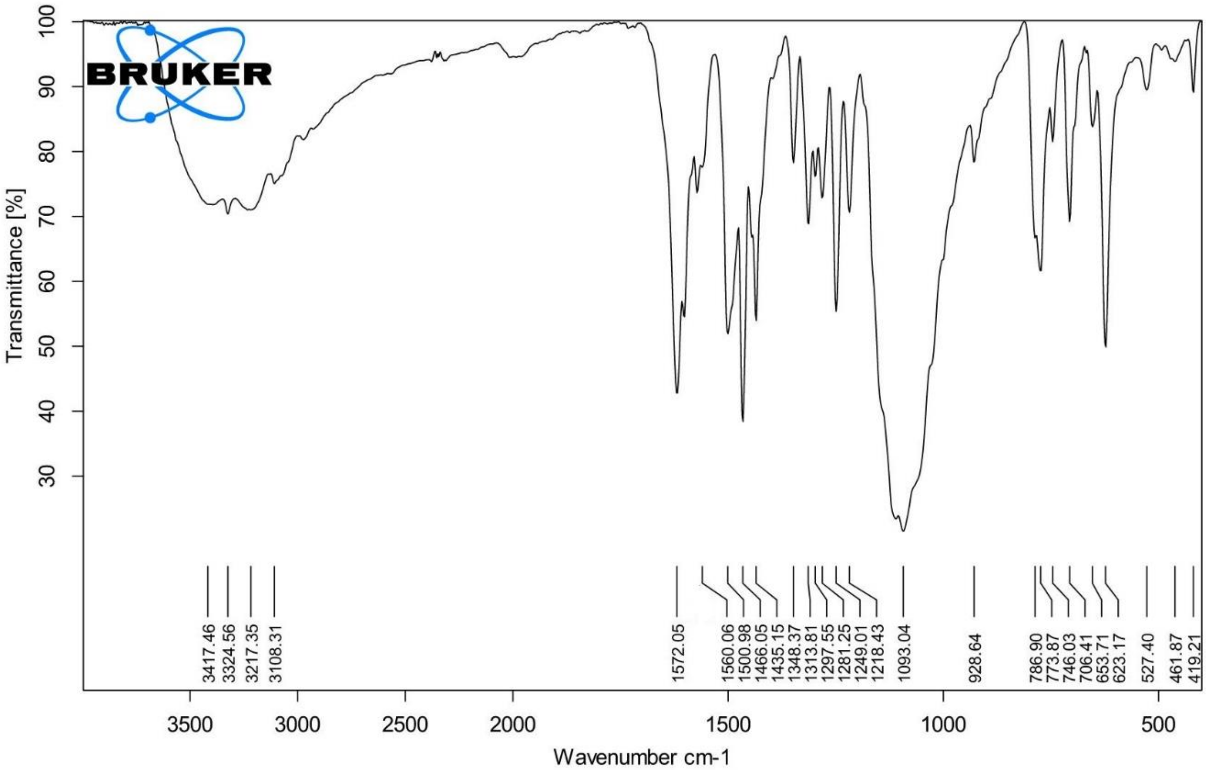

Fig. 6. FTIR spectrum of complex **3**.

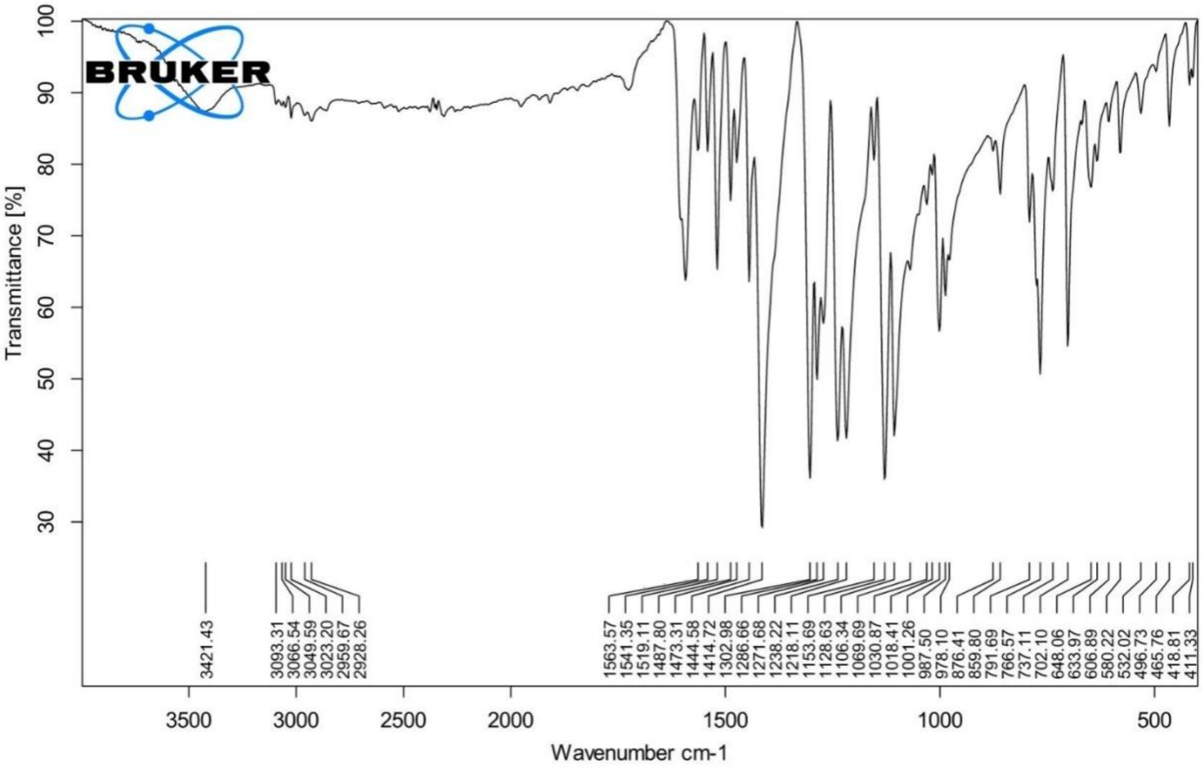

Fig. 7. FTIR spectrum of complex **4**.

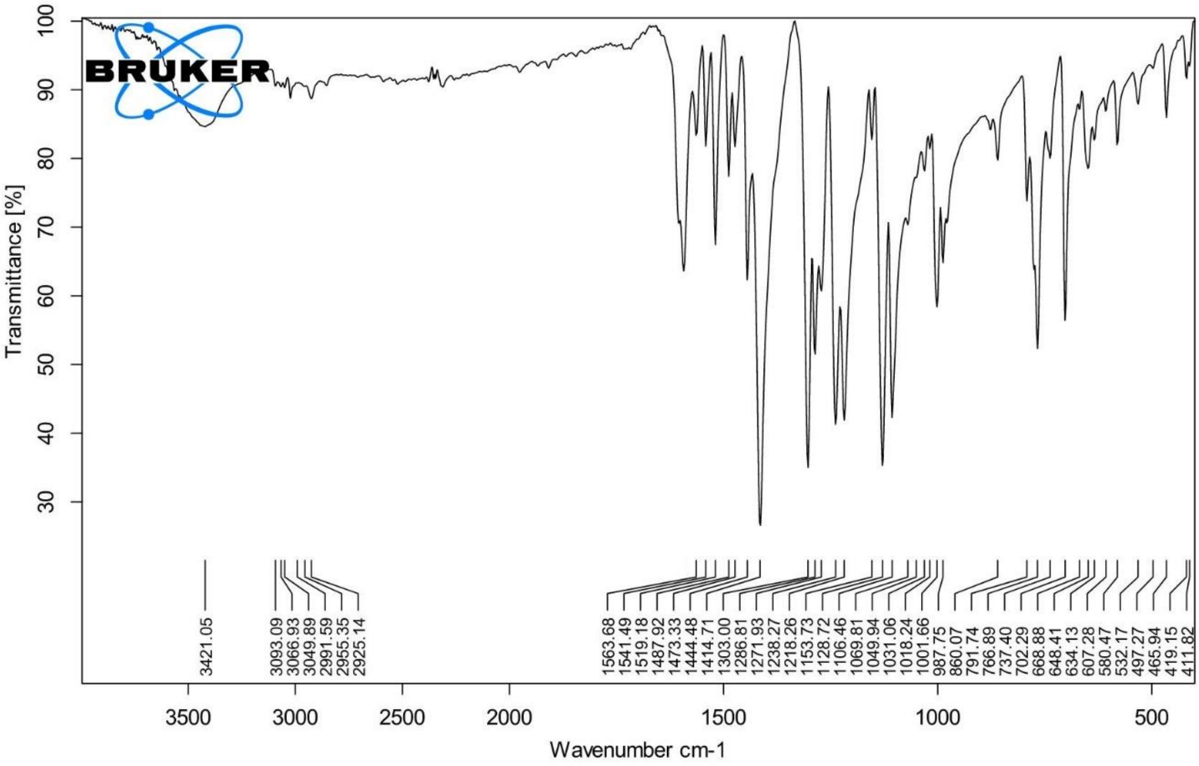

Fig. 8. FTIR spectrum of complex **5**.

3.3 Electronic spectra

Electronic absorption spectra of all complexes were measured in DMSO (1.0 × 10^{-3} M) solutions. The absorption spectra are shown in Fig. 9 and absorption maxima (λ_{max}) are collected in Table 2. The electronic spectra of complexes also provide structural information. The most intense absorption bands for complexes **1-5** was indicated in the range of ~ 490-492 nm owing to ligand to metal charge transfer (LMCT) [40]. The highest energy band shown in the range of 325-329 in spectra of complexes are due to $\pi \rightarrow \pi^*$ transition of aromatic and azomethine groups. The d-d absorption band of each complex is observed due to intense LMCT bands Fig. 10. [38]. Such absorption bands were in good agreement with a square pyramidal geometry around the copper(II) centre [41].

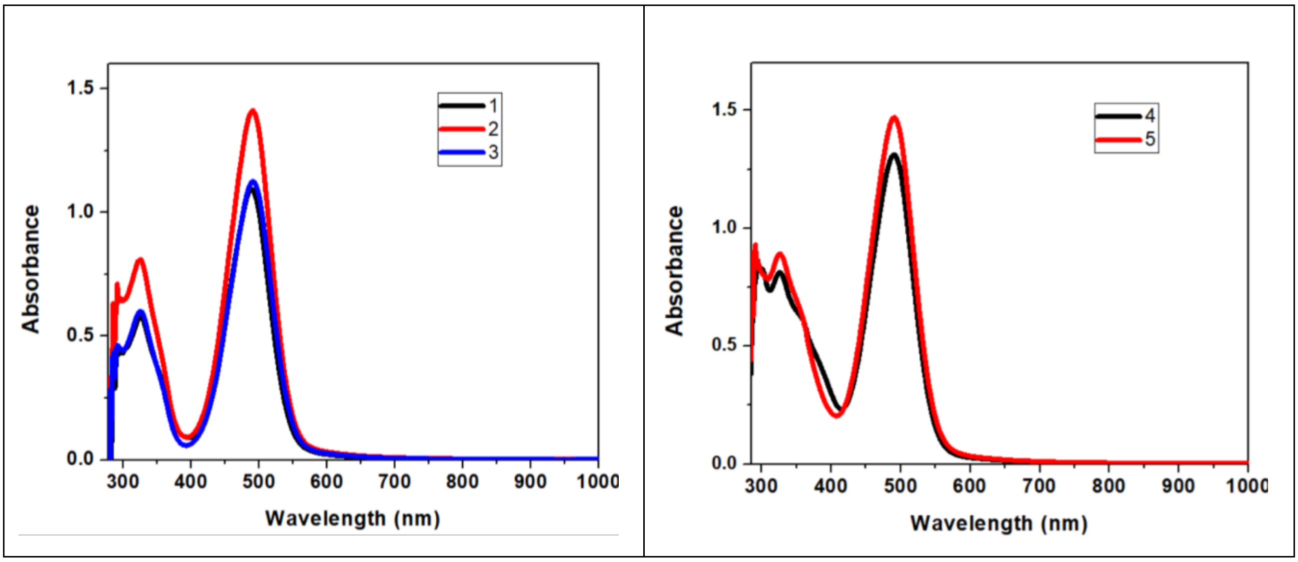

Fig. 9. UV-visible spectra of copper(II) complexes **1-5** in DMSO solution 1.0 x 10^{-3} M.

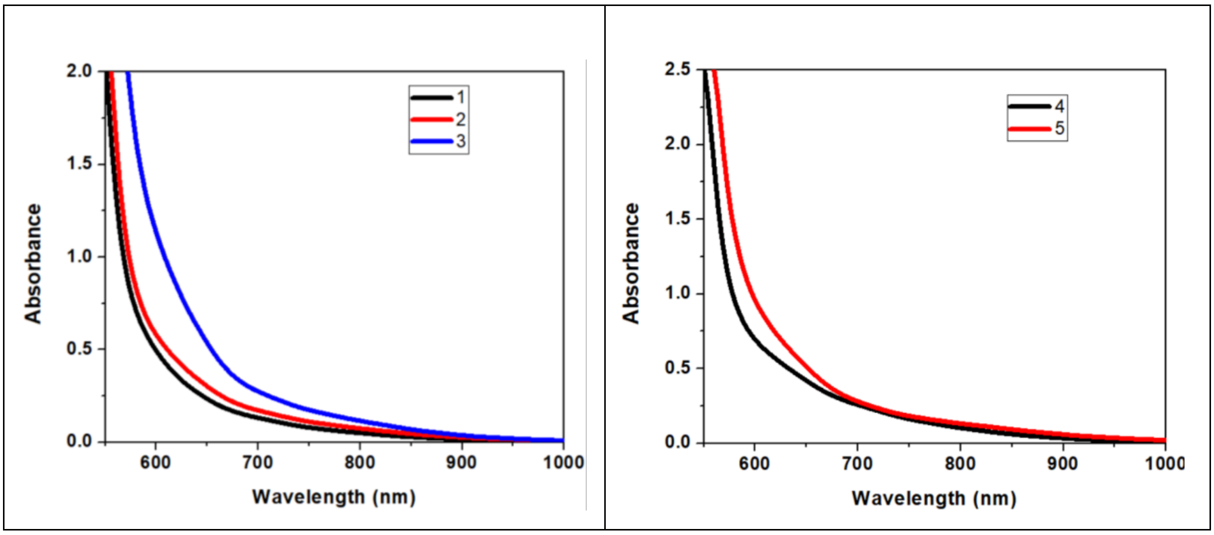

Fig. 10. 1.0 × 10^{-3} M in DMSO solution expanded region of visible region in complexes **1-5**.

Table 2 Electronic spectral band assignment of complexes **1-5**.

Complex	$\pi\rightarrow\pi^*$ (λ_{max}, nm)	LMCT (λ_{max}, nm)	d-d
1	324	492	-
2	327	490	-
3	325	490	-
4	326	491	-
5	329	492	-

3.4 Molar conductance study

The molar conductivity measured for all the complexes **1-5** in 10^{-3} M DMSO solution. The conductance measurements suggest that they are electrolytic in nature having molar conductance value 112-135 Ω^{-1} cm^2 mol^{-1} [42]. The conductivity values are given in Table 3.

Table 3 Molar conductance of complexes **1-5**.

Complexes	Λ^a (Ω^{-1} cm^2 mol^{-1})
1	112.05
2	129.05
3	135.05
4	125.05
5	118.05

3.5 Magnetic susceptibility study

The room temperature magnetic susceptibility data of all complexes collected. The room temperature magnetic moment values are in the range 1.79-1.81 B.M. The magnetic moment values are very close to the spin only value for the discrete magnetically non-coupled copper(II) system, suggesting that the complexes are non-coupled at room temperature [38].

3.6 Mass spectra

The ESI-Mass of complexes **1-5** were done to conform the molecular weight of the complexes. The mass spectra were performed in positive mode only. The mass spectra of complexes show $[M + 1]^+$ mass. The mass of complexes is shown in Fig. 11-15.

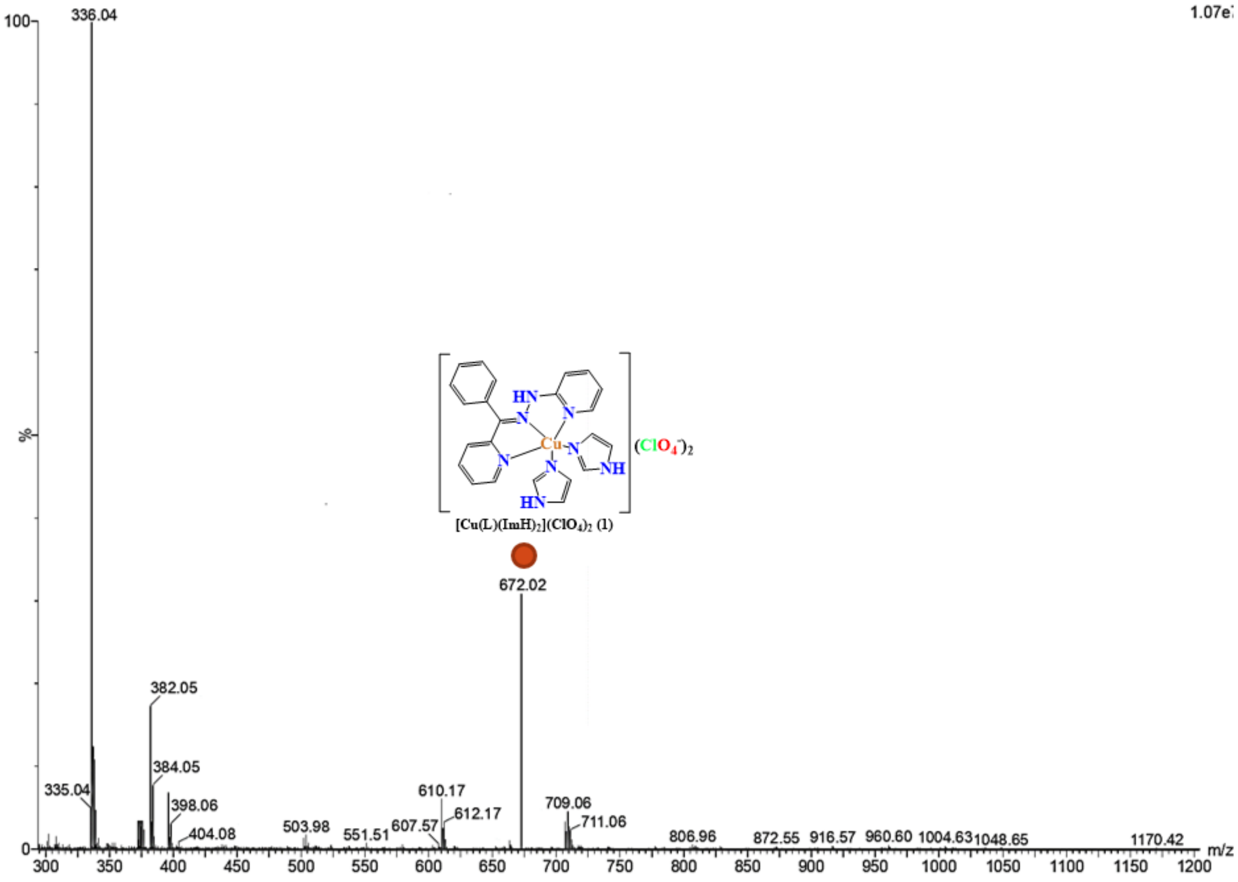

Fig. 11. Mass spectrum of complex **1**.

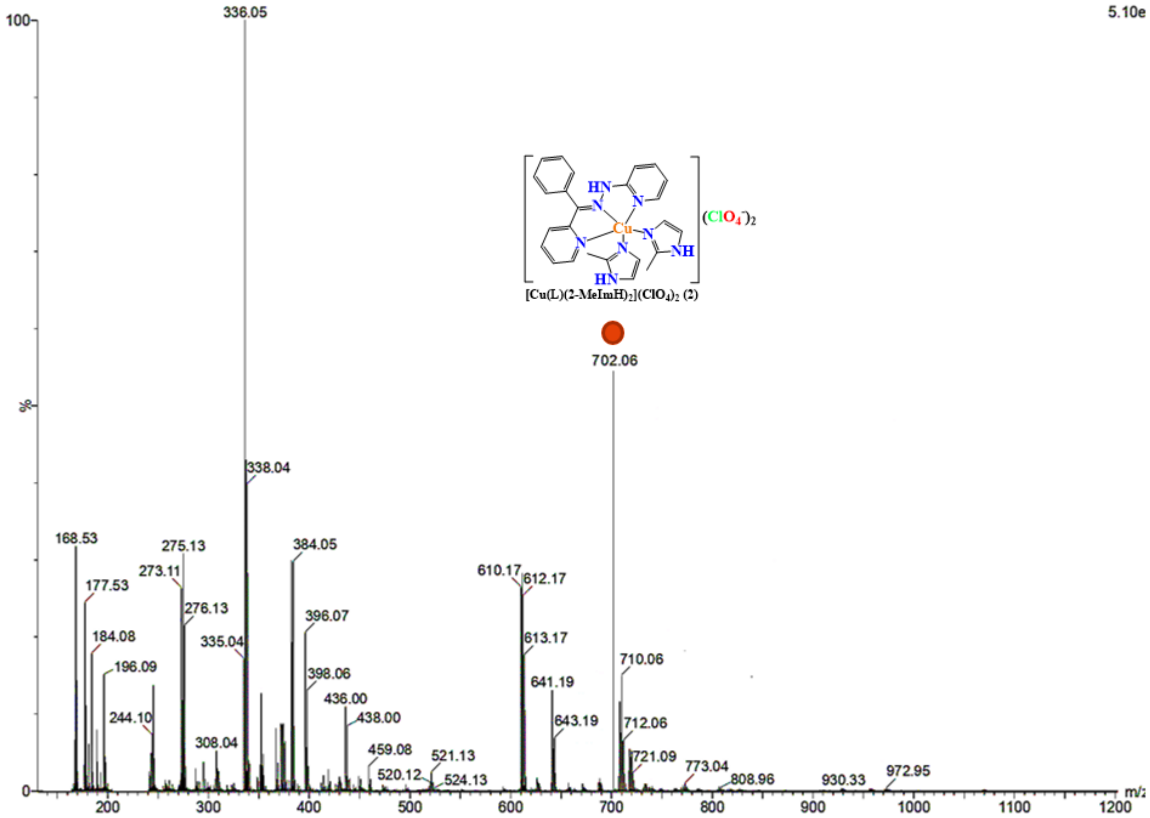

Fig. 12. Mass spectrum of complex **2**.

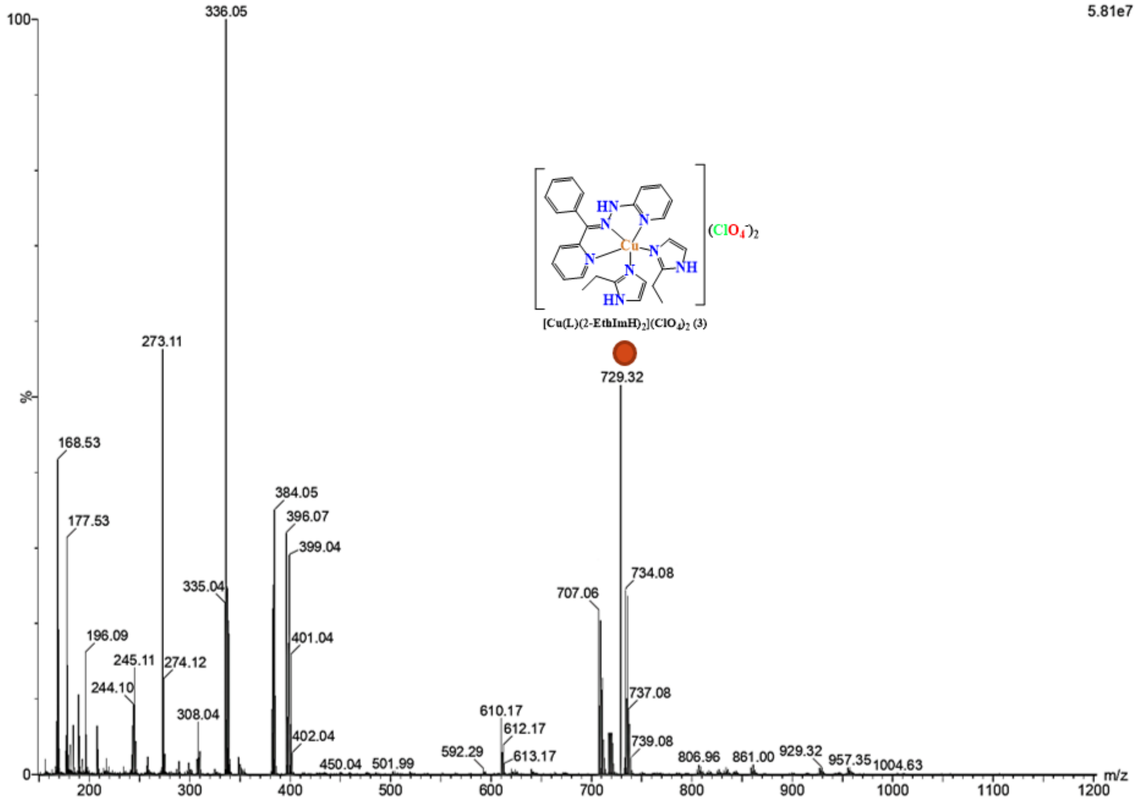

Fig. 13. Mass spectrum of complex **3**.

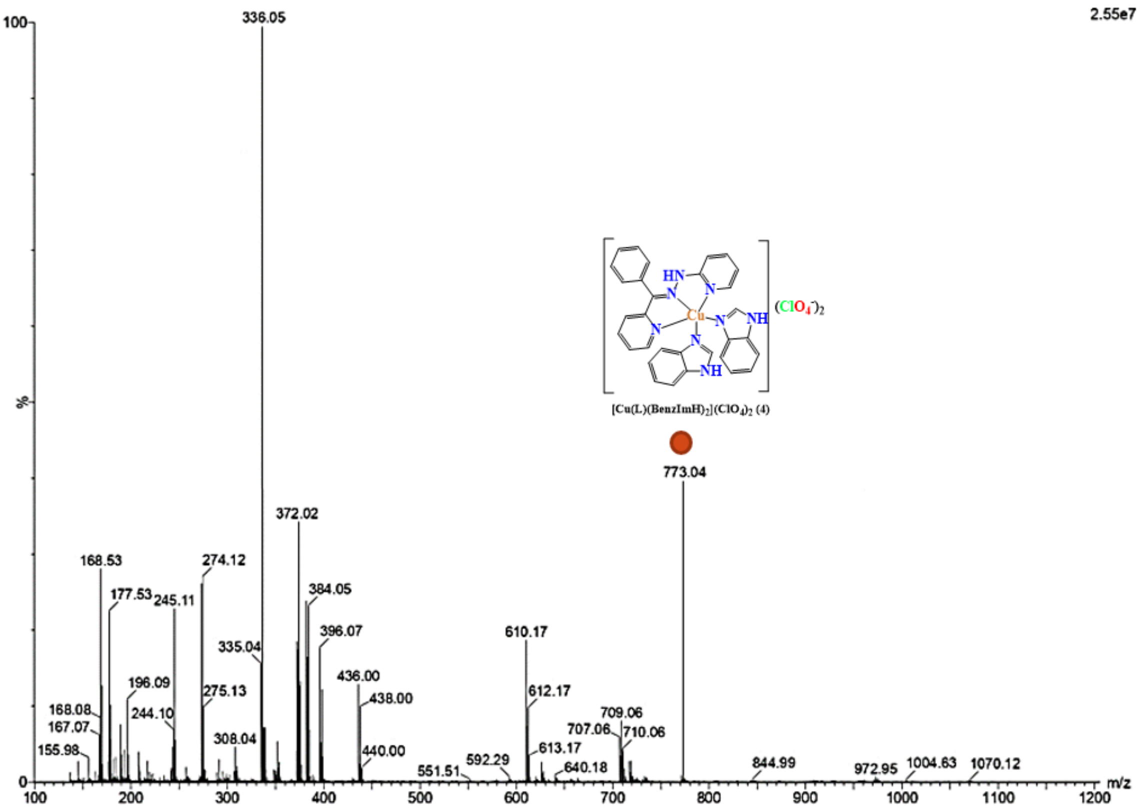

Fig. 14. Mass spectrum of complex **4**.

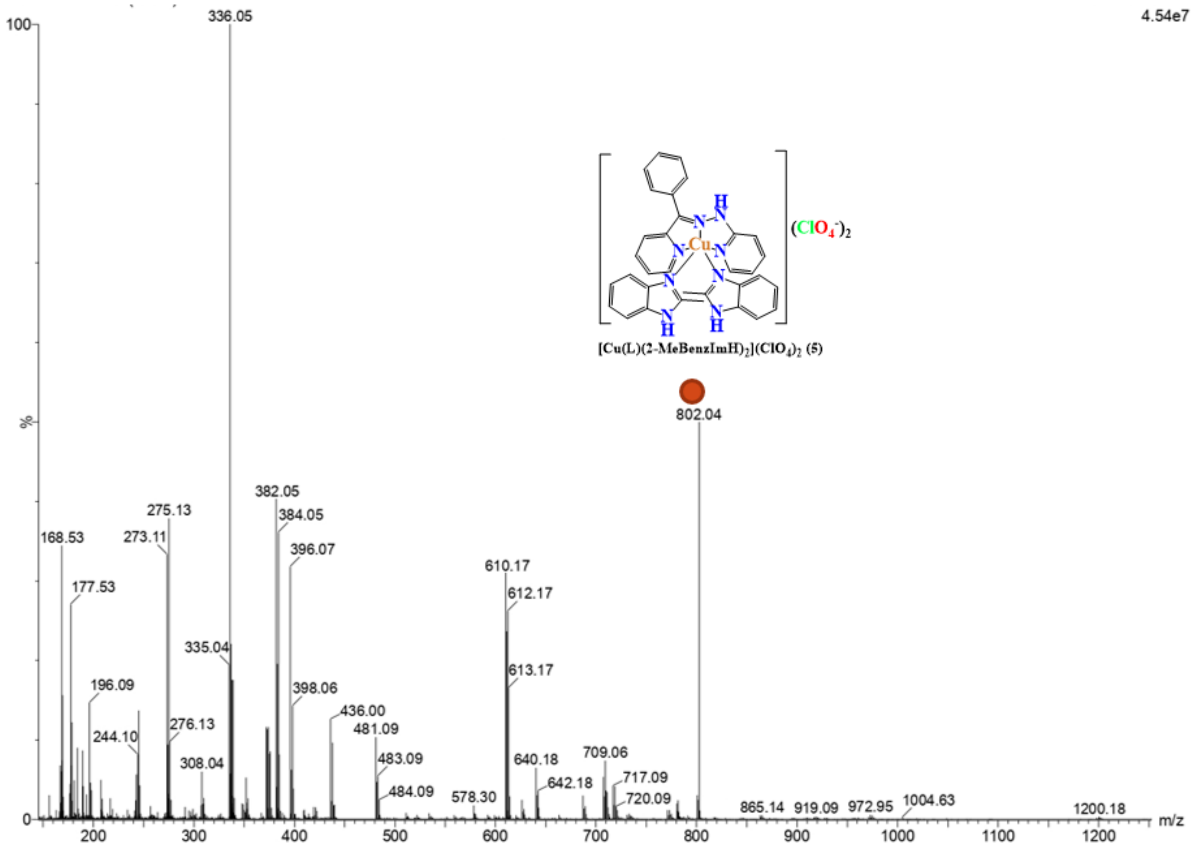

Fig. 15. Mass spectrum of complex **5**.

3.7 EPR spectra

The epr spectra of microcrystalline complexes **1-5** were measured at room temperature. The frozen DMSO solution 3.0×10^{-3} M were also measured at X-band frequency region. The epr spectra are shown in Fig. 16-20 and derived epr parameters are collected in Table 4. The analysis of g values and hyperfine coupling constant (A) throw insight for studying the electronic structures of copper(II) complexes [43, 44]. Copper(II) is epr active because it has only one unpaired electron. In addition, both ^{63}Cu and ^{65}Cu with $I = 3/2$ yield a characteristic four-line $(2nI + 1)$ pattern owing to the electron spin-nuclear spin hyperfine interactions. Microcrystalline epr spectra of complex **1** shows an isotropic epr spectral features with $g_{iso} = 2.084$. Isotropic spectra, comprising one broad signal and thus only one g value is due to dipolar broadnening and increased spin lattice relaxation. Such epr spectra permit no information on the electronic ground state of copper ion present in complexes. The signal for half-field ($\Delta M_S = \pm 2$) is seen at ~1600 G as trailed trace features as shown in inset (Fig. 16-20). Corresponding, epr spectral features revealed interaction of two copper(II) systems through antiferromagnetic coupling S = 2 and showed non-negligible value for the zero-field splitting (D) = 0.0187 cm^{-1} [45, 46]. Although such interactions are lost in frozen DMSO solution. Therefore, one can suggest dipole-dipole interactions [47]. Complexes **2** and **3** show typical axial epr spectral features, will resolved $g_{\parallel}$ and $g_{\perp}$ compound. The g-tensor parameters are similar as determined in DMSO frozen solutions. The exchange parameter $G = (g_{\parallel} - 2.0023)/(g_{\perp} - 2.0023)$ for these complexes (**2** and **3**) are 3.866 and 3.910, respectively [38, 48, 49]. The G values are slightly less than 4, suggesting the local tetragonal axis is misaligned [50, 51]. Also, the $\Delta M_S = \pm 2$ features are weak. These observations are suggestive of weak interactions in microcrystalline state due to molecular exchange interaction with S =½ spin. The epr spectra for remaining complexes (**4** and **5**) reveal a typical axial feature, with well-defined $g_{\parallel}$ and $g_{\perp}$ features. The value of G is greater than 4. The signals corresponding two $\Delta M_S = \pm 2$ were not observed. Therefore, interactions in microcrystalline states are eliminated.

The frozen solution (100% DMSO) X-band epr spectra of all complexes showed well resolved epr spectral features in $g_{\parallel}$-region and is typical of copper(II) mononuclear complex. These observations with $g_{\parallel} > g_{\perp} > 2.0023$ attributed that the unpaired electron is in the $d_{x^2-y^2}$ orbital of copper ions and spectral behaviour is of axial symmetry [52-54]. Also, the

$\Delta M_S = \pm 2$ signals are not observed in these frozen solution epr spectra. Such observations confirm the singlet state epr spectra of all complexes. The $g_\parallel$ values are more or less same in present complexes (**1-5**) suggesting that the bonding in these complexes is controlled by the tridentate hydrazone ligand. The $g_\parallel > g_\perp$ values in all complexes advices to the distorted square pyramidal structure and prevents the chance of a trigonal bipyramidal geometry around copper(II) centres [55, 56].

Table 4 Epr parameters of copper(II) complexes in polycrystalline state at 298K and in DMSO solution at 77K.

Complex	RT (Polycrystalline)				LNT (Solution) in DMSO (77K)		
	$g_\parallel$	**$g_\perp$**	**G**	**D(cm^{-1})**	**$g_\parallel$**	**$g_\perp$**	***$A_\parallel$*(G)**
1	**g_{iso} = 2.084**		-	0.018	2.182	2.047	177
2	2.264	2.070	3.866	0.055	2.177	2.048	187
3	2.263	2.069	3.910	0.056	2.177	2.050	175
4	2.237	2.057	4.290	0.052	2.197	2.047	170
5	2.211	2.053	4.110	0.052	2.222	2.049	177

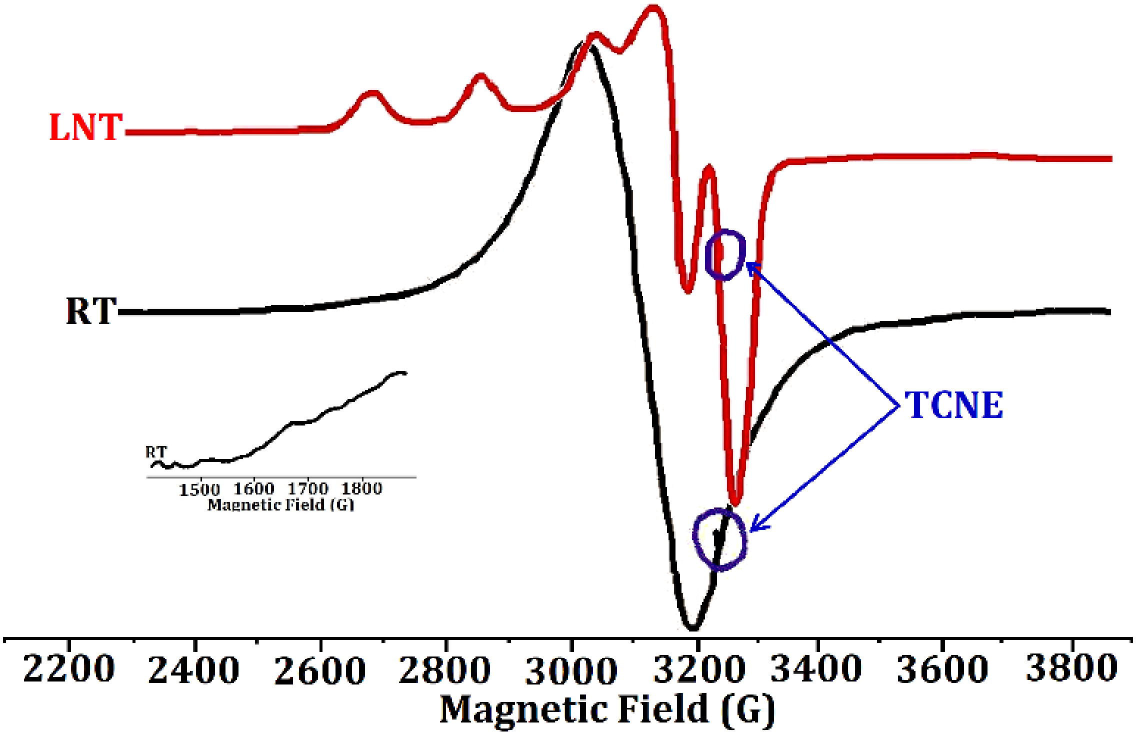

Fig. 16. EPR spectra of complex **1**.

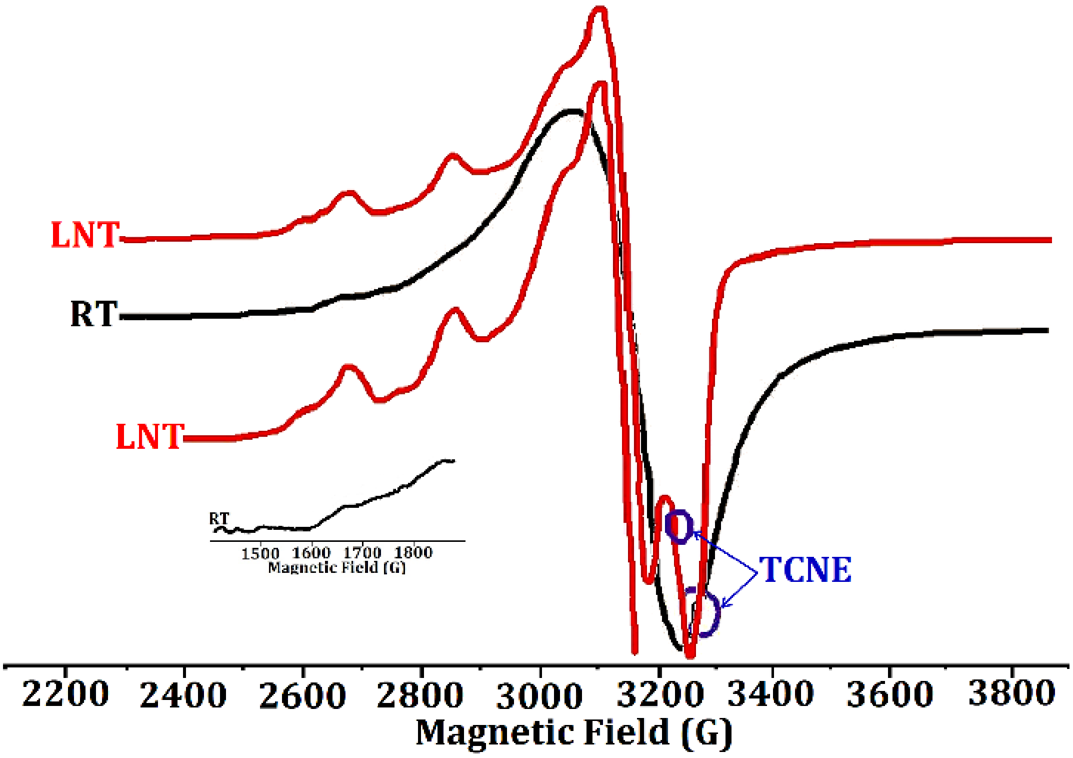

Fig. 17. EPR spectra of complex **2**.

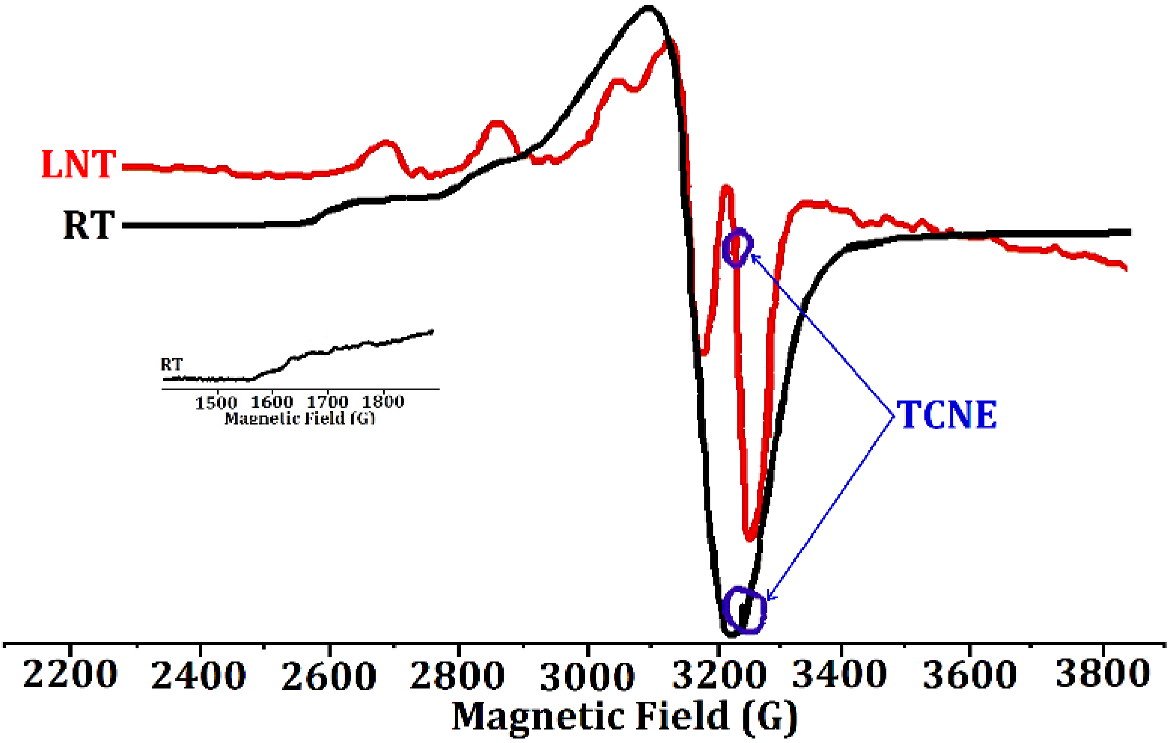

Fig. 18. EPR spectra of complex **3**.

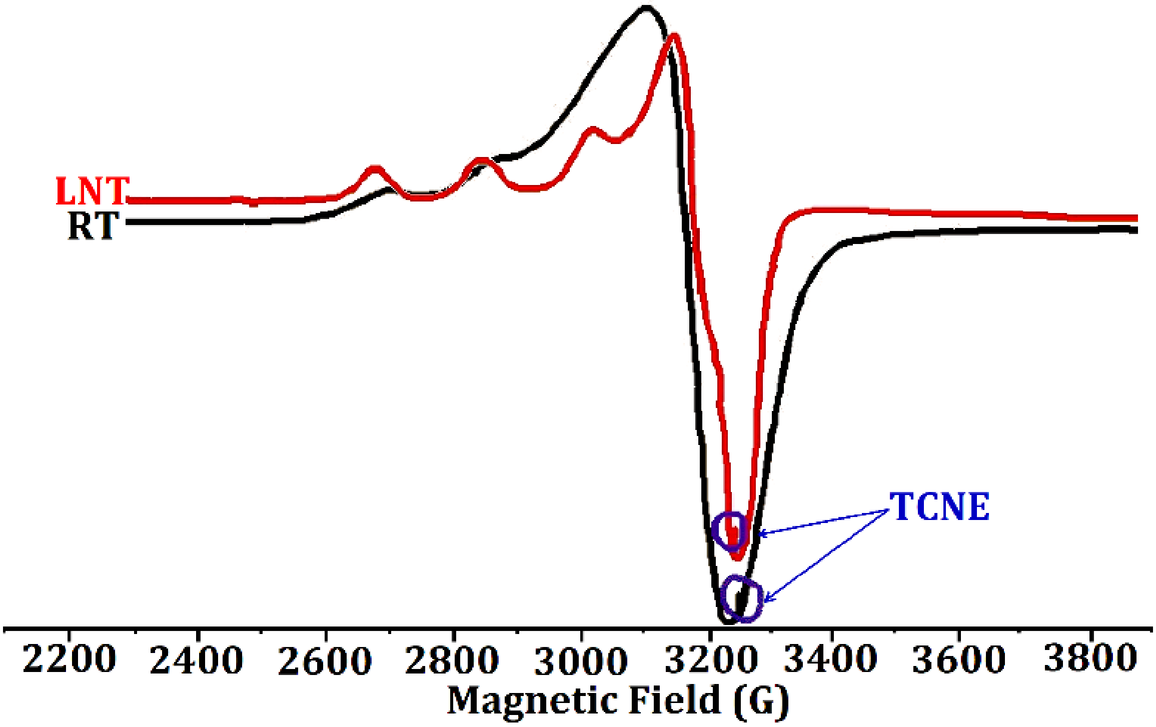

Fig. 19. EPR spectra of complex **4**.

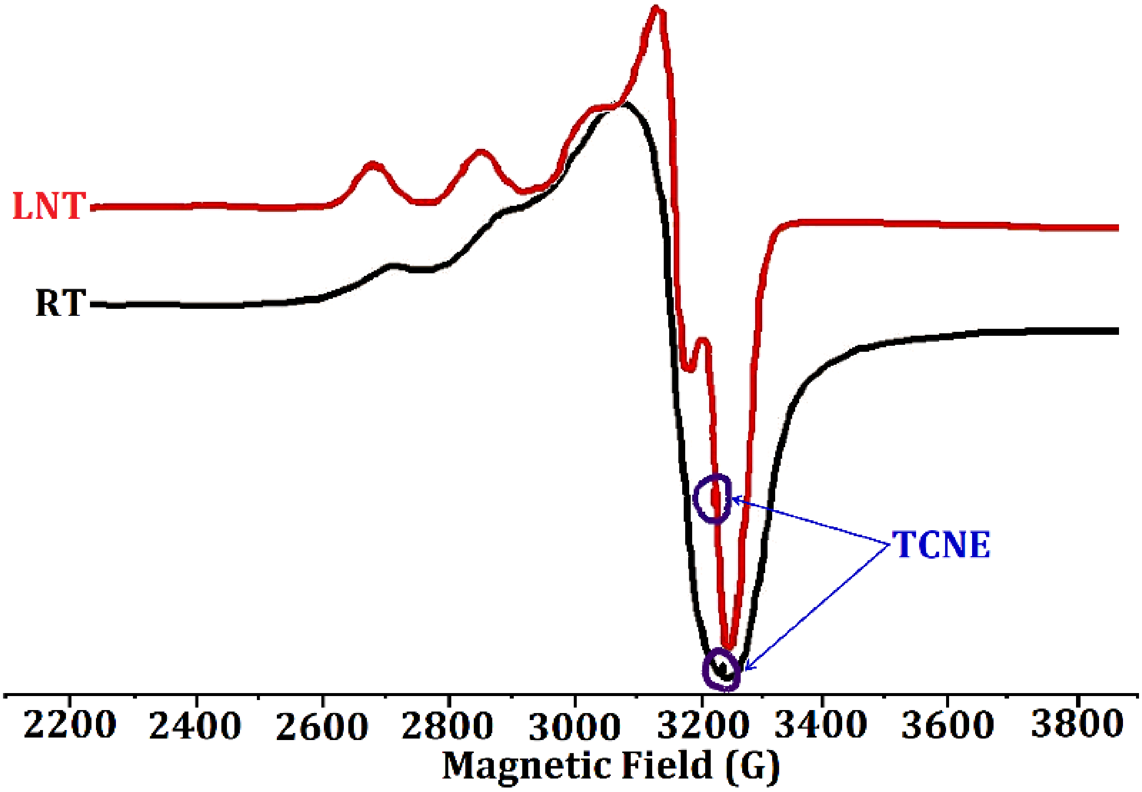

Fig. 20. EPR spectra of complex **5**.

3.8 Electrochemical studies

The electrochemical behaviour of all complexes was studied using cyclic voltammetry and differential pulse voltammetric techniques. The voltammograms (CV and DPV) are shown in Fig. 21 and 22. electrochemical data are collected in Table 5. The CV of complex **1** shows two reductive and two oxidative responses, while **2** shows two reductive and one oxidative response. One reductive wave of this complex does not have its counterpart in the return scan of CV. This shows that this species is unstable in DMSO solution in the CV time scale. The bound hydrazone ligand to the copper centre makes the reduction of metal centre unfavourable, leading to negative reduction potential [57]. The cathodic reduction potential in all complexes are within the range of values reported for the reduction (Cu^{II} / Cu^{I}) of hydrazone copper(II) complexes [58]. The extra reduction and oxidation peaks in the complexes are due to ligand centred electron transfer reaction. The effect of auxiliary ligand is obvious on E_{pc}. E_{pc} of complexes become more negative as the molecular weight increases.

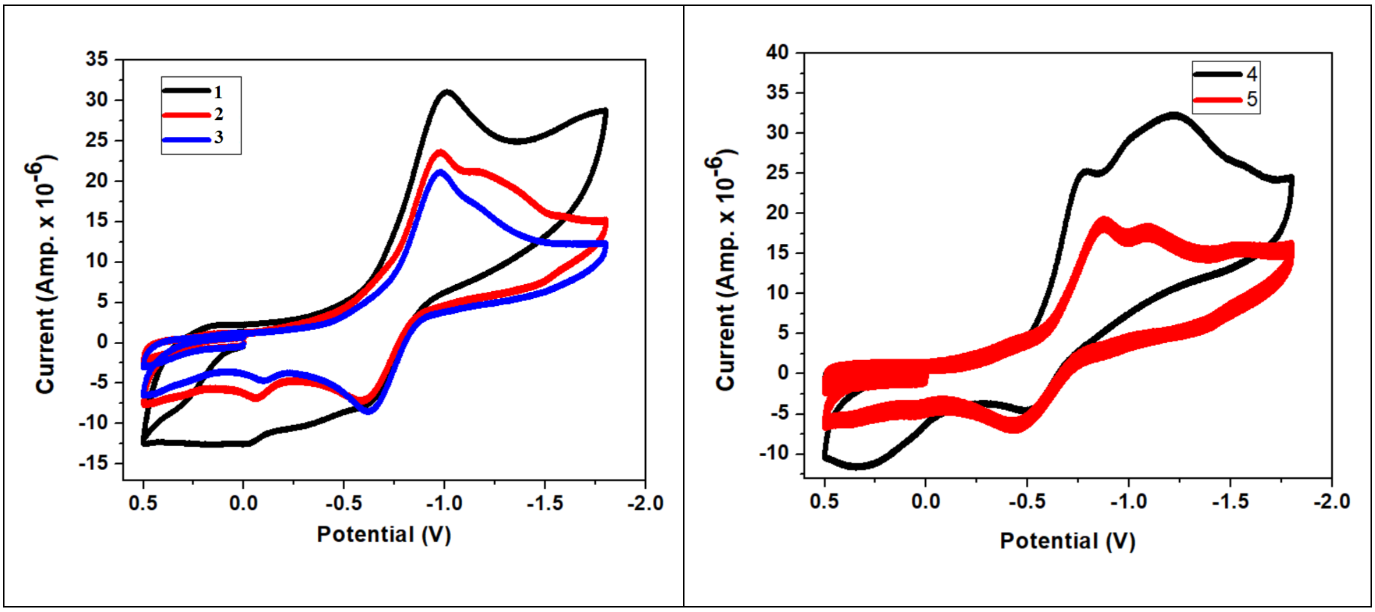

Fig. 21. Cyclic voltammograms of complexes 1-5 in DMSO at an Ag/AgCl electrode with a scan rate of 300 mV s^{-1} and temperature 20°C.

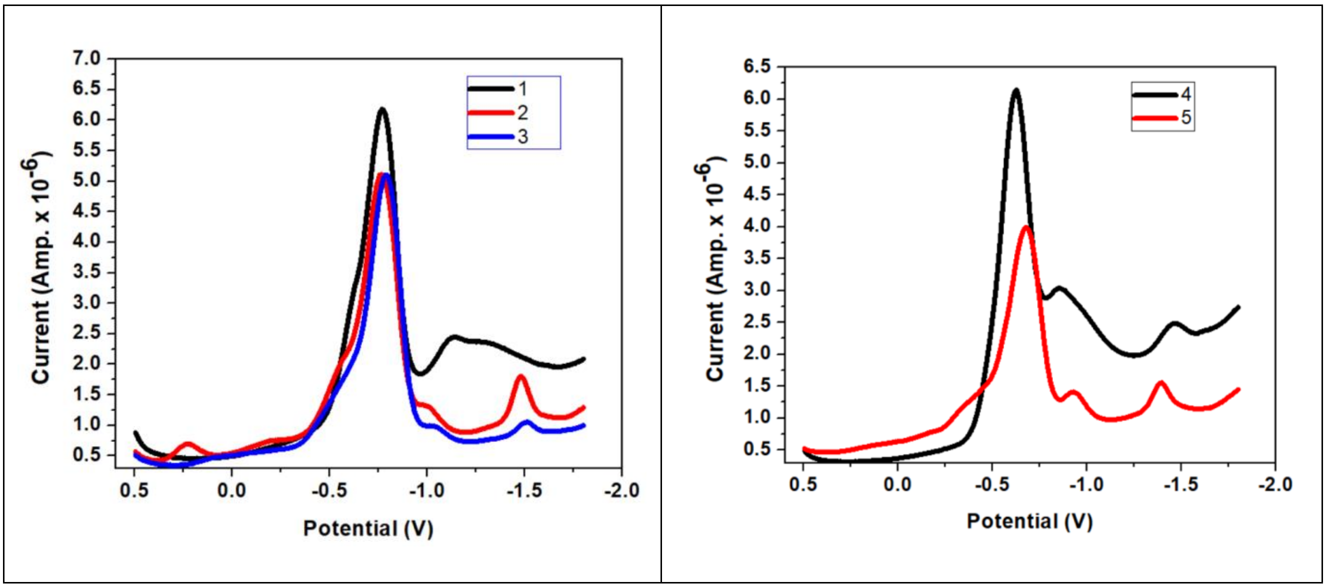

Fig. 22. Differential pulse voltammograms of complexes **1-5** at room temperature using a scan rate of 20 mV s^{-1}in DMSO. The pulse amplitude is 50 mV.

Table 5 Electrochemical data of copper(II) complexes **1-5** in DMSO (1.0 × 10^{-3} M).

Complex	E_{pc1}(V)	E_{pa1}(V)	E_{pc2}(V)	E_{pa2}(V)	D_{Epc1}(V)	D_{Epc2}(V)
1	-0.368	+0.0471	-0.864	-0.432	-0.357	-0.678
2	-0.784	-0.507	-1.121		-0.625	-0.853
3	-0.998	-0.625			-0.763	
4	-0.971	-0.598			-0.757	
5	-0.966	-0.635			-0.790	

3.9 Theoretical studies

3.9.1 Optimized structure

To explain the electronic structure of complexes (**1**-**5**), B3LYP correlation function by the Gaussian 09 package using a density functional theory (DFT) method has been executed. The molecular geometry was optimized in singlet state by using Gaussian 09 with the level of B3LYP [59-61]. The non-metal atoms were recounted by B3LYP/6-31G(d) and copper centers were labelled by B3LYP/LANL2DZ basis sets, respectively. The optimized geometries of the title complexes are displayed in Fig. 23. Some selected bond angles and distances are shown in Table 6. The copper(II) centre in all complexes are penta-coordinated. The proligand has NNN donor sites viz., two pyridine N and one azomethine N atoms whereas co-ligand coordinates through pyridine N atom forming two five membered chelate rings. Both pro and co-ligands are neutral. Thus geometry around copper(II) ion remain square pyramidal. The geometry of metal complexes of any penta-coordinated metal center is in general described by the Addition structural parameter (τ_5)[$\tau_5 = (\alpha-\beta)/60$], where α and β are the two largest angles of penta-coordinated geometry ($\tau_5 = 0$ believes an ideal square pyramidal and $\tau_5 = 1$ believes a perfect trigonal bipyramidal geometry) [62]. In these complexes (C4N5) the equatorial positions are occupied by two nitrogen atoms of pro-ligand (Schiff base) and two nitrogen atoms of imidazole/substituted imidazole's pyridyl nitrogen atoms whereas axial position is occupied by hydrazinic nitrogen atom of pro-ligand. The τ_5 values of theses complexes are in the range 0.177-0.495. Therefore, geometry around the copper ion is distorted trigonal bipyramidal. The Cu-N bond lengths are as usual.

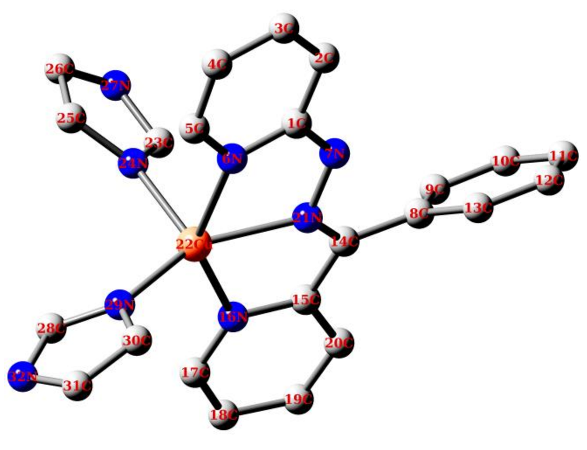	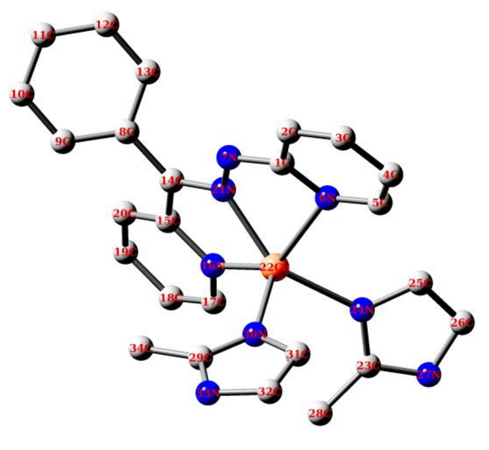
1	2
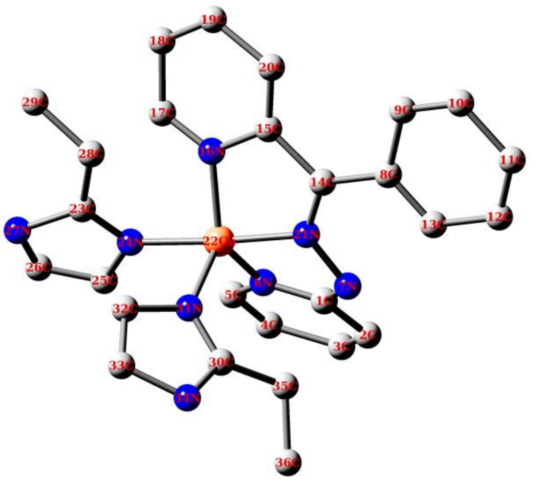	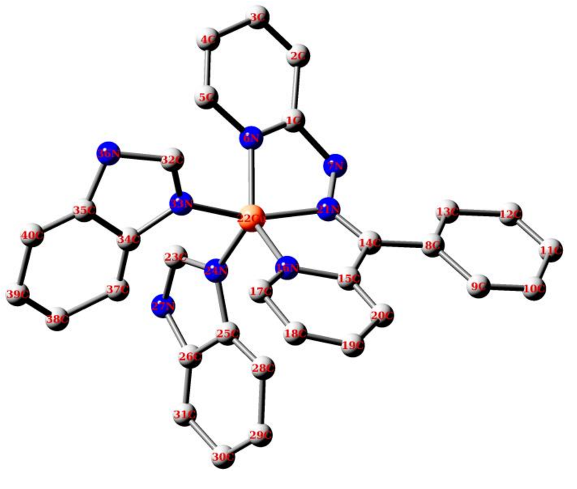
3	4

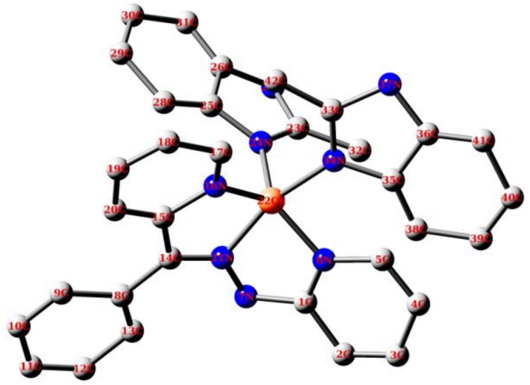

5

Fig. 23. Optimized structure of complexes **1-5**.

Table 6 Theoretical Bond lengths [Å] and angles [°] for complexes **1-5**.

1			
Bond lengths			
Cu(22)-N(6)	1.879	Cu(22)-N(24)	1.870
Cu(22)-N(16)	1.870	Cu(22)-N(29)	1.870
Cu(22)-N(21)	1.884		
Bond angles			
N(6)-Cu(22)-N(16)	138.352	N(16)-Cu(22)-N(24)	103.779
N(6)-Cu(22)-N(21)	78.741	N(16)-Cu(22)-N(29)	98.290
N(6)-Cu(22)-N(24)	117.297	N(21)-Cu(22)-N(24)	103.434
N(6)-Cu(22)-N(29)	86.368	N(21)-Cu(22)-N(29)	161.272
N(16)-Cu(22)-N(21)	85.695	N(24)-Cu(22)-N(29)	93.427
2			
Bond lengths			
Cu(22)-N(6)	1.877	Cu(22)-N(24)	1.870
Cu(22)-N(16)	1.872	Cu(22)-N(30)	1.870
Cu(22)-N(21)	1.884		
Bond angles			
N(6)-Cu(22)-N(16)	138.342	N(16)-Cu(22)-N(24)	98.441
N(6)-Cu(22)-N(21)	79.141	N(16)-Cu(22)-N(30)	103.369
N(6)-Cu(22)-N(24)	86.372	N(21)-Cu(22)-N(24)	161.601
N(6)-Cu(22)-N(30)	117.734	N(21)-Cu(22)-N(30)	103.608
N(16)-Cu(22)-N(21)	85.251	N(24)-Cu(22)-N(30)	93.118
3			
Bond lengths			
Cu(22)-N(6)	1.864	Cu(22)-N(24)	1.870
Cu(22)-N(16)	1.870	Cu(22)-N(31)	1.870
Cu(22)-N(21)	1.868		
Bond angles			
N(6)-Cu(22)-N(16)	131.440	N(16)-Cu(22)-N(24)	90.663

N(6)-Cu(22)-N(21)	81.115	N(16)-Cu(22)-N(31)	120.834
N(6)-Cu(22)-N(24)	102.662	N(21)-Cu(22)-N(24)	106.369
N(6)-Cu(22)-N(31)	107.251	N(21)-Cu(22)-N(31)	98.432
N(16)-Cu(22)-N(21)	85.446	N(24)-Cu(22)-N(31)	82.240
4			
Bond lengths			
Cu(22)-N(6)	1.877	Cu(22)-N(24)	1.870
Cu(22)-N(16)	1.872	Cu(22)-N(33)	1.870
Cu(22)-N(21)	1.884		
Bond angles			
N(6)-Cu(22)-N(16)	138.343	N(16)-Cu(22)-N(24)	103.376
N(6)-Cu(22)-N(21)	79.151	N(16)-Cu(22)-N(33)	98.427
N(6)-Cu(22)-N(24)	117.725	N(21)-Cu(22)-N(24)	103.574
N(6)-Cu(22)-N(33)	86.357	N(21)-Cu(22)-N(33)	161.589
N(16)-Cu(22)-N(21)	85.259	N(24)-Cu(22)-N(33)	93.165
5			
Bond lengths			
Cu(22)-N(6)	1.872	Cu(22)-N(24)	1.870
Cu(22)-N(16)	1.866	Cu(22)-N(34)	1.869
Cu(22)-N(21)	1.873		
Bond angles			
N(6)-Cu(22)-N(16)	134.954	N(16)-Cu(22)-N(24)	103.616
N(6)-Cu(22)-N(21)	80.009	N(16)-Cu(22)-N(34)	101.756
N(6)-Cu(22)-N(24)	121.075	N(21)-Cu(22)-N(24)	101.568
N(6)-Cu(22)-N(34)	85.136	N(21)-Cu(22)-N(34)	164.655
N(16)-Cu(22)-N(21)	86.259	N(24)-Cu(22)-N(34)	89.352

3.9.2 Orbital analysis

The ground-state electronic structures of the present complexes computed to obtain further insight into the electronic structures of complexes. The computed properties of frontier molecular orbital (FMO) is in terms of energies, the present composition of the pro-ligand and metal orbitals and contribution of used different co-ligands (imidazole or substituted imidazoles) are listed in Table 7 and shown in Fig. 24. The highest occupied molecular orbitals (HOMO) are normally assigned by the π-orbitals of pro-ligand (Schiff base) whereas lowest occupied molecular orbitals (LUMO) are devoted by π* of Schiff base.

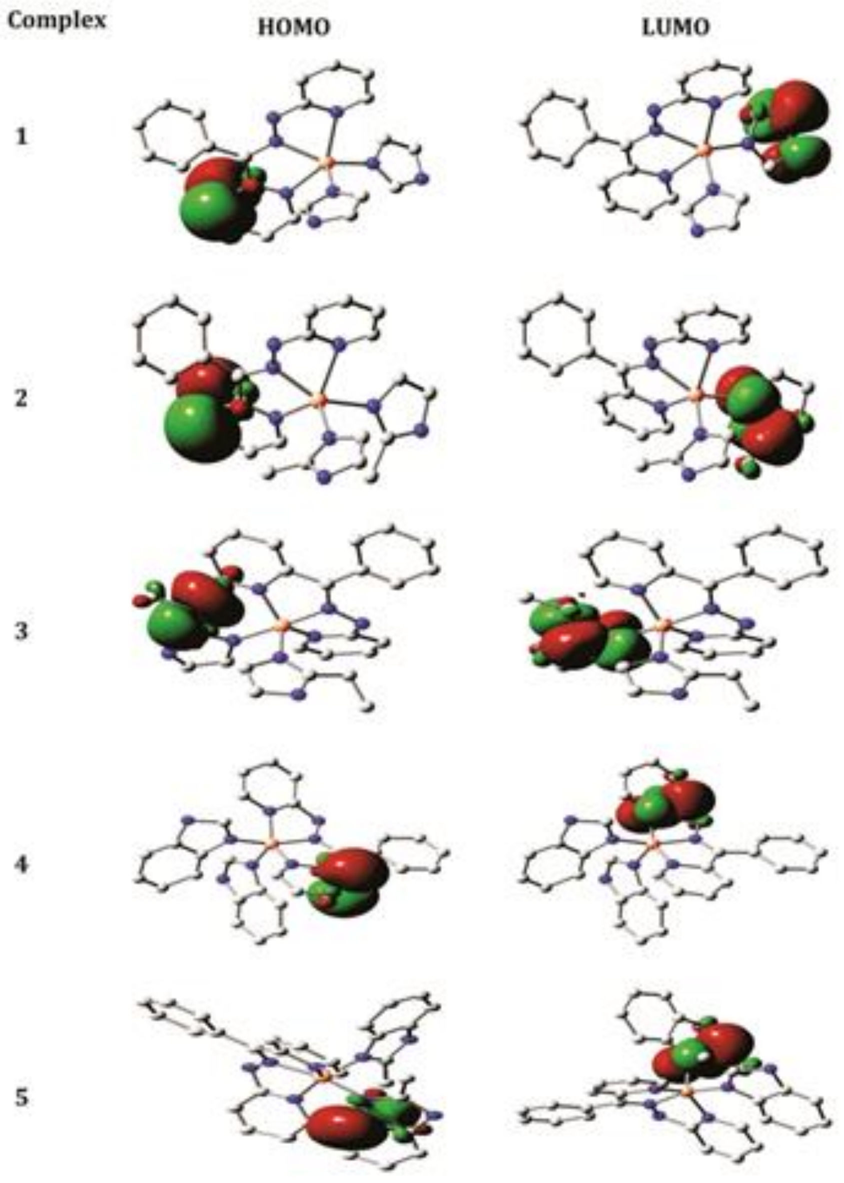

Fig. 24. Presentation of frontier molecular orbitals of complexes **1-5**.

Table 7 The spin densities of metal and donor atoms for complexes **1-5**.

Complexes	Metal and Donor atom	Spin populations	Mulliken populations	Natural populations
1	Cu22	0.044	+0.339	+0.281
	N6	0.042	-0.105	-0.304
	N16	0.123	-0.175	-0.354
	N21	0.349	-0.183	-0.375
	N24	0.007	-0.147	-0.285
	N29	0.002	-0.191	-0.291
	Cu22	0.050	+0.293	+0.280

2	N6	0.043	-0.084	-0.304
	N16	0.126	-0.197	-0.365
	N21	0.342	-0.183	-0.373
	N24	0.001	-0.173	-0.288
	N30	0.008	-0.217	-0.301
3	Cu22	0.002	+0.565	+0.315
	N6	0.056	-0.285	-0.337
	N16	0.046	-0.371	-0.335
	N21	0.199	-0.261	-0.321
	N24	0.002	-0.230	-0.285
	N31	0.025	-0.224	-0.298
4	Cu22	0.481	+0.622	+0.176
	N6	0.076	-0.261	-0.334
	N16	0.125	-0.315	-0.355
	N21	0.360	-0.294	-0.411
	N24	-0.001	-0.337	-0.312
	N33	0.060	-0.321	-0.351
5	Cu22	0.537	+0.540	+0.155
	N6	0.164	-0.503	-0.385
	N16	0.123	-0.303	-0.374
	N21	0.384	-0.267	-0.416
	N24	0.021	-0.321	-0.313
	N34	0.152	-0.286	-0.379

Different quantum chemical parameters were estimated to concentrate on the stability of the complexes (**1-5**). The calculated quantum chemical parameters comprise energies of HOMO and LUMOs (E_{HOMO} and E_{LUMO}), the energy gap (ΔE), absolute electronegativity (χ), chemical potential (P_i), absolute hardness (η), global softness (σ), global electrophilicity (ω) and additional electronic charge (ΔN_{max}) [63-65]. The electronegativity (χ) is obtained by using $\chi = \mathrm{IP} + \mathrm{EA}/2$. Similarly, $\eta = \mathrm{IP} - \mathrm{EA}/2$ and S = ½ [66, 67]. The ΔE between FMOs indicating HOMO and LUMO energies indicating the electron donating and accepting capability describes spectroscopic features of the molecules, molecular chemical stability and chemical reactivity. During the complexation process metal behaves as a Lewis acid (electron acceptor) and ligand acts as electron as a Lewis base (electron donor). Calculated values of these parameters are collected in Table 8. Negative charge of E_{HOMO} and E_{LUMO} suggest the stability of charges [68]. Calculated values of ΔE, global softness and chemical potential also support this suggestion. Absolute hardness (η) and softness (S) are important properties to evaluate the molecular stability and reactivity. The greater the ΔE, the higher is the stability of the complexes. On perusal of calculated values of these parameters it can be concluded that the complexes are stable transition metal complexes [69].

Table 8 Calculated quantum chemical parameters (eV).

Compound	E_{HOMO}	E_{LUMO}	ΔE	χ	η	σ	ω	P_i	ΔN_{max}
1	-2.206	-1.908	0.298	2.057	0.149	3.355	14.197	-2.057	13.805
2	-2.169	-0.241	1.241	1.205	0.620	0.806	1.170	-1.205	1.943
3	-1.644	-0.454	1.190	1.049	0.595	0.840	0.924	-1.049	1.763
4	-3.302	-0.725	2.577	2.013	1.288	0.388	1.572	-2.013	1.562
5	-1.130	-0.995	0.135	1.062	0.067	7.462	8.410	-1.062	15.850

3.9.3 Natural Bond Order (NBO) analysis

The NBO calculations were carried out at the B3LYP/LANL2DZ level of theory [69]. As per computed values of NBO analysis for the copper complex **1**, the electronic arrangement of the copper atom is: [Ar] 4s (0.22) 3d (9.80) 4p (0.37). the 17.994 core electrons, 10.393 valence electron and 0.004 Rydberg electrons, which yields sum of 28.391 electrons and +0.607 charge on copper atom (Table 9). This is in agreement with the natural charge the copper atom (+0.607), which is agree with to the difference between 28.391 and the total number of electrons in an isolated copper atom (29e). Similarly, the core, valence, Rydberg electrons and natural charge on copper atoms of remaining complexes **2-5** have also been calculated and collected in Table 9. The formal charges of donor atoms of pro and co-ligands reveal that the electron distribution not confined to the coordination bonds in between metal and donor atoms as the estimated formal charges of Cu (0.607) is smaller than +2 (Table 10). Such a reduce in the charge value is expected upon complex formation with charge transfer from the metal (copper) centers to the ligand (MLCT). The spin density plots of complexes are shown in Fig. 25.

Table 9 Natural electron configuration of complexes **1-5**.

Complex	Natural Electronic Configuration				Core	Valence	Rydberg
	4s	3d	4p	5s			
1	0.22	9.80	0.37	-	17.994	10.393	0.004
2	0.21	9.81	0.36	-	17.995	10.388	0.004
3	0.25	9.57	0.54	0.01	17.991	10.362	0.009
4	0.26	9.40	0.52	0.01	17.991	10.185	0.011
5	0.27	9.38	0.54	0.01	17.991	10.188	0.011

Table 10 The NBO charge of atoms in complexes.

1		2		3		4		5	
Atom	**NBO charge**	**Atom**	**NBO charge**	**Atom**	**NBO charge**	**Atom**	**NBO charge**	**Atom**	**NBO charge**
Cu22	+0.607	Cu22	+0.613	Cu22	+0.637	Cu22	+0.812	Cu22	+0.809
N6	-0.567	N6	-0.566	N6	-0.616	N6	-0.584	N6	-0.613
N7	-0.48	N7	-0.427	N7	-0.474	N7	-0.504	N7	-0.497
N16	-0.588	N16	-0.606	N16	-0.624	N16	-0.583	N16	-0.621
N21	-0.408	N21	-0.412	N21	-0.437	N21	-0.438	N21	-0.424
N24	-0.562	N24	-0.574	N24	-0.572	N24	-0.628	N24	-0.600
N27	-0.596	N27	-0.604	N27	-0.692	N27	-0.692	N27	-0.696
N29	-0.579	N30	-0.594	N31	-0.561	N33	-0.644	N34	-0.626
N32	-0.597	N33	-0.603	N34	-0.698	N36	-0.686	N37	-0.701

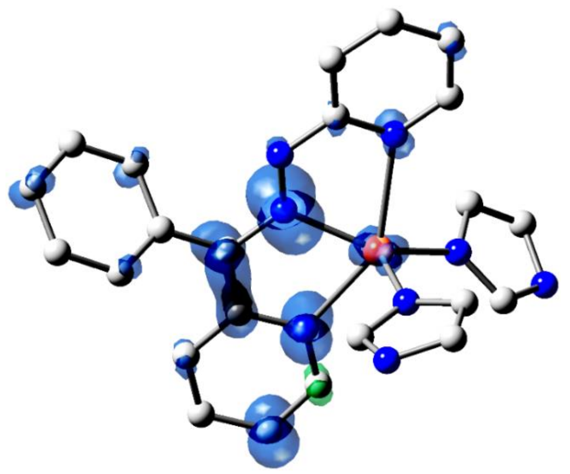

1

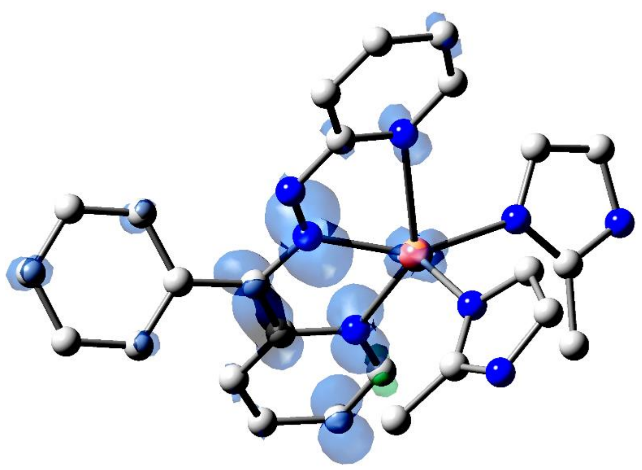

2

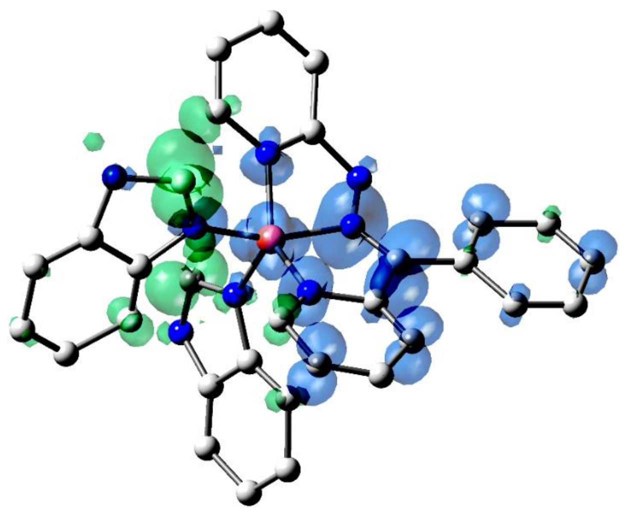

4

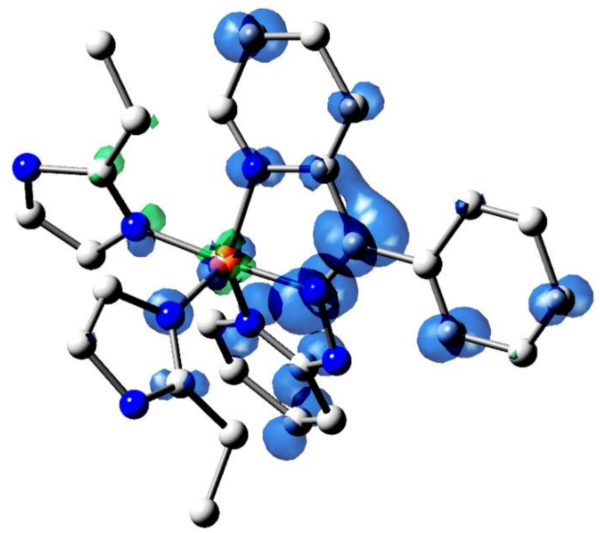

3

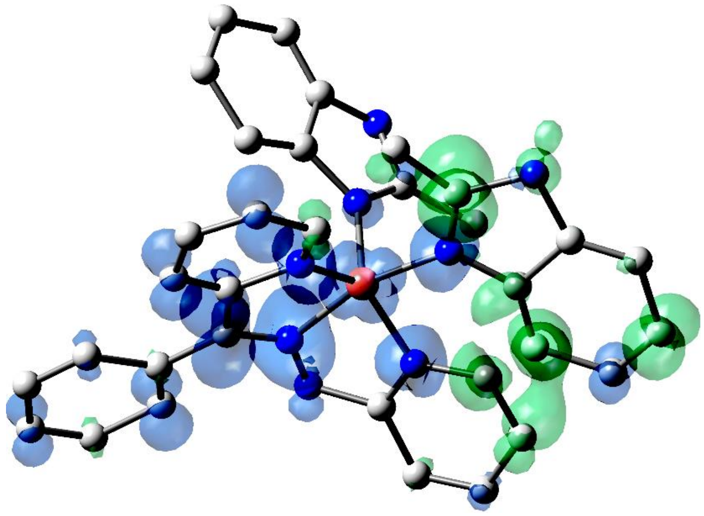

5

Fig. 25. Spin density plots of complexes **1-5**.

3.10 SOD activity

The SOD activity of the complexes was measured using alkaline DMSO nitro blue tetrazolium method [70, 71]. The assay was performed in phosphate buffer (pH = 7.4) at 25˚C. The result of activity measurements are shown in Fig 26. The IC_{50} value of each complex was evaluated from plot shown in above Fig 26. The IC_{50} value is the concentration of the complex which shows the SOD activity equal to one unit of the dismutase. The IC_{50} value of present complexes remains in the range 26-43 µM. SOD activity is also shown calculated and presented in Table 11 along with SOD data of some similar complexes [58, 72-74]. Comparatively high SOD activities of present complexes are expected due to coordination of nitrogen bases and their particular geometry yields high SOD activity. For these complexes kinetic catalytic constant k_{MccF} was calculated using formula $k_{MccF} = k_{NBT} \times [NBT] / IC_{50}$ [42] where $k_{NBT} = 5.94 \times 10^{-4}$ (mol $L^{-1})^{-1}$ s^{-1}. The values are similar to those of similar complexes reported in literature [58, 72-74]. From the perusal of catalytic rate constant values of present complexes, it is clear that these complexes may act as potent SOD mimics.

The catalytic mechanism of these SOD mimics are proposed in Scheme 3 in the first step electron transfer takes place in between copper(II) centre and superoxide anion $O_2^{\cdot -}$ accompanied with bond cleavage of Cu-ImH is assisted by protonation of the solvent and the oxygen molecule is released.$O_2^{\cdot -}$accepts one electron from Cu^{II}. In second step re-oxidation of Cu^{I} to Cu^{II} by attack of second molecule of $O_2^{\cdot -}$ molecule followed by bond reformation and release of hydrogen peroxide take place.

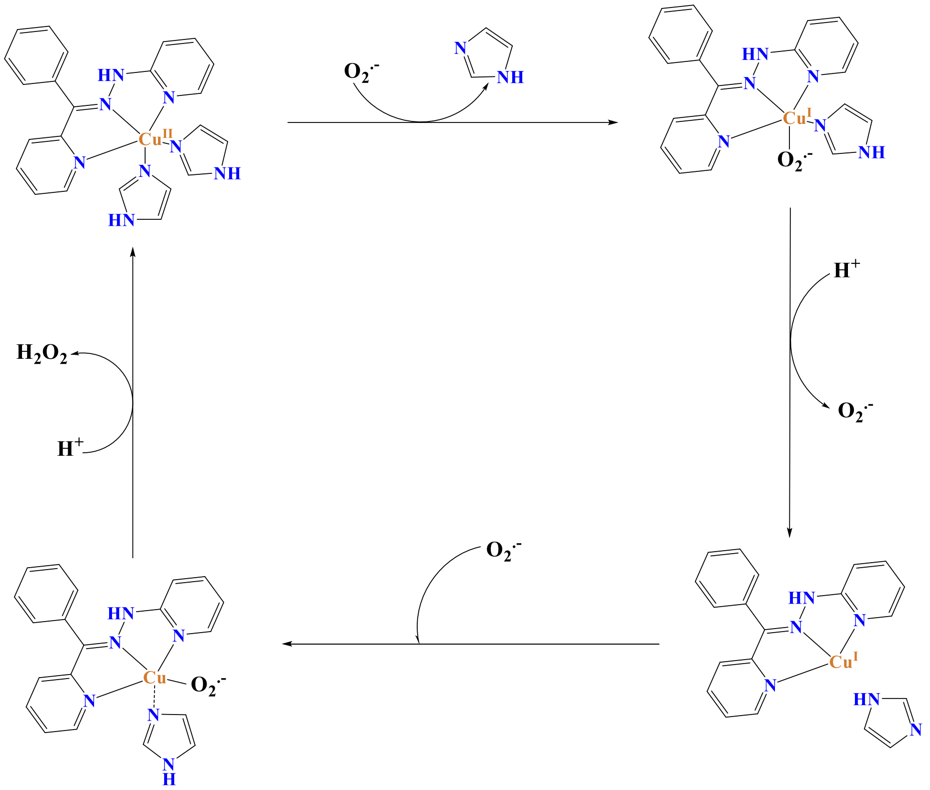

Scheme 3 The proposed SOD catalytic mechanism for $O_2^{\cdot -}$ dismutation reaction.

Table 11 The antioxidant SOD activity IC_{50} and kinetic catalytic constant for complexes **1-5**.

Compound	IC_{50} (µM)	SOD activity (µmol^{-1})	k_{McCF} (molL)$^{-1}$s^{-1} x 10^4	References
[Cu(BHM)ImH].CH_3OH	27	37.03	12.32	72
[Cu(BHM)(bipy)]	62	16.62	5.36	72
[Cu(L)$(NO_3)_2$(4,4-bipy)]	30	33.33	11.08	58
[Cu(L^1)(HL^1)]ClO_4.1/2H2O	25	40.00	13.30	58
[Cu(HL^2)$(H_2O)_2$]$_2NO_2$	16	62.50	20.79	73
Vc	852	1.17	0.39	74
1	26	38.46	12.79	Present work
2	43	23.25	7.73	Present work
3	41	24.39	8.11	Present work
4	39	25.64	8.53	Present work
5	35	28.57	9.50	Present work

BHM = N'-(1E)-[(5-bromo-2-hydroxylphenyl)methelidene]benzoylhydrazone, ImH = Imidazole, bpy = 2,2-bipyridyl, L^1/HL^1 = N'-[(E)-phenyl(pyridine-2-yl)methylidene]benzohydrazide, HL^2 = N'-[(E)-phenyl(pyridine-2-yl)methylidine]acetohydrazide and Vc = Vitamin C

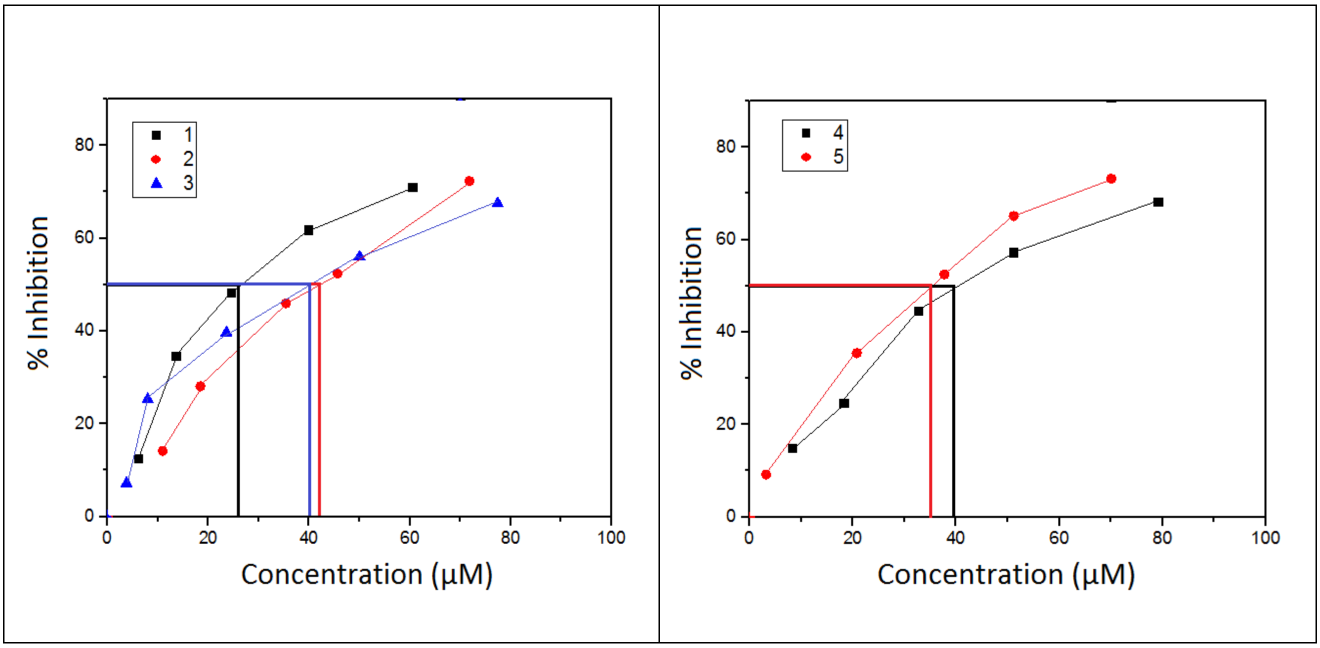

Fig. 26. SOD graphs of complexes **1-5**.

4 Conclusions

In this chapter, we have synthesized five copper complexes using $Cu(ClO_4)_2.6H_2O$ and hydrazone ligand (HL) with using different imidazole series as co-ligand led to the formation of mononuclear complexes. These complexes were isolated in good yield and characterized using UV-Vis, FTIR and EPR spectral physico-chemical techniques. The all complexes are insoluble in water and non-polar organic solvents but are highly soluble in DMSO and CH_3CN. These complexes are stable in air. The molar conductance value of complexes are in the range 118-139 (Ω^{-1} cm^2 mol^{-1}) in DMSO solution. The room temperature magnetic susceptibility data of all complexes collected. The room temperature magnetic moment values are in the range 1.79-1.81 B.M. The magnetic moment values are very close to the spin only value for the discrete magnetically non-coupled copper(II) system, suggesting that the complexes are non-coupled at room temperature. The copper(II) centre in all complexes are penta-coordinated. The proligand has NNN donor sites viz., two pyridine N and one azomethine N atoms whereas co-ligand coordinates through pyridine N atom forming two five membered chelate rings. Both pro and co-ligands are neutral. Thus geometry around copper(II) ion remain square pyramidal. The τ_5 values of theses complexes are in the range 0.177-0.495. The IC_{50} value of present complexes remains in the range 26-43 µM.

References

1 S.J. Lippard, Science 261 (1993) 699-700.

2 W. Kaim, B. Schwederski, Bioinorganic chemistry: Inorganic elements in the chemistry of Life, John Wiley and Sons, New York, 1991.

3 P.A. Bryngelson, S.E. Arobo, J.L. Pinkham, D.E. Cabelli, M.J. Maroney, J. Am. Chem. Soc. 126 (2004) 460–461.

4 J.P. Renault, C.V. Beaur, I.M. Badarau, F. Yamakura, M. Gerloch, Inorg. Chem. 39 (2000) 2666-2675.

5 L.W. Oberley, G.R. Bueftner, Cancer Res. 39 (1979)1141-1149.

6 K.J. Farmer, R.S. Sohal, Free Radical Biol. Med. 7 (1989) 23-29.

7 A.R. Damasio , H. Damasio, Sci. Am. 267 (1992) 88-95.

8 Z.A. Siddiqi, M. Shahid, M. Khalid, S. Kumar, Eur. J. Med. Chem. 44 (2009) 2517-2522.

9 A.L. Abuhijleh, J. Inorg. Biochem. 68 (1997) 167-175.

10 M. Devereux, D.O. Shea, M.O. Connor, H. Grehan, G. Conner, M. McCann, G. Rosair, F. Lyng, A. Kellett, M. Walsh, D. Egan, B. Thati, Polyhedron 26 (2007) 4073-4084.

11 V. Balasubramanian, M. Ezhevskaya, H. Moons, M. Neuburger, C. Cristescu, S.V. Doorslaer, C. Palivan, Phys. Chem. Chem. Phys. 11 (2009) 6778-6787.

12 A.L. Abuhijleh, C. Woods, Inorg. Chem. Commun. 5 (2002) 269-273.

13 J.R.J. Sorenson, Prog. Med. Chem. 26 (1989) 437-568.

14 J.E. Weder, C.T. Dillon, T.W. Hambley, B.J. Kennedy, P.A. Lay, J.R. Biffin, H.L. Regtep, N.M. Davies, Coord. Chem. Rev. 232 (2002) 95-126.

15 T. Fujimori, S. Yamada, H. Yasui, H. Sakurai, Y.I.T. Ishida, J. Biol. Inorg. Chem. 10 (2005) 831-841.

16 C.T. Dillon, T.W. Hambley, B.J. Kennedy, P.A. Lay, O. Zhou, N.M. Davies, J. R. Biffin, H.L. Regtop, Chem. Res. Toxicol 16 (2003) 28-37.

17 D.K. Demertzi, A. Galani, M.A. Demertzis, S. Skoulika, C. Kotoglou, J. Inorg, Biochem 98 (2004) 358-364.

18 G.W. Wangila, K.K. Nagothu, R. Steward III, R. Bhatt, P.A. Iyere, W.M. Willingham, J.R.J. Sorenson, S.V. Shah, D. Portilla, Toxicol. in Vitro 20 (2006) 1300-1312.

19 R.N. Patel, Y. Singh, Y.P. Singh, R.J. Butcher, A. Kamal, I.P. Tripathi, Polyhedron 117 (2016) 20–34.

20 S.K. Patel, R.N. Patel, Y. Singh, Y.P. Singh, D. Kumhar, R.N. Jadeja, H. Roy, A.K. Patel, N. Patel, N. Patel, A. Banerjee, D.C. Lazarte, A. Gutierrez, Polyhedron 161 (2019) 198-212.

21 R.N. Patel, Y.P. Singh, Y. Singh, R.J. Butcher, M. Zeller, R.K.B. Singh, O.U. -Wang, J. Mol. Struct. 1136 (2017) 157–172.

22 R.N. Patel, Y.P. Singh, Y. Singh, R.J. Butcher, M. Zeller, RSC Adv. 6 (2016) 107379–107398.

23 R.N. Patel, Y.P. Singh, Y. Singh, R.J. Butcher, J.P. Jasinski, Polyhedron 133 (2017)

102–109.

24 R.N. Patel, Y.P. Singh, J. Mol. Struct. 1153 (2018) 162–169.

25 A.K. Patel, R.N. Jadeja, H. Roy, R.N. Patel, S.K. Patel, R.J. Butcher, M. Cortijo, S. Herrero, Polyhedron 186 (2020) 114624.

26 G.A. Petersson, M.A. Al-Laham, J. Chem. Phys. 94 (1991) 6081-6090.

27 P.J. Hay, W.R. Wadt, J. Chem. Phys. 82 (1985) 270-283.

28 M.J. Frisch, G.W. Trucks, H.B. Schlegel, G.E. Scuseria, M.A. Robb, J.R. Cheeseman, G. Scalmani, V. Barone, B. Mennucci, G.A. Petersson, H. Nakatsuji, M. Caricato, X. Li, H.P. Hratchian, A.F. Izmaylov, J. Bloino, G. Zheng, J.L. Sonnenberg, M. Hada, M. Ehara, K. Toyota, R. Fukuda, J. Hasegawa, M. Ishida, T. Nakajima, Y. Honda, O. Kitao, H. Nakai, T. Vreven, J.A. Montgomery Jr., J.E. Peralta, F. Ogliaro, M. Bearpark, J.J. Heyd, E. Brothers, K.N. Kudin, V.N. Staroverov, R. Kobayashi, J. Normand, K. Raghavachari, A. Rendell, J.C. Burant, S.S. Iyengar, J. Tomasi, M. Cossi, N. Rega, J.M. Millam, M. Klene, J.E. Knox, J.B. Cross, V. Bakken, C. Adamo, J. Jaramillo, R. Gomperts, R.E. Stratmann, O. Yazyev, A.J. Austin, R. Cammi, C. Pomelli, J.W. Ochterski, R.L. Martin, K. Morokuma, V.G. Zakrzewski, G.A. Voth, P. Salvador, J.J. Dannenberg, S. Dapprich, A.D. Daniels, O. Farkas, J.B. Foresman, J.V. Ortiz, J. Cioslowski, D.J. Fox, Gaussian 09, Revision D.01, Gaussian Inc., Wallingford CT, (2009).

29 R. Bauernschmitt, R. Ahlrichs, Chem. Phys. Lett. 256 (1996) 454-464.

30 R.N. Patel, D.K. Patel, K.K. Shukla, Y. Singh, J. Coord. Chem. 66 (2013) 4131-4143.

31 R.G. Bhirud, T. S. Shrivastava, Inorg. Chim. Acta. 173 (1990) 121–125.

32 R. Konecny, J. Li, C.L. Fisher, V. Dillet, D. Bashford, L. Noodleman, Inorg. Chem. 38 (1999) 940-950.

33 M. Sutradhar, M.V. Kirillova, M.F.C.G. Silva, C.M. Liuc, A.J.L. Pombeiro, Dalton Trans. 42 (2013) 16578-16587.

34 R. Vicente, A. Escuer, E.P. Aalba, X. Solans, M.F. Baria, Inorg. Chim. Acta 255 (1997) 7-12.

35 R.K.B Singh, K.M.A. Malik ,S.O.G. Mahalli, M.S.El Fallah, N.K. Karan, S. Mitra, Inorg. Chem. Commun. 4 (2001) 315-318.

36 L.K. Thompson, B.S. Ramaswamy, R.D. Dawe, Can. J. Chem. 56 (1978) 1311-1318.

37 N.K. Karan, S. Mitra, T. Matsushita, V. Gramlich, G. Rosair, Inorg. Chim. Acta 332 (2002) 87–91.

38 E.B. Seena, M.R.P. Kurup, Polyhedron 26 (2007) 829–836.

39 L. Valencia, R. Bastida, M.C.F. Fernandez, A. Macıas, M. Vicente, Inorg. Chim. Acta 358 (2005) 2618–2628.

40 M. Mikuriya, H. Okawa, S. Kida, Bull. Chem. Soc. Jpn. 53 (1980) 3717-3718.

41 A.B.P Lever, Inorganic Electronic Spectroscopy, Elsevier, New York, (1968), p-507.

42 W.J. Geary, Coord. Chem. Rev. 7 (1971) 81–122.

43 J.E. Wertz, J.R. Bolton, Electron Spin Resonance: Theory and Applications, Mc Graw-Hill, New York, 1972.

44 M.C.R Symons, Chemical and Biochemical Aspects of Electron Spin Resonance Spectroscopy, Van Nostrand Reinhold, New York, 1978.

45 H.M.J. Hendriks, P.J.M.W.L. Birker, G.C. Verschoor, J. Reedijk, J. Chem. Soc., Dalton Trans. (1982) 623-631.

46 K.J. Oberhousen, J.F. Richardson, R.M. Buchanan, J.K. McCusker, D.N. Hendricison, J.M. Latour, Inorg. Chem. 30 (1991) 1357-1365.

47 R.N. Patel, Y.P. Singh, Y. Singh, R.J. Butcher, J.P. Jasinski, Polyhedron 129 (2017) 164-181.

48 R.C. Agrawal, N.K. Singh, R.P. Singh, Inorg Chem. 20 (1981) 2794-2798.

49 R.N. Patel, Inorg. Chim. Acta 363 (2010) 3838-3846.

50 B.J. Hathaway, D.E. Willing, Coord. Chem. Rev. 5 (1970) 143-207.

51 R.L. Belford, N.D. Chasteen, H. So, R.E. Tapcot, J. Am. Chem. Soc. 91 (1969) 4675-4630.

52 M.J. Bew, B.J. Hathaway, R.J. Faraday, J. Chem. Soc., Dalton Trans. (1972) 1229-1237

53 E. Garriba, G. Micera, J. Chem. Educ. 83 (1906) 1229-1232.

54 G. Folks, J.C. Dewan, H.R. Lilienthal, S.J. Lippard, J. Am. Chem. Soc. 100 (1978) 7291-7300.

55 D. Reinen, C. Friebel, Inorg. Chem. 23 (1984) 791-798.

56 A.H. Maki, B.R. Mc Garvey, J. Chem. Phys. 29 (1958) 31.

57 S.A. Cameron, S. Brooker, Inorg. Chem. 50 (2011) 3697–370.

58 R.N. Patel, Y. Singh, Y.P. Singh, A.K. Patel, N. Patel, R. Singh, R.J. Butcher, J. P Jasinski, E. Colacio, M.A. Palacios, New J. Chem. 42 (2018) 3112-3136.

59 G. Micera, E. Garriba, Int. J. Quantum Chem. 112 (2012) 2486-2498.

60 L. Pisano, K. Varnagy, S. Timari, K. Hegetschweiler, G. Micera, E. Garribba, Inorg Chem. 52 (2013) 5260-5272.

61 D. Sanna, K. Varnagy, N. Lihi, G. Micera, E. Garribba, Inorg. Chem. 52 (2013) 8202-8213.

62 A.W. Addison, T.N. Rao, J. Reedijk, J.V. Rijn, G.C. Verchoor, J. Chem. Soc. Dalton Trans. 7 (1984) 1349-1356.

63 X.M. Zhang, H.S. Wu, X.M. Chen, Eur. J. Inorg. Chem. 2003 (2003) 2959-2964.

64 E.J. Jung, U. K. Lee, B. K. Koo, Inorg. Chim. Acta 361 (2008) 2962-2966.

65 M. Masoudi, M. Behzad, A. Arab, A. Tarahhomi, H.A. Rudbari, G. Bruno, J. Mol. Struct. 1122 (2016) 123-133.

66 S. Altruk, D. Avli, O. Tamer, Y. Atlay, O. Sahin, J. Phy. Chem. Solids, 184 (2016) 342-370.

67 T. Koopmans, Physica 1 (1934) 104-113.

68 A.A. Soliman, M.A. Amin, A.M. Sayed, A.A.A. Abou-Hussein, W. Linert, Polyhedron 161 (2018) 213-221.

69 A.E. Reed, L.A. Curtis, F. Weinhold, Chem. Rev. 88 (1988) 899-926.

70 Y. Singh, R.N. Patel, Y.P. Singh, A.K. Patel, N. Patel, R. Singh, R.J. Butcher, J.P Jasinski, E. Colacio, M.A. Palacios, Dalton Trans. 46 (2017) 11860-11874.

71 R.N. Patel, S. Kumar, K.B. Pandeya, J. Inorg. Biochem. 89 (2002) 61-68.

72 R.N. Patel, S.P. Rawat, M. Choudhary, V.P. Sondhiya, D.K. Patel, K.K. Shukla, D.K Patel, Y. Singh, R. Pandey, Inorg. Chim. Acta 392 (2012) 283-291.

73 Y. Singh, R.N. Patel, S.K. Patel, R.N. Jadeja, A.K. Patel, N. Patel, H. Roy, P. Bhagriya, R. Singh, R.J. Butcher, J.P. Jasinski, S. Herrero, M. Cortijo, Inorg. Chim. Acta 503 (2020) 119371.

74 Y. Li, Z.Y. Yang, J.C. Wu, Eur. J. Med. Chem. 45 (2010) 5692-5701.

Chapter 3

Copper(II) complexes incorporating NNN-tridentate hydrazone as proligand

Part (C): Synthesis, spectral characterization and biomimetic activity of homobinuclear copper(II) 2-[(E)-phenyl(pyridine-2-yl-hydrazone)methyl]pyridine complexes containing inorganic salts

1 Introduction

Hydrazones are a member of the Schiff base family with a triatomic $> \mathrm{C} = \mathrm{N} - \mathrm{NH} -$ linkage and play important role in the evolution of coordination chemistry. The coordination behavior of transition metals with this linkage is of importance for their acidity, functional coordination modes and molecular structures, dye and pigmenting behaviour, redox and biological properties [1, 2]. The design and synthesis of transition metal complexes using tridentate hydrazone ligands have been carried out by several inorganic chemists [3-8]. Binuclear metal complexes with such tridentate Schiff bases are interesting to study to mimic the biological properties of Cu-Zn superoxide dismutase (SOD) [9]. Specially copper(II) homobionuclear complexes are of importance due to their structural diversity and the variety of magnetic couplings of these complexes [10-16]. Small molecular weight copper(II) complexes are investigated as structural and functional models of active sites of copper-containing enzymes [17-26]. Cu-Zn SOD catalyzes the disproportionation of the toxic superoxide ion ($\mathrm{O}_2^{\cdot-}$) and protect the living cell against various diseases *viz.*, cancer, inflammation, diabetes and other diseases [27]. During the SOD catalysis, the copper is reversibly oxidized and reduced by consecutive collides with $\mathrm{O}_2^{\cdot-}$ to yield oxygen molecule (O_2) and hydrogen peroxide (H_2O_2) by the following equations (1) and (2) [28].

$$\mathrm{E{-}Cu^{II}} + \mathrm{O}_2^{\cdot-} \rightleftharpoons \mathrm{E{-}Cu^{I}} + \mathrm{O_2}\text{.............(1)}$$

$$\mathrm{E{-}Cu^{I}} + \mathrm{O}_2^{\cdot-} \rightleftharpoons \mathrm{E{-}Cu^{II}} + \mathrm{H_2O_2}\text{.............(2)}$$

Therefore, a large number of low molecular weight copper(II) complexes were designed and their SOD activity was explored [29-39].

In this part of thesis, homo binuclear copper(II) 2-[(E)-phenyl(pyridine-2-yl-hydrazono)methyl]pyridine (L) complexes containing inorganic salts with compositions, $[(L)Cu(H_2O)(C_2O_4)(H_2O)Cu(L)]C_2O_4$ (**1**), $[(L)Cu(H_2O)(C_3H_2O_4)(H_2O)Cu(L)]C_3H_2O_4$ (**2**), $[(L)Cu(H_2O)(C_4H_4O_4)(H_2O)Cu(L)]C_4H_4O_4$ (**3**), $[(L)Cu(H_2O)(C_8H_4O_4)(H_2O)Cu(L)]C_8H_4O_4$ (**4**), $[(L)Cu(H_2O)(ImH)(H_2O)Cu(L)](ImH)_3$ (**5**), $[(L)Cu(H_2O)(2\text{-}MeImH)(H_2O)Cu(L)](2\text{-}MeImH)_3$ (**6**), $[(L)Cu(H_2O)(2\text{-}EthImH)(H_2O)Cu(L)](2\text{-}EthImH)_3$ (**7**), $[(L)Cu(H_2O)(BenzImH)(H_2O)Cu(L)](BenzImH)_3$ (**8**) and $[(L)Cu(H_2O)(2\text{-}MeBenzImH)(H_2O)Cu(L)](2\text{-}MeBenzImH)_3$ (**9**) (Where C_2H_4 = Sodium Oxalate, $C_3H_2O_4$ = Sodium Malonate, $C_4H_4O_4$ = Sodium Succinate, $C_8H_4O_4$ = Sodium Terephthalate, ImH = Imidazole, 2-MeImH = 2-Methylimidazole, 2-EthImH = 2-Ethylimidazole, BenzImH =

Benzimidazole and 2-MeBenzImH = 2-Methylbenzimidazole) have been synthesized and characterized for their spectroscopic and redox properties. In addition, SOD mimetic activities of these complexes have also been investigated.

2 Experimental

2.1 Synthesis of Schiff base (L)

Schiff base was synthesized by condensing 2-benzoyl pyridine with 2-hydrazino pyridine by the earlier reported method [40]. The resulting red compound was filtered and washed with EtOH and dried in a calcium chloride desiccator.

2.2 Synthesis of complex [(L)Cu(H_2O)(C_2O_4)(H_2O)Cu(L)]C_2O_4 1

To a stirred solution (20 mL) of ligand (0.274 g, 1 mmol) was added $CuCl_2.2H_2O$ (0.170 g, 1 mmol) in methanol (10 mL) while stirring. To this reaction mixture, sodium oxalate (0.134 g, 1 mmol) in methanol (10 mL) was added drop-wise and refluxed for 1 hrs. After 1 hrs refluxing, the resulting reaction mixture was cooled at room temperature and filtered. The filtrate was allowed to evaporate slowly in the air. After 2-3 days microcrystalline powder was separated, this was collected upon filtration and stored in a calcium chloride desiccator.

Yield: ~ 76%. Anal. Calc. for $C_{38}H_{32}Cu_2N_8O_{10}$ (887.81 g mol^{-1}): C, 51.41; H, 3.63; N, 12.62%. Found: C, 51.40; H, 3.60; N, 12.61%. FTIR bands (KBr, cm^{-1}): 1613 ν(C=O), 1578 ν(C=N). ESI-Mass (m/z): 887.54.

2.3 Synthesis of complex [(L)Cu(H_2O)($C_3H_2O_4$)(H_2O)Cu(L)]$C_3H_2O_4$ 2

To a stirred solution (20 mL) of ligand (0.274 g, 1 mmol) was added $CuCl_2.2H_2O$ (0.174 g, 1 mmol) in methanol (10 mL) while stirring. To this reaction mixture, sodium malonate (0.148 g, 1 mmol) in methanol (10 mL) was added drop-wise and refluxed for 1 hrs. After 1 hrs refluxing, the resulting reaction mixture was cooled at room temperature and filtered. The filtrate was allowed to evaporate slowly in the air. After 2-3 days microcrystalline powder was separated, this was collected upon filtration and dried in a calcium chloride desiccator.

Yield: ~ 75%. Anal. Calc. for $C_{40}H_{36}Cu_2N_8O_{10}$ (915.87 g mol^{-1}): C, 52.46; H, 3.96; N, 12.23%. Found: C, 52.45; H, 3.94; N, 12.21%. FTIR bands (KBr, cm^{-1}): 1625 ν(C=O), 1533 ν(C=N). ESI-Mass (m/z): 916.57.

2.4 Synthesis of complex $[(L)Cu(H_2O)(C_4H_4O_4)(H_2O)Cu(L)]C_4H_4O_4$ 3

To a stirred solution (20 mL) of ligand (0.274 g, 1 mmol) was added $CuCl_2.2H_2O$ (0.174 g, 1 mmol) in methanol (10 mL) while stirring. To this reaction mixture, sodium succinate (0.270 g, 1 mmol) in methanol (10 mL) was added drop-wise and refluxed for 1 hrs. After 1 hrs refluxing, the resulting reaction mixture was cooled at room temperature and filtered. The filtrate was allowed to evaporate slowly in the air. After 2-3 days microcrystalline powder was separated, this was collected upon filtration and stored in a calcium chloride desiccator.

Yield: ~ 78%. Anal. Calc. for $C_{42}H_{40}Cu_2N_8O_{10}$ (943.92 g mol^{-1}): C, 53.44; H, 4.27; N, 11.87%. Found: C, 53.42; H, 4.28; N, 11.88%. FTIR bands (KBr, cm^{-1}): 1603 ν(C=O), 1580 ν(C=N). ESI-Mass (m/z): 944.99.

2.5 Synthesis of complex $[(L)Cu(H_2O)(C_8H_4O_4)(H_2O)Cu(L)]C_8H_4O_4$ 4

To a stirred solution (20 mL) of ligand (0.274 g, 1 mmol) was added $CuCl_2.2H_2O$ (0.174 g, 1 mmol) in methanol (10 mL) while stirring. To this reaction mixture, sodium terephthalate (0.210 g, 1 mmol) in methanol (10 mL) was added drop-wise and refluxed for 1 hrs. After 1 hrs refluxing, the resulting reaction mixture was cooled at room temperature and filtered. The filtrate was allowed to evaporate slowly at room temperature. After 2-3 days microcrystalline powder was separated, this was collected upon filtration and kept in a calcium chloride desiccator.

Yield: ~ 82%. Anal. Calc. for $C_{42}H_{40}Cu_2N_8O_{10}$ (1040.01 g mol^{-1}): C, 57.74; H, 3.88; N, 10.77%. Found: C, 57.72; H, 3.87; N, 10.74%. FTIR bands (KBr, cm^{-1}): 1612 ν(C=O), 1545 ν(C=N). ESI-Mass (m/z): 1038.65.

2.6 Synthesis of complex $[(L)Cu(H_2O)(ImH)(H_2O)Cu(L)](ImH)_3$ 5

To a well-stirred solution (10 mL) of ligand (0.274 g, 1 mmol) was added $CuCl_2.2H_2O$ (0.174 g, 1 mmol) in methanol (10 mL) while stirring. To this reaction mixture, imidazole (0.136 g, 2 mmol) dissolved in KOH (0.056g, 4 mmol) was added drop-wise and the resulting reaction mixture was refluxed for 1 hrs. After refluxing for 1 hrs, the resulting solution was cooled at room temperature. After one weak brown solid was filtered, washed with methanol and dried in a calcium chloride desiccator.

Yield: ~ 75%. Anal. Calc. for $C_{46}H_{47}Cu_2N_{16}O_2$ (983.08 g mol^{-1}): C, 56.20; H, 4.82; N, 22.80%. Found: C, 56.21; H, 4.83; N, 22.82%. FTIR bands (KBr, cm^{-1}): 1564 ν(C=N), 1003 ν(N-N). ESI-Mass (m/z): 980.96.

2.7 Synthesis of complex $[(L)Cu(H_2O)(2\text{-}MeImH)(H_2O)Cu(L)](2\text{-}MeImH)_3$ 6

To a well-stirred solution (10 mL) of ligand (0.274 g, 1 mmol) was added $CuCl_2.2H_2O$ (0.174 g, 1 mmol) in methanol (10 mL) while stirring. To this reaction mixture, 2-methylimidazole (0.164 g, 2 mmol) dissolved in KOH (0.056g, 4 mmol) was added drop-wise and the resulting reaction mixture was refluxed for 1 hrs. After refluxing for 1 hrs, the resulting solution was cooled at room temperature. After one weak brown solid was filtered, washed with methanol and dried in a calcium chloride desiccator.

Yield: ~ 83%. Anal. Calc. for $C_{50}H_{55}Cu_2N_{16}O_2$ (1039.19 g mol^{-1}): C, 57.79; H, 5.33; N, 21.57%. Found: C, 57.78; H, 5.34; N, 21.56%. FTIR bands (KBr, cm^{-1}): 1564 ν(C=N), 1004 ν(N-N). ESI-Mass (m/z): 1036.47.

2.8 Synthesis of complex $[(L)Cu(H_2O)(2\text{-}EthImH)(H_2O)Cu(L)](2\text{-}EthImH)_3$ 7

To a well-stirred solution (10 mL) of ligand (0.274 g, 1 mmol) was added $CuCl_2.2H_2O$ (0.174 g, 1 mmol) in methanol (10 mL) while stirring. To this reaction mixture, 2-ethylimidazole (0.192 g, 2 mmol) dissolved in KOH (0.056g, 4 mmol) was added drop-wise and the resulting reaction mixture was refluxed for 1 hrs. After refluxing for 1 hrs, the resulting solution was cooled at room temperature. After one weak brown solid was filtered, washed with methanol and dried in a calcium chloride desiccator.

Yield: ~ 80%. Anal. Calc. for $C_{54}H_{63}Cu_2N_{16}O_2$ (1095.30 g mol^{-1}): C, 59.22; H, 5.80; N, 20.46%. Found: C, 59.23; H, 5.81; N, 20.45%. FTIR bands (KBr, cm^{-1}): 1564 ν(C=N), 1002 ν(N-N). ESI-Mass (m/z): 1092.53.

2.9 Synthesis of complex $[(L)Cu(H_2O)(BenzImH)(H_2O)Cu(L)](BenzImH)_3$ 8

To a well-stirred solution (10 mL) of ligand (0.274 g, 1 mmol) was added $CuCl_2.2H_2O$ (0.174 g, 1 mmol) in methanol (10 mL) while stirring. To this reaction mixture, benzimidazole (0.236 g, 2 mmol) dissolved in KOH (0.056 g, 4 mmol) was added drop-wise and the resulting reaction mixture was refluxed for 1 hrs. After refluxing for 1 hrs, the resulting solution was cooled at room temperature. After one weak brown solid was filtered, washed with methanol and dried in a calcium chloride desiccator.

Yield: ~ 78%. Anal. Calc. for $C_{62}H_{55}Cu_2N_{16}O_2$ (1183.32 g mol^{-1}): C, 62.93; H, 4.69; N, 18.94%. Found: C, 62.92; H, 4.70; N, 18.92%. FTIR bands (KBr, cm^{-1}): 1563 ν(C=N), 1001 ν(N-N). ESI-Mass (m/z): 1178.04.

2.10 Synthesis of complex $[(L)Cu(H_2O)(2\text{-}MeBenzImH)(H_2O)Cu(L)](2\text{-}MeBenzImH)_3$ 9

To a well-stirred solution (10 mL) of ligand (0.274 g, 1 mmol) was added $CuCl_2.2H_2O$ (0.174 g, 1 mmol) in methanol (10 mL) while stirring. To this reaction mixture, 2-methyl benzimidazole (0.264 g, 2 mmol) dissolved in KOH (0.056 g, 4 mmol) was added drop-wise and the resulting reaction mixture was refluxed for 1 hrs. After refluxing for 1 hrs, the resulting solution was cooled at room temperature. After one weak brown solid was filtered, washed with methanol and dried in a calcium chloride desiccator.

Yield: ~ 74%. Anal. Calc. for $C_{66}H_{63}Cu_2N_{16}O_2$ (1239.43 g mol^{-1}): C, 63.96; H, 5.12; N, 18.08%. Found: C, 63.93; H, 5.10; N, 18.06%. FTIR bands (KBr, cm^{-1}): 1563 ν(C=N), 1002 ν(N-N). ESI-Mass (m/z): 1235.04.

2.11. Methods and physical measurements

Elemental analyses were carried out using an Elementar Vario EL III Carlo Erba 1108 Analyzer. NMR spectrum of the ligand was recorded in DMSO-d_6 on a Bruker Advance 400

(FT-NMR) multinuclear spectrometer. Chemical shifts were reported in parts per million (ppm) using tetramethylsilane (TMS) as an internal standard. The accelerating voltage was 10 kV and the spectra were recorded at room temperature. UV-Vis spectra were recorded at room temperature using a Shimadzu UV-Vis Spectrophotometer UV-1601 in quartz cells. Infrared (IR) spectra (4000-400cm^{-1}) were collected using the KBr pellet technique on a Perkin-Elmer spectrophotometer. The low and room temperature electron paramagnetic resonance (epr) spectra were recorded using a Varian E-line Century Series Spectrometer equipped with a dual cavity and operating at the X-band with 100 kHz modulation frequency. Varian quartz tubes were used for measuring epr spectra of polycrystalline samples and frozen solutions. The epr spectra were calibrated with tetracyanoethylene (TCNE) as a marker (g = 2.00277). The epr parameters for copper(II) complexes were determined accurately from a computer simulation program19. Cyclic voltammetry was performed using a BAS-100 Epsilon Electrochemical Analyzer on complexes in DMSO solutions using Ag/AgCl and glassy carbon as reference electrodes. All measurements were carried out at room temperature under a nitrogen atmosphere. The solutions were 10^{-3} mol dm^{-3} in the complex and 0.1 mol dm^{-3} in tetrabutylammonium perchlorate (TBAP) as a supporting electrolyte. Ferrocene (Fe) was added to the solution as an internal standard. ESI Mass spectrometry was recorded on a XEVO G2-XS QTOF.

2.12. Computational study

Theoretical calculations by density functional theory (DFT) were performed regarding molecular structure optimization and HOMO-LUMO energies etc. of complexes **1** and **2**. Full geometry optimizations were carried out using the density functional theory (DFT) method at the B3LYP level for the complex [41]. All DFT calculations were carried out starting from the experimental single-crystal X-ray data as input geometries. All elements except Cu were assigned the LANL2DZ basis set [42]. LANL2DZ with effective core potential for Cu atom was used [43]. In the computational model, the cationic complex was taken into account. All calculations were carried out with the GAUSSIAN09 program,[44] with the aid of the Gauss View visualization program. Vertical electronic excitations based on B3LYP optimized geometries were evaluated using the time-dependent density functional theory (TDDFT) formalism [45] in DMSO, using a conductor-like polarizable continuum model (CPCM) [46].

2.13. Antioxidant SOD activity

The antioxidant SOD activities of complexes **1-9** were assessed using alkaline DMSO as a source of superoxide radical ($O_2^{\cdot -}$) and nitro blue tetrazolium chloride (NBT) as scavengers [47-49]. The quantitative reduction of NBT to formazan by $O_2^{\cdot -}$ was followed spectrophotometrically at 450 nm. The SOD activity was obtained by plotting the percentages of inhibition NBT reduction (%) *vs* the concentrations of complexes. The unit of SOD activity is the concentration of the enzyme or complex that induces 50% inhibition (IC_{50}) in the reduction of NBT. Two assays were carried out for each concentration of the metal complex.

3 Results and discussion

3.1 Synthesis and characterization

The tridentate hydrazone ligand (L) has been used for the synthesis of homobinuclear complexes of copper(II) using inorganic salts. This tridentate NNN donor ligand (L) was synthesized by the reported method [50]. The synthetic routes of ligand (L) and its complexes are given in Scheme 1-3.

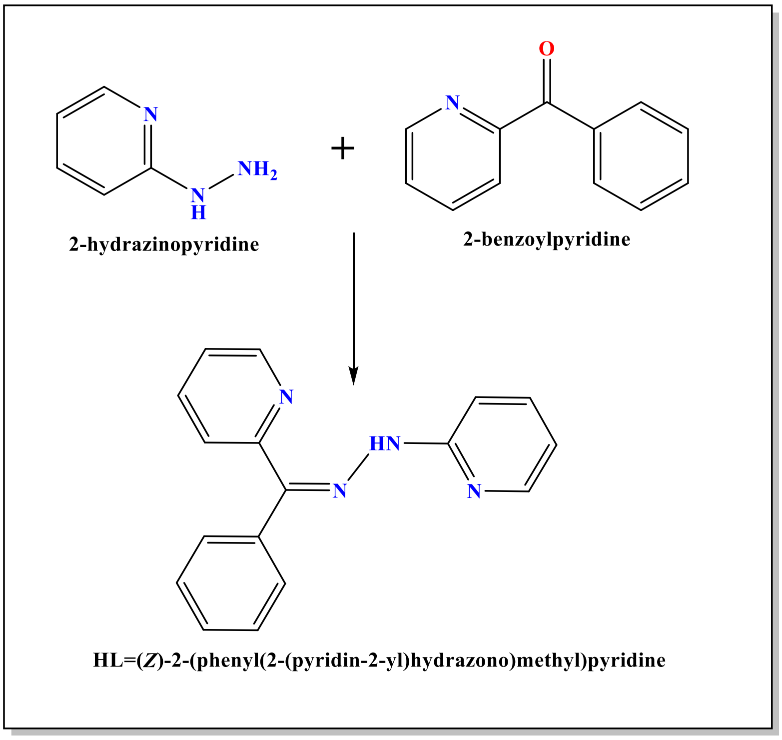

Scheme 1 Synthetic route of hydrazone ligand (L).

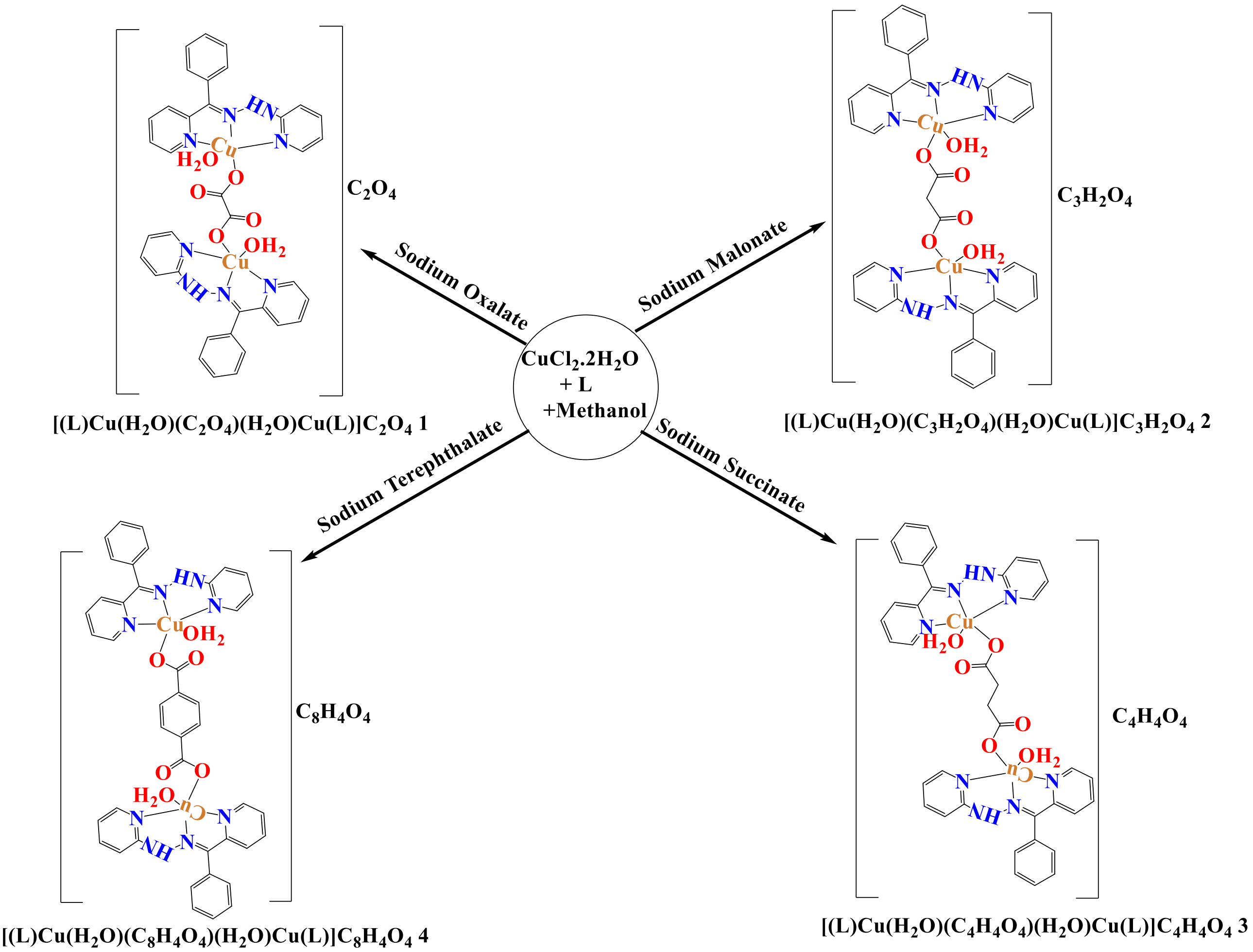

Scheme 2 Synthetic route of complexes **1-4**.

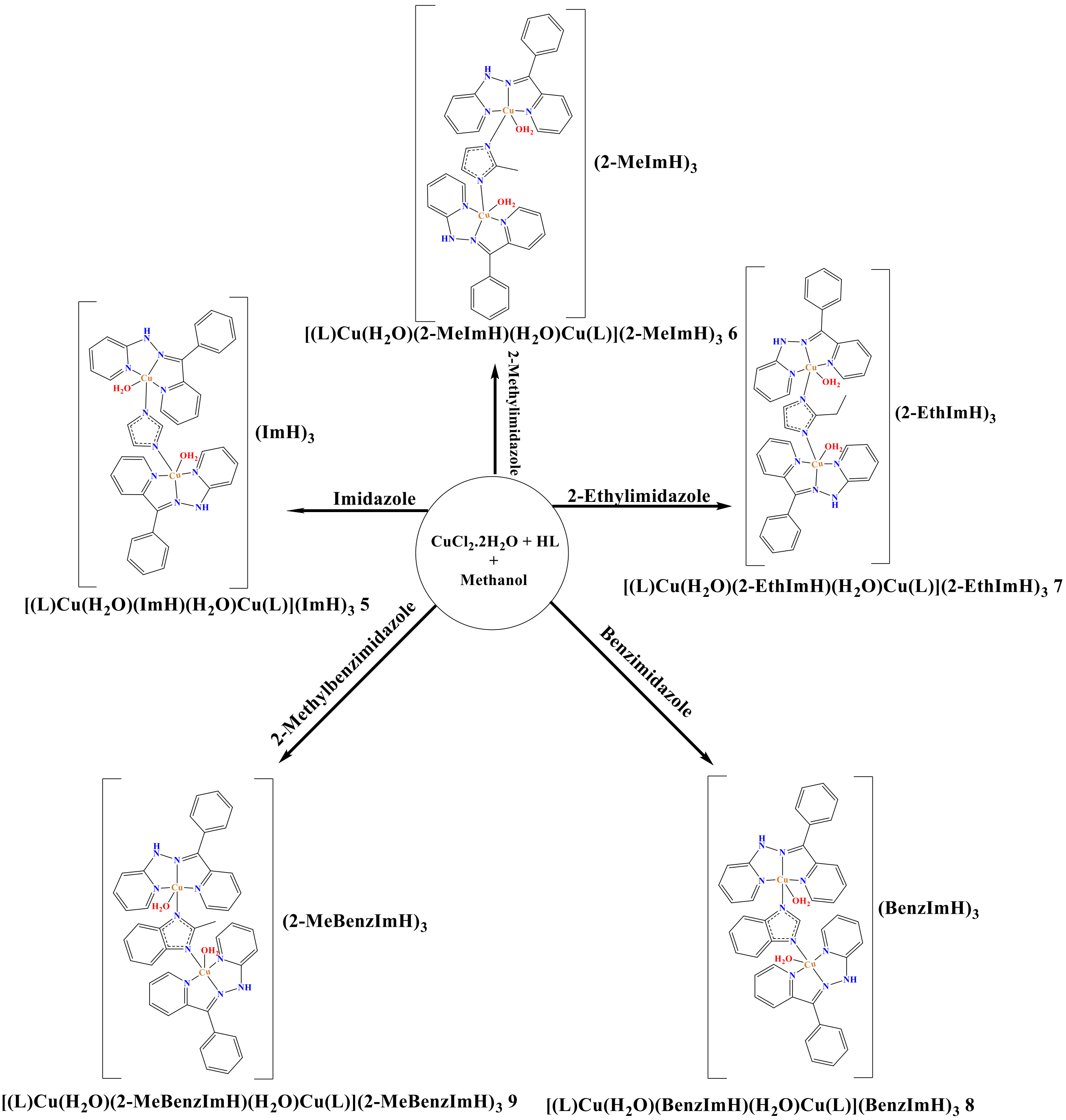

Scheme 3 Synthetic route of complexes **5-9**.

The structural formula of these complexes (**1-9**) is based on elemental analysis, spectroscopic FTIR, UV-Vis and epr data. The NMR spectra of the ligand are discussed in detail in this chapter part (A) section. However, crystals for X-ray analysis of complexes (**1-9**) could not be isolated even by recrystallization efforts. These complexes are air-stable. The solubility of all the nine synthesized complexes in DMF and DMSO is very high while partially soluble in $CHCl_3$ and CH_2Cl_2 and insoluble in water.

3.2 Molar conductance

The molar conductance of complexes **1-9** was performed in a DMSO solution of 10^{-3} M to check the electrolytic behavior of complexes. The molar conductance value of these complexes is in the range of 112-260 Ω^{-1} cm^2 mol^{-1} revels that complexes are highly electrolytic [51]. The molar conductance value of complexes is given in Table 1.

Table 1 Molar conductance value of complexes **1-9.**

Compound	Λ (Ω^{-1} cm^2 mol^{-1})
1	120.34
2	130.45
3	119.24
4	112.45
5	200.60
6	230.68
7	260.20
8	260.76
9	245.89

3.3 FTIR spectroscopy

An FTIR spectral study of all nine copper(II) was performed to get a basic idea about the coordination sites of the ligand and the compared with that of metal complexes and the peaks which have been changed due to complexation with metal ion is interpreted. In FTIR spectra of ligand and complexes, we observed some important bands and their shifting upon complexation. In the spectra of the free ligands, bands at 3084, 1592 and 988 cm^{-1} are attributed to ν(NH), ν(C=N) azomethine and ν(N-N) respectively [50, 52]. In complexes, the shifting of the azomethine band towards the lower frequency region is observed. The new position of the azomethine group in complexes is in the range 1533-1592 cm^{-1}. The observed band for the ν(C=O) stretching vibration of the carboxylate in the complexes (**1-4**) at ~1603-1625 cm^{-1} is characteristic for a monodentate bridging mode of the carboxylic group of the co-ligands in complexes **1-4**. In all complexes, the coordinated water molecule is observed in the range of 3107-3442 cm^{-1}. In all complexes, some non-ligand bands were observed at 418-542 and 411-479 cm^{-1} due to ν(Cu-O) and ν(Cu-N) respectively [50, 53]. The FTIR spectra of complexes **1-9** along with Table 2 are shown in Fig. 1-9.

Table 2 Some important bands of FTIR spectra of complexes **1-9**.

Compounds	ν(NH)	ν(OH)	ν(>C=O)	ν(>C=N)	ν(N-N)	ν(Cu-O)	ν(Cu-N)
HL	3084			1592	988		
1		3289	1613	1578	1068	472	419
2		3233	1625	1533	1089	542	479
3		3107	1603	1580	1026	542	479
4		3061	1612	1545	1108	435	419
5		3424		1564	1003	466	419
6		3442		1564	1004	467	419
7		3425		1564	1002	464	419
8		3408		1563	1001	418	411
9		3421		1563	1002	418	411

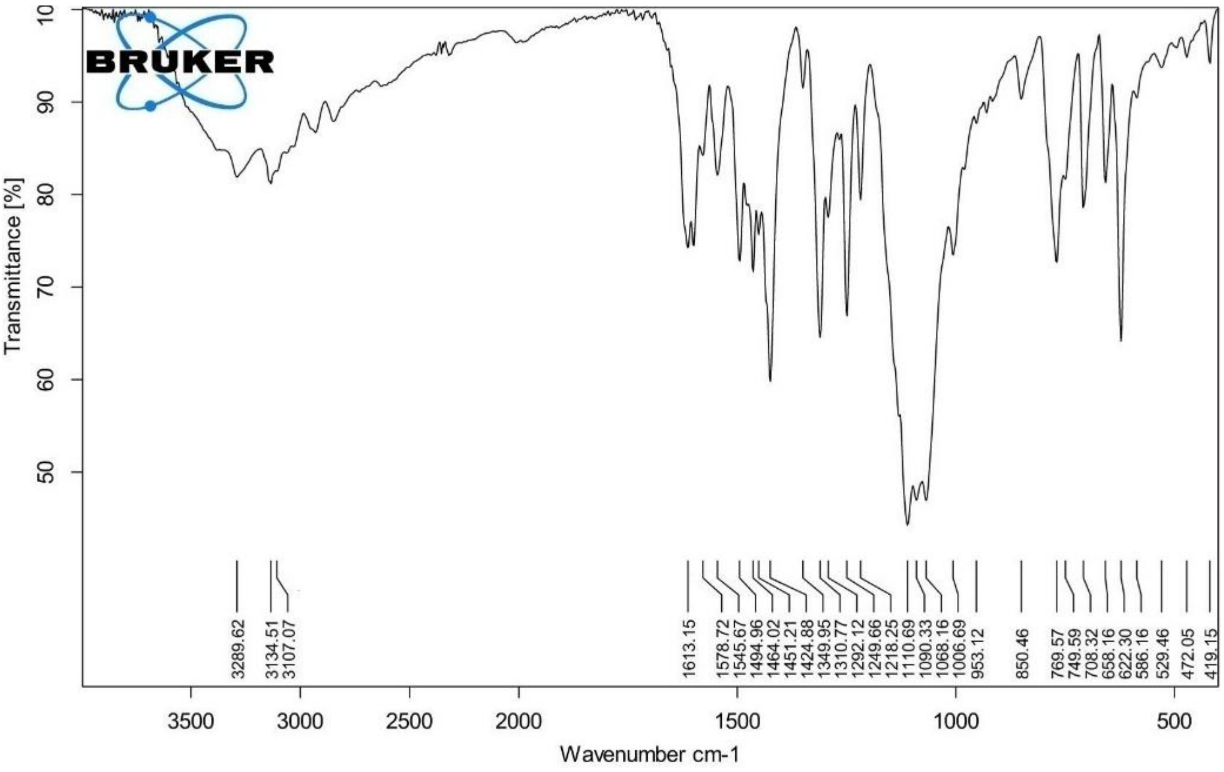

Fig. 1. FTIR spectrum of complex **1**.

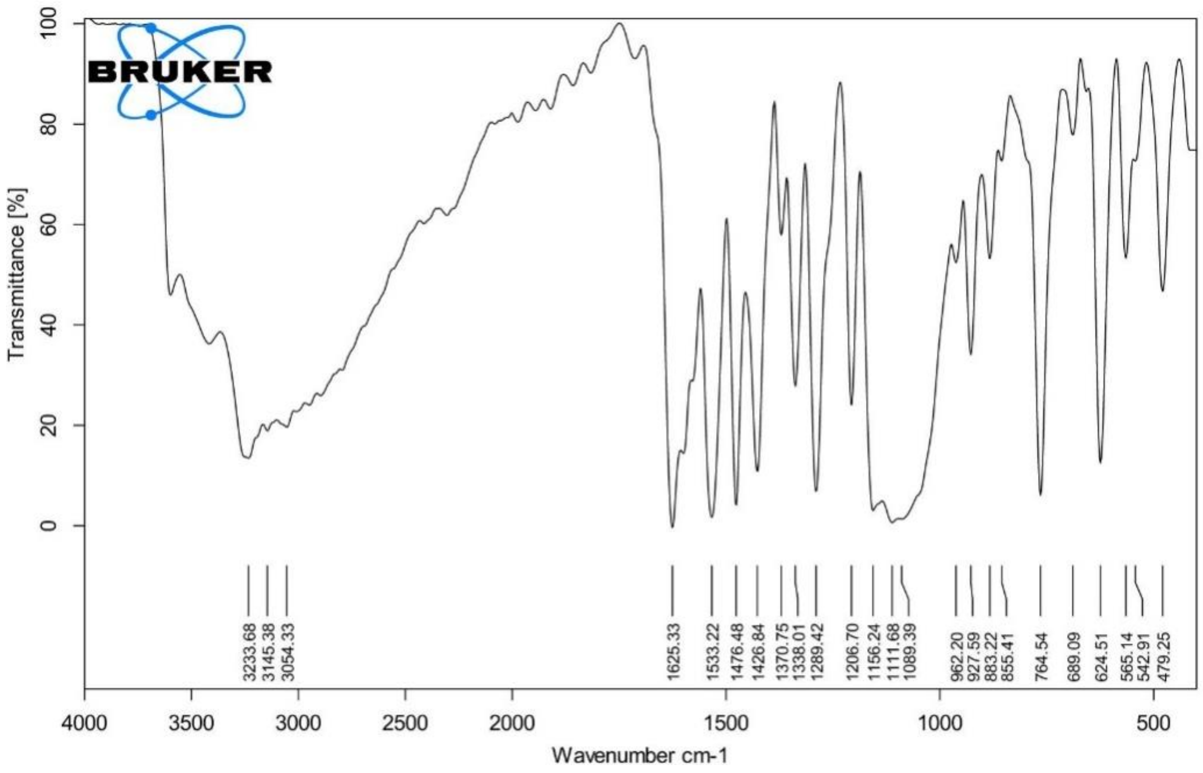

Fig. 2. FTIR spectrum of complex **2**.

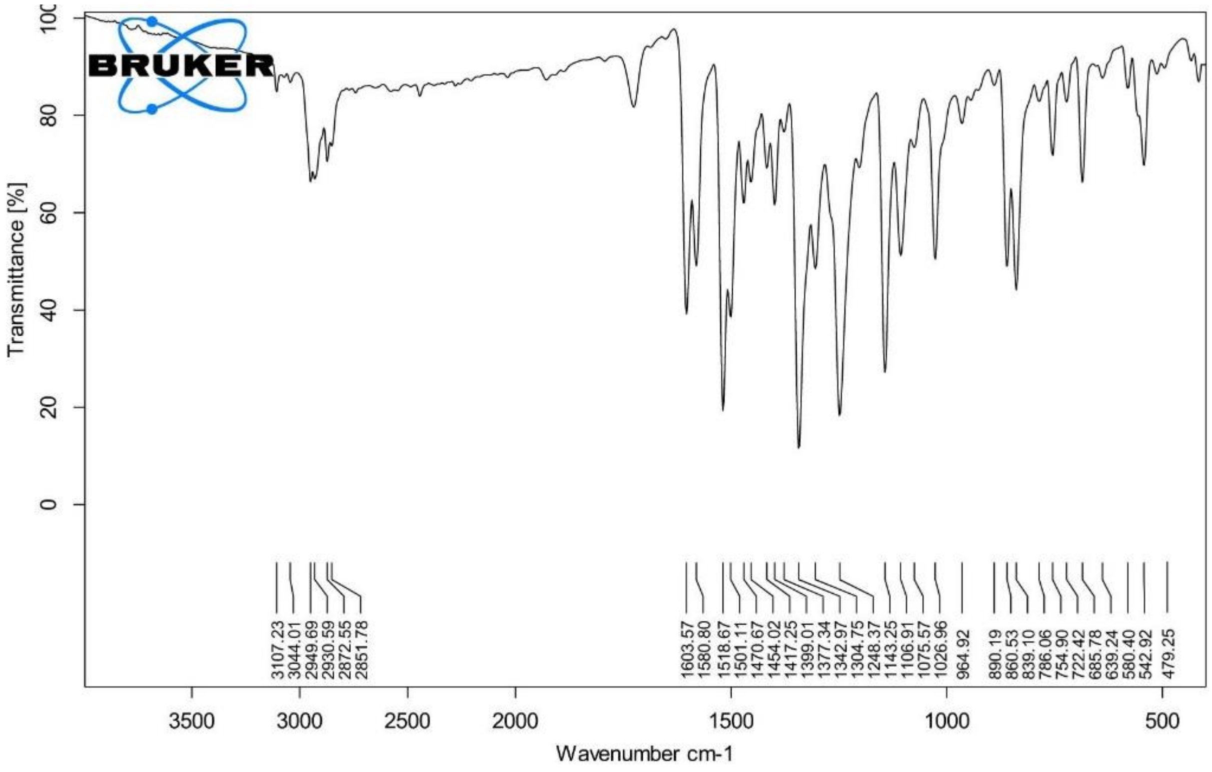

Fig. 3. FTIR spectrum of complex **3**.

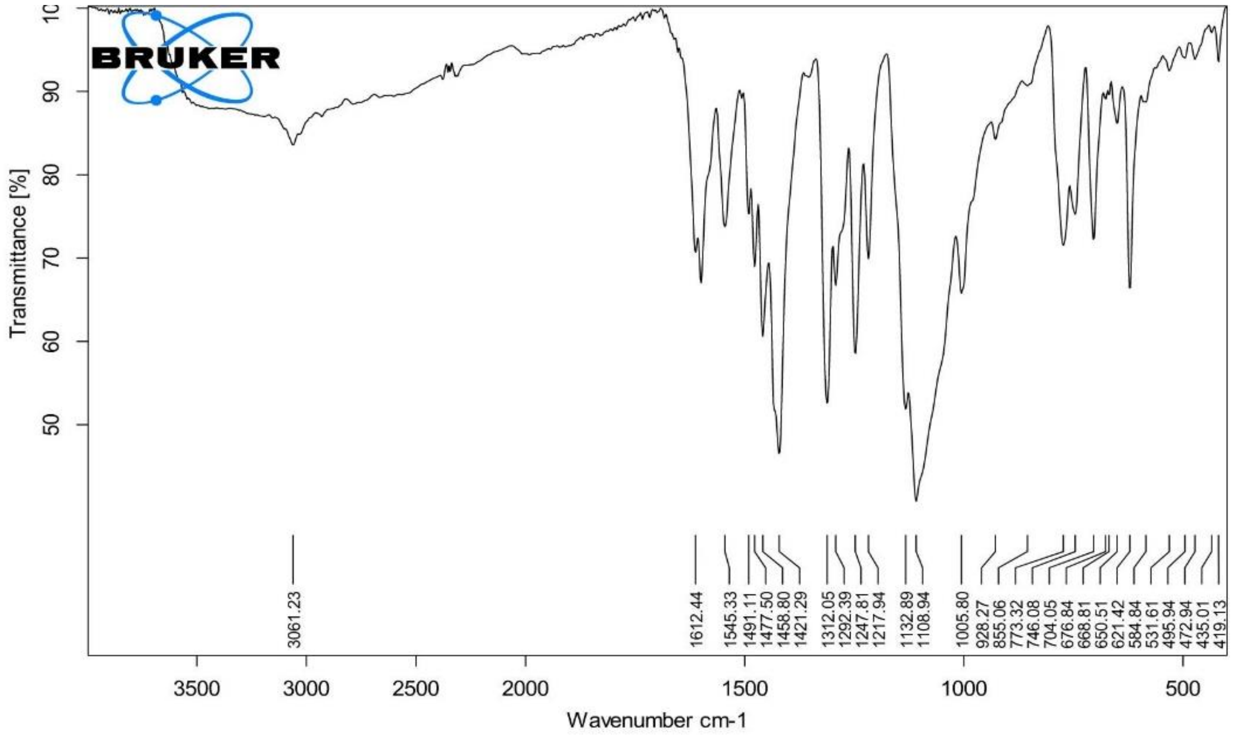

Fig. 4. FTIR spectrum of complex **4**.

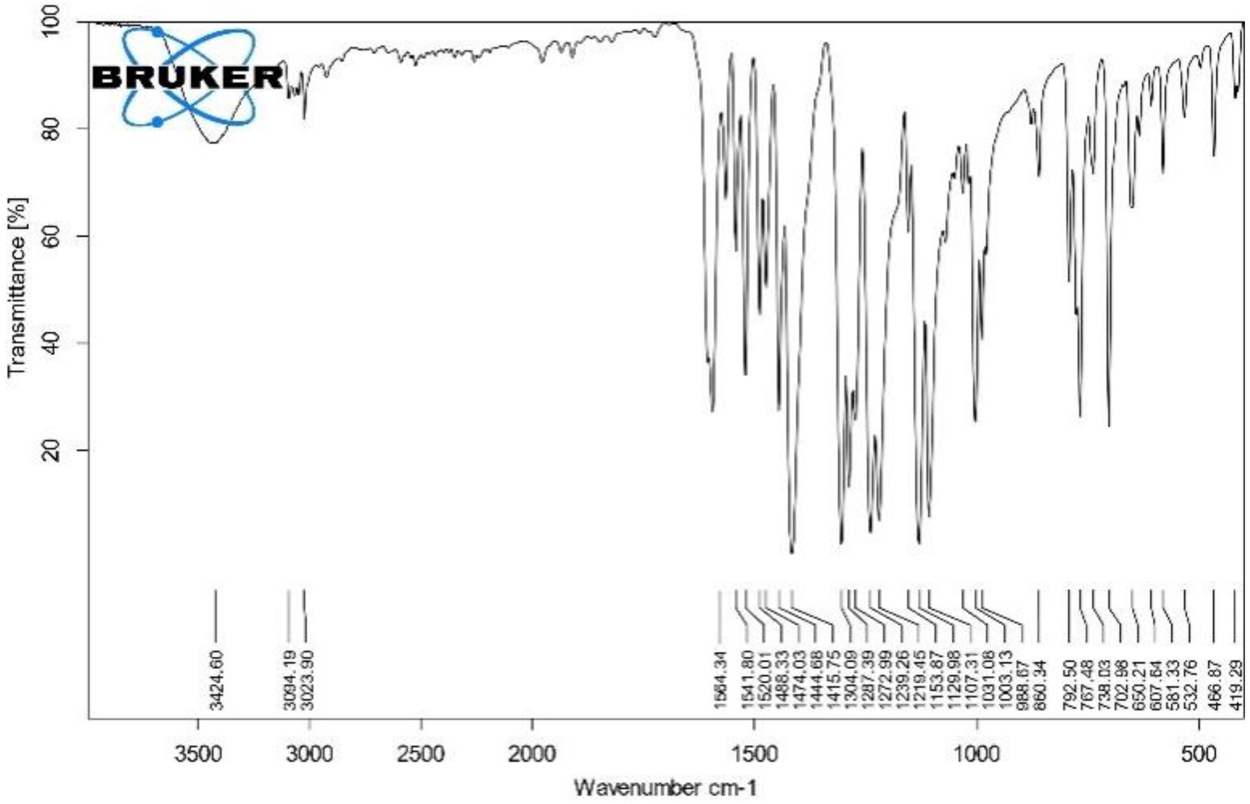

Fig. 5. FTIR spectrum of complex **5**.

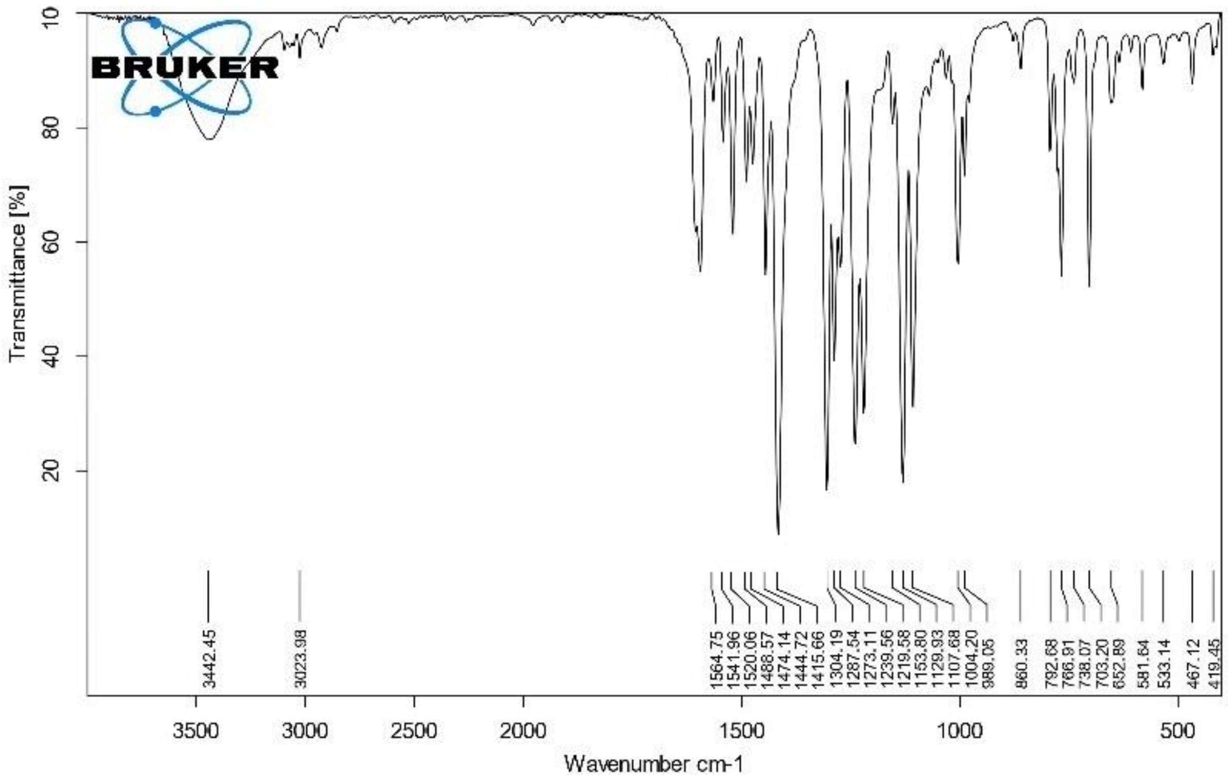

Fig. 6. FTIR spectrum of complex **6**.

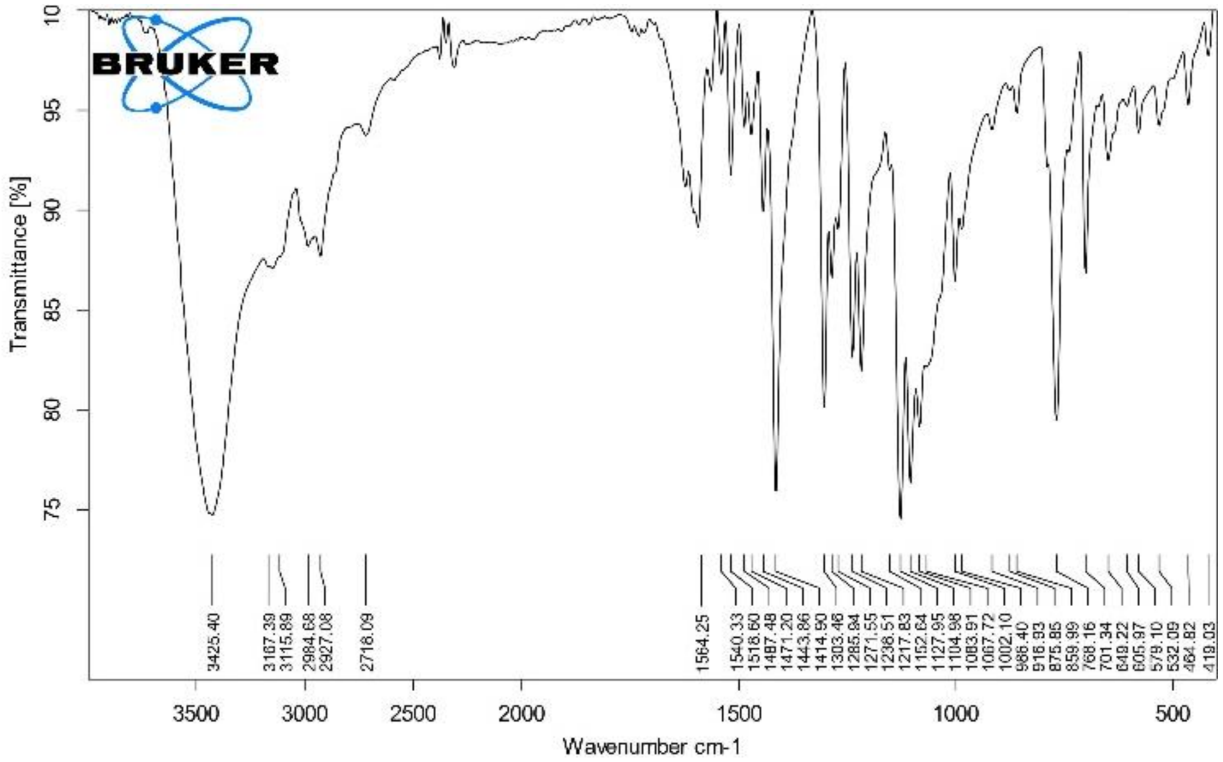

Fig. 7. FTIR spectrum of complex **7**.

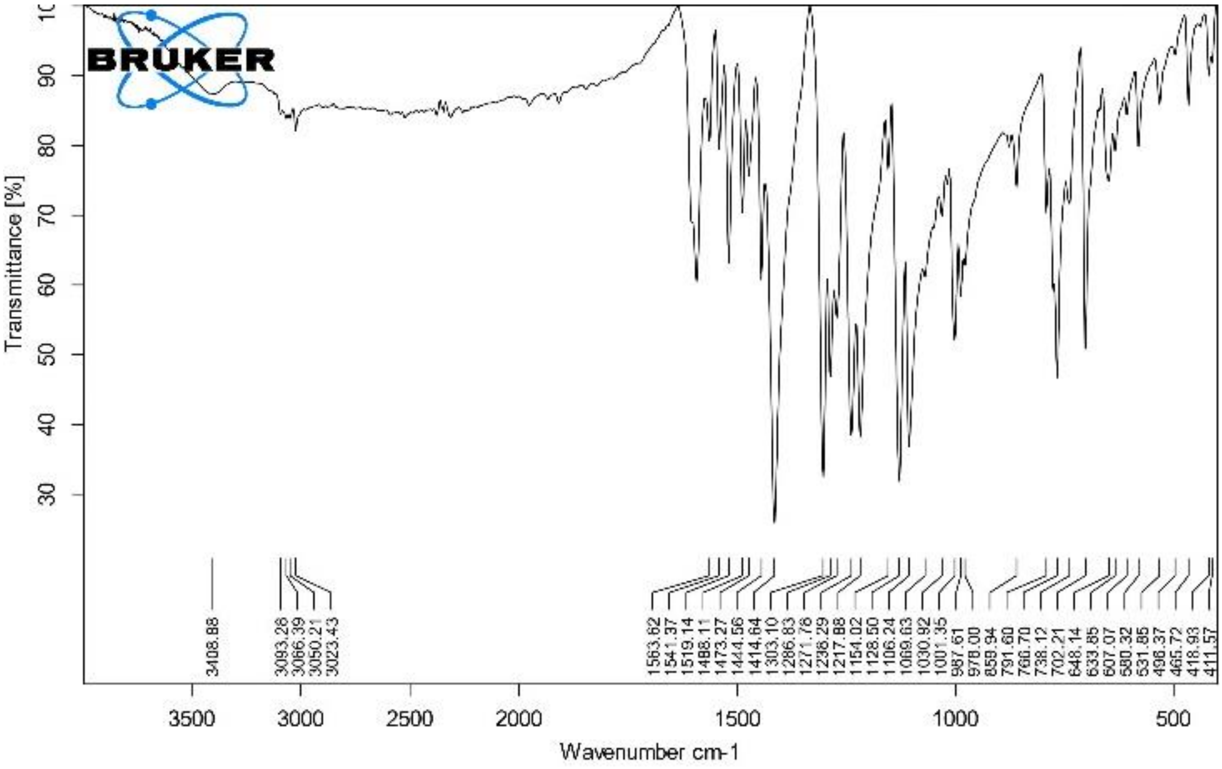

Fig. 8. FTIR spectrum of complex **8**.

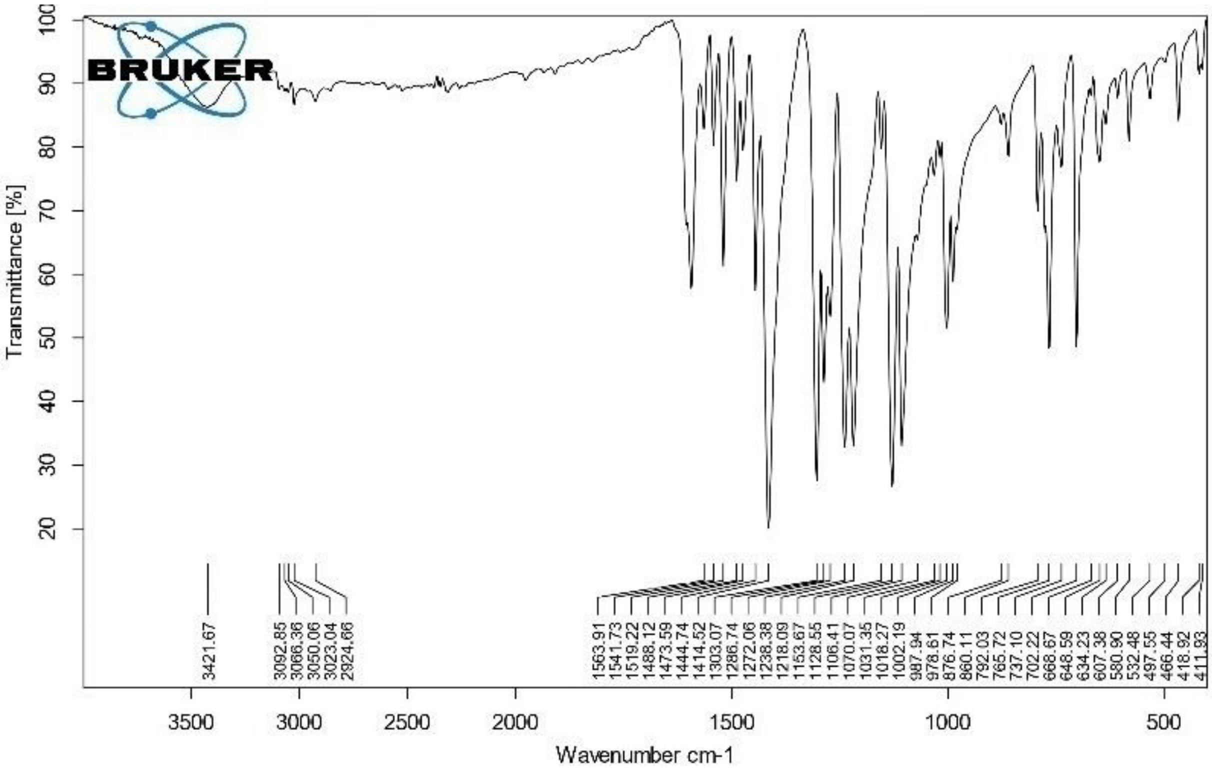

Fig. 9. FTIR spectrum of complex **9**.

3.4 Electronic spectra

The electronic spectra of copper(II) complexes **1-9** were recorded in DMSO (1.0×10^{-3}M). UV visible spectra are shown in Fig. 10 and 11. in the wavelength range 300-1000 nm, three main absorptions are observed. The electronic data of these complexes are in good agreement with their geometrics (Table 3). The absorption band at ~ 488 nm is due to ligand to metal charge transfer (LMCT) transition. Much weaker, less defined shoulders are found at the visible region fall below 700 nm and are more persistent with copper(II) complexes [52]. The bands in the higher energy UV-region (322-379 nm), for the complexes, are likely to be due to ligand-centered transitions [53]. The low energy band (d-d band) position of all complexes is in accordance with a square pyramidal coordination sphere around the Cu(II) centre [54].

Table 3 The electronic absorption spectral dataλ_{max} (nm) of **1-9** in DMSO (1.0×10^{-3}M).

Compound	$\pi - \pi^*$	$d_{xz}, d_{yz} \rightarrow d_{x^2-y^2}$	$d_{xy} \rightarrow d_{x^2-y^2}$
1	379	486	701
2	377	486	701
3	325	485	704
4	378	486	702
5	325	490	ill-defined
6	325	491	ill-defined
7	324	491	ill-defined
8	325	491	ill-defined
9	322	491	725

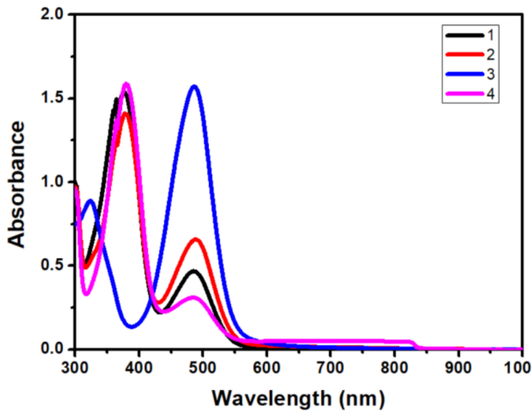

Fig. 10(a) Absorption spectra of 1.0 × 10^{-3} M DMSO solution of complexes **1-4.**

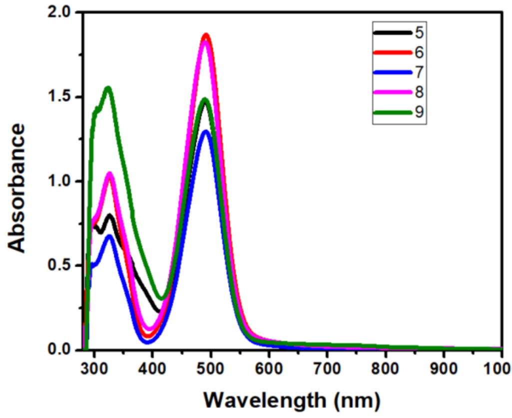

Fig. 10(b) Absorption spectra of 1.0 × 10^{-3} M DMSO solution of complexes **5-9**.

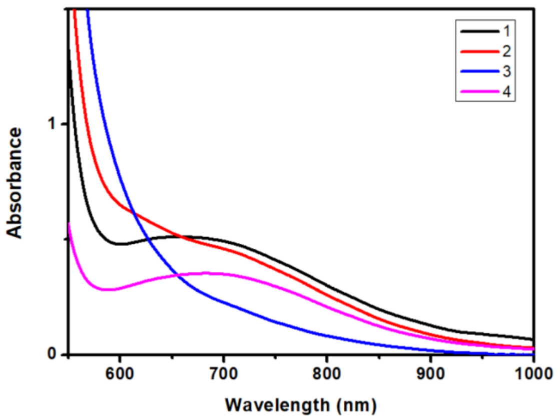

Fig. 11(a) Visible absorption spectra of complexes **1-4.**

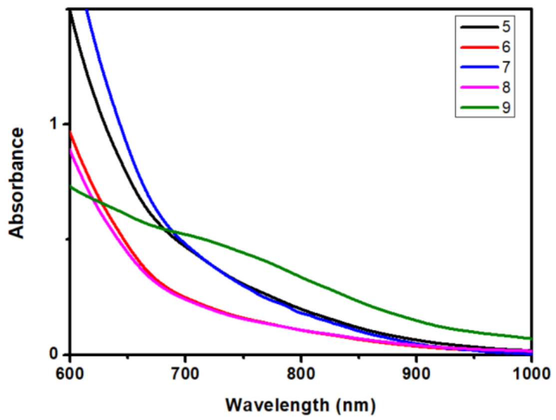

Fig. 11(b) Visible absorption spectra of complexes **5-9**.

3.5 Epr spectral study

Epr spectra of complexes **1-9** in the polycrystalline state were measured at room temperature and low temperature (liquid nitrogen temperature) of DMSO solutions were also measured. The epr parameters are collected in Table 4. The epr spectra show the epr spectral features typical of those for dimeric complexes with axial symmetry [55] for which

$$\mathcal{H} = g\beta H + D(S_{z^2} - 2/3)$$

where S = 1 and the used symbols have their usual meaning. The value of the zero-field splitting parameter (D) is in the range of 0.015-0.032 cm^{-1}. The value is almost similar to those reported in the literature [56-58]. The room temperature polycrystalline epr spectra throw insight into the coordination environment around copper(II) centres in present binuclear complexes. They exhibit normal tetragonal copper(II) environment with $g_{\parallel}$ and $g_{\perp}$ epr features. These epr spectra are shown in Fig. 12-20. These epr spectra are typically axial with well-defined $g_{\parallel}$ and $g_{\perp}$ epr features. The $g_{\parallel}$ value of these complexes is less than 2.3. The less value of 2.3 indicating approximate covalent character in copper-Ligand (Cu-L) bonding [59]. The geometric parameters (G) of these complexes were also estimated. This parameter is also known as the exchange parameter which is a measure of the exchange interaction between the copper centres in polycrystalline. The calculated value of G is less than 4 in all complexes, showing exchange interaction [60]. The trend in g tensor values are $g_{\parallel} > g_{\perp} > 2.0023$ which is expected with a $d_{x^2-y^2}$ ground state in a square planar or square pyramidal geometry [61-64]. In epr spectra of all complexes in the polycrystalline state, a relatively weak signal was seen at the half field of the resonance field ($\Delta M_s = \pm 2$), thus indicating unequivocal proof of the presence of triplet state S = 1 in the polycrystalline state. Although, seven-line hyperfine features are absent in the low field region.

The low temperature of epr spectra of present complexes is resolved quartet hyperfine lines in DMSO solutions. Although fourth $g_{\parallel}$ component merged with $g_{\perp}$ features in all low-temperature solution epr spectra. These hyperfine lines resolved due to the corresponding coupling of the electron spin with the nuclear spin I = 3/2 for copper nuclei. The $g_{\parallel}$ values of all complexes are nearly identical revealing that the bonding is controlled by the hydrazone moiety of the complexes. Also, $g_{\parallel} > g_{\perp}$ values indicate the distorted square pyramidal geometry around each copper(II) centre [65, 66]. These values are consistent with a mononuclear copper(II) species in solution [67-69]. The presence of mononuclear species in solutions reveals the dissociation of the binuclear complex into mononuclear one in DMSO.

Table 4 Epr spectral parameters of copper(II) complexes **1-9**.

Epr parameters	1	2	3	4	5	6	7	8	9
Polycrystalline state(298 K)									
$g_{\parallel}$	2.248	2.171	2.097	2.177	2.158	2.150	2.166	2.154	2.170
$g_{\perp}$	2.079	2.045	2.045	2.073	2.046	2.045	2.045	2.047	2.047
G	3.203	3.950	2.239	2.471	3.680	3.459	3.833	3.512	3.751
D(cm^{-1})	0.027	0.018	0.018	0.032	0.016	0.015	0.018	0.017	0.018
DMSO(77 K)									
$g_{\parallel}$	2.233	2.179	2.199	2.222	2.181	2.189	2.179	2.178	2.172
$g_{\perp}$	2.066	2.051	2.057	2.066	2.066	2.050	2.055	2.065	2.072
$A_{\parallel}$	155	167	175	160	160	163	165	172	169

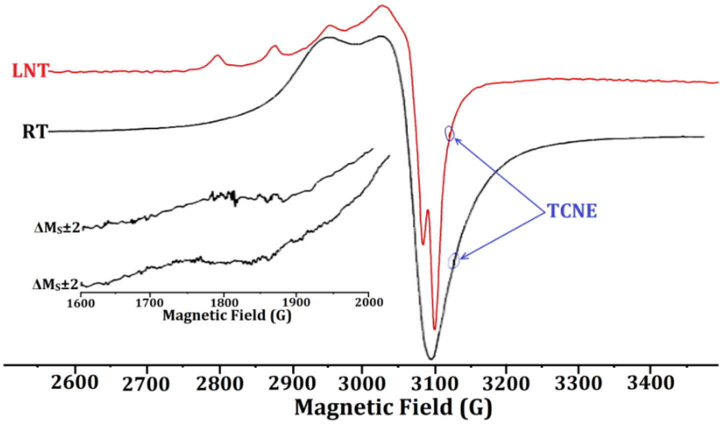

Fig. 12. EPR spectra of complex **1**.

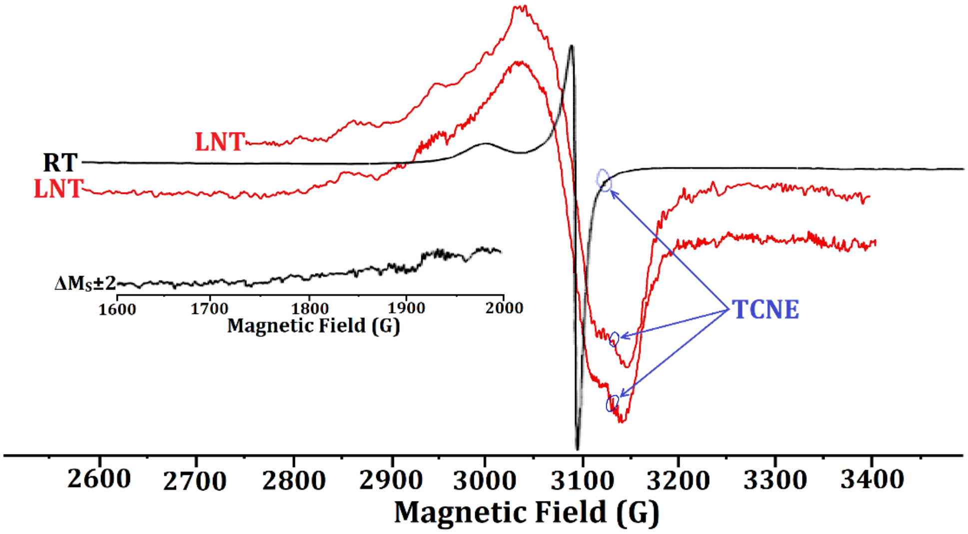

Fig. 13. EPR spectra of complex **2**.

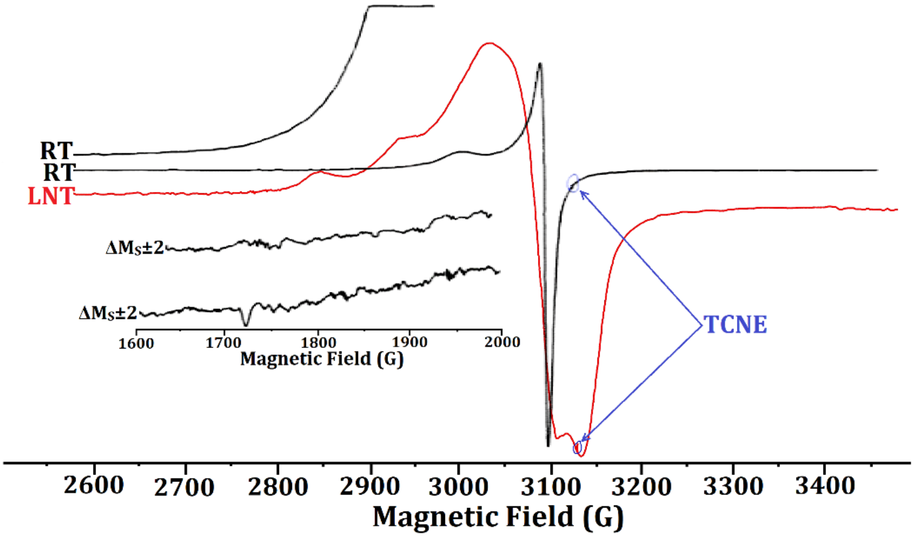

Fig. 14. EPR spectra of complex **3**.

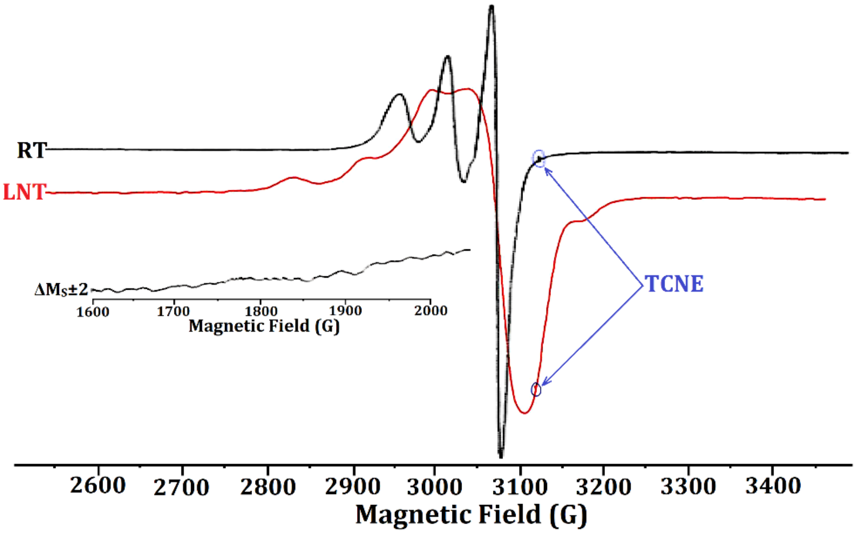

Fig. 15. EPR spectra of complex **4**.

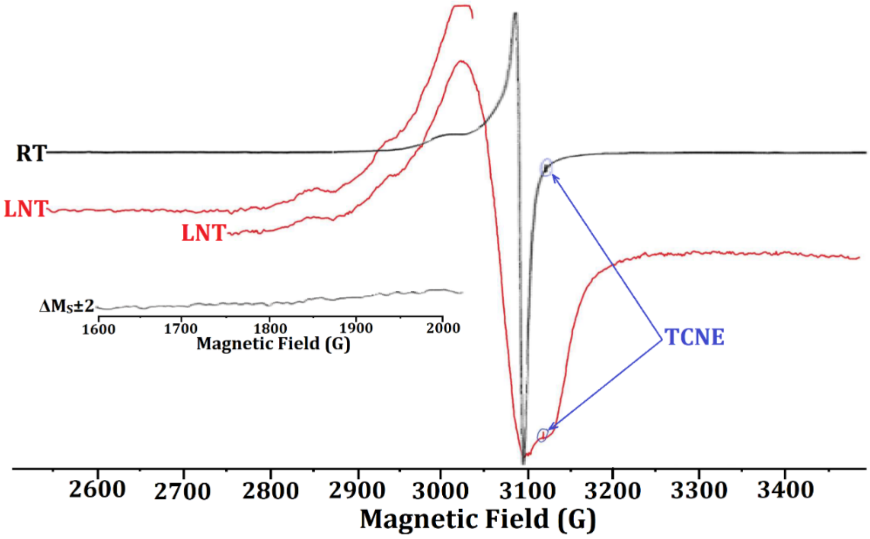

Fig. 16. EPR spectra of complex **5**.

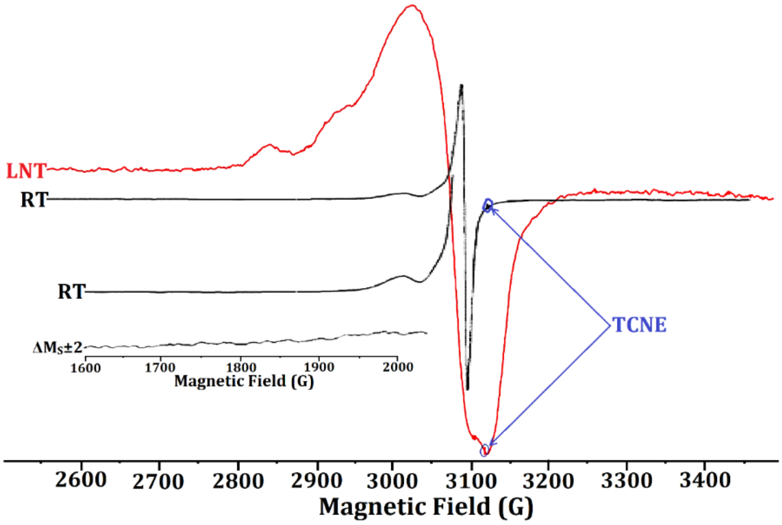

Fig. 17. EPR spectra of complex **6**.

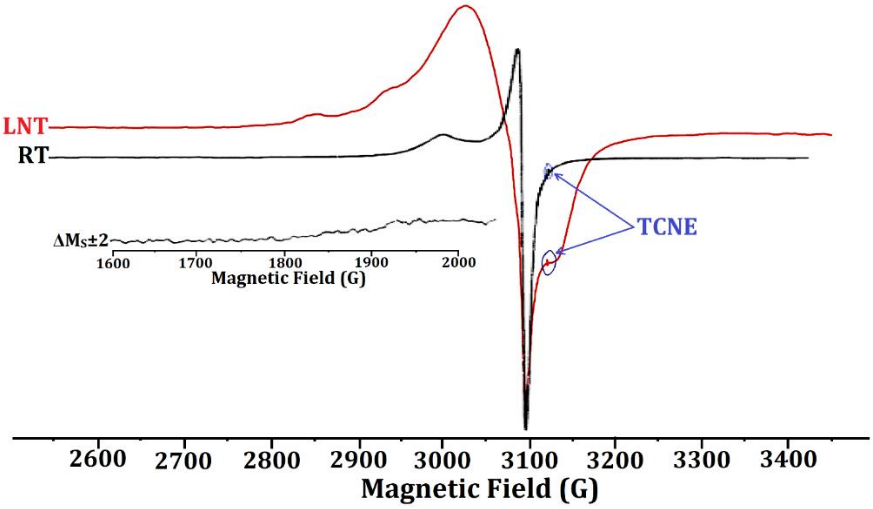

Fig. 18. EPR spectra of complex **7**.

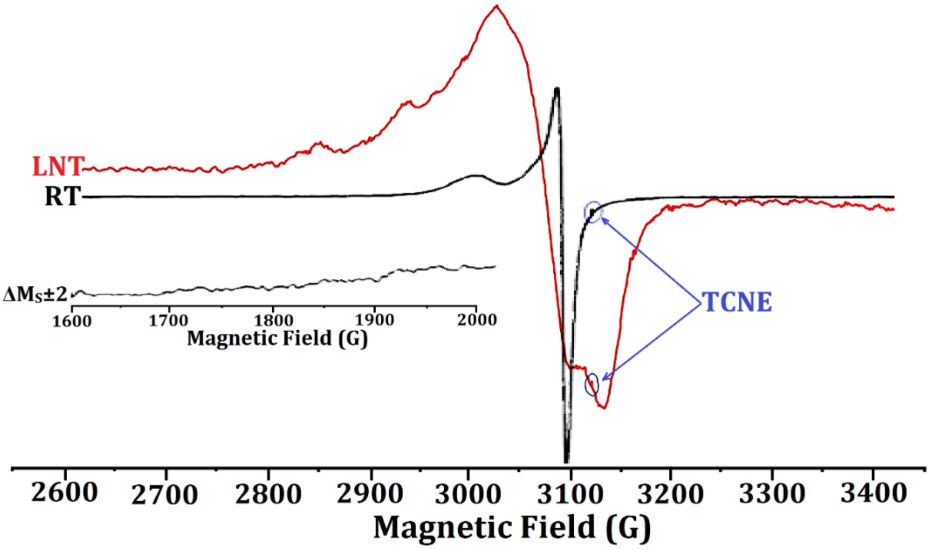

Fig. 19. EPR spectra of complex **8**.

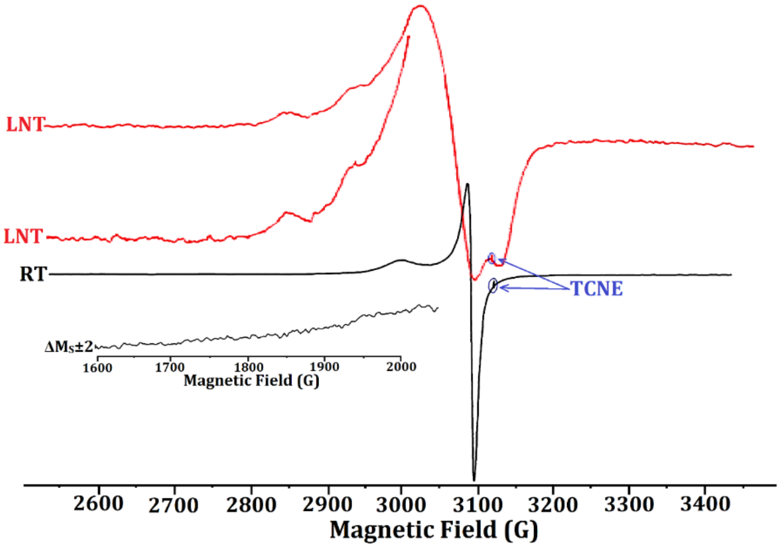

Fig. 20. EPR spectra of complex **9**.

3.6 Electrochemistry

The redox behaviour of complexes **1-9** has been explored using cyclic voltammetry (CV) and differential pulse voltammetry (DPV). The cyclic voltammograms of complexes (1.0×10^{-3} M) in DMSO were recorded with tetrabutylammonium perchlorate (TBAP) as the supporting electrolyte in the potential range 0.3 to -1.8 V versus Ag/AgCl. The voltammograms are shown in Fig. 21 & 22, parameters are collected in Table 5. Fig. 21 & 22 shows cyclic voltammograms of these complexes **1-3**, **6** and **7** which reveal one reversible wave due to Cu(II)/Cu(I) redox couple. The CV of the remaining **4**, **8** and **9** show two redox processes. The values of the half-wave potential of the two redox processes and conproportionation constant k_{con} magnitudes of the relative stability of mixed valent $M^{II}\ M^{I}$ species [70]. These quasireversible redox processes correspond to the $Cu(II)\ Cu(II) \xrightarrow{+\ 1e^-} Cu(II)\ Cu(I)$ and $Cu(II)\ Cu(I) \xrightarrow{+\ 1e^-} Cu(I)\ Cu(I)$. The stability of mixed valent species $Cu^{II}Cu^{I}$ conproportionation constant K_{con} for $Cu^{II}\ Cu^{I} + Cu^{I}\ Cu^{I} \rightleftharpoons 2Cu^{II} + Cu^{I}$ has also been determined electrochemically. The value of K_{con} depends on the separation between the potentials of the couple.

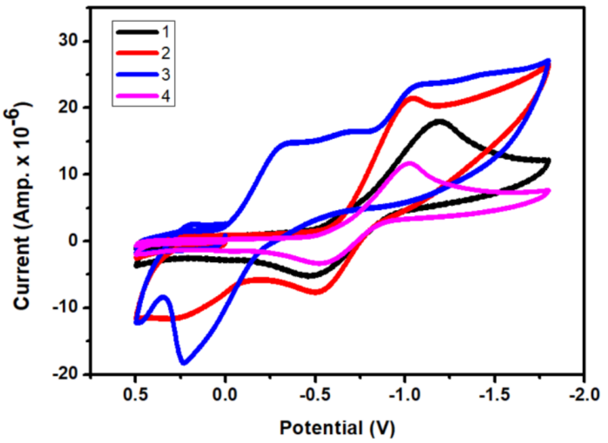

Fig. 21(a) Cyclic voltammograms of complexes **1-4**.

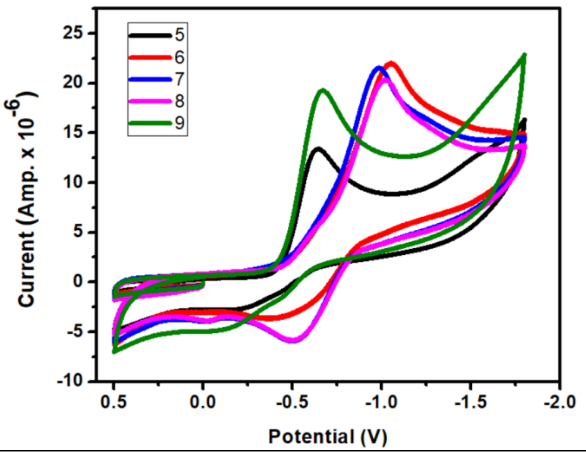

Fig. 21(b) Cyclic voltammograms of complexes **5-9**.

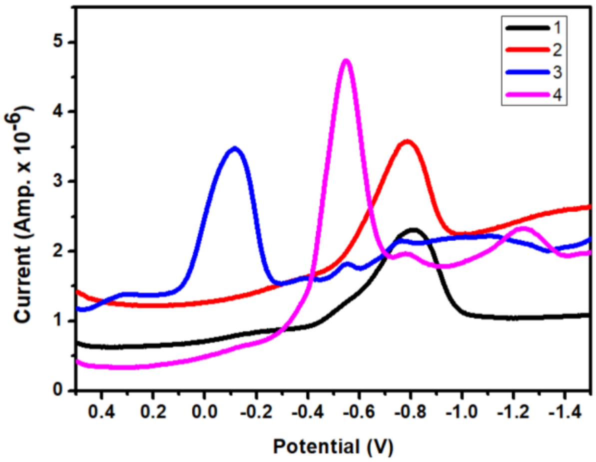

Fig. 22(a) Differential pulse voltammograms of complexes **1-4**.

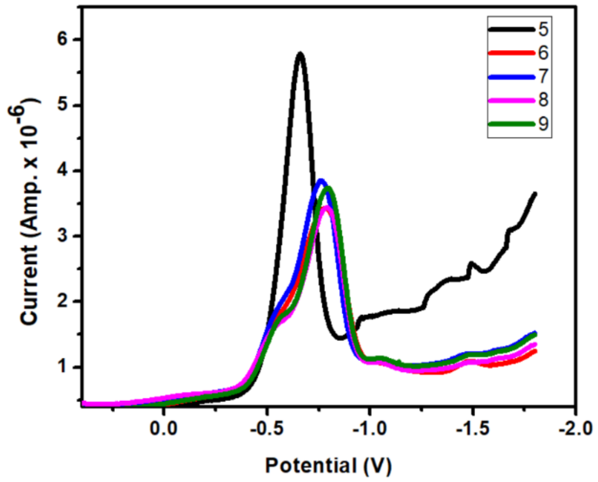

Fig. 22(b) Differential pulse voltammograms of complexes **5-9**.

Table 5 Summary of electrochemical in (V) data **1-9**.

Compound	E_{pc1}	E_{pc2}	E_{pa1}	E_{pa2}	DE_{pc1}	DE_{pc2}	ΔD_{pc}	$E_{1/2}^{1}$	$E_{1/2}^{2}$	$\Delta E_{1/2}$	K_{con}
1	-1.174		-0.475		-0.846			-0.824			
2	-1.067		-0.470		-0.801			-0.768			
3	-0.923		-0.299		-0.779			-0.611			
4	-0.315	-1.041	+0.240	-0.281	+0.324	-0.113	0.437	-0.034	-0.661	0.661	3.948×10^{10}
5	-0.635		-0.031		-0.655			-0.333			
6	-1.030		-0.411		-0.523	-0.774	0.251	-0.720			
7	-0.982		-0.502		-0.528	-0.758	0.230	-0.742			
8	-0.608	-1.025	-0.038	-0.491	-0.534	-0.79	0.256	-0.323	-0.758	0.435	2.248×10^{7}
9	-0.651	-0.993	-0.038	-0.534	-0.576	-0.790	0.214	-0.344	-0.763	0.419	1.205×10^{7}

The differential pulse voltammetric (DPV) is a good electrochemical technique for detecting reduction peak potentials; provide the peak potentials differ in their formal potential by more than 0.18 V [39]. The differential pulse voltammograms of present complexes are shown in Fig. 22(a) and 22(b). The results of DPV experiments are similar to that of CV results. For complexes **4**, **8** and **9** conproportionation constant K_{con} is estimated using the equation, $\log K_{con} = 16.9\ (\Delta E_{1/2})$ [70, 71]. The value of K_{con} of these complexes was found to be large. The large values reveal that the addition of a second electron is more difficult than of first electron and the mixed-valence species is stable concerning K_{con}. The results are comparable to earlier reported bridged di-copper(II) complexes [72-77].

3.7 ESI-Mass spectra

The ESI-Mass spectra of complexes were recorded to get the information of the molecular mass of the complexes. The ESI-Mass spectra of all complexes were performed in positive mode only. The mass spectra of complexes are given in Fig. 23-31.

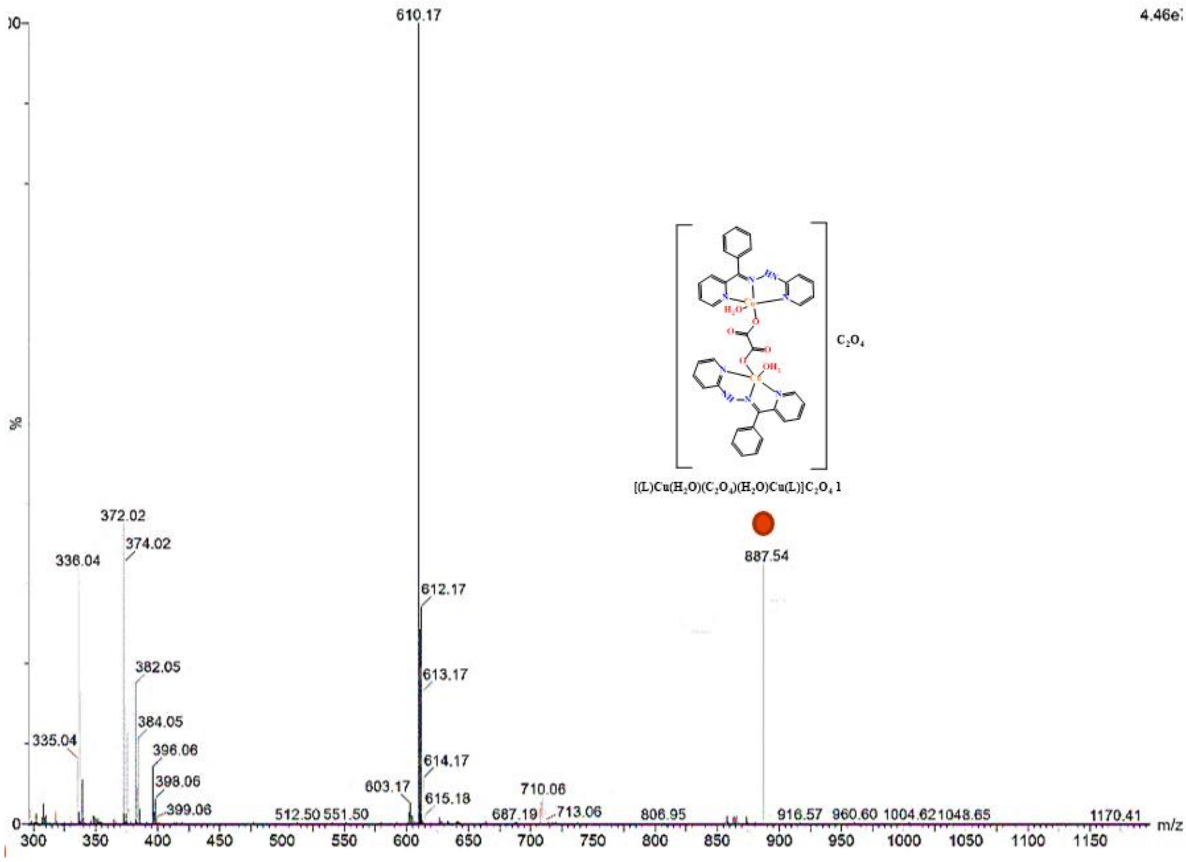

Fig. 23. Mass spectrum of complex **1.**

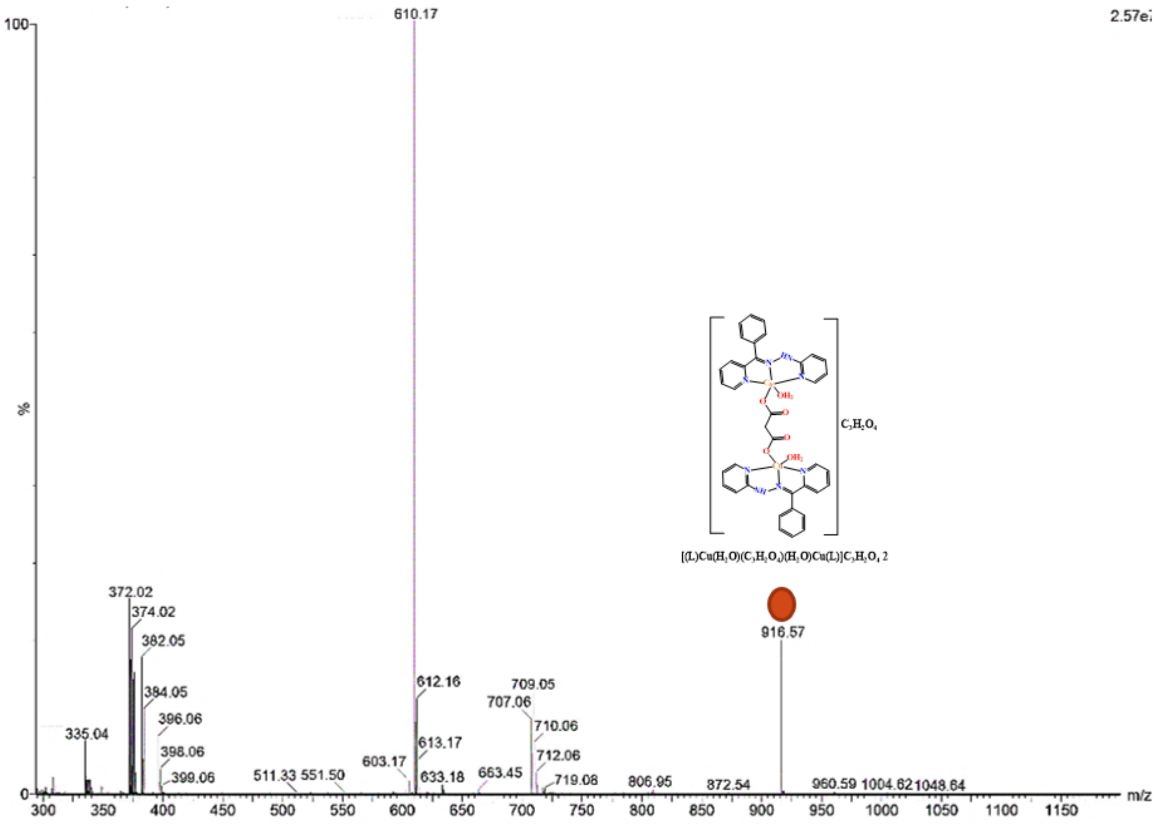

Fig. 24. Mass spectrum of complex **2.**

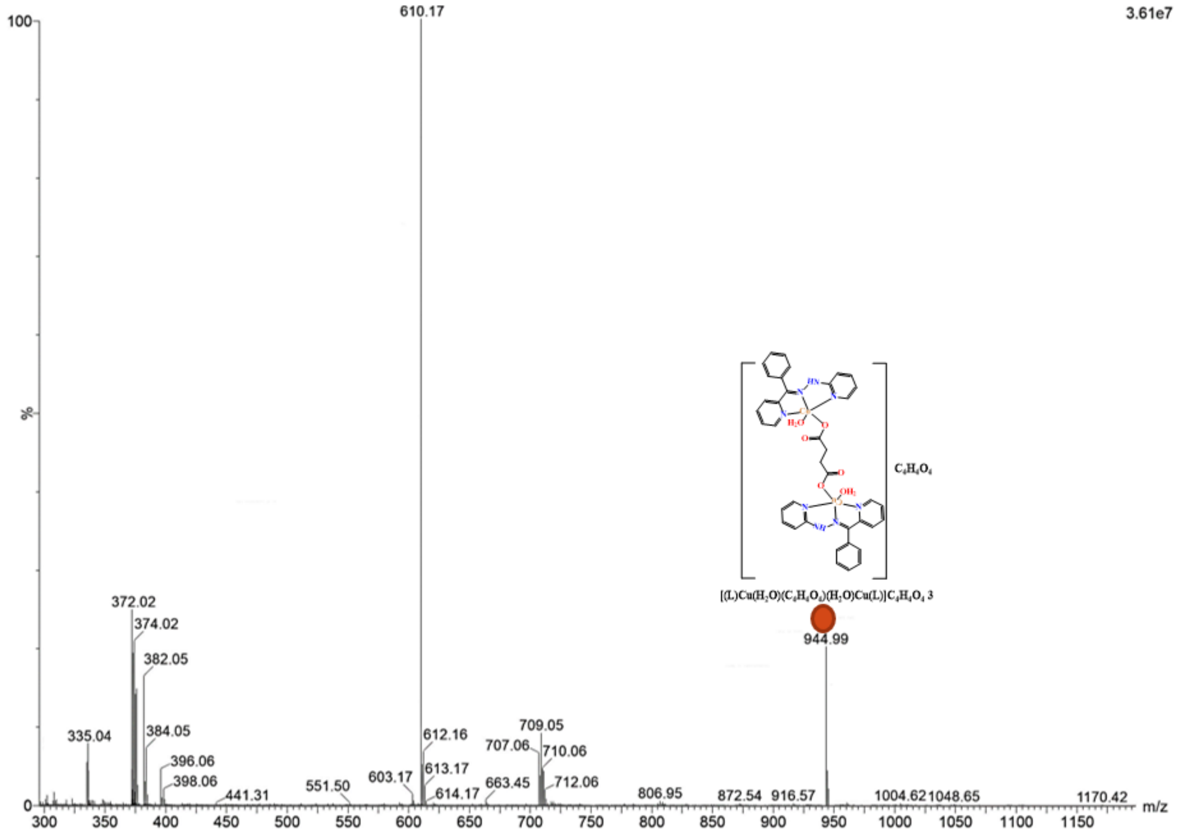

Fig. 25. ESI-Mass spectrum of complex **3**.

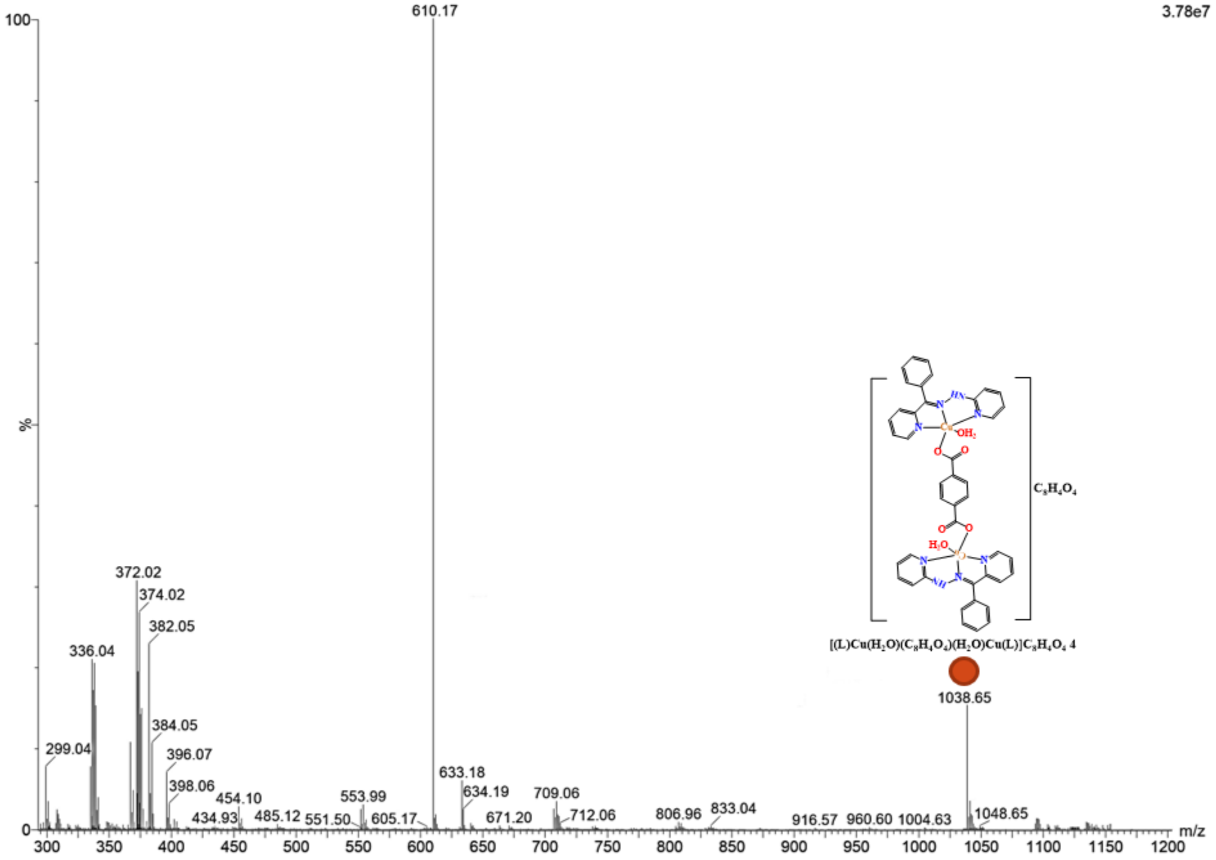

Fig. 26. ESI-Mass spectrum of complex **4**.

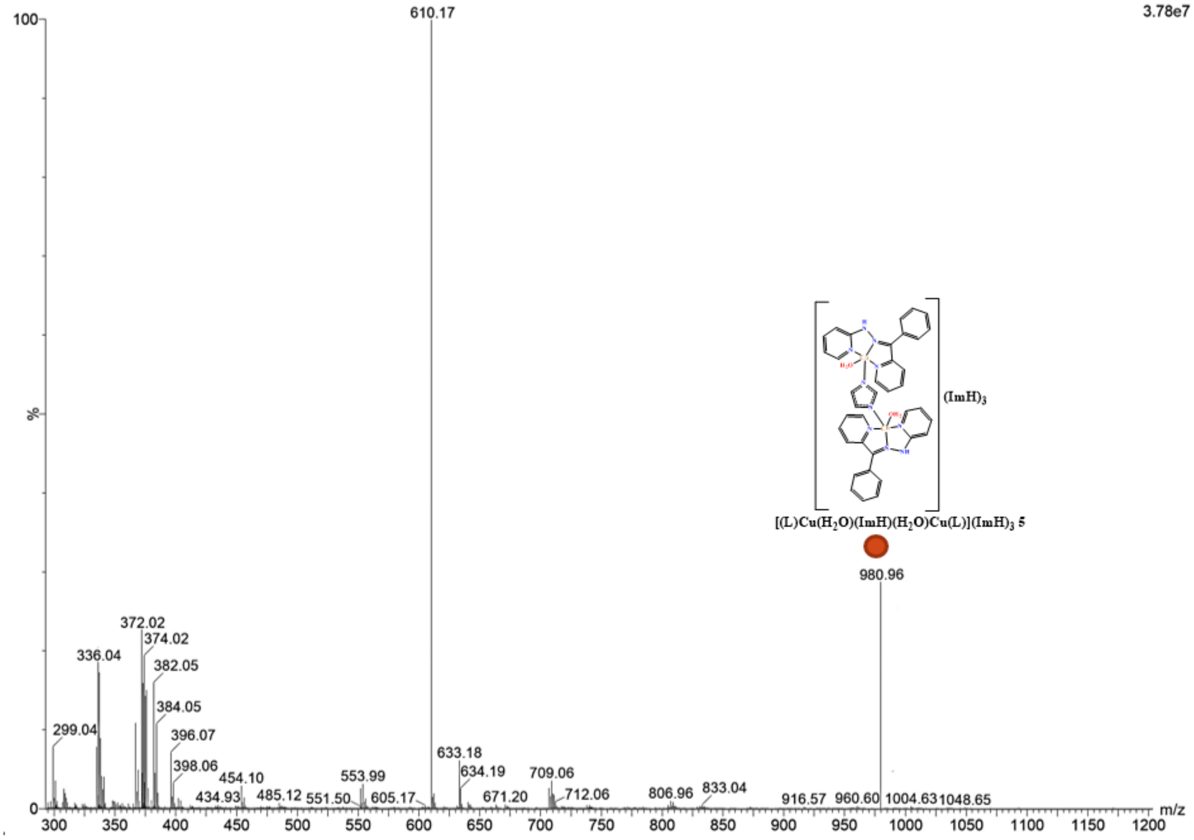

Fig. 27. ESI-Mass spectrum of complex **5**.

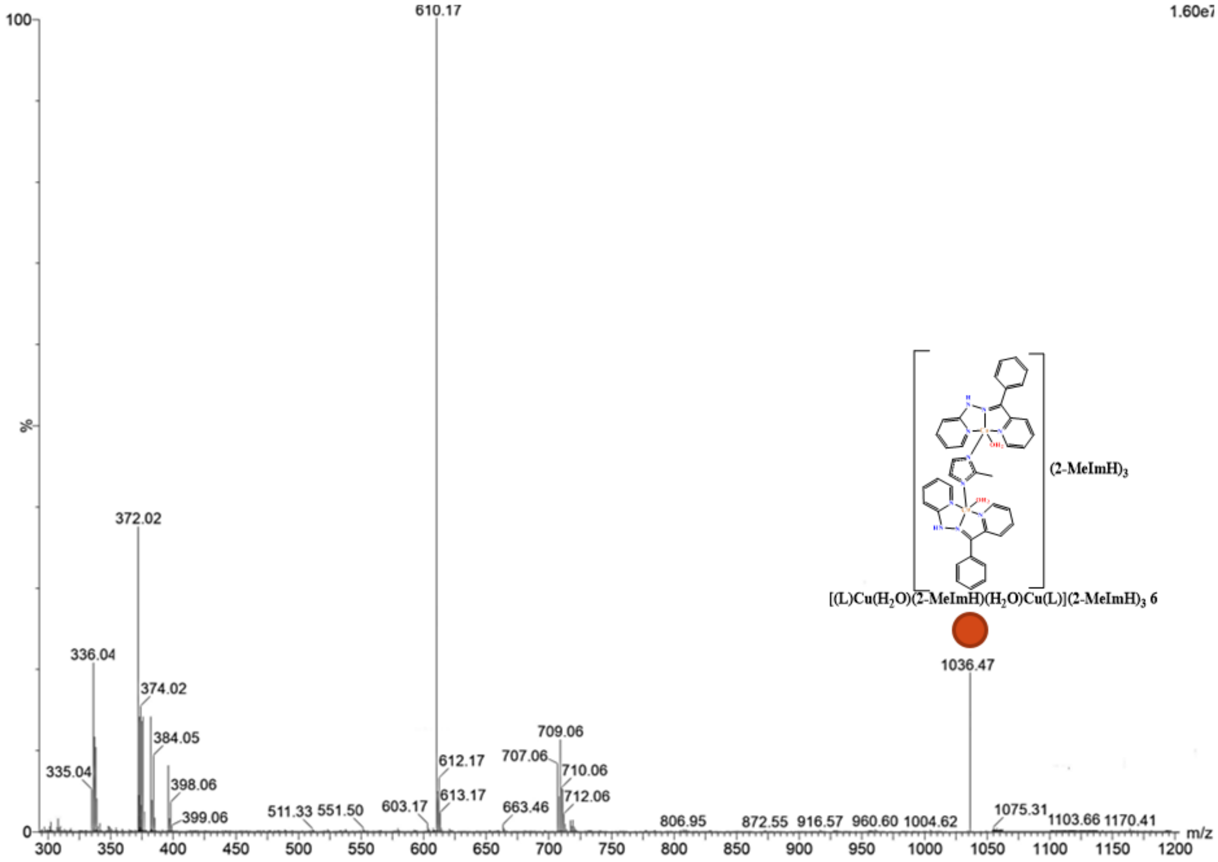

Fig. 28. ESI-Mass spectrum of complex **6**.

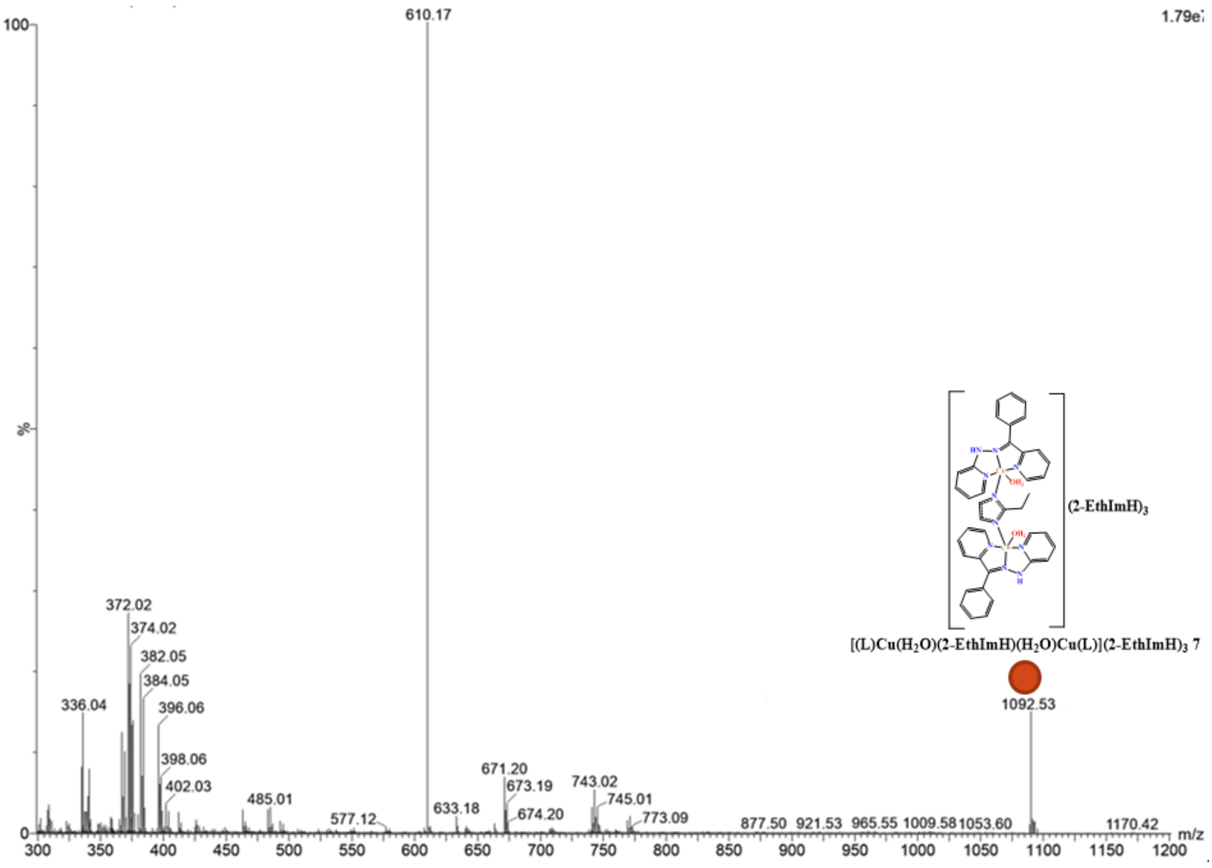

Fig. 29. ESI-Mass spectrum of complex **7**.

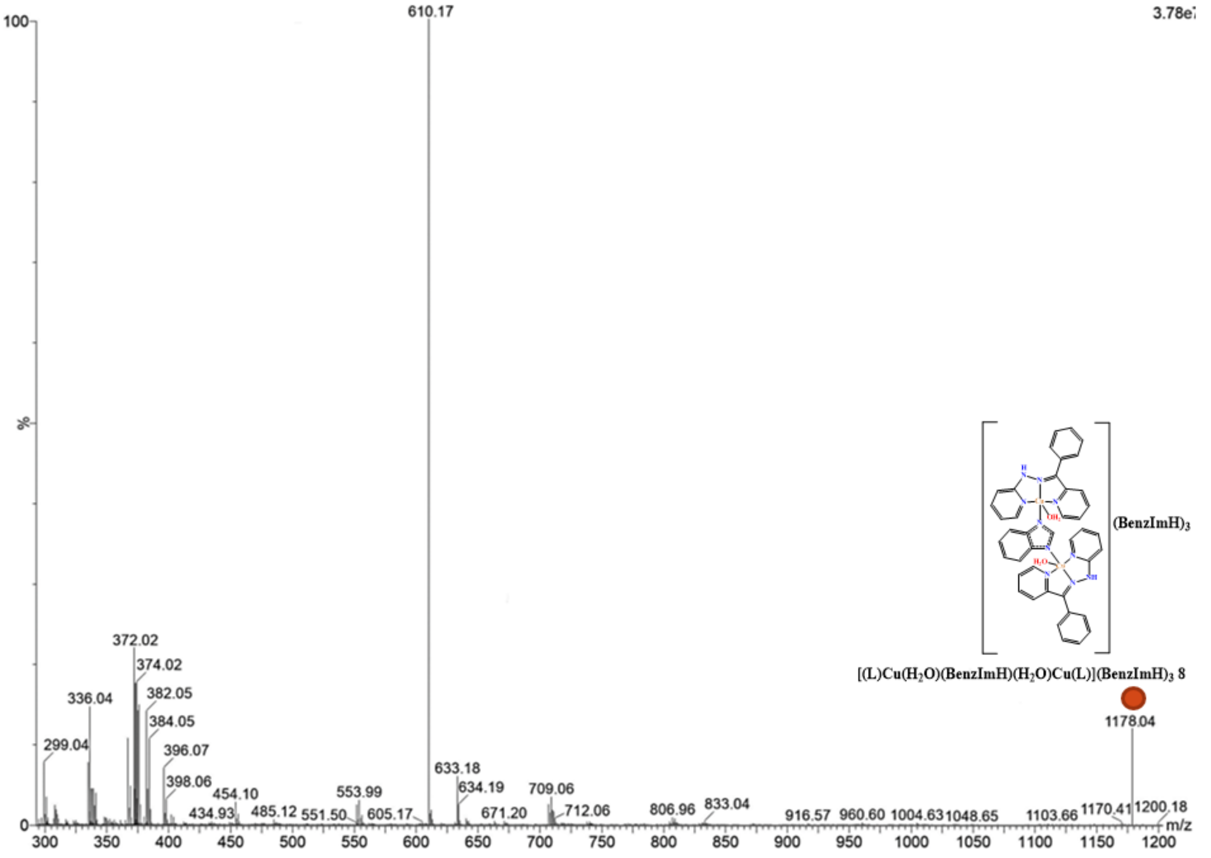

Fig. 30. ESI-Mass spectrum of complex **8**.

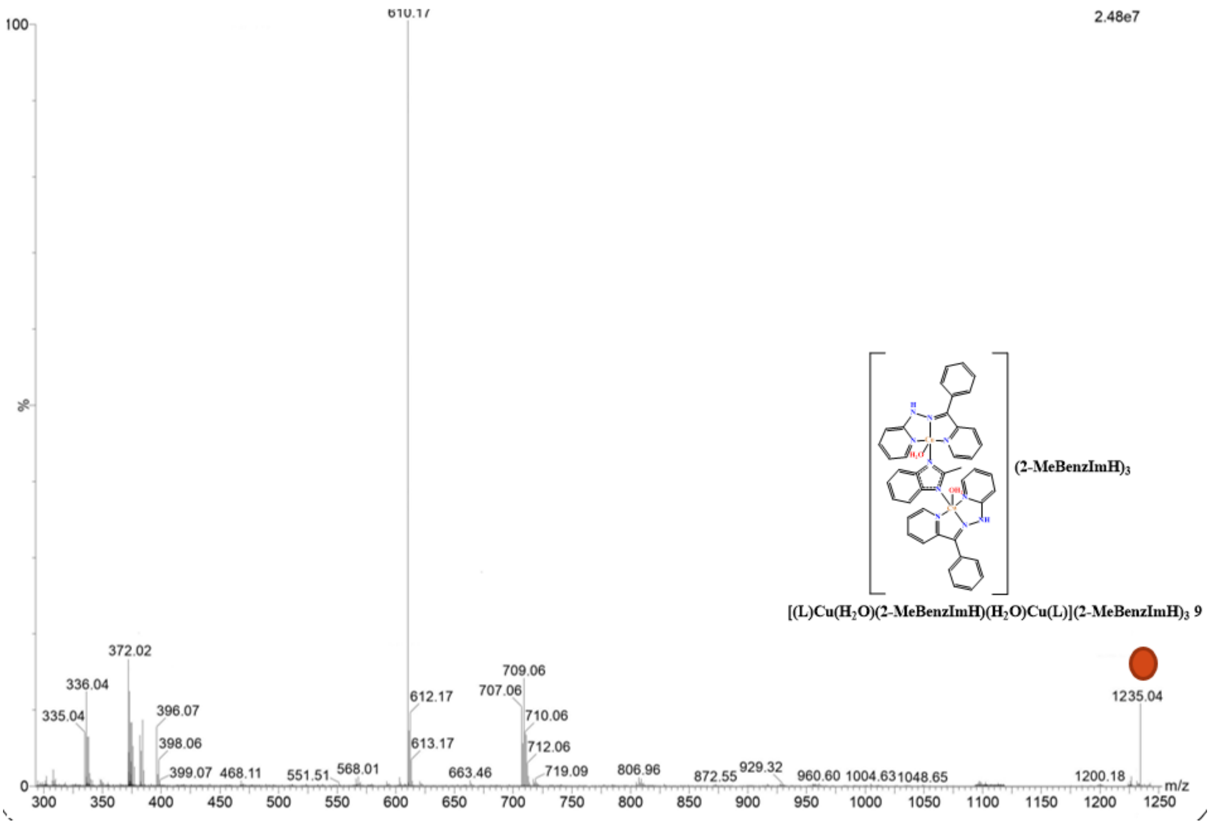

Fig. 31. ESI-Mass spectrum of complex **9**.

3.8 Computational study of complexes 1-4

3.8.1 Quantum chemical Analysis

Quantum chemical analyses for complexes **1-4** were carried out to deduce quantitative relationships of the theoretical descriptors with the superoxide antioxidant relationship activity by using density functional theory calculations at B3LYP/LANL2DZ level.

3.8.2 Geometry optimization

The Geometry optimized structures of complexes **1-4** are shown in Fig 32. The bond parameters (bond distances and bond angles) are collected in Table 6. In these binuclear complexes, each copper(II) centre has distorted square pyramidal geometry. The equatorial sites around copper(II) centres are occupied by the NNN atom of hydrazone ligand and the fourth position is occupied by the O atom of bridging carboxylate moiety whereas the axial position is occupied by the O atom of the coordinated water molecule.

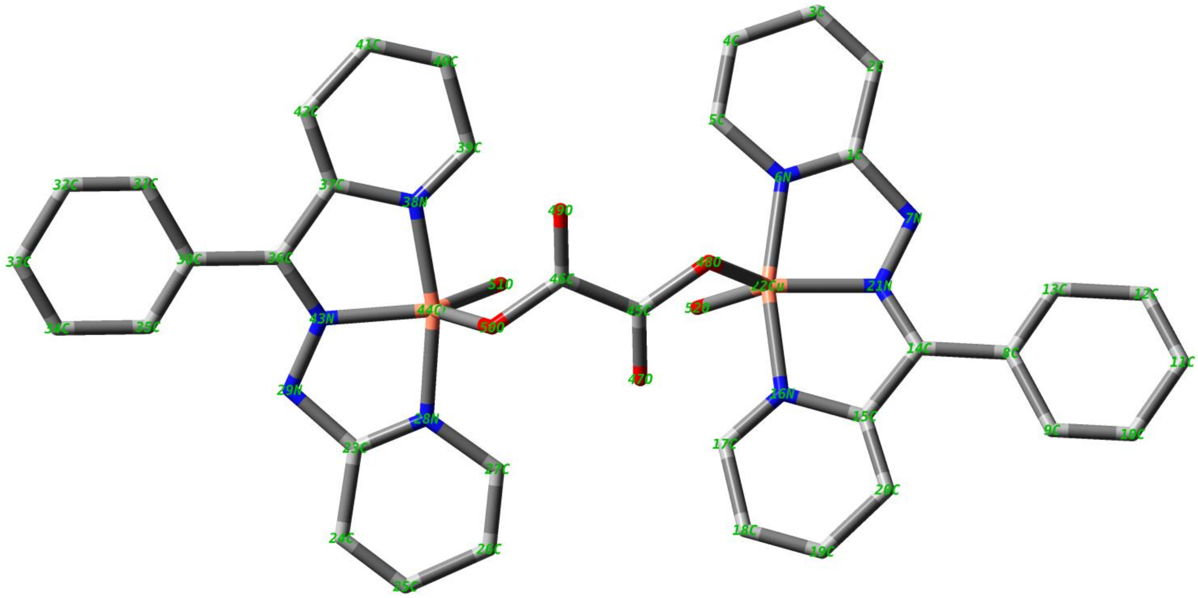
41C
40C
42C
39C
32C
31C
37C
38N
33C
30C
36C
49O
48O
51O
45C
44Cu
43N
50O
46C
52O
22Cu
21N
34C
35C
47O
29N
28N
23C
27C
24C
26C
25C
3C
4C
2C
5C
6N
1C
7N
13C
12C
14C
8C
11C
16N
15C
17C
9C
10C
20C
18C
19C

1

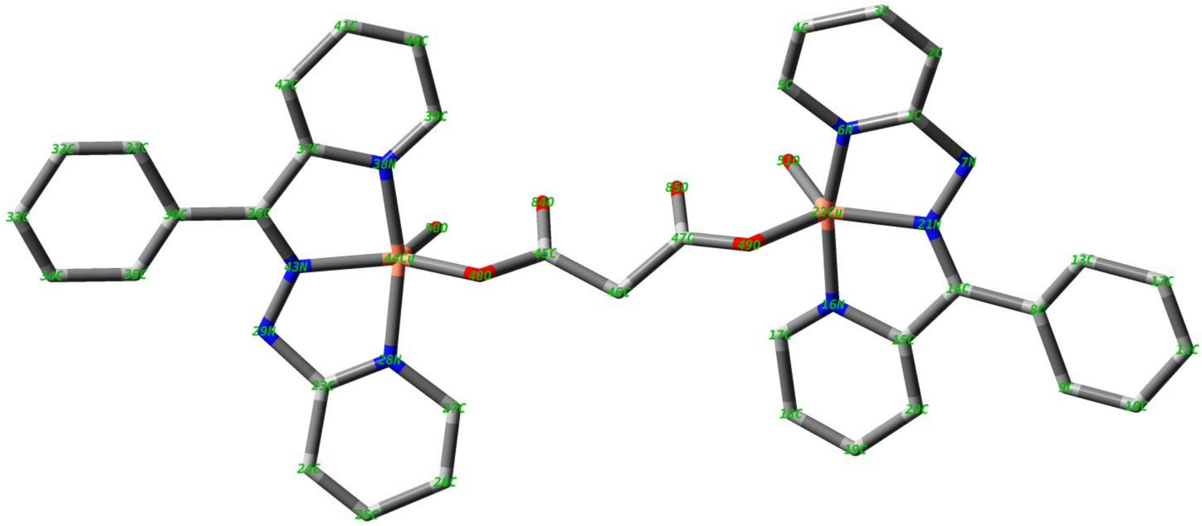
41C
40C
42C
39C
32C
31C
37C
38N
33C
30C
36C
43N
44Cu
50O
48O
84O
45C
46C
85O
47C
49O
51O
22Cu
21N
29N
28N
34C
35C
23C
27C
24C
26C
25C
3C
4C
2C
5C
6N
1C
7N
13C
12C
14C
8C
11C
16N
15C
17C
9C
10C
20C
18C
19C

2

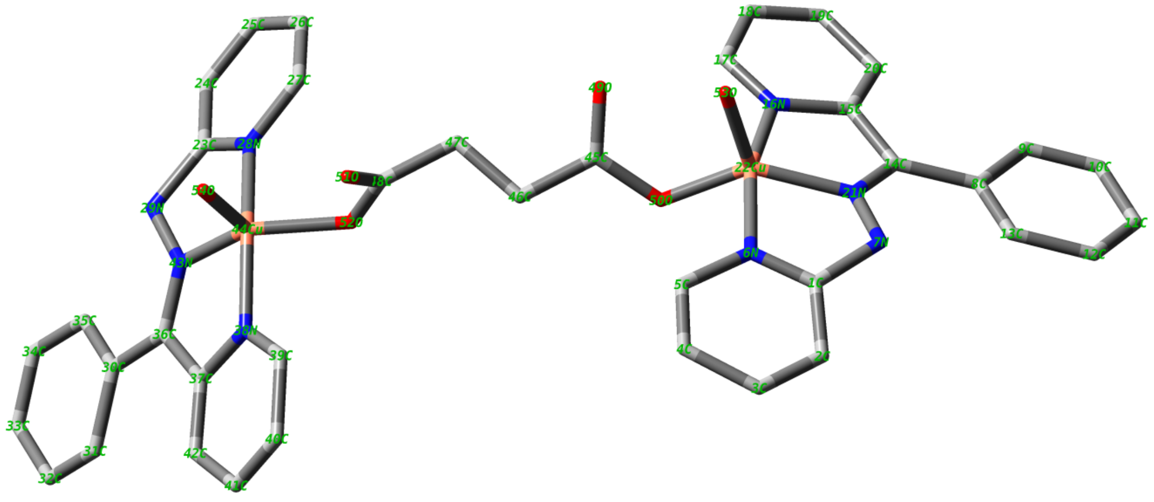

3

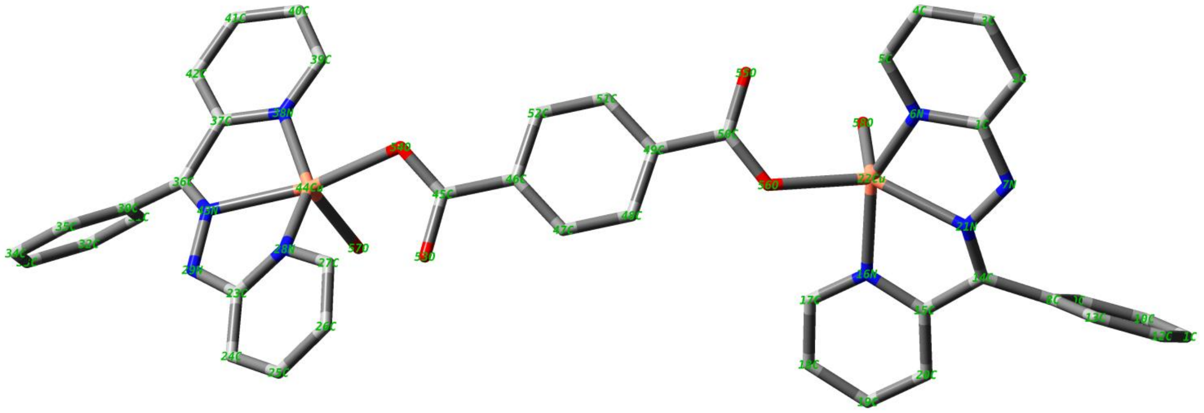

4

Fig. 32. Optimized structures of complexes **1-4**.

The distortion parameter,($\tau_5 = \beta-\alpha$ / 60°, where β and α are the largest bond angles) in these complexes are recognized by four bonds in equatorial and one bond at axial position (Table 6) [78]. The distortion structural parameters τ_5 remain in the range of 0.127-0.558. The distortion in square pyramidal geometry of Cu^{2+} ions arises due to the Jahn-Teller effect with d^9 electronic configuration. In these complexes extent of distortion is in accordance with bond parameters (bond distances and angles). The Cu-N/O bond distances remain in a range of 1.829-1.898 Å.

Table 6 Theoretical Bond lengths [Å] and angles [°] of bridged complexes complexes **1-4**.

1			
Bond lengths			
Cu(22)-N(6)	1.876	C u(44)-N(28)	1.873
Cu(22)-N(16)	1.876	Cu(44)-N(38)	1.873
Cu(22)-N(21)	1.893	Cu(44)-N(43)	1.888
Cu(22)-O(48)	1.829	Cu(44)-O(50)	1.830
Cu(22)-O(52)	1.829	Cu(44)-O(51)	1.829
Bond angles			
N(6)-Cu(22)-N(16)	164.60	N(28)-Cu(44)-N(38)	161.79
N(6)-Cu(22)-N(21)	80.97	N(28)-Cu(44)-N(43)	81.84
N(6)-Cu(22)-O(48)	90.45	N(28)-Cu(44)-O(50)	92.89
N(6)-Cu(22)-O(52)	98.79	N(28)-Cu(44)-O(51)	96.47
N(16)-Cu(22)-N(21)	84.31	N(38)-Cu(44)-N(43)	84.86
N(16)-Cu(22)-O(48)	95.43	N(38)-Cu(44)-O(50)	95.49
N(16)-Cu(22)-O(52)	93.14	N(38)-Cu(44)-O(51)	90.65
N(21)-Cu(22)-O(48)	129.52	N(43)-Cu(44)-O(50)	122.92
N(21)-Cu(22)-O(52)	123.83	N(43)-Cu(44)-O(51)	128.31
O(48)-Cu(22)-O(52)	106.60	O(50)-Cu(44)-O(51)	108.76
2			
Bond lengths			
Cu(22)-N(6)	1.875	Cu(44)-N(28)	1.878
Cu(22)-N(16)	1.875	Cu(44)-N(38)	1.877
Cu(22)-N(21)	1.888	Cu(44)-N(43)	1.895
Cu(22)-O(49)	1.830	Cu(44)-O(48)	1.829
Cu(22)-O(51)	1.830	Cu(44)-O(50)	1.830

Bond angles			
N(6)-Cu(22)-N(16)	163.46	N(28)-Cu(44)-N(38)	160.49
N(6)-Cu(22)-N(21)	80.83	N(28)-Cu(44)-N(43)	80.57
N(6)-Cu(22)-O(49)	94.74	N(28)-Cu(44)-O(48)	89.73
N(6)-Cu(22)-O(51)	95.42	N(28)-Cu(44)-O(50)	101.31
N(16)-Cu(22)-N(21)	84.35	N(38)-Cu(44)-N(43)	84.32
N(16)-Cu(22)-O(49)	89.21	N(38)-Cu(44)-O(48)	93.06
N(16)-Cu(22)-O(51)	98.82	N(38)-Cu(44)-O(50)	96.53
N(21)-Cu(22)-O(49)	130.22	N(43)-Cu(44)-O(48)	137.27
N(21)-Cu(22)-O(51)	123.20	N(43)-Cu(44)-O(50)	117.22
O(49)-Cu(22)-O(51)	106.56	O(48)-Cu(44)-O(50)	105.45
3			
Bond lengths			
Cu(22)-N(6)	1.879	Cu(44)-N(28)	1.879
Cu(22)-N(16)	1.879	Cu(44)-N(38)	1.876
Cu(22)-N(21)	1.898	Cu(44)-N(43)	1.896
Cu(22)-O(50)	1.830	Cu(44)-O(52)	1.831
Cu(22)-O(53)	1.829	Cu(44)-O(54)	1.830
Bond angles			
N(6)-Cu(22)-N(16)	159.92	N(28)-Cu(44)-N(38)	160.58
N(6)-Cu(22)-N(21)	80.34	N(28)-Cu(44)-N(43)	80.59
N(6)-Cu(22)-O(50)	89.73	N(28)-Cu(44)-O(52)	89.94
N(6)-Cu(22)-O(53)	101.66	N(28)-Cu(44)-O(54)	101.24
N(16)-Cu(22)-N(21)	84.19	N(38)-Cu(44)-N(43)	84.36
N(16)-Cu(22)-O(50)	93.37	N(38)-Cu(44)-O(52)	92.84
N(16)-Cu(22)-O(53)	96.73	N(38)-Cu(44)-O(54)	96.50

N(21)-Cu(22)-O(50)	138.34	N(43)-Cu(44)-O(52)	137.25
N(21)-Cu(22)-O(53)	117.01	N(43)-Cu(44)-O(54)	117.16
O(50)-Cu(22)-O(53)	104.59	O(52)-Cu(44)-O(54)	105.54
4			
Bond lengths			
Cu(22)-N(6)	1.876	Cu(44)-N(28)	1.877
Cu(22)-N(16)	1.877	Cu(44)-N(38)	1.879
Cu(22)-N(21)	1.891	Cu(44)-N(43)	1.892
Cu(22)-O(56)	1.830	Cu(44)-O(54)	1.829
Cu(22)-O(58)	1.829	Cu(44)-O(57)	1.830
Bond angles			
N(6)-Cu(22)-N(16)	155.44	N(28)-Cu(44)-N(38)	153.64
N(6)-Cu(22)-N(21)	79.90	N(28)-Cu(44)-N(43)	79.56
N(6)-Cu(22)-O(56)	94.12	N(28)-Cu(44)-O(54)	94.66
N(6)-Cu(22)-O(58)	100.05	N(28)-Cu(44)-O(57)	101.13
N(16)-Cu(22)-N(21)	84.16	N(38)-Cu(44)-N(43)	83.73
N(16)-Cu(22)-O(56)	88.25	N(38)-Cu(44)-O(54)	87.87
N(16)-Cu(22)-O(58)	103.14	N(38)-Cu(44)-O(57)	103.89
N(21)-Cu(22)-O(56)	144.96	N(43)-Cu(44)-O(54)	146.04
N(21)-Cu(22)-O(58)	111.61	N(43)-Cu(44)-O(57)	111.40
O(56)-Cu(22)-O(58)	103.42	O(54)-Cu(44)-O(57)	102.54

3.8.3 Frontier molecular orbitals and chemical reactivity

To predict reactive sites of hydrazone Schiff base and its complexes, frontier molecular orbitals (FMO) and their energies are exploited [79]. These frontier molecular orbitals are the highest occupied molecular orbital (HOMO) and the lowest unoccupied molecular orbital (LUMO). The HOMO is the highest energy orbital and acts as an electron donor whereas LUMO is the lower energy orbital and can accept the electron. These donor and acceptor features are related to ionization potential and electron affinity. The charge distribution in HOMO and LUMO orbitals is shown in Fig. 33. The charge distribution in **3** is on the donor atom of hydrazone moiety and in remaining complexes, it is on both copper and donor atom of complexes.

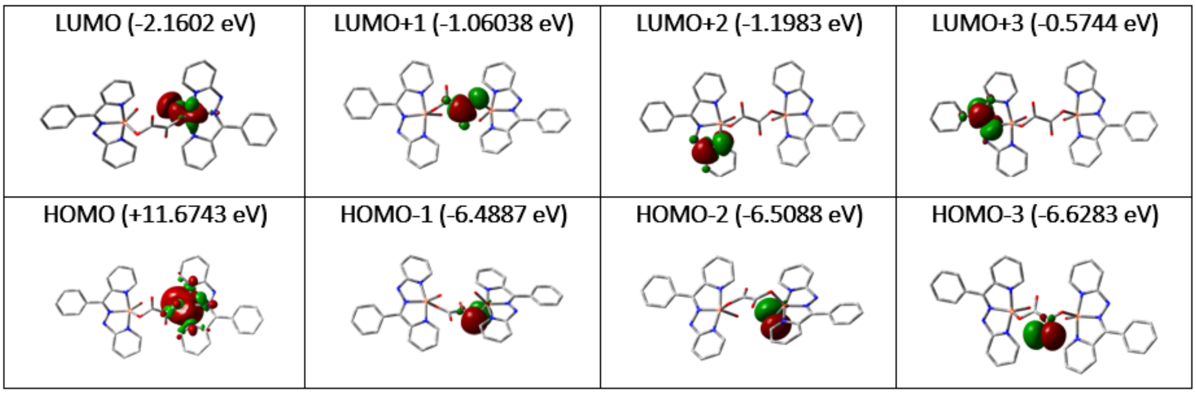

1

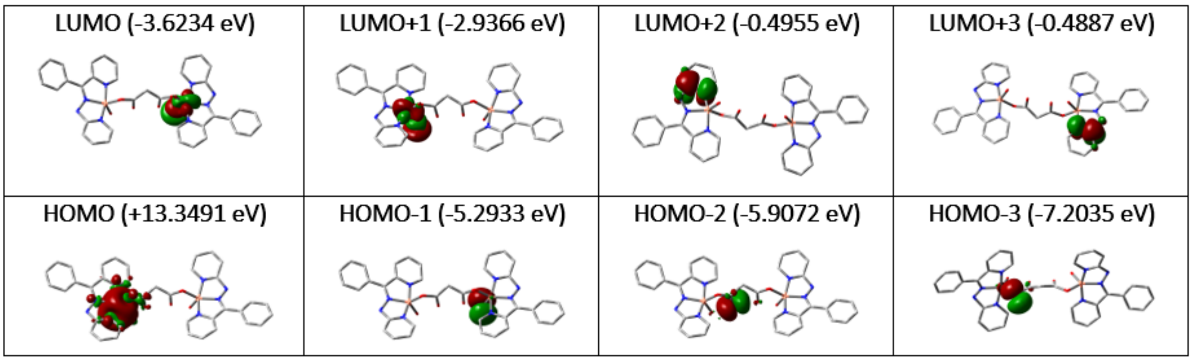

2

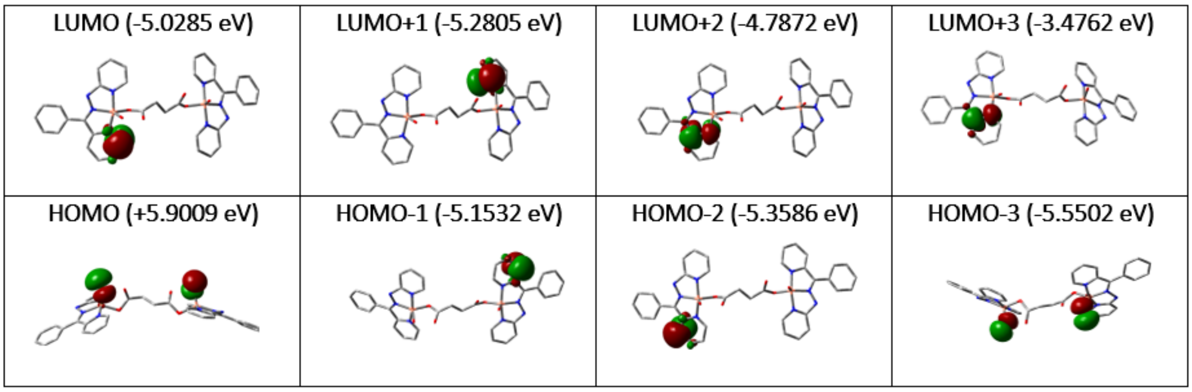

3

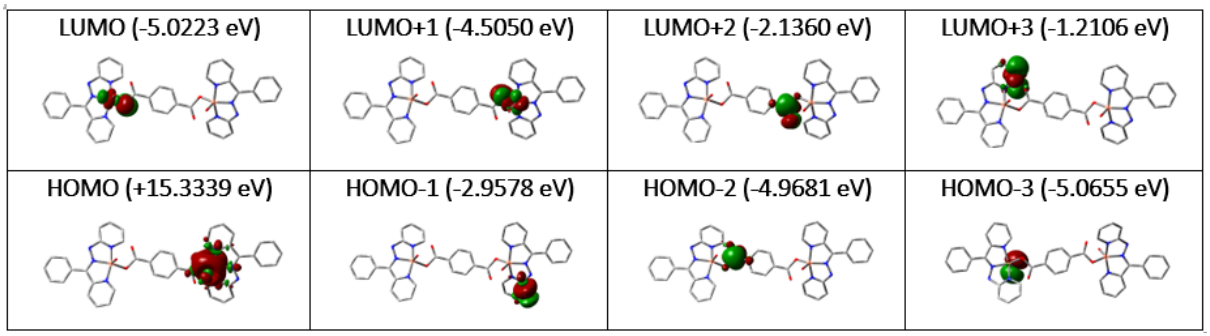

4

Fig. 33. HOMO-LUMO energy level diagram of complexes **1-4**.

The electronic parameters of FMO provide a wide range of information regarding the nature of molecules. Some electronic properties are calculated and collected in Table 7. The electronic properties are useful in yielding theoretical insights into chemical reactivity and selectivity in terms of electronic parameters [80, 81]. These calculated electronic parameters are the energy of HOMO (E_{HOMO}), the energy of LUMO (E_{LUMO}), energy gap (ΔE), ionization potential (I), electron affinity (IA), electronegativity (χ), chemical potential (μ), global hardness (η), global softness (S) and electrophilicity index (ω).

Table 7 Global reactivity descriptors complexes **1-4** in eV calculated by DFT/B3LYP/LANL2DZ basic.

Molecular properties	Mathematical description	1	2	3	4
E_{HOMO}	Energy of HOMO	+11.6743	+13.3491	5.9009	+15.3339
E_{LUMO}	Energy of LUMO	-2.1602	-3.6234	-5.0285	-5.0223
Energy gap	$\Delta E_g = E_{HOMO} - E_{LUMO}$	13.8345	16.9725	10.9294	20.3562
Ionization potential (IP)	$IP = -E_{HOMO}$	11.6743	13.3491	5.9009	15.3339
Electron affinity (EA)	$EA = -E_{LUMO}$	2.1602	3.6234	5.0285	5.0203
Electronegativity (χ)	$(\chi) = -½ (E_{Homo} + E_{Lumo})$	4.7570	4.8628	0.4362	5.1558
Chemical Potential(μ)	$\mu = ½ (E_{Homo} + E_{Lumo})$	-4.7570	-4.8628	-0.4362	-5.1558
Global Hardness (Ƞ)	$(\eta) = ½ (E_{LUMO} - E_{HOMO})$	6.9172	8.4862	5.4647	10.1781
Softness (S)	$(S) = 1/2\eta$	0.0722	0.0589	0.0914	0.0491
Electrophilicity index(ω)	$\omega = \mu^2/2\eta$	1.6356	1.3932	0.0174	1.3058

Parr et. al. has established the relationship of density functional theory of chemical reactivity with the first derivative of energy concerning the n number of electrons and hence with the negative of electronegativity (χ). Ionization potential (I) can be obtained from the energy required to remove an electron from a molecule [81]. Similarly, electron affinity (IA) is the amount of energy released when a proton is added to the system and related to the E_{HOMO} and E_{LUMO} as:

$$I = - E_{HOMO},\ EA = - E_{LUMO}$$

Other electronic parameters *viz.*, electronegativity (χ) and global hardness (η) can be obtained from I and EA. Electronegativity (χ) is the measure of the power of an atom or group of atoms to attract electrons towards itself. The global hardness (η) is the second derivative of the energy, which measures the stability and reactivity of the molecule. The electronegativity (χ) and global hardness (η) can be derived using the equations [82].

$$\chi = -\frac{1}{2}(E_{HOMO} + E_{LUMO})$$

$$\eta = \frac{1}{2}(E_{HOMO} - E_{LUMO})$$

Global softness (S) is the measure of the capacity of an atom or moiety to gain electrons and is mathematically shown as:

$$S = 1/2\eta$$

Finally, electrophilicity index (ω) which is a measure of electrophilicity of ligand, may be expressed as

$$\omega = \mu^2/2\eta$$

Therefore, the propensity of chemical species to accept electrons is measured by this index. These electronic parameters also decide the type of nucleus and electrophiles. The lower values of η and ω are indicative of good and reactive nucleophiles. Similarly, the high value of μ and ω are indicative of good electrophile.

The theoretically calculated parameters especially electron affinity (EA) have been a good descriptor for predicting superoxide antioxidant activity [83-86]. It is found that EA is a suitable parameter in ascertaining the rate of electron transfer from $O_2^{\cdot-}$ to Cu(II) ion. The compounds with the lowest value of EA carried the highest electron transfer rate, thus possessing the highest SOD activity [86]. Although such a trend of SOD activity w.r.t. EA is contradicted by few more observations [87, 88]. The trend of EA for complexes **1-4**: **4**≈**3** > **2** > **1** whereas the trend of SOD activity is **1** > **3** > **2** > **4**. A probable reason for some discrepancies can be made based on the geometry of the Cu(II) ion and attached constituent moieties [87, 88].

3.8.4 Spin density

The surfaces of the spin densities for all binuclear complexes are calculated. The spin density plot for **1-4** are shown in Fig. 34 and the spin and Mulliken population of copper centers are collected in Table 8. With the perusal of spin density and Mulliken population values, it is concluded that the similar values of these two parameters remain in all copper centers. The calculated charges (spin density and Mulliken population) are very low than the formal charges of +2. Such a decline in charge value is due to charge transfer from the metal center to the ligand (MLCT) [89]. The spin density and Mulliken populations in complexes **1-4** are almost similar. It is found that the largest part of the spin density population is located on Cu(II) centres where an important delocalization of unpaired electrons takes place. In complex **4** benzene ring also carries electron density. Spin density plots (Fig. 34) represent how the *3d* electron of the copper places some spin density on other atoms of molecules [90]. On other hand, the molecular orbital that contains the unpaired electron density, even with a major contribution from $d_{x^2-y^2}$ orbital of Cu(II) centres yields striking contribution from the donor atoms.

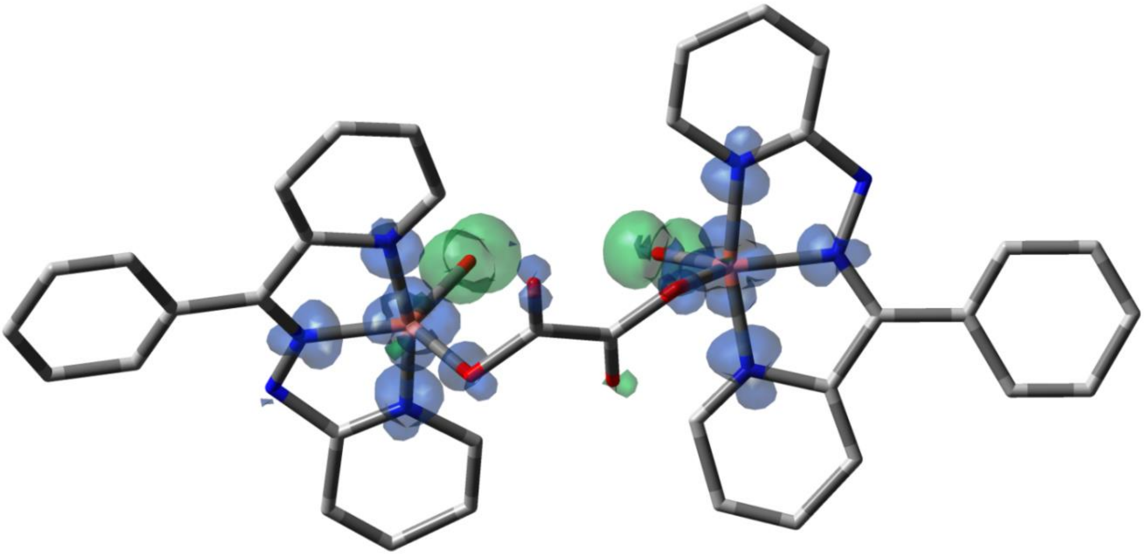

1

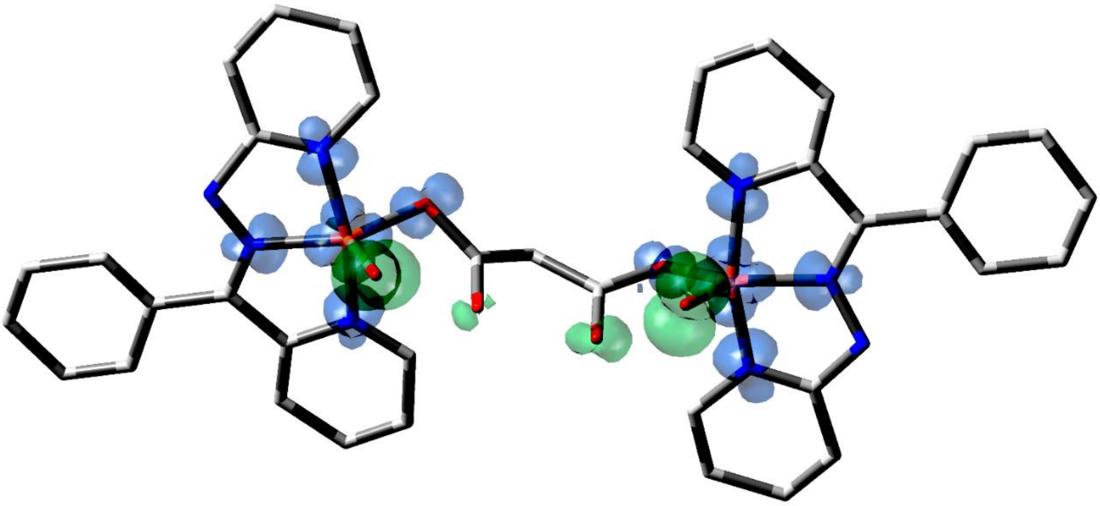

2

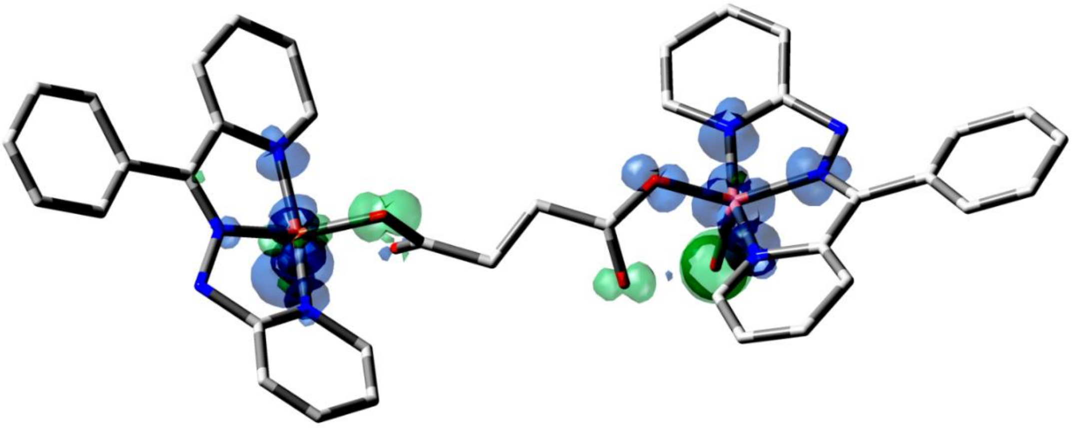

3

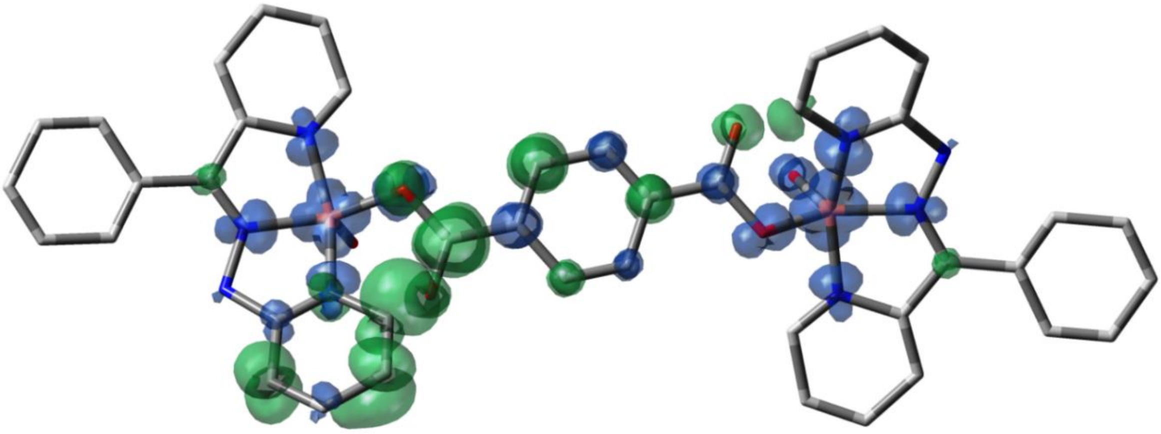

4

Fig. 34. Spin density plots of complexes **1-4**.

Table 8 Spin and Mulliken population analysis of complexes **1-4**.

Complexes	Spin density		Mulliken density	
	Cu22	Cu44	Cu22	Cu44
1	0.6253	0.5394	0.5467	0.4279
2	0.5602	0.4296	0.4132	0.3430
3	0.6821	0.4167	0.5507	0.2922
4	0.6083	0.5523	0.5199	0.4698

3.8.5 Molecular geometry optimization of complexes 5-9

The density functional theory (DFT) method was used for molecular geometry optimization of complexes **5-9**. Molecular orbital geometry optimization permits quantitative analysis of the geometry and the ground electronic properties of the compounds. Optimization molecular geometry and their atom numbering diagrams are shown in Fig 35. The selected bond parameters (bond lengths and angle) are collected in Tables. The geometrical parameters viz; bond parameters, optimized energies, frontier molecular orbital (FMO), highest occupied molecular orbital (HOMO), lowest unoccupied molecular orbital (LUMO) energy gaps have been calculated with the B3LYP6-31G/LANL2DZ levels using the gaussian 09 computer program [43]. The geometry of copper metal centre in these complexes in the distorted trigonal pyramid as ascertained by addition structural parameters τ_5 ($\tau_5 = \theta_1 - \theta_2 / 60$, where θ_1 and θ_2 are two largest angles) [78]. From this formula, the index of the degree of trigonality in five-coordinate complexes can be easily calculated. Therefore, a square pyramidal structure with D_3h molecular symmetry has $\tau_5 = 1$, while a square pyramidal structure with C_{4v} molecular symmetry has $\tau_5 = 0$. For complexes **5-9** the values of addition structural parameters remain in the range 0.118-0.468. Hence geometry in each copper centre is distorted square pyramidal. In these complexes, the extent of distortion depends on the molecular weight and structure of bridging ligands. The observed trend in distortion is found to be: **5** > **6** > **7** > **8** > **9**. As bridging molecules become bulky the less distortion is a reversal in molecular geometry. The bond lengths Cu-N and Cu-O are comparable to these reported in similar binuclear complexes [91, 92]. The various bond angle around copper(II)ions have been noticed to lie in the 81.22- 160.26° range (Table 9).

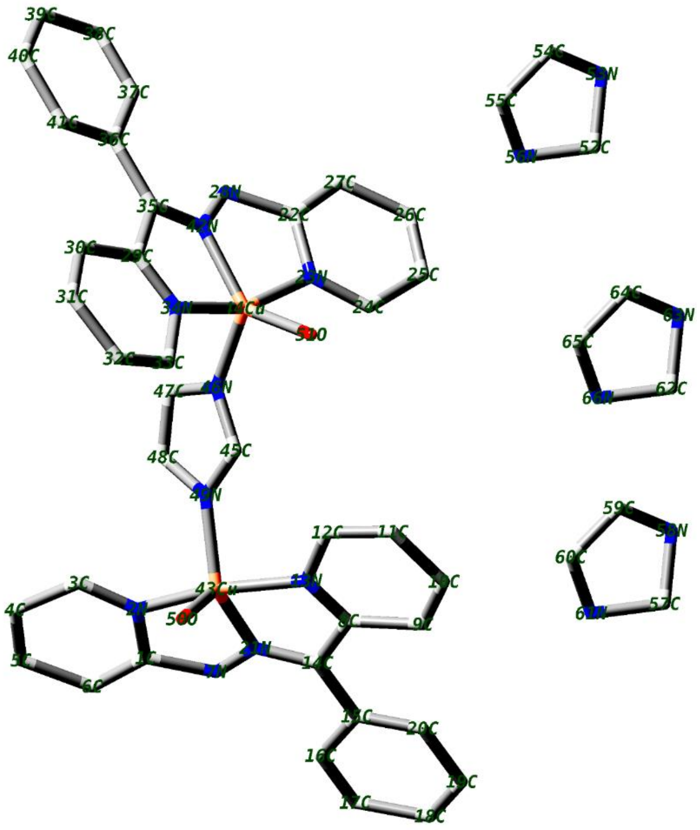
39C
38C
40C
37C
41C
36C
54C
55C
56N
57C
35C
27C
26C
22C
29C
30C
25C
31C
24C
64C
65C
62C
51O
32C
33C
47C
46N
48C
45C
12C
11C
59C
60C
57C
3C
43Cu
10C
4C
50O
8C
9C
5C
6C
14C
13C
20C
16C
19C
17C
18C

5

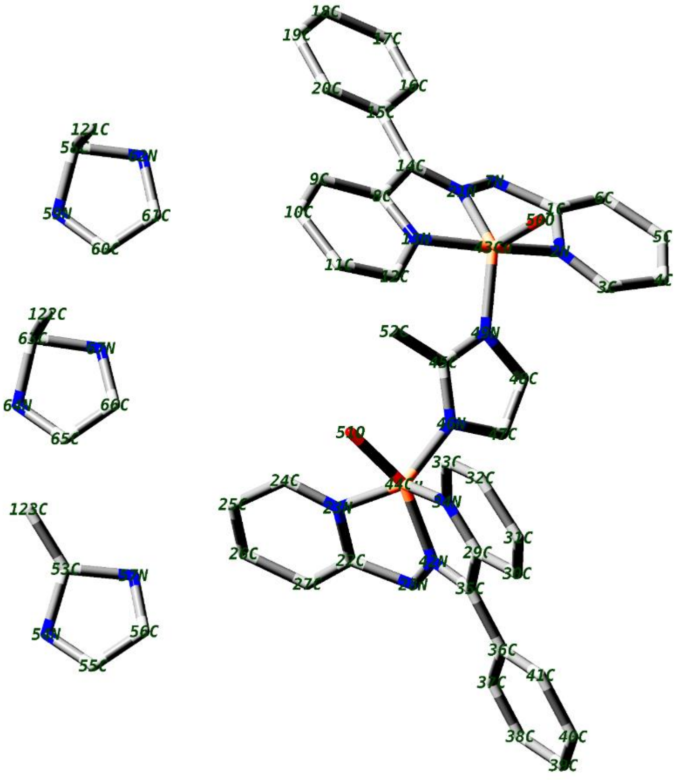
18C
19C
17C
20C
16C
15C
121C
14C
9C
10C
6C
5C
50O
11C
12C
3C
4C
61C
60C
122C
52C
46C
66C
65C
51O
33C
32C
24C
25C
123C
31C
29C
30C
26C
53C
27C
35C
36C
56C
55C
41C
38C
40C
39C

6

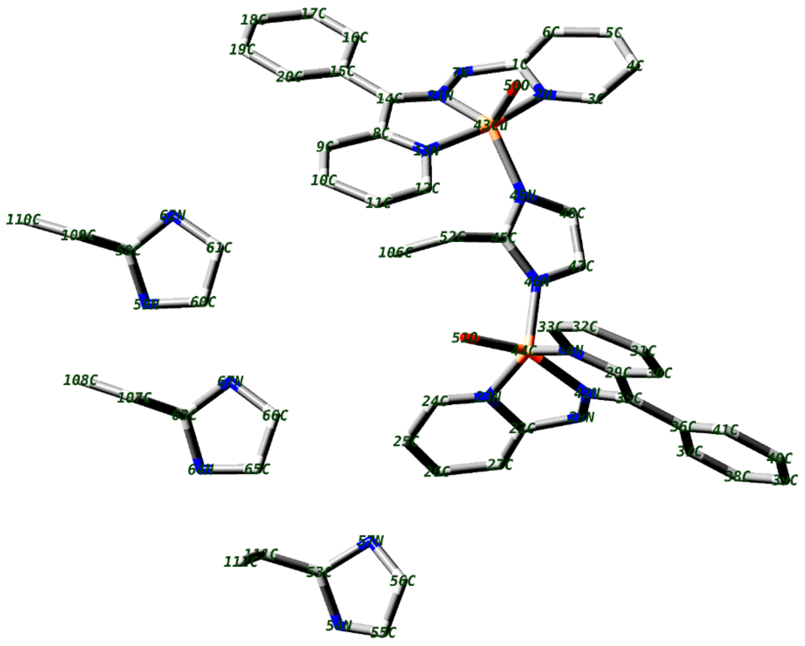
18C
17C
16C
19C
20C
15C
6C
5C
1C
4C
3C
14C
8C
9C
10C
11C
12C
40C
110C
109C
61C
60C
52C
106C
47C
33C
32C
31C
29C
30C
108C
107C
66C
24C
25C
41C
65C
56C
55C

7

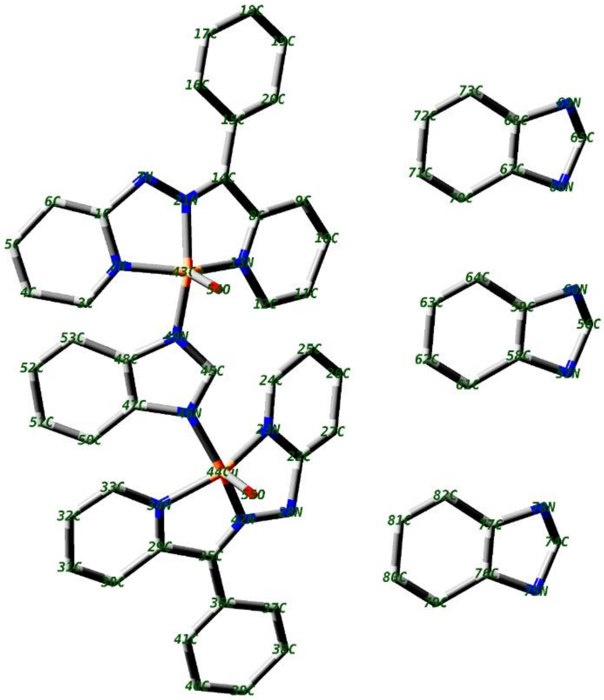
18C
17C
19C
16C
20C
15C
73C
72C
71C
70C
14C
6C
1C
9C
10C
4C
3C
11C
64C
63C
62C
61C
53C
52C
51C
50C
47C
25C
26C
24C
27C
33C
32C
31C
30C
82C
81C
80C
37C
41C
40C

8

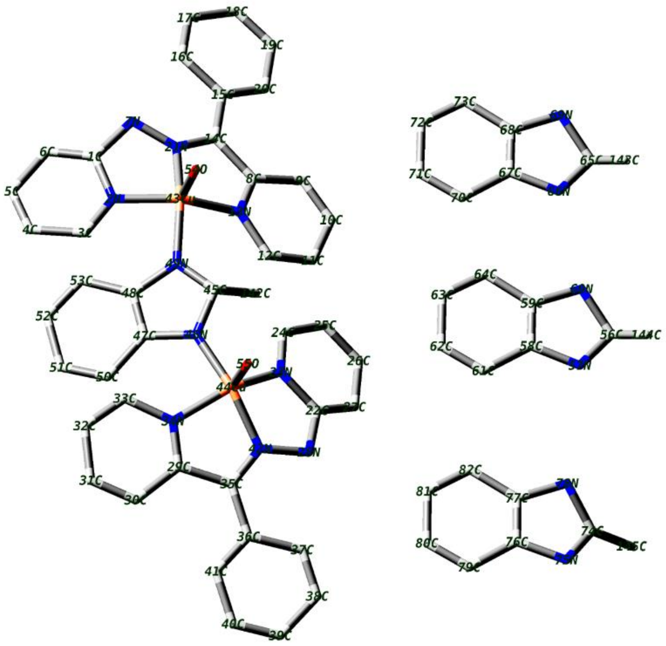

9

Fig. 35. Optimized structures of complexes **5-9**.

Table 9 Theoretical Bond lengths [Å] and angles [°] for complexes **5-9** of imidazole bridged complexes.

5			
Bond lengths			
Cu(43)-N(2)	1.868	Cu(44)-N(23)	1.868
Cu(43)-N(13)	1.882	Cu(44)-N(34)	1.883
Cu(43)-N(21)	1.892	Cu(44)-N(42)	1.896
Cu(43)-N(49)	1.869	Cu(44)-N(46)	1.870
Cu(43)-O(50)	1.829	Cu(44)-O(51)	1.830
Bond angles			
N(2)-Cu(43)-N(13)	158.63	N(23)-Cu(44)-N(34)	160.26
N(2)-Cu(43)-N(21)	82.58	N(23)-Cu(44)-N(42)	81.90
N(2)-Cu(43)-N(49)	97.39	N(23)-Cu(44)-N(46)	101.84
N(2)-Cu(43)-O(50)	92.43	N(23)-Cu(44)-O(51)	88.28
N(13)-Cu(43)-N(21)	83.30	N(34)-Cu(44)-N(42)	82.99
N(13)-Cu(43)-N(49)	90.52	N(34)-Cu(44)-N(46)	96.41
N(13)-Cu(43)-O(50)	96.55	N(34)-Cu(44)-O(51)	94.32
N(21)-Cu(43)-N(49)	130.85	N(42)-Cu(44)-N(46)	117.90
N(21)-Cu(43)-O(50)	122.25	N(42)-Cu(44)-O(51)	137.43
N(49)-Cu(43)-O(50)	106.87	N(46)-Cu(44)-O(51)	104.62
6			

Bond lengths			
Cu(43)-N(2)	1.867	Cu(44)-N(23)	1.871
Cu(43)-N(13)	1.881	Cu(44)-N(34)	1.875
Cu(43)-N(21)	1.892	Cu(44)-N(42)	1.883
Cu(43)-N(49)	1.869	Cu(44)-N(46)	1.869
Cu(43)-O(50)	1.830	Cu(44)-O(51)	1.829
Bond angles			
N(2)-Cu(43)-N(13)	142.37	N(23)-Cu(44)-N(34)	138.62
N(2)-Cu(43)-N(21)	82.64	N(23)-Cu(44)-N(42)	79.89
N(2)-Cu(43)-N(49)	96.08	N(23)-Cu(44)-N(46)	116.61
N(2)-Cu(43)-O(50)	93.14	N(23)-Cu(44)-O(51)	85.89
N(13)-Cu(43)-N(21)	83.34	N(34)-Cu(44)-N(42)	84.67
N(13)-Cu(43)-N(49)	91.67	N(34)-Cu(44)-N(46)	104.19
N(13)-Cu(43)-O(50)	95.75	N(34)-Cu(44)-O(51)	98.81
N(21)-Cu(43)-N(49)	130.08	N(42)-Cu(44)-N(46)	103.20
N(21)-Cu(43)-O(50)	122.49	N(42)-Cu(44)-O(51)	161.73
N(49)-Cu(43)-O(50)	107.41	N(46)-Cu(44)-O(51)	93.36
7			
Bond lengths			
Cu(43)-N(2)	1.864	Cu(44)-N(23)	1.867
Cu(43)-N(13)	1.881	Cu(44)-N(34)	1.879
Cu(43)-N(21)	1.888	Cu(44)-N(42)	1.884
Cu(43)-N(49)	1.870	Cu(44)-N(46)	1.870
Cu(43)-O(50)	1.829	Cu(44)-O(51)	1.829
Bond angles			
N(2)-Cu(43)-N(13)	143.18	N(23)-Cu(44)-N(34)	142.89
N(2)-Cu(43)-N(21)	83.29	N(23)-Cu(44)-N(42)	81.22
N(2)-Cu(43)-N(49)	96.40	N(23)-Cu(44)-N(46)	109.53
N(2)-Cu(43)-O(50)	91.84	N(23)-Cu(44)-O(51)	88.69
N(13)-Cu(43)-N(21)	83.47	N(34)-Cu(44)-N(42)	83.97
N(13)-Cu(43)-N(49)	91.06	N(34)-Cu(44)-N(46)	107.06
N(13)-Cu(43)-O(50)	96.39	N(34)-Cu(44)-O(51)	91.51
N(21)-Cu(43)-N(49)	130.20	N(42)-Cu(44)-N(46)	104.59
N(21)-Cu(43)-O(50)	122.20	N(42)-Cu(44)-O(51)	156.27
N(49)-Cu(43)-O(50)	107.58	N(46)-Cu(44)-O(51)	99.00
8			
Bond lengths			
Cu(43)-N(2)	1.861	Cu(44)-N(23)	1.861
Cu(43)-N(13)	1.874	Cu(44)-N(34)	1.874
Cu(43)-N(21)	1.873	Cu(44)-N(42)	1.873
Cu(43)-N(49)	1.869	Cu(44)-N(46)	1.869
Cu(43)-O(54)	1.830	Cu(44)-O(55)	1.830

Bond angles			
N(2)-Cu(43)-N(13)	145.23	N(23)-Cu(44)-N(34)	145.14
N(2)-Cu(43)-N(21)	83.11	N(23)-Cu(44)-N(42)	83.10
N(2)-Cu(43)-N(49)	88.47	N(23)-Cu(44)-N(46)	88.43
N(2)-Cu(43)-O(54)	108.85	N(23)-Cu(44)-O(55)	108.94
N(13)-Cu(43)-N(21)	84.85	N(34)-Cu(44)-N(42)	84.82
N(13)-Cu(43)-N(49)	89.26	N(34)-Cu(44)-N(46)	89.36
N(13)-Cu(43)-O(54)	105.64	N(34)-Cu(44)-O(55)	105.64
N(21)-Cu(43)-N(49)	155.63	N(42)-Cu(44)-N(46)	155.73
N(21)-Cu(43)-O(54)	103.59	N(42)-Cu(44)-O(55)	103.58
N(49)-Cu(43)-O(54)	100.75	N(46)-Cu(44)-O(55)	100.66
9			
Bond lengths			
Cu(43)-N(2)	1.864	Cu(44)-N(23)	1.826
Cu(43)-N(13)	1.861	Cu(44)-N(34)	1.909
Cu(43)-N(21)	1.863	Cu(44)-N(42)	1.884
Cu(43)-N(49)	1.881	Cu(44)-N(46)	1.874
Cu(43)-O(54)	1.835	Cu(44)-O(55)	1.860
Bond angles			
N(2)-Cu(43)-N(13)	146.98	N(23)-Cu(44)-N(34)	145.54
N(2)-Cu(43)-N(21)	83.31	N(23)-Cu(44)-N(42)	84.26
N(2)-Cu(43)-N(49)	87.24	N(23)-Cu(44)-N(46)	90.92
N(2)-Cu(43)-O(54)	111.38	N(23)-Cu(44)-O(55)	95.20
N(13)-Cu(43)-N(21)	86.07	N(34)-Cu(44)-N(42)	82.49
N(13)-Cu(43)-N(49)	88.87	N(34)-Cu(44)-N(46)	86.66
N(13)-Cu(43)-O(54)	101.25	N(34)-Cu(44)-O(55)	118.68
N(21)-Cu(43)-N(49)	154.06	N(42)-Cu(44)-N(46)	152.83
N(21)-Cu(43)-O(54)	100.50	N(42)-Cu(44)-O(55)	102.53
N(49)-Cu(43)-O(54)	105.43	N(46)-Cu(44)-O(55)	104.52

3.8.6 HOMO-LUMO analysis

The calculated values of quantum chemical parameters such as the energy of the highest occupied molecular orbitals (E_{HOMO}), the energy of the lowest unoccupied molecular orbitals (E_{LUMO}), energy gap (ΔE_g), ionization potentials (IP) and electron affinity (EA) are shown in Table 10. HOMO-LUMO analysis is one of the best methods to disclose the chemical stability of compounds [93]. Some representative HOMO-LUMO plots are shown in Fig. 36. These molecular orbitals can be employed to define electron donors and electron acceptors, which influence the biological activity and decide the way a molecule interacts with the living species [94, 95]. The examination of these molecular orbitals can reveal useful facts for the working mechanism of the biologically active compounds [96, 97]. The HOMO and LUMO of complexes **5-9** are localized primarily on tridentate hydrazone ligand except in **7** where it is on imidazolium cation and tridentate Schiff base. The fact that the copper(II) ions assistance makes to Frontier molecular orbitals in these complexes is following the finding of UV-vis spectra that there is electron transfer between copper(II) ions and the used ligands. Thus, HOMO-LUMO analysis suggests that the copper(II), the coordinated ligands and anions if any may be the reactive sites of present complexes. The molecular orbitals (Frontier molecular orbital) are shown in Fig. 36. The energies of Frontier molecular orbitals are important features for the chemical and bioactivity of compounds [98]. The negative magnitude of the HOMO and LUMO energies substantiate the stability of compounds.

Complex **7** showed the highest energy gap (ΔE_g) which reveals its higher stability and therefore is less reactive. Similarly, complex **8** exhibits the lowest energy gap (ΔE_g) revealing is the lowest stability and highest reactivity. The other two molecular properties like IP and EA are greatly important and values of these properties are helpful to estimate the global reactivity parameters. Both these parameters are related to one-electron orbital energies of the frontier molecular orbitals. The less value of IP denotes its electron donor capacity whereas the more EA reveals electron acceptor features of compound. The observed trend in IP and EA are **7** > **9** > **6** > **5** > **8** and **7** > **9** > **5** > **6** > **8**, respectively.

Table 10 Global reactivity descriptors of copper binuclear complexes **5-9** in eV calculated by DFT/B3LYP/LANL2DZ basic.

Molecular properties	Mathematical description	5	6	7	8	9
E_{HOMO}	Energy of HOMO	-3.7074	-4.5012	-7.2735	-2.6704	-5.9537
E_{LUMO}	Energy of LUMO	-3.6990	-3.2106	-5.1268	-1.7366	-5.0443
Energy gap	$\Delta E_g = E_{HOMO} - E_{LUMO}$	0.0084	1.2906	2.1467	0.9338	0.9094
Ionization potential (IP)	$IP = -E_{HOMO}$	3.7074	4.5012	7.2785	2.6704	5.9537
Electron Affinity (EA)	$EA = -E_{LUMO}$	3.6990	3.2106	5.1268	1.7366	5.0443
Electronegativity (χ)	$(\chi) = -½ (E_{Homo} + E_{Lumo})$	3.7032	3.8559	6.2001	2.2035	8.4758
Chemical Potential (μ)	$\mu = ½ (E_{Homo} + E_{Lumo})$	-3.7032	-3.8559	-6.2001	-2.2035	-8.4758

Global Hardness (η)	(η) = - ½ (E_{Homo} - E_{Lumo})	0.0042	0.6453	1.0733	0.4669	3.4315
Softness (S)	(S) = 1/2η	119.0476	0.7748	0.4658	0.9338	6.8631
Electrophilicity index(ω)	$\omega = \mu^2/2\eta$	1632.5821	11.5201	17.9071	5.1996	1.7157

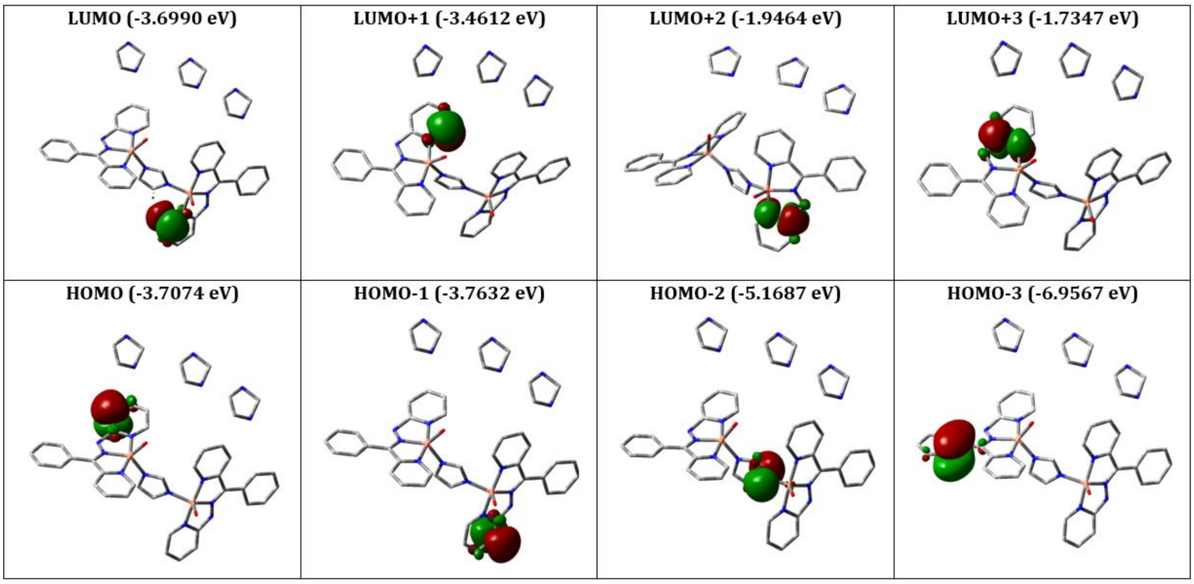

5

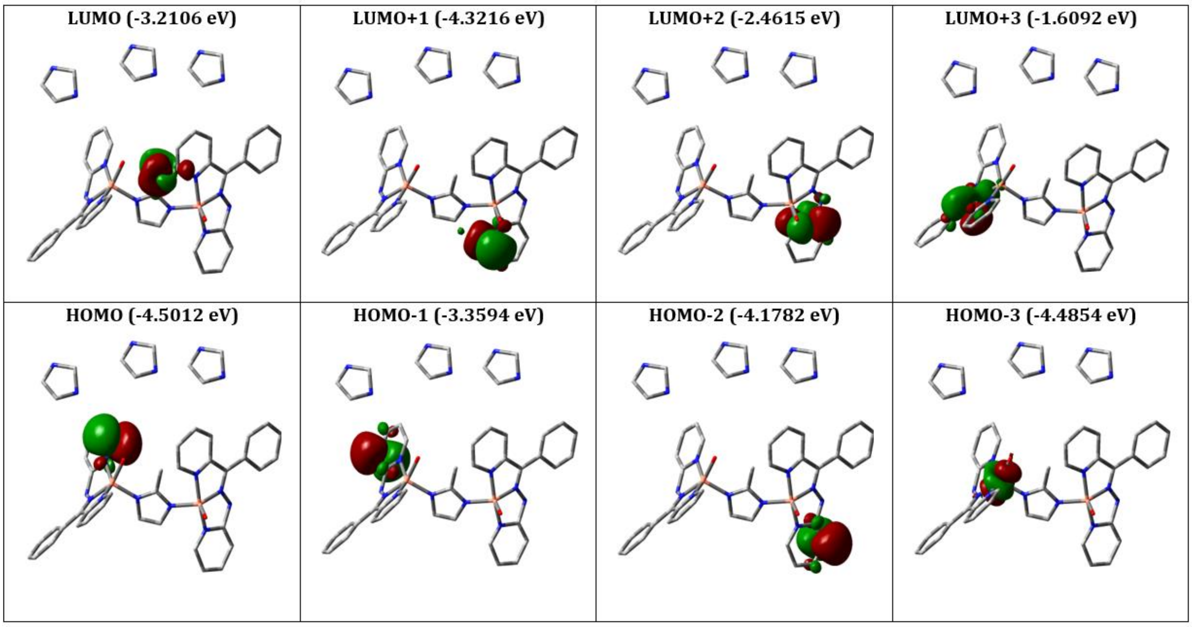

6

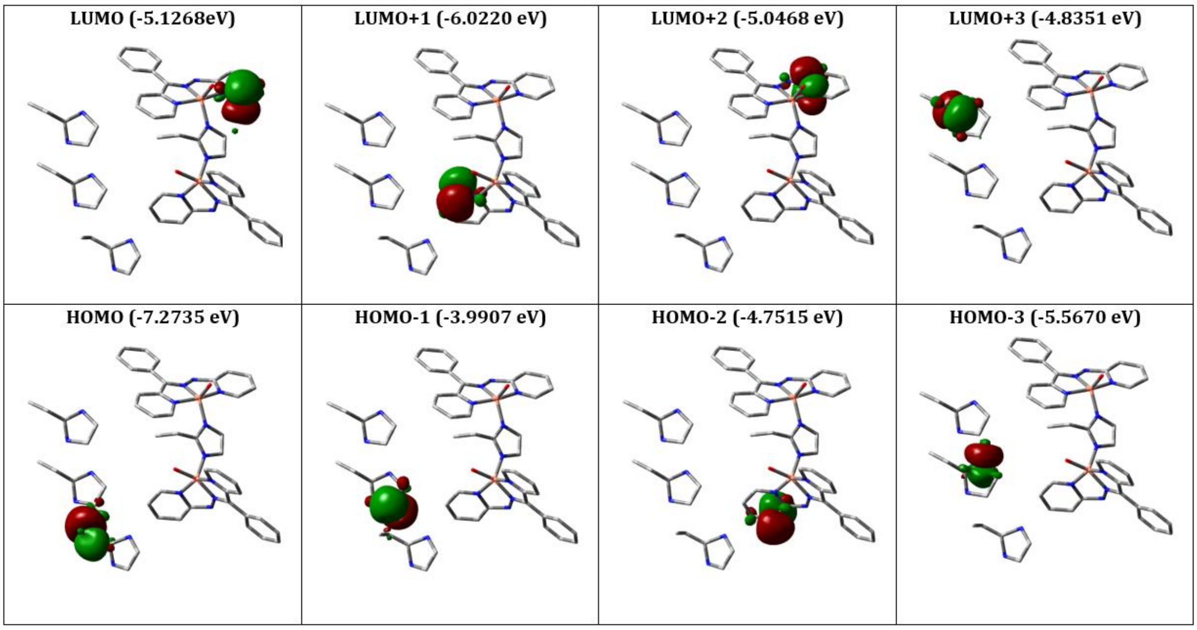
LUMO (-5.1268eV)
LUMO+1 (-6.0220 eV)
LUMO+2 (-5.0468 eV)
LUMO+3 (-4.8351 eV)
HOMO (-7.2735 eV)
HOMO-1 (-3.9907 eV)
HOMO-2 (-4.7515 eV)
HOMO-3 (-5.5670 eV)

7

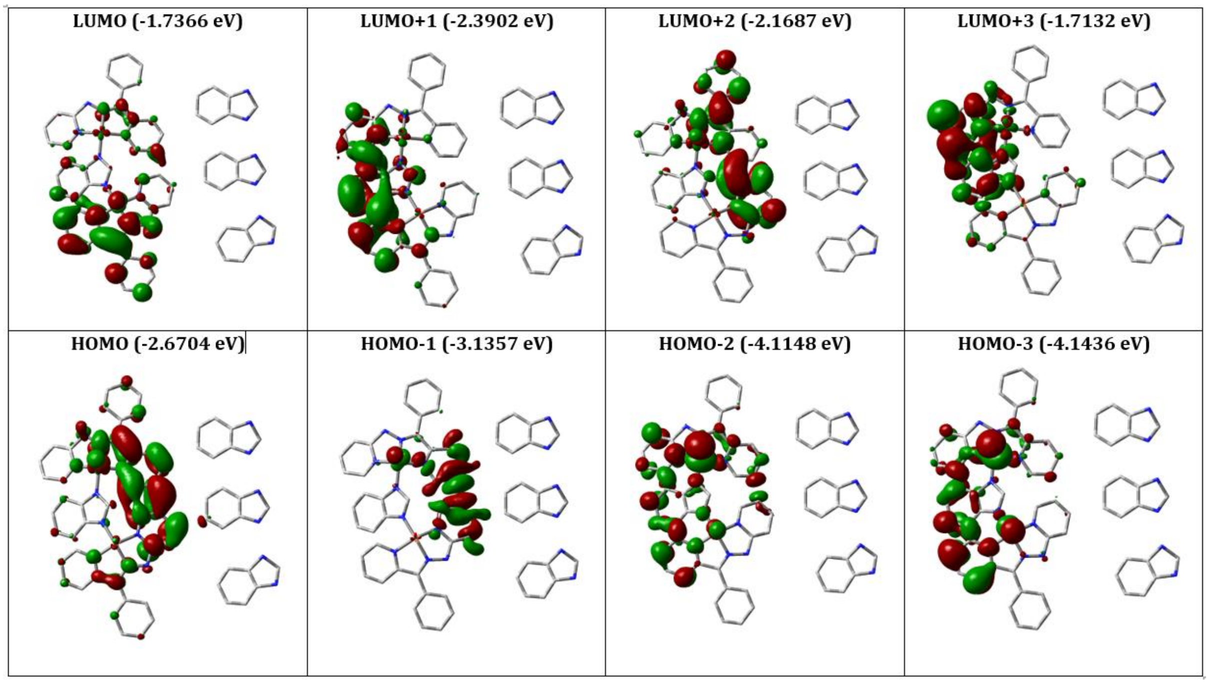
LUMO (-1.7366 eV)
LUMO+1 (-2.3902 eV)
LUMO+2 (-2.1687 eV)
LUMO+3 (-1.7132 eV)
HOMO (-2.6704 eV)
HOMO-1 (-3.1357 eV)
HOMO-2 (-4.1148 eV)
HOMO-3 (-4.1436 eV)

8

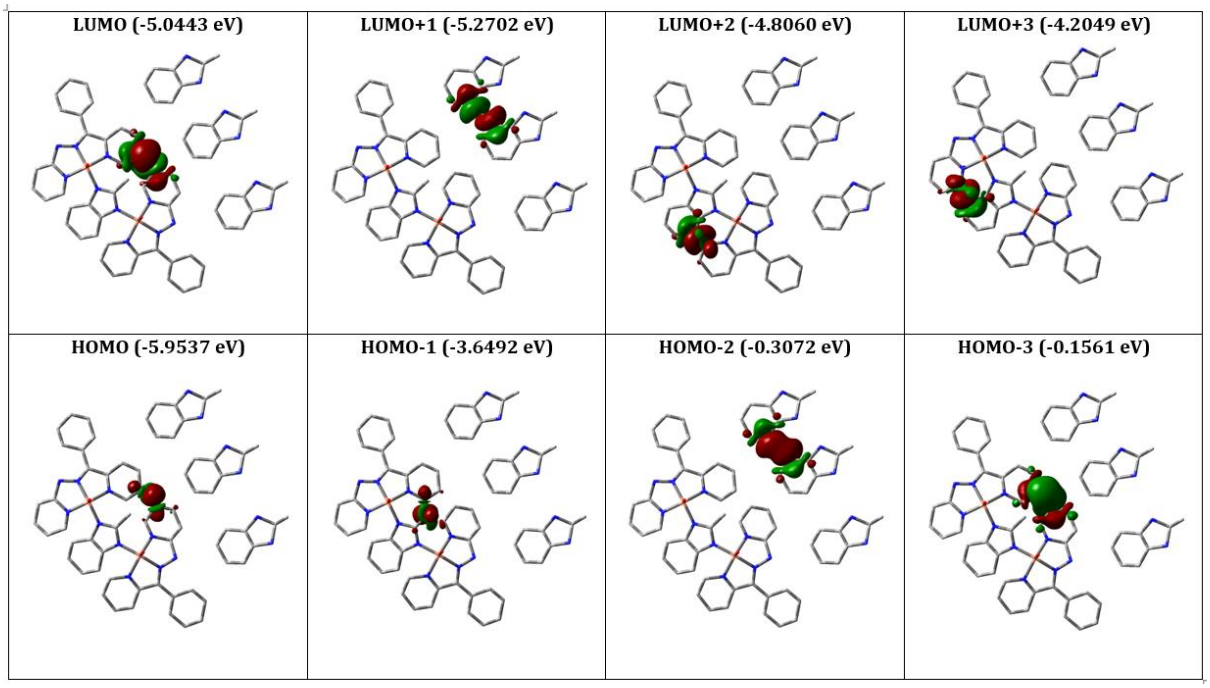

9

Fig. 36. HOMO-LUMO analysis of complex **5-9**.

3.8.7 Quantum Chemical reactivity descriptors

The chemical reactivity of any compound can be defined explained as the tendency to undergo a chemical reaction with another chemical compound. The nature of chemical interactions and the prediction of chemical reactivity of any compound is a complicated issue for chemists. Therefore, the present quantum chemical reactivity study aims to find a correlation between the biological activities of these synthesized complexes with the most effective quantum chemical descriptors. For complexes, **5-9** different quantum chemical descriptors like chemical potential (μ), softness (s) and electrophilicity index (ω) have been calculated [99, 100]. These parameters are collected in Table 10.

From the values given in Table 10, it is clear that among these complexes, **7** has the highest value of Ƞ (1.0733 eV) and is chemically soft and more active among all. The observed trend in Ƞ is as: **9** >**7** > **6** > **5** > **8**. This trend is inconsistent with the ΔE_g. The chemical potential (μ) shows an idea about the charge transfer within any complex in its ground state. The observed trend in μ is as: **9** > **7** > **6** > **5** > **8**. The values ΔE_g and S show that these complexes reveal the highest chemical reactivity [101]. The electrophilicity index (ω) is a thermodynamic property of a compound that exploits the change in energy when the compound becomes saturated by adding electrons. The value of ω shows a crucial role in demonstrating the chemical reactivity of compounds. The perusal of values of ω (Table 10) shows that **9** has the lowest value (1.7157) and is nucleophilic, whereas **5** has the highest value of S for 119.0476 eV and is indicating its electrophilic nature. The electronegativity (χ), illustrated the ability of a chemical compound to attract the electron towards itself. For present complexes, **7** has the highest χ value (6.2001 eV) among all and thus it is the best electron acceptor. The order in χ in complexes **5-9** is as: **9** > **5** > **6** > **8** > **9** > **7**.

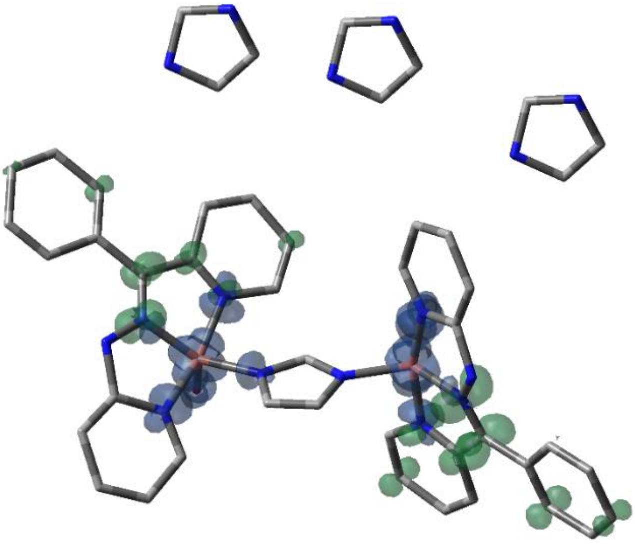

5

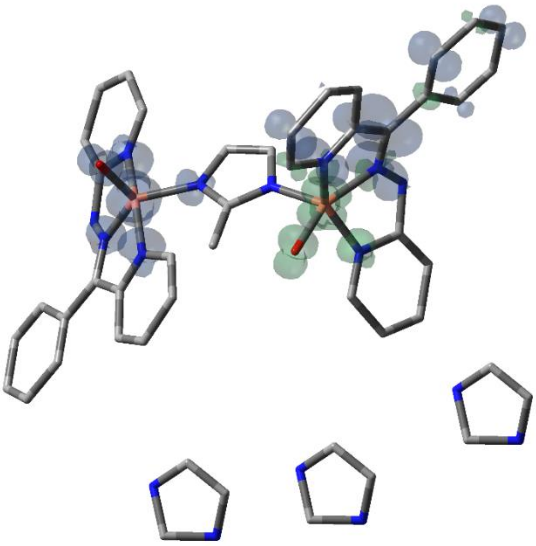

6

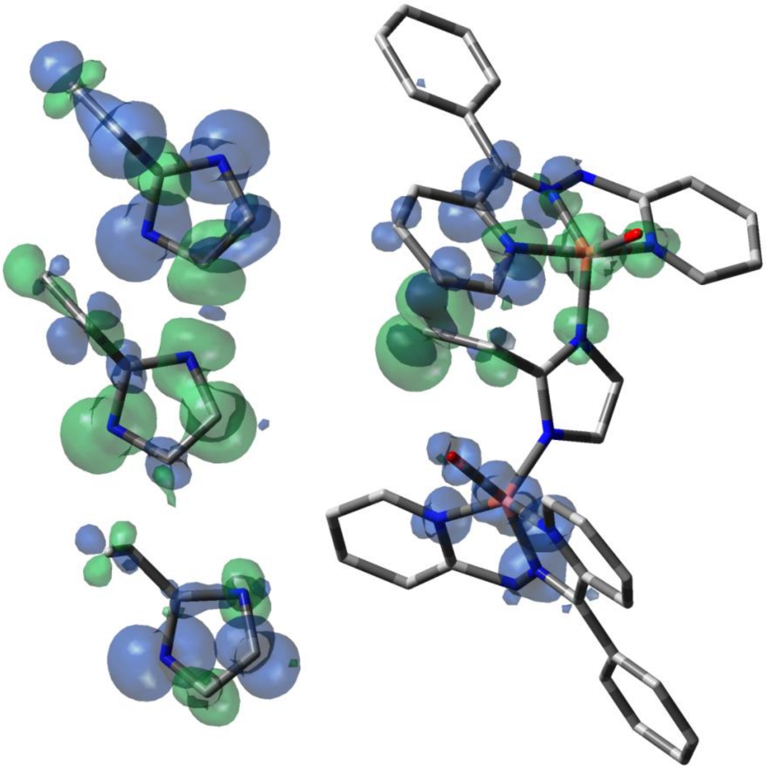

7

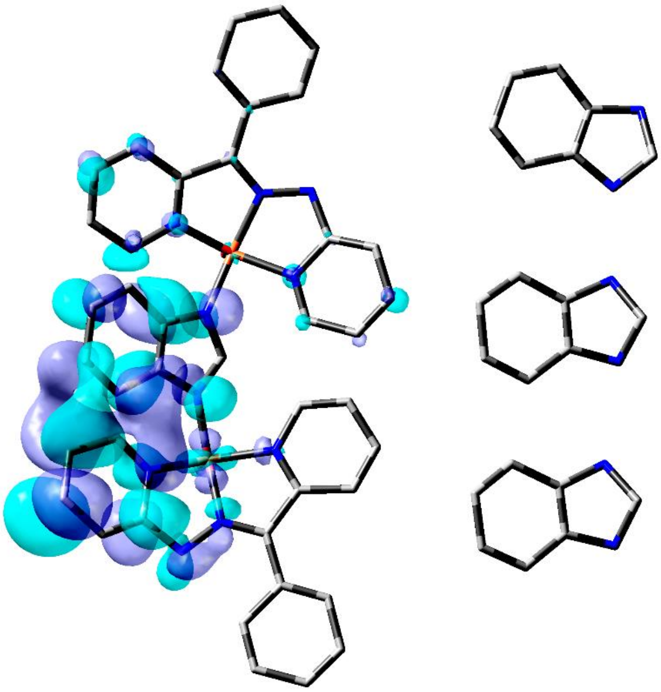

8

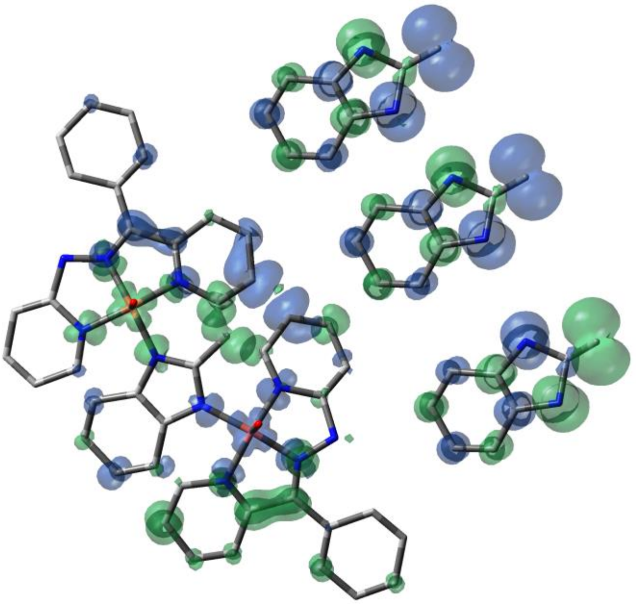

9

Fig. 37. Spin density plots of complexes **5-9**.

3.8.8 Mulliken charge analysis

Mulliken charges of complexes **5-9** are evaluated from the Mulliken population analysis and presented in Table 11. The atomic charge population of a chemical compound is closely associated with the active site in its nucleophilic or electrophilic reaction and charge interactions between two compounds [102]. These interactions perform a crucial role in inhibiting the growth of fungi [103]. Polarization decreases due to the transfer of charges of the atom [104]. The Cu^{2+}center gains electron to show positive charges in the range 0.613 e for complexes **5-9**. While other involved atoms lose electrons and are responsible for the reduction of polarity in the complexes and thus assist to enhance the bioactivities since the reduction of the polarity of the atoms contributes to the enhanced diffusion of the metal complexes into the lipid membranes [104-106].

Table 11 Spin density and Mulliken population analysis of complexes **5-9**.

Atoms	Mulliken charges	Spin density
5		
Cu43	0.5261	0.5780
Cu44	0.4196	0.5664
N(2)	-0.2126	0.1133
N(13)	-0.2525	0.0517

N(21)	-0.2704	-0.0544
N(23)	-0.1864	0.1129
N(34)	-0.2429	0.0164
N(42)	-0.2754	-0.0867
N(46)	-0.3779	0.0114
N(49)	-0.3690	0.0548
O(50)	-0.6968	0.0647
O(51)	-0.6624	0.1154
6		
Cu43	0.5283	0.5701
Cu44	0.4107	-0.5385
N(2)	-0.2017	0.1151
N(13)	-0.3719	0.1257
N(21)	-0.2679	0.0684
N(23)	-0.2664	-0.0787
N(34)	-0.2893	0.0805
N(42)	-0.2990	0.1144
N(46)	-0.3589	0.0011
N(49)	-0.3767	0.0626
O(50)	-0.6886	0.0972
O(51)	-0.6467	-0.1416
7		
Cu43	0.5382	-0.5536
Cu44	0.5316	0.5873
N(2)	-0.2503	-0.1133
N(13)	-0.2555	-0.1829
N(21)	-0.2964	0.0400
N(23)	-0.3011	0.1206
N(34)	-0.3034	0.1058
N(42)	-0.2502	0.1810
N(46)	-0.3990	0.0067
N(49)	-0.4050	0.0869
O(50)	-0.6479	-0.0091
O(51)	-0.6504	0.0716
8		
Cu43	0.5715	0.6002
Cu44	0.5681	0.6039
N(2)	-0.3227	0.0949
N(13)	-0.2789	0.0989
N(21)	-0.2680	-0.0284
N(23)	-0.2692	0.1475
N(34)	-0.3215	0.0925

N(42)	-0.2533	0.1008
N(46)	-0.2859	0.1034
N(49)	-0.2432	0.0886
O(54)	-0.7241	0.0055
O(55)	-0.7062	0.0370
9		
Cu43	0.5919	-0.5309
Cu44	0.5506	0.5387
N(2)	-0.3338	-0.1022
N(13)	-0.2812	0.0613
N(21)	-0.3226	0.0375
N(23)	-0.3638	0.0835
N(34)	-0.3202	-0.0183
N(42)	-0.2824	-0.0874
N(46)	-0.3254	0.0971
N(49)	-0.3104	-0.1119
O(54)	-0.6757	0.0005
O(55)	-0.6642	-0.0012

The main delocalization of the single unpaired d-electron from copper(II) center in these binuclear complexes is to primarily donor atoms of tridentate hydrazone ligand and bridging imidazolate ions in complex **5** and **6**. In the remaining complexes (**7** and **8**) it is both on imidazolium cations and donor atom of bridging and tridentate ligands. Some representative spin density plots are shown in Fig. 37.

3.9 Antioxidant superoxide dismutase (SOD) activity

The SOD activity of complexes **1-9** was measured by the nitro blue tetrazolium chloride (NBT) assay using the alkaline DMSO as a source of superoxide anion ($O_2^{\cdot -}$) [107-110]. NBT reduced by $O_2^{\cdot -}$ forming blue formazan (MF^+), which is kinetically followed using a spectrophotometer at 560 nm [111]. The concentrations of SOD mimics required to obtain 50% inhibition of the reduction (denoted as IC_{50}) were evaluated for complexes **1-9** Fig. 38a and 38b. Obtained IC_{50} values along with other SOD data are collected in Table 12. In the same Table 12 SOD data of some similar SOD mimics are also given for comparison [111-114].

Table 12 The antioxidant SOD activity IC_{50} and kinetic catalytic constant for complexes **1-9**.

Compound	IC_{50} (µmol)	SOD activity (µmol^{-1})	k_{M_cCF} (molL)$^{-1}$s^{-1} x 10^4	References
$[Cu_IL^1Im]$	2.5	-	-	111
$[CuZnL^1Im]$	30	-	-	111
$[Na_2Cu_4Na_2(TACNTA)_4.(H_2O)_6].(H_2O)_{26}$	1.08	-	-	112
$[Cu_2(\mu SCN)_2L^2_2]$	24	41.66	13.86	40
$[Cu(L^2)(HL^2)][Cu(L)(HL^2)]ClO_4.H_2O$	55	18.8	6.05	77
$[Cu(L^2)(NO_3)(\mu$-2-aminopyrazine$)Cu(L^2)(NO_3)].2H_2O$	15	66.67	22.17	77
Vc	852	1.17	0.39	113
1	25	40	13.30	This work
2	40	25	8.32	This work
3	30	33.33	11.08	This work
4	50	20	6.65	This work
5	24	41.67	13.86	This work
6	40	25	8.32	This work
7	38	26.31	8.75	This work
8	42	23.80	7.92	This work
9	25	40	13.30	This work

L^1 = 5,5”pentaazater-pyridinophane, TACNTA = 1,4,7-triazacyclononane-1,4,7-triacetate, L^2 = N’-[(E)-phynyl(pyridine-2-yl)methylidne] acetohydrazide and Vc = Vitamin C

The mild activity shown by complexes **1-9** can be exemplified by rigidity enforced by the two pyridine rings of L that would not allow significant molecular rearrangements along the catalytic pathway. Another possible reason may be analyzed by considering a probable correlation between the strength of the equatorial field and superoxide activity [115]. Similar SOD activity was reported for other copper(II) complexes [40, 77, 111-114]. The proposed model for the catalytic pathway is shown in Scheme 4. In the very first step (I) $O_2^{\cdot -}$ displaces the axial H_2O molecule and inner-sphere electron transfer takes place in between the coordinated $O_2^{\cdot -}$ and the copper(II) centre of the mimic. The $O_2^{\cdot -}$ reduces the Cu(II) to Cu(I) with the simultaneous breaking of the bond between carboxylate group and copper(II) centre and oxygen molecule is released. In step (II) reoxidation of Cu(I) to Cu(II) by the second $O_2^{\cdot -}$ molecule reform the bond between water molecule along with transfer of a proton to hydro-peroxide ion and finally neutral H_2O_2 released.

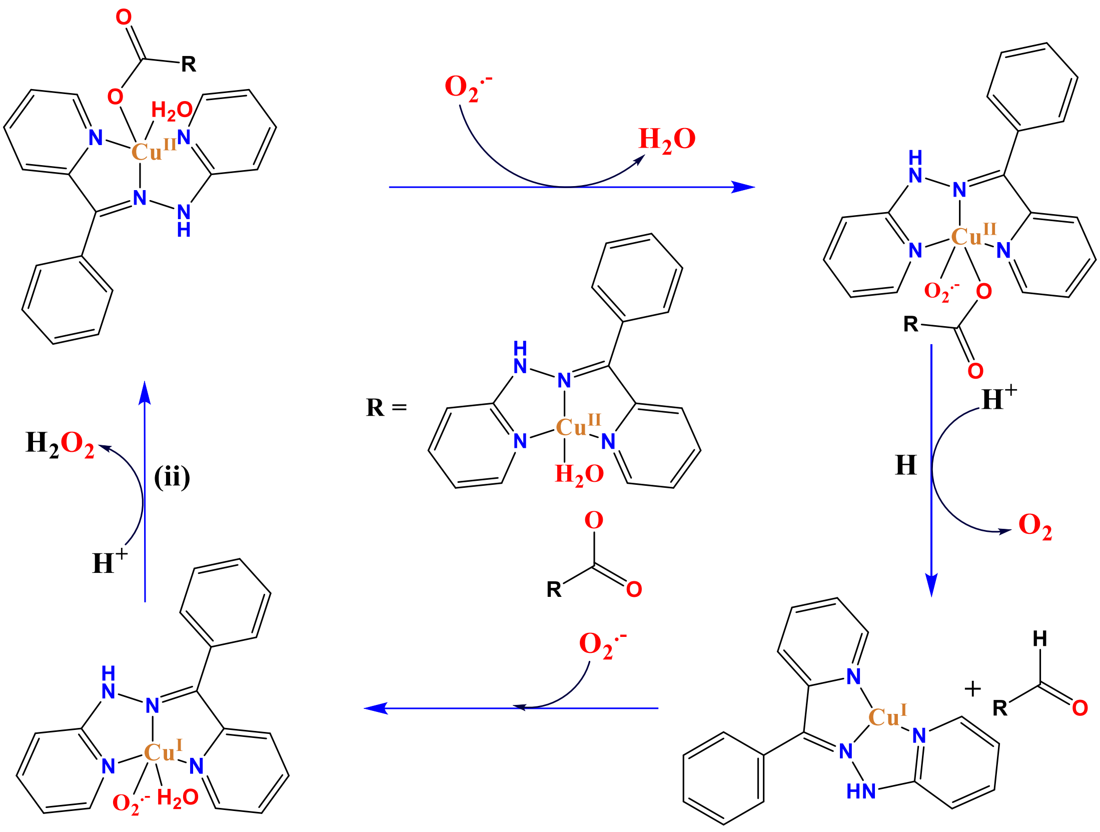

Scheme 4 The proposed catalytic model for the catalytic pathway.

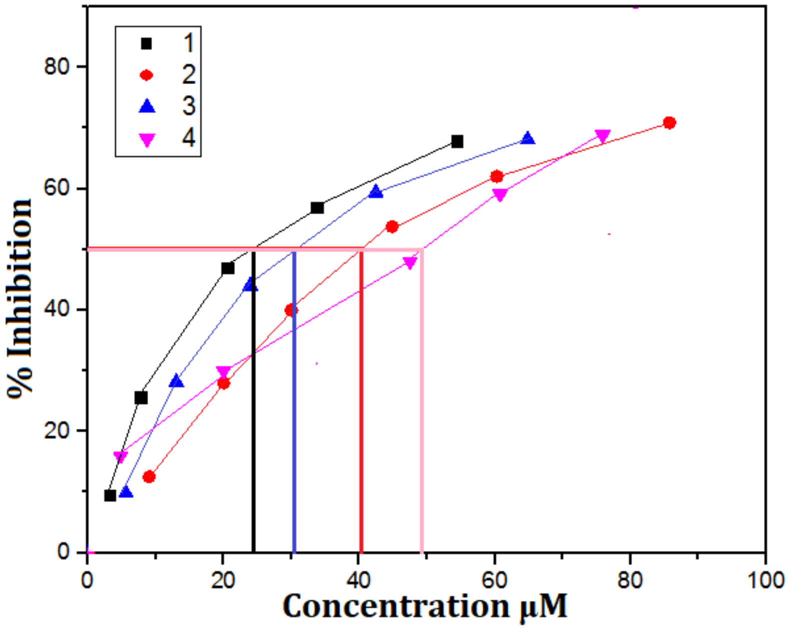

Fig. 38(a) SOD graph of complexes **1-4.**

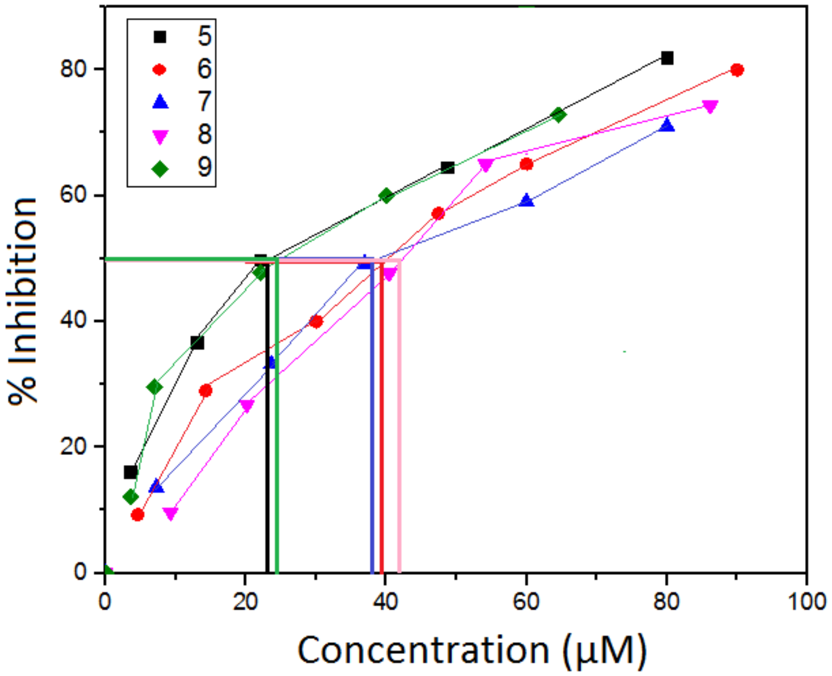

Fig. 38(b) SOD graph of complexes **5-9.**

4 Conclusions

In this chapter, we have synthesised nine binuclear complexes by using NNN (L = 2-[(E)-phenyl(pyridine-2-yl-hydrazono)methyl]pyridine) containing inorganic salts with compositions, $[(L)Cu(H_2O)(C_2O_4)(H_2O)Cu(L)]C_2O_4$ (**1**), $[(L)Cu(H_2O)(C_3H_2O_4)(H_2O)Cu(L)]C_3H_2O_4$ (**2**), $[(L)Cu(H_2O)(C_4H_4O_4)(H_2O)Cu(L)]C_4H_4O_4$ (**3**), $[(L)Cu(H_2O)(C_8H_4O_4)(H_2O)Cu(L)]C_8H_4O_4$ (**4**), $[(L)Cu(H_2O)(ImH)(H_2O)Cu(L)](ImH)_3$ (**5**), $[(L)Cu(H_2O)(2\text{-}MeImH)(H_2O)Cu(L)](2\text{-}MeImH)_3$ (**6**), $[(L)Cu(H_2O)(2\text{-}EthImH)(H_2O)Cu(L)](2\text{-}EthImH)_3$ (**7**), $[(L)Cu(H_2O)(BenzImH)(H_2O)Cu(L)](BenzImH)_3$ (**8**) and $[(L)Cu(H_2O)(2\text{-}MeBenzImH)(H_2O)Cu(L)](2\text{-}MeBenzImH)_3$ (**9**). These complexes have been characterized by various physicochemical techniques. The Geometry optimized structures of complexes **1-9** were carried out using density functional theory calculations at B3LYP/LANL2DZ level. In these binuclear complexes, each copper(II) centre has distorted square pyramidal and distorted trigonal pyramid geometry. These complexes also show good antioxidant activity.

References

1 S. Roy, M. Bohme, S.P. Dash, M. Mohanty, A. Buchholz, W. Plass, S. Majumder, S. Kulanthaivel, I. Banerjee, H. Reuter, W. Kaminsky, R. Dinda, Inorg. Chem. 57 (2018) 5767-5781.

2 A. Bianchi, E.D.-Pinar, E.G. Espana, C. Giorgi, F. Pina, Coord. Chem. Rev. 260 (2014) 156-215.

3 R. Karmakar, C.R. Choudhury, D.L. Hughes, G.P.A. Yap, M.S.E. Fallah, C. Desplanches, J.-P. Sutter, S. Mitra, Inorg. Chim. Acta 359 (2006) 1184–1192.

4 C. Adhikary, D. Mal, K.I. Okamoto, S. Chaudhuri, S. Koner, Polyhedron 25 (2006) 2191–2197.

5 S. Banerjee, M.G.B. Drew, C.Z. Lu, J. Tercero, C. Diaz, A. Ghosh, Eur. J. Inorg. Chem. (2005) 2376–2383.

6 N.R. Sangeetha, S. Pal, Polyhedron 19 (2000) 1593–1600.

7 Y. Singh, R.N. Patel, S.K. Patel, A.K. Patel, N. Patel, R. Singh, R.J. Butcher, J.P. Jasinski, A. Gutierrez, Polyhedron 171 (2019) 155–171.

8 Y.P. Singh, R.N. Patel, Y. Singh, D.C. Lazarteb, R.J. Butcher, Dalton Trans. 46 (2017) 2803–2820.

9 N. Petrovic, A. Comi, M.J. Ettinger, J. Biol. Chem. 271 (1996) 28331–28334.

10 P. Kapoor, A. Pathak, R. Kapoor, P. Venugopalan, M. Corbella, M. Rodriguez, J. Robles, A. Llobet, Inorg. Chem. 41 (2002) 6153–6160.

11 M. Rodrı-guez, A. Llobet, M. Corbella, Polyhedron 19 (2000) 2483–2491.

12 M. Rodrı-guez, A. Llobet, M. Corbella, A.E. Martell, Reibenspies, J. Inorg. Chem. 38 (1999) 2328–2334.

13 E. Pardo, J. Faus, M. Julve, F. Lloret, M.C. Mun-oz, J. Cano, X. Ottenwaelder, Y. Journaux, R. Carrasco, G. Blay, I. Fernandez, R. Ruiz-Garcı-a, J. Am. Chem. Soc. 125 (2003) 10770–10771.

14 G. Psomas, C.P. Raptopoulou, L. Iordanidis, C. Dendrinou-Samara, V. Tangoulis, D.P. Kessissoglou, Inorg. Chem. 39 (2000) 3042–3048.

15 S. Ferlay, A. Jouaiti, M. Loi, M.W. Hosseini, A. De Cian, P. Turek, New J. Chem. (2003) 1801–1805.

16 J. Cano, E. Ruiz, P. Alemany, F. Lloret, S. Alvarez, J. Chem. Soc. Dalton Trans. (1999) 1669–1676.

17 L.M. Mirica, X. Ottenwaelder, T.D.P. Stack, Chem. Rev. 104 (2004) 1013-1046.

18 S. Itoh, S. Fukuzumi, Acc. Chem. Res. 40 (2007) 592-600.

19 I.A. Koval, P. Gamez, C. Belle, K. Selmeczi, J. Reedijk, Chem. Soc. Rev. 35 (2006) 814-840.

20 F.G. Mutti, G. Zoppellaro, M. Gullotti, L. Santagostini, R. Pagliarin, K. K. Anderson, L. Casella, Eur. J. Inorg. Chem. (2009) 554-566.

21 B. Sreenivasulu, Aust. J. Chem. 62 (2009) 968-979.

22 Z.A. Siddiqi, M. Shahid, M. Khalid, S. Kumar, Eur. J. Med. Chem. 44 (2009) 2517-2522.

23 A.L. Abuhijleh, J. Inorg. Biochem. 68 (1997) 167-175.

24 M. Devereux, D.O. Shea, M.O. Connor, H. Grehan, G. Conner, M. McCann, G. Rosair,

F. Lyng, A. Kellett, M. Walsh, D. Egan, B. Thati, Polyhedron 26 (2007) 4073-4084.

25 V. Balasubramanian, M. Ezhevskaya, H. Moons, M. Neuburger, C. Cristescu, S. V. Doorslaer, C. Palivan, Phys. Chem. Chem. Phys. 11 (2009) 6778-6787

26 A.L. Abuhijleh, C. Woods, Inorg. Chem. Commun. 5 (2002) 269-273.

27 B. J. Dervall, Nature, 189 (1961) 311.

28 D. Klug, J. Rahani, I. Fridovich, J. Biol. Chem., 247 (1972) 483-4842.

29 J.R.J. Sorenson, Prog. Med. Chem. 26 (1989) 437-568.

30 J.E. Weder, C.T. Dillon, T.W. Hambley, B.J. Kennedy, P.A. Lay, J.R. Biffin, H.L. Regtep, N.M. Davies, Coord. Chem. Rev. 232 (2002) 95-126.

31 T. Fujimori, S. Yamada, H. Yasui, H. Sakurai, Y.I.T. Ishida, J. Biol. Inorg. Chem. 10 (2005) 831-841.

32 C.T. Dillon, T.W. Hambley, B.J. Kennedy, P.A. Lay, O. Zhou, N.M. Davies, J.R. Biffin, H.L. Regtop, Chem. Res. Toxicol. 16 (2003) 28-37.

33 D.K. Demertzi, A. Galani, M.A. Demertzis, S. Skoulika, C. Kotoglou, J. Inorg, Biochem. 98 (2004) 358-364.

34 G.W. Wangila, K.K. Nagothu, R. Steward III, R. Bhatt, P.A. Iyere, W.M. Willingham, J.R.J. Sorenson, S.V. Shah, D. Portilla, Toxicol. in Vitro 20 (2006) 1300-1312.

35 M. Valko, D. Leibfritz, J. Moncol, M.T. Cronin, M. Mazur, J. Teleser, Int. J. Biochem. Cell Biol. 39 (2007) 44-84.

36 R.N. Patel, S.P. Rawat, M. Choudhary, V.P. Sondhiya, D.K. Patel, K.K. Shukla, D.K. Patel, Y. Singh, R. Pandey, Inorg. Chim. Acta 392 (2012) 283-291.

37 Y. Singh, R.N. Patel, S.K. Patel, A.K. Patel, N. Patel, R. Singh, R.J. Butcher, J.P. Jasinski, A. Gutierrez, Polyhedron 171 (2019) 155-171.

38 R.N. Patel, D.K. Patel, V.P. Sondhiya, K.K. Shukla, Y. Singh, A. Kumar, Inorg. Chim. Acta 405 (2013) 209-217.

39 R.N. Patel, S.K. Patel, D. Kumhar, N. Patel, A.K. Patel, R.N. Jadeja, N. Patel,R.J. Butcher, M. Cortijo, S. Herrero, Polyhedron 188 (2020) 114687.

40 Y. Singh, R.N. Patel, S.K. Patel, R.N. Jadeja, A.K. Patel, N. Patel, H. Roy, P. Bhagriya, R. Singh, R.J. Butcher, J.P. Jasinski, S. Herrero, M. Cortijo, Inorg. Chim. Acta 503 (2020) 119371

41 G.A. Petersson, M.A. Al-Laham, J. Chem. Phys. 94 (1991) 6081-6090.

42 P.J. Hay, W.R. Wadt, J. Chem. Phys. 82 (1985) 270-283.

43 M.J. Frisch, G.W. Trucks, H.B. Schlegel, G.E. Scuseria, M.A. Robb, J.R. Cheeseman, G. Scalmani, V. Barone, B. Mennucci, G.A. Petersson, H. Nakatsuji, M. Caricato, X. Li, H.P. Hratchian, A.F. Izmaylov, J. Bloino, G. Zheng, J.L. Sonnenberg, M. Hada, M. Ehara, K. Toyota, R. Fukuda, J. Hasegawa, M. Ishida, T. Nakajima, Y. Honda, O. Kitao, H. Nakai, T. Vreven, J.A. Montgomery Jr., J.E. Peralta, F. Ogliaro, M. Bearpark, J.J. Heyd, E. Brothers, K.N. Kudin, V.N. Staroverov, R. Kobayashi, J. Normand, K. Raghavachari, A. Rendell, J.C. Burant, S.S. Iyengar, J. Tomasi, M. Cossi, N. Rega, J.M. Millam, M. Klene, J.E. Knox, J.B. Cross, V. Bakken, C. Adamo, J. Jaramillo, R. Gomperts, R.E. Stratmann, O. Yazyev, A.J. Austin, R. Cammi, C. Pomelli, J.W. Ochterski, R.L. Martin, K. Morokuma, V.G. Zakrzewski, G.A. Voth, P. Salvador, J.J. Dannenberg, S. Dapprich, A.D. Daniels, O. Farkas, J.B. Foresman, J.V. Ortiz, J.

Cioslowski, D.J. Fox, Gaussian 09, Revision D.01, Gaussian Inc., Wallingford CT, (2009).

44 R. Bauernschmitt, R. Ahlrichs, Chem. Phys. Lett. 256 (1996) 454-464.

45 M. Cossi, N. Rega, G. Scalmani, V. Barone, J. Compute. Chem. 224 (2003) 669-681.

46 T. Mosmann, J. Immunol. 65 (1993) 55-63.

47 R.N. Patel, D.K. Patel, K.K. Shukla, Y. Singh, J. Coord. Chem. 66 (2013) 4131-4143.

48 R.G. Bhirud, T.S. Shrivastava, Inorg. Chim. Acta. 173 (1990) 121–125.

49 R. Konecny, J. Li, C.L. Fisher, V. Dillet, D. Bashford, L. Noodleman, Inorg. Chem. 38 (1999) 940-950.

50 A.K. Patel, R.N. Jadeja, H. Roy, R.N. Patel, S.K. Patel, R.J. Butcher, M. Cortijo, S. Herrero, Polyhedron 186 (2020) 114624.

51 W.J. Geary, Coord. Chem. Rev., 1971, 7, 81–122.

52 M. Sutradhar, M.V. Kirillova, M.F.C.G. Silva, C.M. Liu, A.J.L. Pombeiro, Dalton Trans. 42 (2013) 16578-16587.

53 L. Valencia, R. Bastida, M.C.F. -Fernández, A. Macías, M. Vicente, Inorg. Chim. Acta. 358 (2005) 2618-2628.

54 A.W. Addison, T.N. Rao, J. Reedijk, J.V. Rijn, G.C. Verschoor, J. Chem. Soc. Dalton Trans. 7 (1984) 1349-1356.

55 M. Melnik, Coord. Chem. Rev. 36 (1981) 1-44.

56 M. Melnik, M.D. Jurco, M. Handlovic, Inorg. Chim. Acta 86 (1984) 185-190.

57 N.D. Chasteen, Inorg. Chem. 10 (1971) 2339.

58 J.R. Wasson, C.I. Shyr, C. Trapp, Inorg. Chem. 7 (1968) 469-473.

59 A. Sreekanth, M.R.P. Kurup, Polyhedron 22 (2003) 3321-3332.

60 X.Wang, J. Ding, J.D. Ranford, J.J. Vittal, J. Appl. Phys. 93 (2006) 7819-7821.

61 I.M. Procter, B.J. Hathaway, P. Nicholls, J. Chem. Soc. A, (1968) 1678-1684.

62 M.J. Bew, B.J. Hathaway, R.R. Faraday, J. Chem. Soc. Dalton Trans. (1972) 1229-1237.

63 D. Reinen, C.Friebal, Inorg. Chem. 23 (1984)791-798.

64 F.E. Mabbs, Chem. Soc. Rev. 22 (1993)313-324.

65 A.H. Maki, B.R. McGasecy, J. Chem. Phys. 29 (1958) 31.

66 Á.G. -Raso, J.J. Fiol, B. Adrover, P. Tauler, A. Pons, I. Mata, E. Espinosa, E. Molins, Polyhedron 22 (2003) 3255-3264.

67 B. Sarkar, M. G.B. Drew, M. Estrader, C. Diaz, A. Ghosh, Polyhedron 27 (2008) 2625 -2633.

68 R.N. Patel, S.P. Rawat, M. Choudhary, V.P. Sondhiya, D.K. Patel, K.K. Shukla, D.K. Patel, Y. Singh, R. Pandey, Inorg. Chim. Acta 392 (2012) 283-291.

69 A. Trugillo, F. Justaud, L. Toupet, O. Cador, D. Carrillo, C. Manzur, J.R. Hamon, New J. Chem. 35 (2011) 2027-2036.

70 J.P. Lancaster, The Bioinorganic Chemistry of Nickel, Wiley-VCH, Newyork, (1998).

71 P. Zanello, Inorganic Electrochemistry: Theory, practice and applications, The Royal Society of Chemistry, UK, (2003) p.110.

72 C. Belle, C. Beguin, I. Gautier-Luneau, S. Hamman, C. Philouze, J. L. Pierre, F. Thomas, S. Torelli, E. Saint-Aman, M. Bonin, Inorg. Chem. 41 (2002) 479-491.

73 S.K. Mandal, K.J. Nag, J. Chem. Soc., Dalton Trans. (1983) 2429-2434.

74 C. Creutz, H. Taube, J. Am. Chem. Soc. 95 (1935) 1086-1094.

75 W.H. Morrison, S. Krogsrud, D.N. Hendrickson, Inorg. Chem. 12 (1973) 1998–2004.

76 R.R. Gagne, C.A. Keval, T.J. Smith, M.C. Cimolino, J. Am. Chem. Soc. 101 (1979) 4571-4580.

77 R.N. Patel, Y. Singh, Y.P. Singh, A.K. Patel, N. Patel, R. Singh, R.J. Butcher, J.P. Jasinski, E. Colacio, M.A. Palacios, New J. Chem. 42 (2018) 3112-3136.

78 A.W. Addison, T.N. Rao, J. Reedisk, J. van Rijn, J. Chem. Soc. Dalton Trans. (1984) 1349-1356.

79 N. Chaudhary, S. Bee, A. Gupta, P. Tandon, Comp. Theor. Chem. 1016 (2013) 8-11.

80 L. Von Szentpaly, Int. J. Quantum. Chem. 76 (2000) 222-234.

81 R.G. Parr, L Von szentpoly , S. Liu, J. Am. Chem. Soc. 121 (1999) 1922-1924.

82 P.Geerling, F.de Proft, J.M.L. Martin, Theoretical and Computational Chemistry 4, Elsevier, Amsterdam, 1996, p.773

83 L. Shen, H.Y. Zhang, H.F. Ji, J. Mol. Struct. Theo. Chem. 817 (2007)161-162.

84 G. de Oliveira, J.M. Martin, F. de Proft, P. Geerling, Phys. Chem. A60 (1999) 1034-1045.

85 H.F. Ji, H.Y. Zhang, Biorg. Med. Chem. Lett. 15 (2005) 21-24.

86 H.F. Li, H.Y. Zhang, Chem. Res. Toxicol. 17 (2004) 471-475.

87 R.J.F. Branco, P.A. Fernedes, M.J. Ramos, Theor. Chem. A.C.C. 115 (2006) 27-31.

88 R.J.F. Branco, P.A. Fernedes, M.J. Ramos, J. Mol. Struct. Theochem. 729 (2005)141-146.

89 A.A. Soliman, M.A. Amin, A.M. Sayed, A.A.A.A. Hussian, W. Linert, Polyhedron 161 (2018) 213-221.

90 E. Ruiz, J. Cirera and S. Alvarej, Coord. Chem. Rev. 249 (2005) 2649-2660.

91 R.N. Patel, S.K. Patel, D. Kumhar, N. Patel, A.K. Patel, R.N. Jadeja, N. Patel, R.J. Butcher, M.Cortijo, S. Herrero, Polyhedron 188 (2020)114687.

92 Y. Singh, R.N. Patel, S.K. Patel, A. K. Patel, Neetu Patel, Rita Singh, R.J. Butcher, J. P Jasinski, A. Gutierrez, Polyhedron 171 (2019) 155-171.

93 S. Gunasekaran, R.A. Balaji, S. Kumeresan, G. Anand, and S. Srinivasan, Can. J. Anal. Sci. Spectrosc. 53 (2008) 149-162.

94 J. X. Mu, Z. W. Zhai, M. Y. Yang, Z. H. Sun, H. K. Wu and X. H. Liu, Crystals 6 (2016) 4.

95 Larif, A. Adad, R. Hmammouchi, A.I. Taghki, A. Soulaymani, A. Eimidaoui, M. Bouachrine, T. Lakhlifi, Arabian J. Chem. 10 (2017) 946–955.

96 J.X. Mu, Y.X. Shi, M.Y. Yan, Z.H. Sun, X.H. Liu, Molecules 21 (2016) 68.

97 W. Boufas, N. Dupont, M. Berredjem, K. Berrezag, I. Becheker, H. Berredjem, N.E. Aouf, J. Mol. Struct. 1074 (2014) 180–185.

98 A.M. Mansour, Inorg. Chim. Acta 394 (2013) 436-445.

99 R.G. Pearson, Proc. Natl. Acad. Sci. U. S. A. 83 (1986) 8440-8441.

100 A.K. Chandra, T. Uchimaru. Phys. Chem. A 105(2001) 3578–3582.

101 P. Thanikaivelan, V. Subramanian, J.R. Rao, B.U. Nair, Chem. Phys. Lett. 323 (2000) 59-70.

102 P. Govindasamy , S. Gunasekaran, S. Srinivasan, Spectrochim. Acta A 130 (2014) 329-336.

103 K. C. Zheng, J. P. Wang, W. L. Peng, Y. Shen, F. C. Yun, Inorg. Chim. Acta 328 (2002) 247–253.

104 V. Balachandran, S. Rajeswari, S. Lalitha, J. Mol. Struct. 1007 (2012) 63–73.

105 G.B. Bagihalli, P.G. Avaji, S.A. Patil, P.S. Badami, Eur. J. Med. Chem. 43 (2008) 2639–2649.

106 C.R.A. María, C.L.S. Estefania, S. Jesús, P. Pelagatti, F. Zani, J. Inorg. Biochem. 99 (2005) 2231–2239.

107 C. Beauchamp, I. Fridovich, Anal. Biochem. 44 (1971) 276-287.

108 R.G. Bhirud, T.S. Shrivastava, Inorg. Chim Acta 40 (1990) 331-338.

109 Y. Singh, R.N. Patel, Y.P. Singh, A.K. Patel, N. Patel, R. Singh, R.J. Butcher, J.P. Jasinski, E. Colacio, M.A. Palacios, Dalton Trans. 46 (2017) 11860-11874.

110 R.N. Patel, S. Kumar, K.B. Pandeya, J. Inorg. Biochem. 89 (2002) 61-68.

111 B.H.J. Bielski, G.G. Shiue, Stanley Bajuk, J. Phys. Chem. 84 (1980) 830-833.

112 B. Verdejo, S. Blasco, E. García-España, F. Lloret, P. Gaviña, C. Soriano, S. Tatay, H. R. Jimenez, A. Domenech, J. Latorre, Dalton Trans. (2007) 4726-4737.

113 Q.X. Li, Q. Li, R. Chen, X.L. Yang, J.Y. Zhou, H.B. Xu, Inorg. Chem. Commun. 13 (2010) 1293-1295.

114 Y. Li, Z.Y. Yang, J.C. Wu, Eur. J. Med. Chem. 45 (2010) 5692-5701.

115 C. Amar, E. Vilkas, J. Foos, J. Inorg. Biochem. 17 (1982) 313-323.